

A fundamental method to quantify phase change in microalloyed steels

by

Nasseh Khodaie

A thesis submitted in partial fulfillment of the requirements for the degree of

Doctor of Philosophy

in

Materials Engineering

Department of Chemical and Materials Engineering

University of Alberta

©Nasseh Khodaie, 2018

Abstract

Microalloyed steels are a class of High Strength Low Alloy (HSLA) steels that contain a low concentration of carbon and up to 0.1% by weight of microalloying elements such as Ti, Nb, V and B. Microalloyed steels are known for their excellent combination of strength, toughness and weldability. The trio of properties makes these steels a material of choice for the pipeline industry. In addition to the above mentioned properties, pipelines can benefit from large wall thickness. This allows microalloyed steel pipes to be used at higher operating pressures that result in better productivity for the pipeline. However, manufacturing heavy sections of high strength microalloyed steels is hindered by inhomogeneous cooling cycles through the thickness of the plate. This results in non-homogeneous mechanical properties that stem from differences in phase transformations which depend on the cooling conditions.

The issue with non-homogenous phase transformations is more pronounced for higher strength grades of microalloyed steel since the need for higher strength dictates that transformations occur at lower temperatures which necessitates employing higher cooling rates on the runout table. These higher cooling rates result in an even more complex cooling cycle that includes a period of heating in the near surface layers that could induce auto tempering.

To understand the effect of the complex cooling cycle on the kinetics of phase transformations, an analysis tool is designed that can calculate the amount of phase transformation and product type using dilatometry data. This computer code is named the Master Fitter program and it executes an algorithm called Unit Cell Dilation. The Unit Cell Dilation technique is capable of calculating the amount of phase transformation considering the compositional changes to the product and austenite phases during phase transformation. It is shown that the results generated by the Master Fitter program agree with phase content measurements using quantitative metallography.

Preface

This thesis is the original work of Nasseh Khodaie. The dilatometry data used in this research is collected using the facilities at Canmet Materials, Hamilton Canada. Chapter 3 of this thesis is published as N. Khodaie, D.G. Ivey, H. Henein, Extending an empirical and a fundamental bainite start model to a continuously cooled microalloyed steel, *Mater. Sci. Eng. A.* 650 (2016) 510–522. Chapter 4 of this thesis is published as on the published article of N. Khodaie, D.G. Ivey, H. Henein, Unit cell dilation technique for analyzing dilatometry data in microalloyed steels, *Mater. Charact.* 135 (2018) 84–95.

To my late father and loving mother who never lost faith in me

and

To the love my life, Maryam, whose patience in living with this weirdo is off the charts

Acknowledgements

I would like to thank my professors, advisors and role models Professors Dr. Hani Henein and Dr. Douglas Ivey for their patience, guidance and contributions. The generous financial support of EVRAZ North America Inc. and the Natural Sciences and Engineering Research Council of Canada (NSERC) has been essential for this research work. My special gratitude goes to Dr. Fateh Fazeli and Dr. Benoit Voyzel of CanMet Materials for conducting the dilatometry measurements and Dr. Shahrooz Nafisi of EVRAZ for assisting with microstructural analysis. I would like to thank Dr. Pouya Delshad Khatibi, Dr. Ata Kamyabi, Dr. Arash Ilbagi and Ms. Katherine Johnson and all of my friends and colleagues in our research group who have been a great source of knowledge and inspiration. Finally, I must thank Dr. Abolfazl Noorjahan and Dr. Mehdi Towhidi for their help with MATLAB and Python programming languages.

Table of Contents

Abstract	ii
Preface.....	iii
Acknowledgements.....	v
List of figures	ix
List of tables	xiii
Chapter 1 Introduction	1
1.1 Pipeline steel	1
1.2 Statement of the problem.....	3
1.3 Outline of the thesis	4
Chapter 2 Literature review	6
2.1 Microalloyed steels and thermo-mechanical controlled processing (TMCP)	6
2.2 Phase transformation of austenite to ferrite in microalloyed steels	10
2.2.1 Redistribution of alloying elements	12
2.2.2 Microstructure development in microalloyed steels	16
2.3 Quantification of microstructure	22
2.4 Strengthening mechanisms	24
2.4.1 Dislocation strengthening	26
2.4.2 Solid solution strengthening	27
2.4.3 Precipitation strengthening.....	33
2.4.4 Grain boundary strengthening.....	38
2.4.5 Overall strength.....	40
Chapter 3 Extending an empirical and a fundamental bainite start model to a continuously cooled microalloyed steel.....	44
3.1 Introduction.....	44
3.2 Experimental procedure.....	46

3.3 Results and discussion	49
3.3.1 Dilatometry and kinetics of transformation	49
3.3.2 Evolution of microstructure	51
3.3.3 Observed microconstituents	56
3.3.4 Measurement of phase fractions using quantitative metallography.....	62
3.3.5 Continuous cooling and bainite start temperature.....	62
3.4 Summary	80
Chapter 4 Unit cell dilation technique for analyzing dilatometry data.....	81
4.1 Introduction.....	81
4.1.1 The lever rule.....	82
4.2 Experimental procedure.....	83
4.3 Results	85
4.4 Discussion.....	86
4.4.1 Continuous sequential phase transformation (CSPT)	86
4.4.2 UCD algorithm	90
4.4.3 Determination of product type(s)	92
4.4.4 Volume per atom.....	93
4.4.5 Multiple phase transformation	98
4.4.6 Implementation of UCD algorithm.....	99
4.4.7 Convergence.....	103
4.5 Application of the UCD algorithm	104
4.5.1 Steel X80-N	104
4.5.2 Steel X80-K.....	108
4.5.3 Sensitivity analysis of Master Fitter	112
4.6 Advantages and disadvantages of UCD algorithm compared with alternatives.....	120
4.7 Summary	122
Chapter 5 Conclusions and recommendations for future work.....	124

5.1 Conclusions.....	124
5.2 Recommendations for future work.....	125
References.....	127
Appendix.....	141
A1- Calculation of T_0 and T'_0	141
A-2 Computer codes.....	142
A2-1 Master Fitter Program	142
A2-2 Master Fitter	144
A2-3 Result Saver.....	187
A2-4 Data Plotter.....	190
A2-5 Data-set Conditioner.....	191
A2-6 Cython tools.....	196

List of figures

Figure 1-1. Projection of operating pressure of North American natural gas pipelines. Data is obtained from reference [5].	2
Figure 1-2. Development of line pipe steels from 1950 to the early 2000s. DSAW denotes double submerged arc welding, a technique for welding plate into the pipe. SMLS denotes seamless pipe [6].	3
Figure 1-3. Evolution of microalloyed steels. TMCP denotes thermomechanical controlled processing, ACC denotes accelerated cooling and DQ denote direct quenching [7].	4
Figure 2-1. An example of TMCP for a microalloyed steel. T_s denotes the soaking temperature and A_{R1} denotes the temperature at which austenite begins transforming to pearlite during cooling.	6
Figure 2-2. Effect of austenite grain size and cooling rate on ferrite grain size after transformation. d_α and d_γ denote the ferrite and austenite grain size, respectively [25].	9
Figure 2-3. Evolution of austenite grain structure due to plastic deformation below T_{nr} . Samples are plastically deformed with strains of a) 0.2, b) 0.4 and c) 0.6. As the amount of deformation increases, the morphology of the austenite grains changes from equiaxed to elongated in the direction of rolling [24].	10
Figure 2-4. Fe-Fe ₃ C phase diagram [34].	11
Figure 2-5. Redistribution of alloying elements during transformation of austenite to ferrite [36].	15
Figure 2-6. a) PF in a Nb microalloyed steel [51]. b) QPF in an ultra low carbon steel containing 0.005 %C and 3 %Mn [50].	17
Figure 2-7. a) TEM image of lamellar pearlite in a Nb microalloyed steel. b) TEM image of degenerate pearlite in a Nb microalloyed steel [52].	18
Figure 2-8. Different types of bainite as classified by Zajac et al [54].	19
Figure 2-9. a) Microstructure of granular bainite consisting of large bainitic ferrite and blocky M/A. b) TEM image showing the micron size blocky M/A microconstituent in GB [56].	20
Figure 2-10. a) SEM micrograph of martensite and upper bainite in an Nb microalloyed steel cooled at 50°C/s. b) TEM image of upper bainite. Arrows show the thin austenite film between BF plates. c) TEM image of the martensite phase [56].	20
Figure 2-11. Lower bainite and martensite in a Nb-V microalloyed steel cooled from 900°C at 40°C/s. a) SEM micrograph and b) TEM image of lower bainite showing cementite precipitates in the lath [57].	21
Figure 2-12. Acicular ferrite in a) V microalloyed steel cooled at 4°C/s [56]. b) Ti killed weld metal. Black arrows point to large Ti containing inclusions that acted as intragranular nucleation sites for acicular ferrite [59].	22
Figure 2-13. Application of IQ map for phase content quantification for a dual phase steel [64].	24
Figure 2-14. Dislocation encountering an obstacle on its glide plane. τ is the applied shear stress on the dislocation line.	25
Figure 2-15. Interaction of substitutional impurity atoms with an edge dislocation. a) Impurity atom is smaller than the host atom and b) impurity atom is larger than the host atom [34].	28

Figure 2-16. Solid solution strengthening in different Copper binary alloys. a) Linear trend for strength gain with C23 (confirmation of Labusch theory for solid solution strengthening). b) Effect of the alloying element mismatch strength gain. This plot is shown on a log scale. The 4/3 slope of the trendline matches the exponent for ϵL suggested by Eq. 2-9 [77].	30
Figure 2-17. Change in yield strength as a function of a) weight percent of alloying elements and b) atomic percent of alloying elements. Reproduced based on the data found in the literature [2,83].	31
Figure 2-18. The strength of martensite (ferrite) as a function of carbon content. a) Hardness [87] and b) calculated yield strength as a function of the square root of C concentration.	32
Figure 2-19. Mechanism of dislocation looping [2].	34
Figure 2-20. Comparison of solubility limit product for microalloying precipitates [2].	37
Figure 2-21. a) Precipitation on dislocations in a Nb microalloyed steel. Left, bright field and right dark field image [92]. b) Rows of precipitates formed periodically on the moving phase boundary in a Ti-Mo microalloyed steel [98].	38
Figure 2-22. Dislocation pile-up emitted from source 1 in grain 1 creates enough local stress at the boundary to activate source 2 in grain 2.	39
Figure 2-23. Change in strength as a function of grain size $d - 12$. Line AB shows the effect of precipitation strengthening added to grain boundary strengthening. Line C shows the estimated GB strengthening effect when k in the Hall-Petch equation is increased [7].	41
Figure 2-24. The value of superposition exponent q is a function of critical bend angle for two different types of obstacles [114].	42
Figure 3-1 Optical images of the microstructure for as rolled plate at the mid-thickness, from which dilatometer samples were sectioned. a) Surface normal to WD. b) Surface normal to RD.	47
Figure 3-2. Schematic of thermal cycle used for the continuous cooling experiments.	48
Figure 3-3 Analysis of sample dilatometry data at a cooling rate of 10°C/s. a) Dilatometry curve. b) Calculated fraction transformed versus time. In this graph $t=0$ corresponds with $X=0.01$.	50
Figure 3-4. CCT diagram for the steel studied (X80-N). Start and finish lines were determined by 1% and 99% transformation criteria calculated from the dilatometry results.	51
Figure 3-5. Optical image of prior austenite grains after austenitization at 950°C for 15 minutes. The average grain size is 12.7 μm .	52
Figure 3-6. SE-SEM micrographs of the microstructures that form at different cooling rates. a) 1°C/s, b) 3°C/s, c) 10°C/s, d) 25°C/s, e) 30°C/s, f) 40°C/s.	55
Figure 3-7. SE-SEM micrograph of sample cooled at 1°C/s. Examples of QPF are shown.	56
Figure 3-8. SE-SEM micrograph showing nucleation of WBF on QPF during continuous cooling at 10°C/s. The dashed line appears to be the location of an annealing twin boundary within an austenite grain and the arrow shows the direction of progress of the transformation.	57
Figure 3-9. SE-SEM micrograph of sample cooled at 25°C/s. Elongated B/M with BF laths are present on both sides. Above the scale bar, lightly etched low angle boundaries of BF are visible.	58
Figure 3-10. SE-SEM micrograph of sample cooled at 10°C/s. Blocky B/M regions are marked by arrows.	59

Figure 3-11. Mechanism for formation of blocky B/M. a) Formation of allotriomorphic ferrite in the form of a partial ring. b) Growth of the partial ferrite ring. c) Reduction in temperature allows nucleation of B/M. d) SE-SEM image of ferrite and blocky B/M (marked by arrows) in a sample cooled at 3°C/s.	60
Figure 3-12. SE-SEM micrograph of sample cooled at 1°C/s. DP coexists with B/M in one prior austenite grain (outlined by dashed line). Arrows show the direction of growth of each microconstituent.	61
Figure 3-13. SE-SEM micrograph of the sample cooled at 1°C/s. Coexistence of QPF, DP and B/M within one prior austenite grain (outlined by dashed line) is shown. This micrograph suggests DP can nucleate at the α/γ interface.	62
Figure 3-14. Distribution of volume fraction of microconstituents for different cooling rates.	63
Figure 3-15. T_0 and T_0' as a function of carbon calculated for steel X80-N.	65
Figure 3-16. Calculated bainite start (B_s) temperature for the austenite phase versus time during transformation. Temperature and fraction transformed curves are plotted to help determine the time and phase fraction for the change in transformation from polygonal ferrite to bainite. The cooling rate is 10°C/s.	66
Figure 3-17. Calculation of the amount of austenite that transforms to QPF using the BIT method. B_s in this graph is calculated using Eq. 1 but could alternatively be calculated using T_0' . The cooling rate is 10°C/s.	67
Figure 3-18. Calculated volume fraction (using the BIT method) of PF/QPF as a function of cooling rate.	67
Figure 3-19. Example of inaccuracy of visual methods in distinguishing between bainite and polygonal ferrite. a) Sample isothermally transformed at 500°C. b) Higher magnification image of the flat area. Two BF plates and M/A platelets between them are visible.	68
Figure 3-20. Hardness vs volume fraction of polygonal ferrite measured using the BIT method. Results for both the empirical and fundamental methods of calculating B_s are shown. The linear trend line suggests that the rule of mixtures applies and the measured volume fractions for polygonal ferrite are correct regardless of the method used for calculating B_s . This provides support for the BIT method.	69
Figure 3-21. Concentration of C and N in ferrite under paraequilibrium.	73
Figure 3-22. a) TEM carbon extraction replica of the sample cooled at 10°C/s. b) Energy dispersive x-ray (EDX) spectra from the precipitates, indicating chemical composition of different precipitates. The Cu peak is from the Cu grid used to support the replica and the Si peak is from the C film.	76
Figure 3-23. Hardness of isothermally transformed samples. The transformation below 600°C and above the martensite start temperature of this steel (452°C) is bainitic. The average hardness in this temperature range is 253 HV which is close to calculated hardness of the mixed microconstituent using BIT analysis (247 HV).	78
Figure 3-24. Hardness vs QPF content for steels X80-K and Grade 80-L used for validation of BIT analysis.	78
Figure 3-25. CCT diagram for the steel studied (X80-N). Start and finish lines were determined by 1% and 99% transformation criteria calculated from the dilatometry results. Bainite start (narrow dashed lines) are calculated using the BIT method.	79
Figure 3-26. CCT diagram from Figure 3-25 with added transformed phase fraction points.	79
Figure 4-1. Example of dilatometry data for the austenite to ferrite transformation. The grey line is the actual dilatometer data and the black straight lines show the extrapolated austenite and ferrite dilation lines, as considered in	

the lever rule. The dashed line shows a schematic extrapolation of the austenite line, considering the effect of carbon accumulation in austenite.	83
Figure 4-2. Normalized dilation graphs obtained at different cooling rates for steel X80-N.	86
Figure 4-3. Sequential phase transformation of austenite to polygonal ferrite and bainitic ferrite.	91
Figure 4-4. Flowchart for the UCD algorithm.	94
Figure 4-5. Temperatures used for determining product types that form within a time step. For steel X80-N.	95
Figure 4-6. Fraction transformed as a function of temperature calculated using different intervals for steel X80-N at the cooling rate of 5°C/s. Smaller intervals mean smaller time steps. This figure shows that the UCD algorithm results converge as the time step become smaller.	104
Figure 4-7. Phase content of steel X80-N calculated by the Master Fitter program.	105
Figure 4-8. Comparison of calculations made using the UCD algorithm with quantitative metallography measurements for steel X80-N. UCD stands for unit cell dilation technique and LR stands for lever rule method.....	106
Figure 4-9. Continuous cooling at 1°C/s. Sequential phase transformation is confirmed by the formation of a linear region (dashed line) at about 600°C.	107
Figure 4-10. Product volume fraction vs temperature at 1°C/s calculated using UCD and the lever rule.	107
Figure 4-11. Lattice parameter of austenite as a function of temperature at different cooling rates. Arrows show the point at which the carbon content of austenite begins following the solubility limit of carbon in austenite with respect to cementite.	108
Figure 4-12. Comparison of calculations made using the UCD algorithm with quantitative metallography measurements for steel X80-K. Reproduced with permission from [132].	110
Figure 4-13. CTE of austenite during cooling after austenitization for steels X80-K and X80-N.	110
Figure 4-14. Effect of elimination of data collected at 1°C/s on dilation curve (top) and calculated fraction of transformation (bottom).	113
Figure 4-15. Effect of elimination of data collected at 3°C/s on dilation curve (top) and calculated fraction of transformation (bottom).	114
Figure 4-16. Effect of elimination of data collected at 10°C/s on dilation curve (top) and calculated fraction of transformation (bottom).	115
Figure 4-17. Effect of elimination of data collected at 25°C/s on dilation curve (top) and calculated fraction of transformation (bottom).	116
Figure 4-18. Effect of elimination of data collected at 30°C/s on dilation curve (top) and calculated fraction of transformation (bottom).	117
Figure 4-19. Effect of elimination of data collected at 40°C/s on dilation curve (top) and calculated fraction of transformation (bottom).	118
Figure 4-20. Sensitivity analysis of Master Fitter program. The figures show the relative change in the material parameter as a function of elimination of a data file from the complete dataset.	119
Figure 4-21. Analysis of the microstructure needed to ensure reasonable results from Master Fitter.	120

List of tables

<i>Table 2-1. Strength increase due to addition of 1 wt% for alloying elements for ferritic steels - all values are in MPa.</i>	<i>31</i>
<i>Table 2-2. Hall-Petch parameters found in the literature for steel.....</i>	<i>40</i>
<i>Table 3-1. Chemical composition (wt%) of the steel used in this study.....</i>	<i>46</i>
<i>Table 3-2. Chemical composition (wt%) of Grade 80-L and X80-K steels used for validation of BIT analysis.....</i>	<i>49</i>
<i>Table 3-3. Hardness of microconstituents in steel X80-N calculated using linear regression of hardness vs calculated PF/QPF content using BIT method.....</i>	<i>70</i>
<i>Table 3-4. Strengthening mechanisms involved in microalloyed steel</i>	<i>71</i>
<i>Table 3-5. Chemical composition of austenite phase after austenitization in percent by weight.....</i>	<i>72</i>
<i>Table 3-6. Solid solution strengthening coefficients of common alloying elements for steel [2,74]</i>	<i>73</i>
<i>Table 3-7. Strengthening effect of precipitates found in continuously cooled X80-N steel - Min and Max values are calculated based on the standard deviation of the measured precipitate diameter.....</i>	<i>75</i>
<i>Table 3-8. Strengthening mechanisms involved in X80-N microalloyed steel</i>	<i>76</i>
<i>Table 4-1. Chemical composition (wt%) of steels X80-N and X80-K used in this study</i>	<i>84</i>
<i>Table 4-2. Change in lattice parameter of ferrite derivatives as a function of carbon content.....</i>	<i>96</i>
<i>Table 4-3. Material parameters used by the Fitter program before and after optimization by the Master Fitter*</i>	<i>105</i>
<i>Table 4-4. Material parameters used by the Fitter program before and after optimization by Master Fitter*</i>	<i>109</i>

Chapter 1 Introduction

1.1 Pipeline steel

Pipeline steels in North America are named according to the American Petroleum Institute (API) standard. The designations are done based on the minimum yield strength of the steel in kilopounds per square inch (ksi), i.e., API X80 specifies a steel that has minimum 80 ksi yield strength which is equal to 555 MPa [1]. Microalloyed steels are the most common type of steel used for line pipes to transport oil and gas. Microalloyed steels are a group of high strength low alloy (HSLA) steels which contain small amounts-usually less than 0.1% by weight- of microalloying elements including Nb, Ti and V[2]. What makes microalloyed steels uniquely suitable for pipeline application is the way these steels are strengthened. Unlike plain carbon and most alloy steels, pipeline microalloyed steels are not designed to be strengthened by the formation of cementite (Fe_3C) or martensite (α'), but primarily by grain refinement and to a lesser degree by the presence of nano precipitates. Although the occurrence of the two mentioned microconstituents can increase strength of the microalloyed steels, neither are considered as major strengthening features for microalloyed steels. Both Fe_3C and α' require moderate to high carbon content to produce a significant contribution to strength. Since high carbon content is not needed to strengthen microalloyed steels, carbon content can be lowered significantly. As a result of this carbon content reduction, microalloyed steels exhibit excellent resistance to formation of hard phases during welding which are detrimental to the toughness of welded parts. This gives microalloyed steels excellent weldability. In addition to weldability, microalloyed steels exhibit good toughness after rolling without annealing processes such as tempering. This high toughness originates from the small grain size in the microalloyed steels and their chemical composition design as well as tight control of the steel making process. These properties make microalloyed steels a material of choice for pipelines, pressure vessels, marine structures and the automotive industry.

In pipelines, it is beneficial to increase the pressure of the media inside the pipe. At higher working pressure, more of the media can be pumped for longer distances before needing another pumping station to compensate for the pressure drop that occurs as the media travels along the pipeline. Additionally, at higher gas pressures, the turbine that pumps the gas runs at higher efficiency resulting in reduction of gas transport costs [3]. All these factors reduce the installation and operation costs of a pipeline, especially for long transport lines. As a result, there is a demand for pipes that can tolerate higher internal pressures. Figure 1-1 shows the projection of the operating pressure of North American pipeline based on the available data between 1920 and 2010. Increasing a pipe's working pressure requires either increasing the thickness of the pipe or increasing the yield strength of

the pipe material. Although increasing strength and thickness of the microalloyed steel used for pipelines is done primarily for economic reasons, it also introduces new functionality to the steel. Higher strength steels exhibit higher resistance to collapse under high external pressures. Pipe collapse is especially a risk for large diameter pipes. High strength/thickness pipes are suitable for applications such as deep sea pipelines or underground pipelines in heavily populated areas [4]. Figure 1-2 shows the development of line pipe steels since the 1950s until the year 2000. This figure shows the response of the steel industry to market demand for higher strength steels.

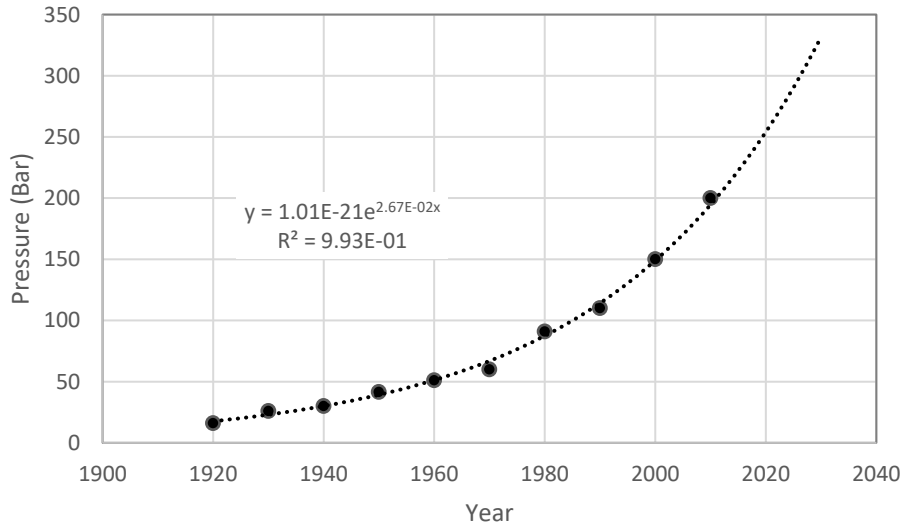


Figure 1-1. Projection of operating pressure of North American natural gas pipelines. Data is obtained from reference [5].

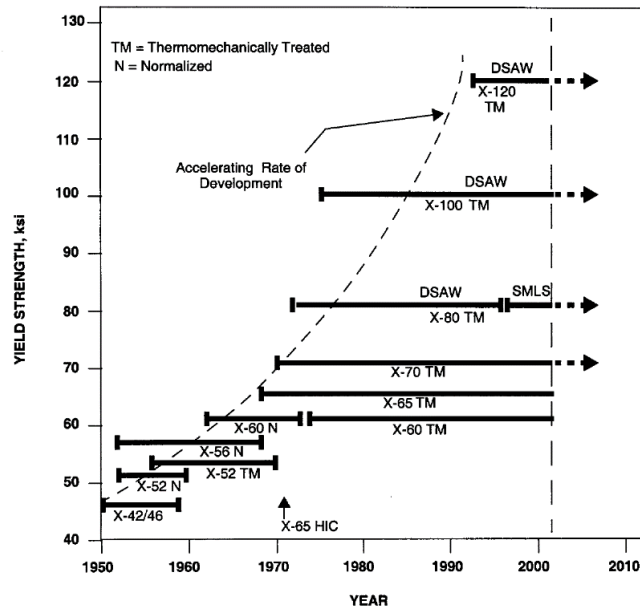


Figure 1-2. Development of line pipe steels from 1950 to the early 2000s. DSAW denotes double submerged arc welding, a technique for welding plate into the pipe. SMLS denotes seamless pipe [6].

1.2 Statement of the problem

Microstructure is the primary factor in determining the mechanical properties of any steel and microalloyed steels are no exception. Over the years the microstructure of microalloyed plates and strips has changed from simple ferrite-pearlite produced by normalizing to a complex multicomponent microstructure produced by sophisticated cooling systems capable of accelerated cooling and even heating. Figure 1-3 shows the evolution of microstructure of microalloyed steels. The final microstructure of microalloyed steel is controlled primarily by the austenite phase transformation. As so, an enormous amount research is devoted to understanding the parameters that affect the phase transformation of austenite in microalloyed steels. One of the most used methods in studying phase transformation of steels is thermomechanical simulation using dilatometry instruments such as the Gleeble. In dilatometry analysis, a specimen of known dimensions is subjected to a thermal or thermomechanical cycle and its temperature and dimensional changes are recorded as a function of time. Using dilatometry data it is possible to accurately measure/calculate some basic information such as transformation start and finish temperatures and thermal expansion coefficient with minimal effort for a given cooling or heating condition. However, more useful data such as transformation kinetics needs a more thorough analysis. Traditionally, the lever rule has been used to calculate kinetics from dilatometry data, but as discussed later in this thesis (see Sections 4.1.1 and 4.5.1) this method can produce inaccurate kinetics data for complex

transformation of austenite in microalloyed steel. There are other methods proposed to analyze dilatometry data that are discussed in Section 4.6. A critical review of these methods presented in this section shows the limitations of these methods. As such, the goal of this research is improving analysis methods for dilatometry experiments to overcome limitations of the previous methods.

1.3 Outline of the thesis

This thesis is a paper-based thesis. The second chapter includes a literature review on the subjects that closely relate to this research but are not covered in the papers that constitute the third and fourth chapters. The third chapter is based on a paper titled “Extending an empirical and a fundamental bainite start model to a continuously cooled microalloyed steel”. It is shown that by considering the effect of carbon rejection from polygonal ferrite to austenite, the temperature at which the austenite transformation changes from polygonal ferrite (PF) to bainitic ferrite (BF) can be determined. This method is named Bainite Intersect Temperature (BIT). Using the BIT method, the volume fraction of PF is calculated from the dilatometry data. It is shown that a linear relationship exists between the volume fraction of PF calculated with the BIT method and the hardness of the specimen. This implies that the rule of mixtures applies to microalloyed steels when considering a two component mixture in which the components are PF and mixed bainitic ferrite and bainite/martensite (B/M).

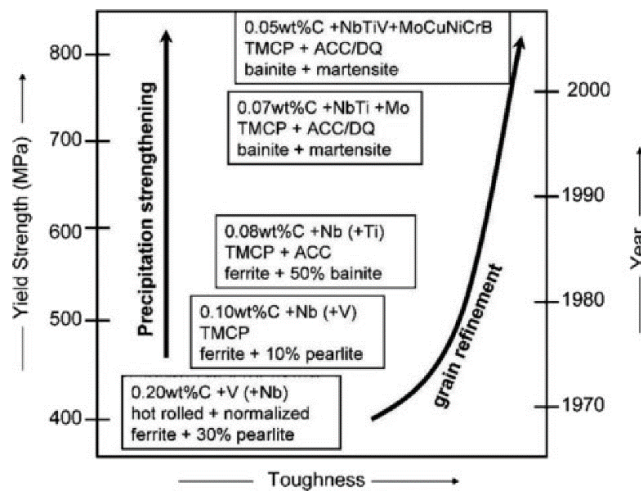


Figure 1-3. Evolution of microalloyed steels. TMCP denotes thermomechanical controlled processing, ACC denotes accelerated cooling and DQ denote direct quenching [7].

The fourth chapter is a paper titled “Unit cell dilation technique for analyzing dilatometry data”. This paper is an extension of the BIT method proposed in the first paper. In this paper, it is shown that the lever rule is not

an adequate method for analyzing dilatometry data when carbon redistribution takes place and there is more than one possible product phase (i.e., polygonal ferrite, bainitic ferrite, martensite, etc.). This carbon redistribution during transformation has a strong effect on the physical properties of austenite. As a result, during the diffusive transformation to ferrite, the properties of austenite continuously change. This affects the calculations when relating observed dilation to phase transformation. Using the findings of the first paper an algorithm called “Unit Cell Dilation” (UCD) is proposed. This algorithm considers the effect of carbon redistribution on the lattice parameter of ferrite and austenite, the coefficient of thermal expansion of austenite and all the product phases, and transition temperature between product phases. The UCD algorithm is implemented as the computer code “Fitter” and its optimization capable version “Master Fitter”. The source code for the Master Fitter program along with a short user manual is included in Appendix section.

The fifth chapter provides the Conclusions and Recommendations for Future Work followed by references and the Appendix. The Appendix includes relevant information that is not explained with enough detail in Chapters three and four. This includes detailed calculations and source codes for the algorithm developed for this research. Included with source codes are user guide that should be used to run the codes properly.

Chapter 2 Literature review

2.1 Microalloyed steels and thermo-mechanical controlled processing (TMCP)

Microalloyed steels need microalloying elements to achieve their unique properties, but just adding microalloying elements is not enough. Precise control of temperature and deformation during hot working and cooling processes is also needed for microalloyed steels to achieve good strength and toughness. This technology is named thermo-mechanical controlled processing or TMCP for short. Figure 2-1 shows a generic example of TMCP design for microalloyed steels.

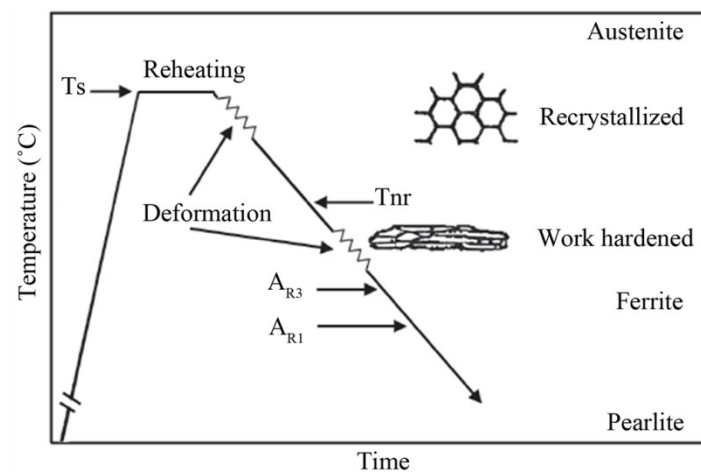


Figure 2-1. An example of TMCP for a microalloyed steel. T_s denotes the soaking temperature and A_{R1} denotes the temperature at which austenite begins transforming to pearlite during cooling.

Generally, TMCP for rolling consists of 5 steps:

1. **Reheating:** This is also known as soaking, during which steel is kept at high temperature ($\sim 1200^\circ\text{C}$) for enough time to reduce the effects of segregation during continuous casting and dissolve the microalloying precipitates[8]. TiN is the most stable of the microalloying precipitates and only partially dissolves during reheating. Although in TMCP it is preferred to have all of the microalloying elements in solid solution form before the hot deformation step, the undissolved TiN can have the beneficial effect of inhibiting the excessive growth of austenite grains during reheating. Excessive austenite grain growth during reheating can impact the ability of the rough rolling step in reducing austenite grain size before finish rolling.

2. **Hot deformation** (aka rough rolling): Rough rolling takes place in temperatures lower than the reheating temperature and above the non-recrystallization temperature (T_{nr}). T_{nr} is the temperature below which no recrystallization can happen during hot rolling. The importance of T_{nr} will be explained in the warm/finish rolling section. The goal of hot deformation is achieving the final shape of the product while improving the integrity and continuity of steel by closing the porosity and breaking the larger inclusions/precipitates that might be in the microstructure. Rough rolling also reduces the austenite grain size. As the temperatures for rough rolling are higher than T_{nr} , plastic deformation at this stage is inevitably accompanied by recrystallization of austenite [2]. This is especially necessary for microalloyed steels due to excessive austenite grain growth after long soaking times at high reheating temperatures. It will be explained later that smaller grain size austenite transforms into smaller grain size ferrite, ultimately improving the strength and toughness of the final product.
3. **Finish rolling**: This step is done at temperatures lower than T_{nr} . The goal of finish rolling is to produce heavily deformed austenite. This will be discussed later, but at temperatures lower than T_{nr} recrystallization of steel practically stops. Since no recrystallization occurs, the plastically deformed microstructure retains the deformed austenite grains. It will be explained later that heavily deformed austenite is vital for improving the mechanical properties of microalloyed steel.
4. **Accelerated cooling**: This step is employed to prevent the austenite to ferrite transformation at higher temperatures. At lower transformation temperatures finer ferrite forms [9]. The effect of temperature on ferrite grain size is explained using nucleation and growth theory for diffusional transformations later in this chapter. In addition to ferrite grain refinement, accelerated cooling can alter the transformation products from (quasi-)polygonal ferrite to bainitic ferrite or martensite. These low-temperature microstructures have higher strength which is beneficial in producing higher strength microalloyed steels.
5. **Coiling**: This step allows the steel to spend time at temperatures below A_{r3} (temperature at which austenite begins transforming to ferrite during cooling). Coiling temperature can be altered to allow precipitation in the ferrite phase and to lesser extent completion of any slow transformation, e.g., high carbon retained austenite to bainite. Precipitates that form in ferrite are more effective in strengthening than those formed in austenite. This difference is mostly due to the fact that precipitates that form in austenite can grow to larger diameters due to the higher temperature and higher diffusion rate in austenite. It will be shown in the “Precipitation strengthening” section that fine precipitates are more effective in increasing the strength than larger ones. Precipitates that form during coiling are usually fine complex microalloying carbonitrides [10–14] that may contain

Mo and Cr or Cu precipitates, if Cu is incorporated in the chemistry of steel [15–18]. Coiling can also be used to induce or control the redistribution of elements, especially carbon, to modify retained austenite [19]. High carbon retained austenite can improve the strain hardening rate and uniform ductility of microalloyed steel [20].

The primary strengthening mechanisms in most microalloyed steels is grain boundary strengthening achieved by reduction of the ferrite grain size [21]. In TMCP steels, ferrite grain refinement is done by increasing the ratio of nucleation to growth rate during the austenite to ferrite transformation. The logic behind this approach is very simple; create more grains before all the austenite is consumed by the previously created ferrite grains. Therefore in TMCP the goal is to increase the nucleation rate and to reduce the growth rate.

Growth rate can be reduced by alloying with elements that reduce the transformation driving force (austenite stabilizers such as Ni, Mn and C). However, reducing the driving force of transformation reduces the nucleation rate as well which is not favorable for grain refinement [9]. The most effective method to reduce the growth rate of diffusional transformations without compromising the nucleation rate is reduction of the transformation temperature [22] which is widely used in TMCP in the form of accelerated cooling. Another method to reduce growth rate without reducing the nucleation rate is by precipitation of Nb bearing precipitates on the austenite/ferrite phase boundary [23].

Increasing the nucleation rate is possible by reducing the critical energy for nucleation or by increasing the number of nucleation sites, i.e., austenite grain boundary area. The former is accomplished by accelerated cooling and the latter is achieved by austenite grain refinement. It is known that ferrite nucleates heterogeneously on austenite grain boundaries and deformation bands inside the austenite grains[24]. Figure 2-2 shows the effect of cooling rate and austenite grain size on the resulting ferrite grain size after phase transformation.

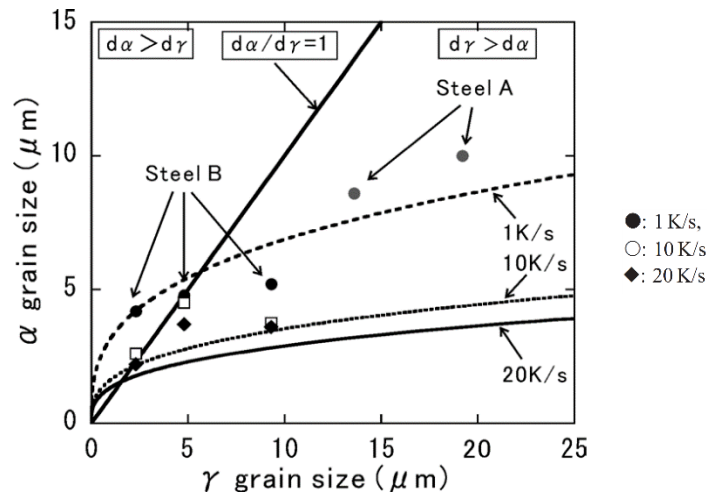


Figure 2-2. Effect of austenite grain size and cooling rate on ferrite grain size after transformation. $d\alpha$ and $d\gamma$ denote the ferrite and austenite grain size, respectively [25].

In commercial microalloyed steels, austenite grain refinement is achieved by plastically deforming austenite grains. This is a purely geometrical manipulation to elongate austenite grains to increase grain boundary area. In addition to elongated grains, plastic deformation greatly increases dislocation density and creates deformation bands. Deformation bands have been shown to provide intra-granular nucleation sites for ferrite [26]. The added dislocations increase the energy of austenite to which the system responds by recrystallizing to reduce the dislocation density. Recrystallization and subsequent grain growth remove the added grain boundary area and deformation bands required for increasing nucleation rate. This is where microalloying elements play their major role. Ti and Nb, in the presence of C and N, can hinder or even completely stop recrystallization through a process called strain induced precipitation (SIP). SIP occurs when plastic deformation creates a high dislocation density. The added dislocations act as high energy nucleation sites which reduce the energy barrier for nucleation, thereby increasing the nucleation rate of the precipitates. Additionally, dislocations provide high diffusion paths along the dislocation core which increase the rate at which precipitating elements can be supplied to the precipitates, thereby enhancing the growth rate. The overall effect is orders of magnitude increase in the precipitation rate in the presence of dislocations [23,27]. The precipitates created by SIP stop the propagation of austenite grain boundary during recrystallization.

The effectiveness of the microalloying carbonitrides in inhibiting recrystallization of austenite depends on the amount of the precipitating elements, temperature, rolling parameters and even concentration of non precipitating elements such as Mn [28–31]. As introduced before, the temperature below which no recrystallization can occur is called non-recrystallization temperature or T_{nr} . The hot deformation done above T_{nr} can only increase austenite grain boundary area moderately and is not considered a primary factor in the final ferrite grain size. In contrast, the deformation below T_{nr} is perhaps the most important factor in ferrite

grain refinement [2]. In rolling, deforming the austenite grains below T_{nr} creates a unique microstructure known as a pancaked microstructure. Figure 2-3 shows the evolution of equiaxed grains to pancaked grains as a result of hot deformation. The pancaked austenite grains provide a lot of grain boundary area for nucleation of ferrite. Higher nucleation rates translate to high grain boundary strengthening [32]. In Section 2.4, strengthening mechanisms utilized in microalloyed steels are discussed in detail.

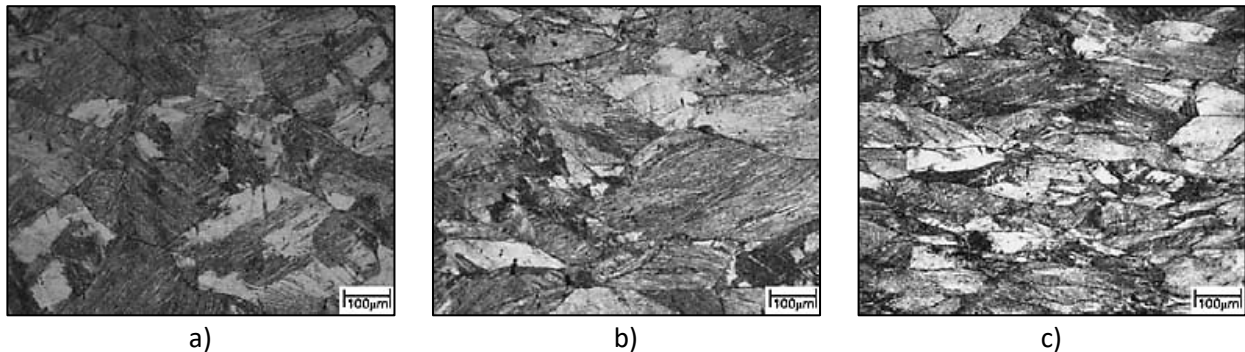


Figure 2-3. Evolution of austenite grain structure due to plastic deformation below T_{nr} . Samples are plastically deformed with strains of a) 0.2, b) 0.4 and c) 0.6. As the amount of deformation increases, the morphology of the austenite grains changes from equiaxed to elongated in the direction of rolling [24].

2.2 Phase transformation of austenite to ferrite in microalloyed steels

Most of the mechanical properties of pipeline microalloyed steels are controlled or affected by the phase transformation of austenite during cooling to room temperature after hot deformation. A typical microalloyed steel containing more than 0.02 wt% carbon that is cooled at a very slow rate will transform under near thermodynamic equilibrium conditions. Under equilibrium conditions, the transformation of austenite begins at the A3 temperature by nucleation of ferrite on the austenite grain boundaries or triple points and ends at the A1 temperature by simultaneous formation of cementite and ferrite in the form of pearlite. Equilibrium A1 and A3 temperatures are functions of the chemical composition of the steel. In plain carbon steels, the A1 and A3 temperatures can be found in the $Fe - Fe_3C$ phase diagram (Figure 2-4). In alloy steels, A1, A3 and Acm can be calculated using empirical formulas or using CALPHAD software [33]. Using the lever rule with Figure 2-4 to calculate phase content of a typical 0.04-0.07 wt% carbon microalloyed steel at room temperature shows that the major equilibrium microconstituent in microalloyed steels is a very low carbon ferrite; however, in a more practical setting than extremely slow cooling, the transformation does not take place at equilibrium conditions.

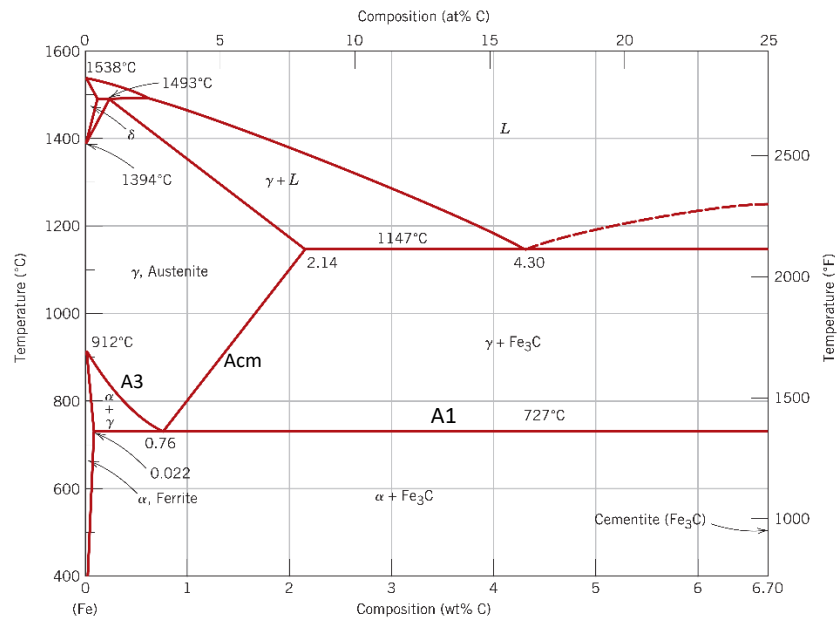


Figure 2-4. Fe-Fe₃C phase diagram [34].

The deviation from equilibrium at higher cooling rates is created by the kinetic aspect of the phase transformation. The kinetics of a phase transformation are controlled primarily by the mechanism of the phase transformation. Phase transformation of austenite to ferrite can happen by two mechanisms – reconstructive or displacive. These mechanisms differ in the way atoms (Fe and substitutional atoms) are transferred from the austenite to ferrite phase.

In reconstructive transformation, lattice atoms diffuse from austenite to ferrite and during the process lose connection to their immediate neighboring atoms in the austenite and form new bonds in the ferrite phase [35]. In microalloyed steels, it is believed that transformation of austenite to allotriomorphic ferrite is reconstructive. The microstructure resulting from the full transformation to allotriomorphic ferrite consists of polygonal or quasi polygonal ferrite (PF/QPF) grains. One of the features of the ferrite created by a reconstructive mechanism is its low density of crystalline defects such as dislocations. This is an important feature since in TMCP microalloyed steels the austenite phase undergoes a significant amount of plastic deformation and contains a high dislocation density which is not inherited by allotriomorphic ferrite[36].

In displacive transformations, atoms join the new phase by a coordinated movement of a large number of atoms. As a result, the immediate neighboring lattice atoms are the same before and after transformation [22]. In steels, this type of transformation is observed in martensite, bainite and acicular ferrite and is theorized for Widmanstätten ferrite [36,37]. Unlike reconstructive transformation of austenite to ferrite that only creates a volumetric expansion around the ferrite phase due to lower atomic packing factor of BCC compared with FCC

unit cell of austenite, the displacive transformation to martensite is accompanied by a large shear strain in addition to the volumetric expansion. The volumetric expansion observed in martensite is more than the expansion of a reconstructive ferrite. This extra expansion is caused by carbon supersaturation. This additional volumetric expansion creates a compressive stress field in both austenite and martensite. This compressive stress field acts as a barrier and reduces the driving force available for transformation. The amount of this stress field is directly related to the amount of martensite that is formed. This means after a certain amount of displacive transformation, the buildup of the compressive stress field reaches a condition that it balances the chemical driving force for the austenite transformation. This reduces the overall driving force for transformation, possibly to less than the amount required for displacive transformation, which results in halting of the displacive transformation. At this point, further transformation is only possible if more chemical driving force is provided by either lowering the temperature or by a reduction of the mechanical barrier, i.e., the compressive stress field. It is well known that progression of the martensitic transformation in steel is linked to reduction in the temperature and unlike diffusive transformation of ferrite, isothermal holding does not increase martensite volume fraction. This is the reason martensitic reaction is often called an athermal reaction [9,22,38].

The displacive transformation of bainite is different than that of martensite. Unlike martensite, bainite can transform isothermally. Bainite forms by intermittent formation and cessation of bainitic ferrite plates or laths. These plates form by a displacive mechanism. Bhadeshia believes the reason for stoppage of bainitic ferrite growth is the accumulation of dislocations in the adjacent austenite due to the plastic accommodation of shear strain during the displacive transformation[36,39]. In bainite, after the displacive transformation stops, carbon leaves the supersaturated state by diffusing to the remaining austenite (upper bainite) or by forming carbide precipitates inside the transformed region (lower bainite).

With regards to transformation of bainite and Widmanstätten ferrite in steel, it should be mentioned that an alternative transformation path based on a reconstructive mechanism is also proposed [40]. Both theories have been partially successful in explaining the attributes of the bainitic reaction such as incomplete transformation phenomena [36,41,42]. At the same time current versions of both theories have been shown to fail as well [43,44]. However, there seems to be more evidence in support of the displacive theory for the bainitic reaction[45,46].

2.2.1 Redistribution of alloying elements

An important phenomenon to consider for both reconstructive and displacive transformation of steels is the redistribution of alloying elements during transformation. In the presence of both α and γ phases, the

alloying elements redistribute to reduce the free energy of the system. This redistribution begins by diffusion of elements across the α/γ phase boundary under the chemical potential difference at two sides of the boundary. It can be expected that the diffusion rate through the boundary is much greater than diffusion rates in either of the crystals on both sides of the boundary. The diffusion through the boundary continues until the chemical potential of the element on the austenite side of the boundary is equal to that on the ferrite side. Following rapid diffusion across the boundary, slower diffusion into the center of the grain takes place. The driving force for this diffusion is the concentration gradient from high grain boundary concentration to the lower concentration of the element in the center of the austenite grains. These two diffusion processes take place while the phase boundary itself is moving due to progression of the phase transformation. For elements that have lower energy in austenite than ferrite, such as C, Mn, Ni, Al and N, there is a competition between the diffusing elements and the moving phase boundary, both of which are moving toward the center of the austenite grain. For a hypothetical element X three classes for redistribution can be defined:

1. The phase boundary moves very fast with respect to element X's diffusion rate across the boundary and diffusion in the austenite phase. In this case, before the atoms of element X can diffuse, the phase boundary moves and element X will be supersaturated in ferrite. In class 1, no local or bulk redistribution can occur.
2. Element X diffuses fast through the boundary, but slowly in austenite compared with the speed at which the phase boundary moves. This will result in formation of a pile up of element X in front of the moving boundary. The amount of the pile up is determined by the equilibrium between the amount of alloying element forced into ferrite due to the motion of the boundary and the amount that diffuses across the boundary back to the austenite phase under chemical potential gradient across the phase boundary. In this class, boundary redistribution can occur locally but bulk redistribution will not happen. The result of this local redistribution is a drop in the driving force for transformation. In this class of redistribution, travel speed of the phase boundary is determined by the diffusion rate if element X is in the austenite phase.
3. Element X diffuses much faster across the phase boundary and in the austenite phase than the speed of the moving phase boundary. In this case bulk redistribution can happen and the two phases would be at equilibrium with each other. The kinetics of transformation are controlled by the amount of driving force available for transformation, which determines the phase boundary travel speed.

These three classes are the extreme cases for the competition of two diffusional processes for element X and the motion of the phase boundary. In reality the concentration of the alloying element at the grain boundary

is determined by a dynamic equilibrium between the amount of the alloying element being left behind by the moving phase boundary and the rate of diffusion across the boundary and through the austenite. For a detailed review of mathematical treatment of this equilibrium, readers are referred to the review by Goune' et al. [47].

In commercial steels with multiple alloying elements, the mentioned three redistribution classes can happen for each alloying element. Considering the number of alloying elements in commercial steel, this can make analysis of the redistribution of alloying elements rather difficult. However, in general due to similarities between diffusional properties of substitutional and interstitial alloying elements, it is possible to simplify the analysis by considering alloying element type rather than the individual elements. Using this approach five scenarios have been identified to happen to the alloying elements during phase transformation of steel:

1. At low undercooling, the phase boundary moves very slowly. As a result, class 3 will happen for both interstitial and substitutional elements. This case is called local equilibrium (LE) partitioning. This is observed at temperatures close to the A3 temperature of the steel.
2. At moderate undercooling, the phase boundary moves faster than the interstitial elements but not too fast compared with the diffusion rate of interstitial elements. In this case, substitutional elements would fall in the second redistribution class but interstitials would still behave as class 3. This case is called local equilibrium negligible partitioning (LENP, NPLE or NP-LE). It is believed that allotriomorphic ferrite, especially in the later stages of growth, exhibits LENP redistribution in the presence of Mn and Ni [47]. However, the early stages of nucleation are experimentally shown to follow the paraequilibrium partitioning model which is explained next [48].
3. At higher under cooling, the phase boundary moves much too fast for substitutional elements to exhibit any local diffusion across the boundary so they are class 1, but interstitials can still redistribute freely and achieve equal chemical potential at both sides of the phase boundary. This condition is called paraequilibrium (PE). Upper bainite [36] and prior mentioned allotriomorphic ferrite in the early stages of phase transformation exhibit this type of partitioning.
4. At temperatures lower than the upper bainite transformation, lower bainite forms. This phase is a gradual transition from zero carbon supersaturation of upper bainite to full supersaturation of martensite. This transition state is characterized by partial supersaturation of carbon in the ferrite. In this case, interstitials exhibit a class 1 redistribution and interstitials show a transition from class 2 redistribution to class 1 as the temperature drops to Ms.
5. At extremely high phase boundary moving speeds; e.g., martensitic transformation, none of the alloying element types can keep up with the motion of the boundary due to high travel speed of

the boundary and/or low diffusion rate of the alloying elements at low temperature. In this case both types of alloying elements exhibit class 1 redistribution and the transformation is diffusionless.

Figure 2-5 summarizes the concentration of carbon and the substitutional elements during transformation for all of the mentioned cases.

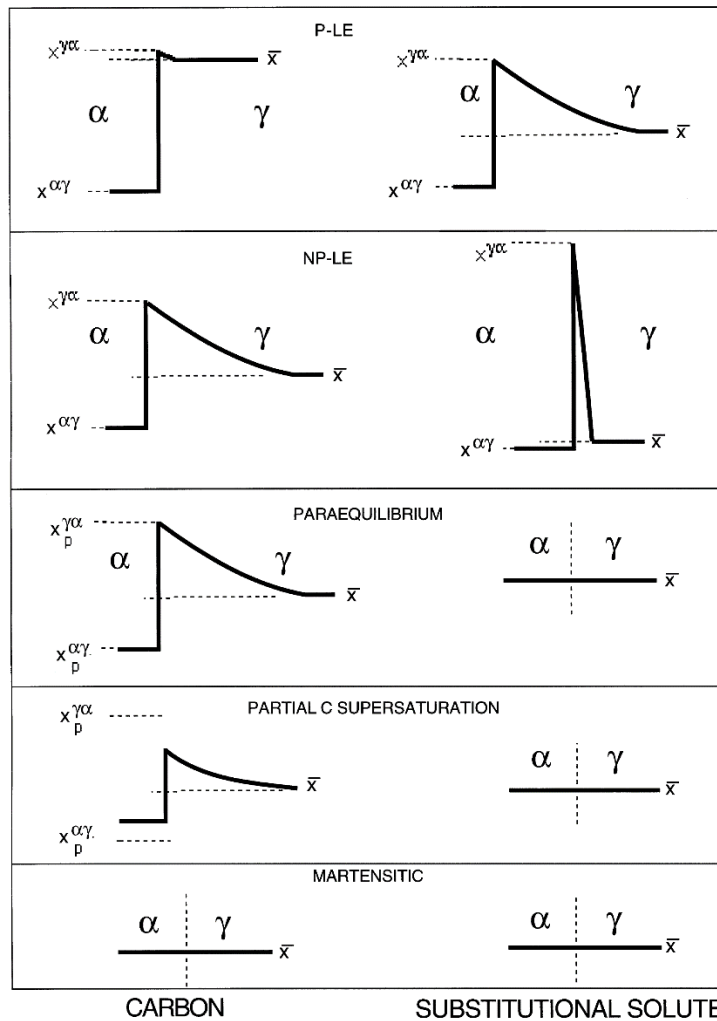


Figure 2-5. Redistribution of alloying elements during transformation of austenite to ferrite [36] .

Redistribution of alloying elements, especially carbon, has a profound effect in the development of microstructure in microalloyed steels. Additionally, for this research, understanding partitioning is also crucial because the thermo-physical properties of austenite and the product phases are a function of chemical composition which is determined by the partitioning of alloying elements. In Chapter 4, a computational method

for interpretation of dilatometry data, named Unit Cell Dilation, is proposed that relies on accurate knowledge of the chemical composition of phases.

2.2.2 Microstructure development in microalloyed steels

Microalloyed steels can have a wide range of microstructures each made up of a combination of a number of microconstituents. To understand the development of a certain type of microstructure in microalloyed steels, it is important to identify the parameters influencing the phase transformation. Generally, phase transformation happens in response to change of a state variable. For this discussion only two state variables of temperature and chemical composition will be considered but other state variables such as electric and magnetic fields and mechanical stress can also influence phase transformation [22,49]. Before further discussion it is helpful to understand what is meant exactly by change in temperature and chemical composition. In microalloyed line pipe manufacturing, temperature change is imposed on the system through controlled cooling. If the release of heat of transformation is negligible compared with the flux of heat out of the system, temperature can be considered to be an independent variable of the system. Although this assumption helps simplify the upcoming discussion, the statement is not generally true especially for transformations that happen at large undercoolings.

In the case of microalloyed pipeline steels, the change in chemical composition is more of a local kind rather than a system wide change. In pipeline manufacturing, after melting and casting of the steel, with the exception of some decarburization on the surface, the steel does not experience a considerable change in the overall chemical composition. However, as discussed in Section 2.2.1, diffusive phase transformations can redistribute alloying elements. This microscopic scale change in chemical composition has a profound effect on the development of the microstructure in microalloyed steels. The most notable element to redistribute is carbon. As such, the average carbon content of the microconstituent with respect to the parent austenite prior to transformation is used to classify the microconstituents. A low carbon microconstituent (LCM) is a microconstituent where its average carbon content is less than that of the parent austenite. A high carbon microconstituent (HCM) is a microconstituent where its average carbon content is higher than that of the parent austenite.

2.2.2.1 Diffusive transformation microstructures

When a diffusive transformation is active, microalloyed steels develop a microstructure that is composed of at least one LCM such as polygonal ferrite and at least one HCM such as pearlite. This type of microstructure forms due to the low solubility of carbon in ferrite and long range diffusion of carbon in the austenite. What determines which microconstituents form is the austenite's state prior to transformation (e.g., deformed vs undeformed austenite), chemical composition of austenite and temperature during transformation. Two of the diffusive microconstituents commonly seen in microalloyed steels are (quasi) polygonal ferrite and (degenerate) pearlite.

Polygonal ferrite (PF) and quasi polygonal ferrite (QPF)

PF and QPF are LCMs that form at low to medium cooling rates and above the bainite start temperature. PF grains are typically in the form of a concave polygons with curved edges. The curved edges in PF are created by impingement of the growing ferrite grains [50]. PF is a soft and ductile phase with low carbon content which can be estimated using LENP or PE models as explained in Section 2.2.1 . Quasi polygonal ferrite (QPF) forms at lower temperatures compared with polygonal ferrite. Unlike concave polygonal ferrite grains, QPF has an irregular grain shape. PF and QPF are shown in Figure 2-6.

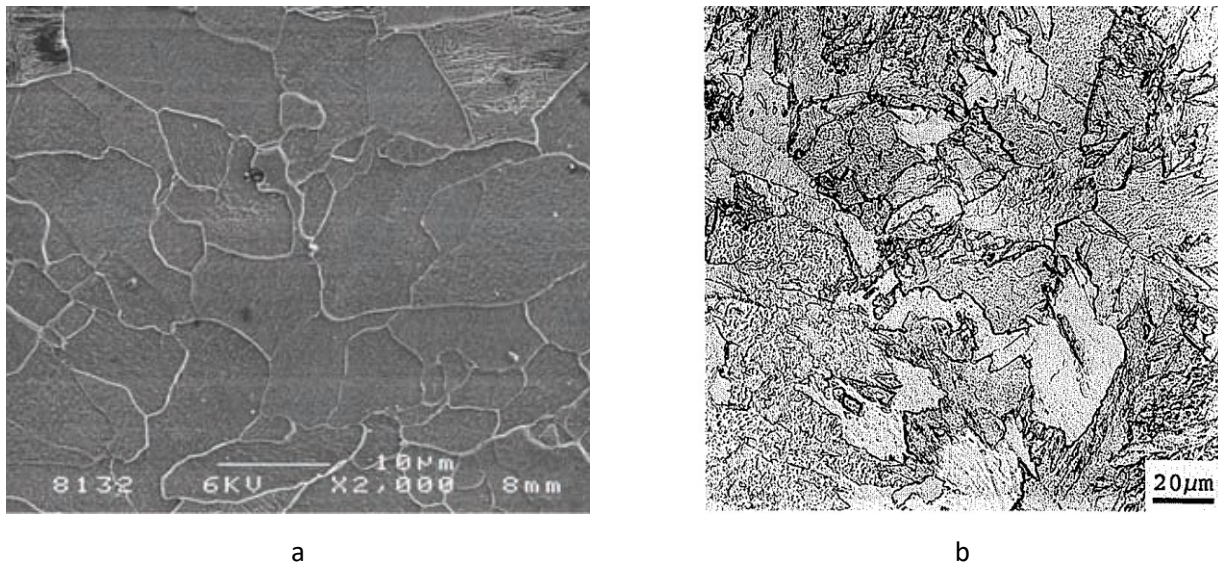


Figure 2-6. a) PF in a Nb microalloyed steel [51]. b) QPF in an ultra low carbon steel containing 0.005 %C and 3 %Mn [50].

Pearlite

Pearlite is an HCM and is composed of ferrite and cementite phases. Pearlite forms from fully saturated austenite with carbon. In microalloyed steel this level of carbon concentration can only be achieved only if most of the austenite transforms into low carbon ferrite so that the excess carbon that cannot dissolve in ferrite and accumulates in the remaining austenite. When the solubility limit of carbon in austenite is reached, no more carbon can be accumulated in the austenite; therefore, the formation of new ferrite is only possible if the excess carbon precipitates out of both ferrite and austenite in the form of cementite. This simultaneous formation of ferrite and cementite creates pearlite [22]. Pearlite can have two morphologies, lamellar pearlite and degenerate pearlite. In lamellar pearlite, as the name implies, the mixture of ferrite and cementite has a layered structure. In degenerate pearlite the mixture is more irregular with broken cementite which appears as particle scattered in the ferrite matrix. Figure 2-7 shows both lamellar and degenerate pearlite in a microalloyed steel.

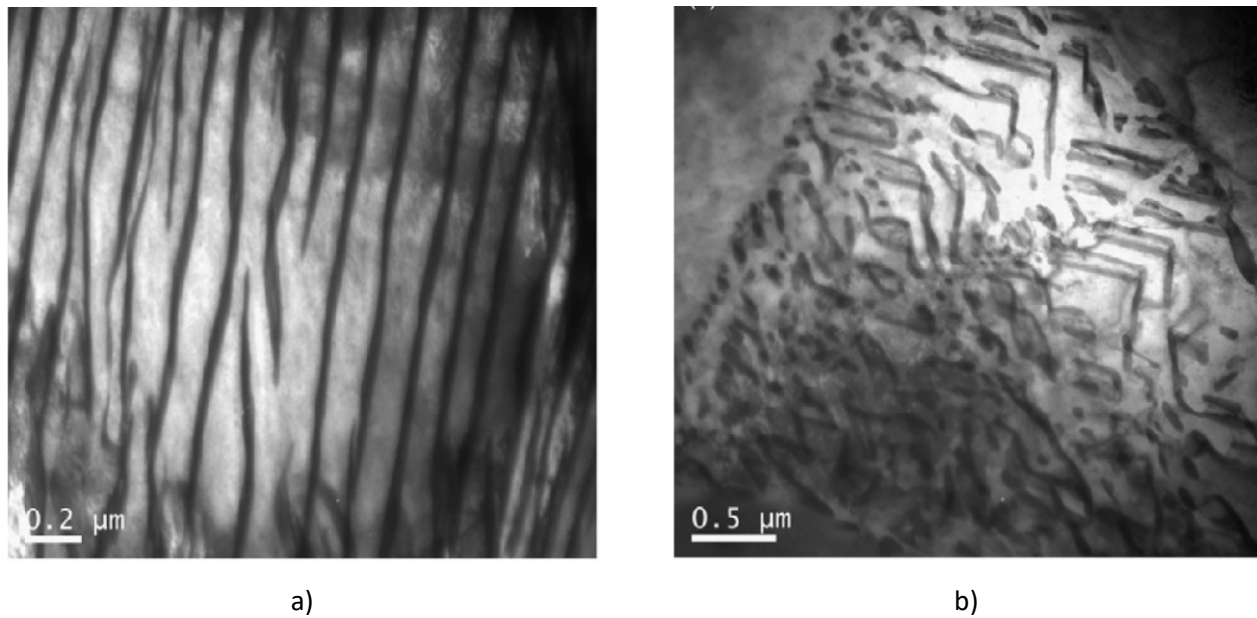


Figure 2-7. a) TEM image of lamellar pearlite in a Nb microalloyed steel. b) TEM image of degenerate pearlite in a Nb microalloyed steel [52].

2.2.2.2 Displacive transformation microstructures

In the manufacturing of microalloyed line pipe steels, temperature is generally not constant during transformation and continuously drops. Reduction of temperature can affect the phase transformation of austenite in a number of ways, one of which is the promotion of displacive transformation. This is done via two mechanisms. The first is by slowing the diffusive transformation and the second is by creating the needed driving

force to initiate a displacive transformation. Therefore, depending on the cooling rate and kinetics, it is possible for the austenite transformation mechanism to shift from diffusive to displacive. In microalloyed steels, the most commonly found displacive microconstituents are various forms of bainite and martensite.

Bainite

Bainite is a two component microconstituent containing bainitic ferrite and an HCM such as cementite, retained austenite or M/A. The most prevalent theory regarding transformation of bainite is the two step mechanism suggested by Bhadeshia and Edmonds [39], which states bainite forms by rapid formation of ferrite by a displacive mechanism followed by diffusion of carbon out of the ferrite. According to Zajac’s classification [53], bainite divides into 5 types that are schematically shown in Figure 2-8.

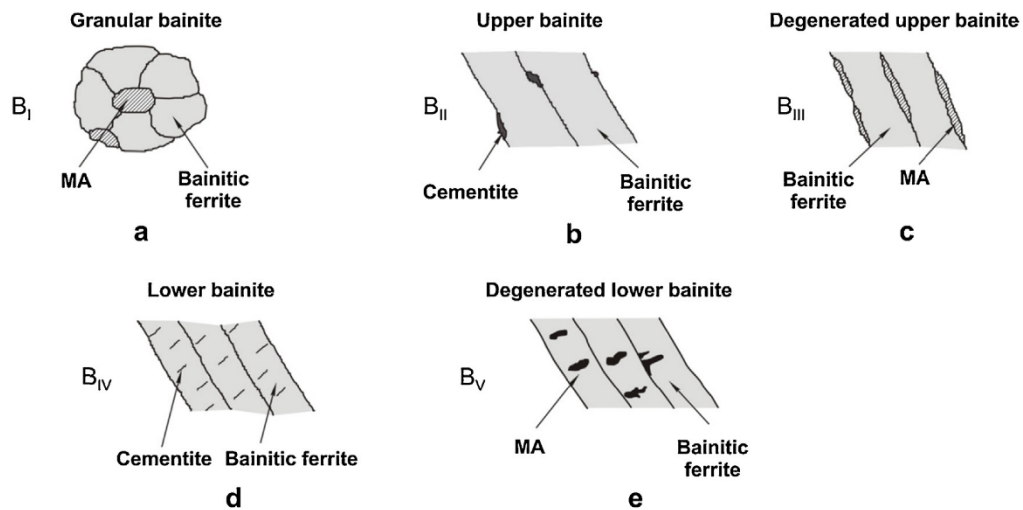


Figure 2-8. Different types of bainite as classified by Zajac et al [54].

Granular bainite (GB) consists of bainitic ferrite (BF) grains and blocky HCM (as opposed to elongated or film) [36,55]. The HCM in GB can be degenerate pearlite, bainite, martensite or M/A. The shape of these islands is the same as the remaining austenite grain before the displacive transformation began. Figure 2-9 shows the microstructure of GB in a microalloyed steel.

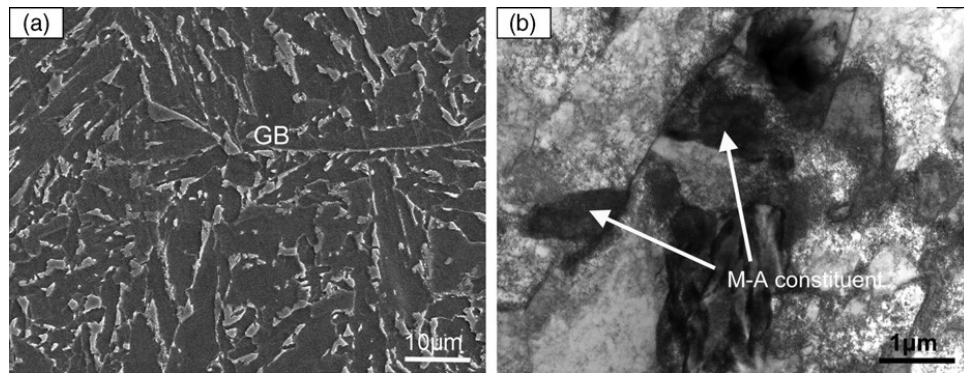


Figure 2-9. a) Microstructure of granular bainite consisting of large bainitic ferrite and blocky M/A. b) TEM image showing the micron size blocky M/A microconstituent in GB [56].

Unlike GB, in upper and lower bainite the ferrite phase of the microstructure appears as elongated narrow bands separated by low angle grain boundaries. The differentiating factor between upper and lower bainite is the placement of the HCM of the microstructure. In upper bainite the HCM is cementite and is located between the BF plates but in lower bainite the cementite occurs within the BF plate (Figure 2-11). As shown in Figure 2-8, if the HCM in upper and lower bainite is M/A rather than cementite the prefix degenerate is added to the name.

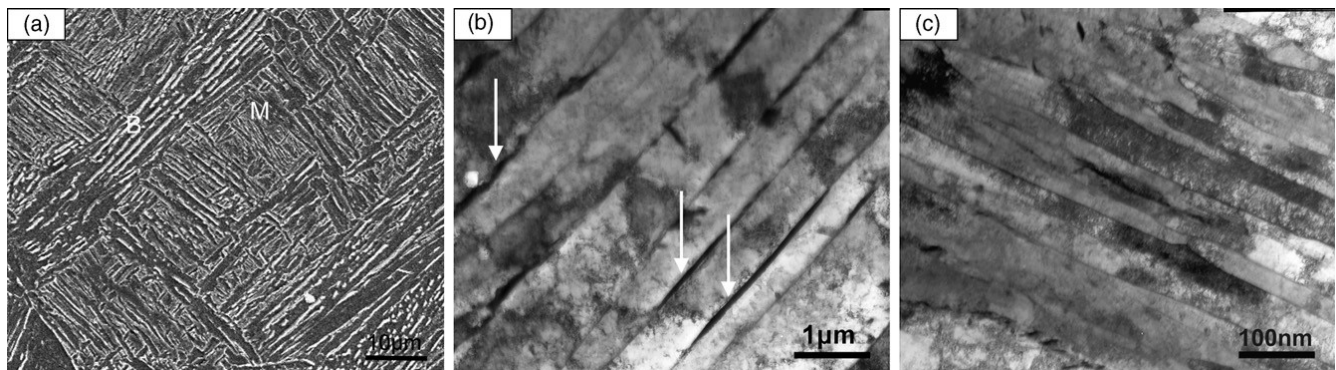


Figure 2-10. a) SEM micrograph of martensite and upper bainite in an Nb microalloyed steel cooled at 50°C/s. b) TEM image of upper bainite. Arrows show the thin austenite film between BF plates. c) TEM image of the martensite phase [56].

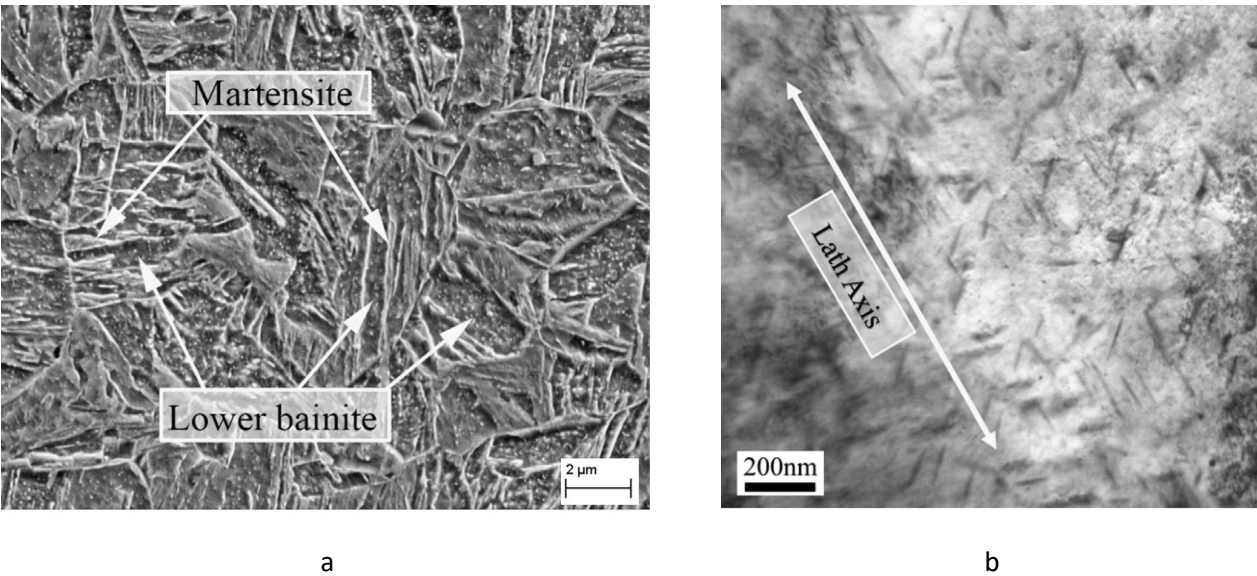


Figure 2-11. Lower bainite and martensite in a Nb-V microalloyed steel cooled from 900°C at 40°C/s. a) SEM micrograph and b) TEM image of lower bainite showing cementite precipitates in the lath [57].

Bainitic ferrite (BF) and acicular ferrite (AF)

BF is the ferrite component of bainite and is believed to nucleate in the austenite grain boundaries and form by a displacive mechanism [36]. Figure 2-8 shows the appearance of bainitic ferrite in different types of bainite. It is common in microalloyed steels to have bainitic ferrite identified separately and not necessarily in association with bainite. The reason for this is that due to the low carbon content, it is possible to form large quantities of bainitic ferrite without having to form an HCM to accommodate the rejected carbon from ferrite. This results in bainitic ferrite appearing as an independent phase. The granular bainite microstructure is an example of this kind of microstructure. To address this varying appearance of the bainitic microstructure some scholars have used the term conventional bainite (CB) to point to a bainitic microstructure in which the LCM and HCM are located much closer to one another [58].

Acicular ferrite (AF) is believed to be a bainitic ferrite that nucleates inside the austenite grain as opposed to the austenite grain boundary. Intragranular nucleation is possible on the deformation bands for a deformed austenite or on nonmetallic inclusions [59]. Acicular ferrite appears as interwoven, non-parallel ferrite laths [60]. Figure 2-12 shows two kinds of acicular ferrite in microalloyed steels. Figure 2-12a shows AF that formed inside the deformed austenite grain and Figure 2-12b shows AF that nucleated intragranularly on the large Ti-based inclusions indicated by black arrows. The white arrows in this image show smaller secondary Ti, Mn precipitates that did not act as nucleation site for AF.

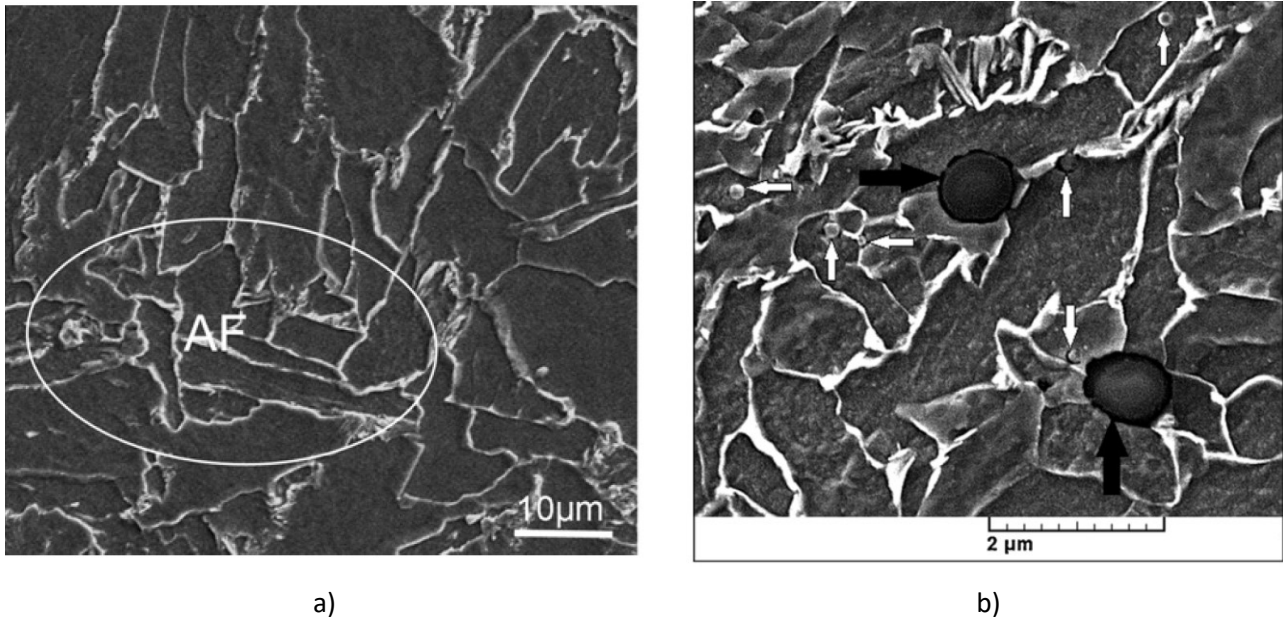


Figure 2-12. Acicular ferrite in a) V microalloyed steel cooled at 4°C/s [56]. b) Ti killed weld metal. Black arrows point to large Ti containing inclusions that acted as intragranular nucleation sites for acicular ferrite [59].

Martensite and martensite/austenite (M/A) microconstituent

In continuously cooled microalloyed steels, martensite can be found as a component in bainite in the form of M/A as seen in Figure 2.9b or as an independent microconstituent as seen in Figures 2.10a and 2.11a. Martensite in microalloyed steels usually consists of parallel plates of ferrite similar to bainite, but unlike bainite martensite's transformation does not involve carbon redistribution during transformation. Martensite plates are generally packed closer and unless tempered, do not show a second phase between plates [22,38] as shown in Figure 2-10 c. M/A microconstituent is a partially transformed austenite to martensite. The austenite component of M/A is usually rich in carbon. High carbon content along with the compressive stresses arising from the martensitic transformation stabilize the retained austenite and prevent full transformation to martensite [61,62].

2.3 Quantification of microstructure

Microalloyed steels are known to produce complex microstructures, especially in the continuously cooled condition. The complexity of these microstructures arises primarily from the number of possible microconstituents that can form from austenite. These microconstituents include various morphologies of ferrite such as polygonal ferrite, quasi-polygonal ferrite, bainitic ferrite and non-ferritic microconstituents such as retained austenite, cementite and martensite [54]. The microconstituents can appear alone or together to form

mixed microconstituents such as upper, lower and granular bainite, pearlite and degenerate pearlite. Just the number of possible microconstituents in a microstructure can make quantification an overwhelming task. Added to the mentioned difficulty is the fact that the major microconstituents in microalloyed steel are different morphologies of the same phase - ferrite. This makes bulk quantification methods such as XRD useless for ferritic microconstituents.

Traditionally quantification of these complex microstructures has been done using a visual method. In the visual method, quantification is done by measuring the area fraction of microconstituents using micrographs of the etched surface. Calculation of area fractions is done by either direct area fraction measurement using image analysis software or by a point count method. Both of these methods are tedious, prone to human error and subject to the bias of the person identifying the microconstituents. In recent years, however, new methods have been developed around the use of electron back scattered diffraction (EBSD). In this method, crystallographic data for individual points on the polished surface are obtained by analyzing Kikuchi patterns. In the majority of the EBSD based methods the distribution of a certain parameter is calculated for a given dataset, then the overall distribution is deconvoluted to sum the individual peaks for different microconstituents. These parameters include image quality (IQ), confidence index (CI), kernel average misorientation (KAM), FIT index (FIT), band contrast (BC) and band slope (BS) [63–67]. Wu and DeArdo have demonstrated the use of IQ map analysis for microstructure quantification for microalloyed steels [64,65]. IQ is a parameter representing the quality of the Kikuchi lines. A perfect lattice produces sharp Kikuchi lines resulting in a high IQ value. However, the presence of lattice imperfections such as dislocations and dissolved atoms distorts the crystal resulting in broader Kikuchi lines which lead to a lower IQ value. Using a mathematical process explained in [64], a normalized IQ map of a sample is deconvoluted to a sum of multiple peaks. The area fraction under each peak equals the area fraction of each phase in the micrograph. Figure 2-13 shows an example of this process for a dual phase steel. In this figure, each peak represents an IQ distribution for a microconstituent. The location of the peak for a microconstituent is determined by the amount of dislocations, which in steels corresponds to the temperature at which the phase formed. Polygonal and quasi polygonal ferrite form at the highest transformation temperatures and have low dislocation densities; therefore they have high IQ values. Lower temperature ferrite morphologies, such as bainite and martensite, have low IQ values due to the displacive transformation mechanism that leaves the product phase with an abundance of dislocations and subgrain boundaries.

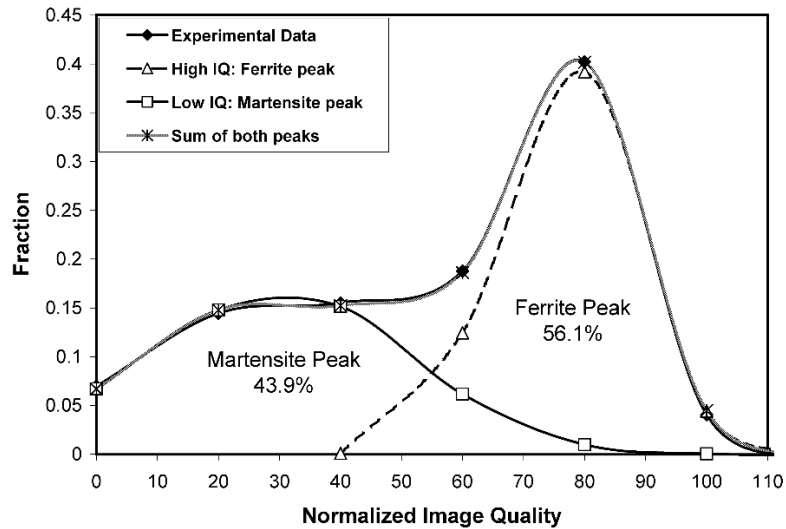


Figure 2-13. Application of IQ map for phase content quantification for a dual phase steel [64].

The IQ map analysis is advantageous over traditional visual techniques in that it is less prone to human interference. However, there are some areas for improvement. For instance, the number of peaks to be used for deconvolution is determined by the user based on the expected number of microconstituent types. This opens the door for human interference. Also, the location of the peaks seems to be arbitrarily affected by the intensity of the highest recorded IQ value in the collected data. This can be seen in Figures 10 and 13 from reference [64] for the ferrite peak. A certain degree of variation is expected for bainite and martensite as their microstructures depend on the transformation temperature. However, polygonal ferrite does not get supersaturated with carbon nor does it have a high dislocation density; therefore, it seems reasonable that an identification method would assign polygonal ferrite a relatively similar value with minor variation caused by a change in substitutional element content. This lack of consistency in assigning the peak locations can potentially create confusion in identifying peaks for microconstituents with peaks close to each other; e.g., acicular ferrite and bainitic ferrite which form by a similar mechanism with the difference being their nucleation sites [68].

2.4 Strengthening mechanisms ¹

Increasing yield strength to produce a stronger material has a number of benefits from a mechanical design point of view. For higher strengths, less material is needed to support a given stress. This translates to smaller

¹ This section is intended to provide the theoretical background for the strength calculations done in Section 3.3.5.

and lighter structures. To increase the yield strength, processes that interrupt elastic deformation must be inhibited. In ductile metals, the onset of plastic deformation marks the yield point; therefore, to increase the yield strength in metals, plastic deformation must be hindered. In most metals at temperatures less than $(0.3T_m)$, plastic deformation occurs via dislocation glide or twinning [69]. In microalloyed steels deformation with dislocation glide is the preferred plastic deformation mechanism at low temperatures. Therefore, in order to increase yield strength, dislocation glide must be stopped.

There are 4 ways by which dislocation glide can be stopped. These dislocation stopping methods are known as strengthening mechanisms. The four strengthening mechanisms are dislocation strengthening, solid solution strengthening, precipitation strengthening and grain boundary strengthening. All but grain boundary strengthening inhibit dislocation glide using obstacles. When a moving dislocation encounters an obstacle, it bends around the obstacle as shown in Figure 2-14. At low applied stress the bend radius and dislocation bend angle (ϕ) are large, but as the applied stress increases both parameters decrease until at a critical stress level the dislocation breaks away from the obstacle. The critical bend angle (ϕ_c) at which dislocation breaks free from the obstacle is a measure of the strength of the obstacle. ϕ_c ranges from 0° for a strong obstacle to 180° for a weak one [2]. The critical angle of an obstacle depends on the physical properties of the obstacle such as shear modulus, size and surrounding hydrostatic stress fields. Critical bend angle is a parameter that is often used in modeling the effect of multiple types of obstacles on yield strength.

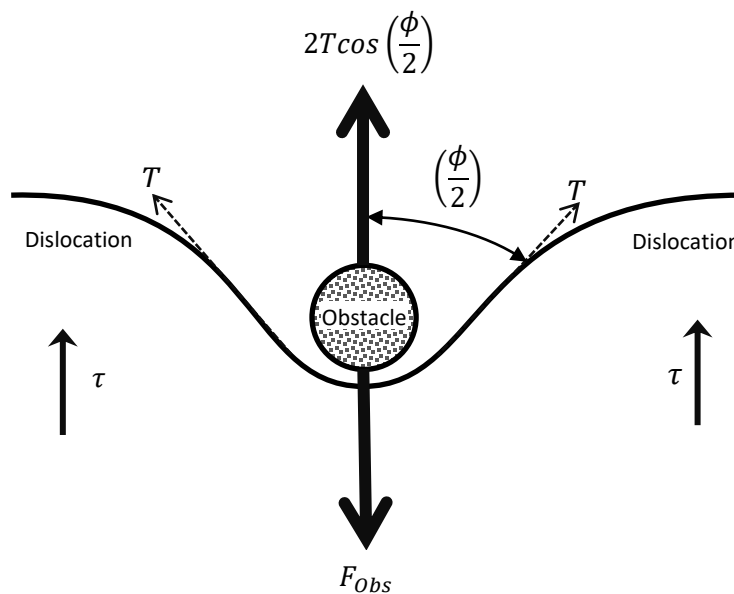


Figure 2-14. Dislocation encountering an obstacle on its glide plane. τ is the applied shear stress on the dislocation line.

If the average distance between the obstacles is L , using the schematic shown in Figure 2-14, the following equations can be written.

$$F_{Obs} = \tau \cdot b \cdot L \quad \text{Eq. 2-1}$$

$$F_{Obs} = 2T \cos\left(\frac{\phi}{2}\right) \quad \text{Eq. 2-2}$$

where T is the dislocation tension and can be calculated using Eq. 2-3.

$$T = \frac{Gb^2}{2} \quad \text{Eq. 2-3}$$

Combining Eq. 2-1, Eq. 2-2 and Eq. 2-3 results in an equation that relates the applied shear stress to dislocation bend angle as Eq. 2-4.

$$\tau = G \cdot b \cdot \cos\left(\frac{\phi}{2}\right) \cdot \left(\frac{1}{L}\right) \quad \text{Eq. 2-4}$$

Eq. 2-4 is the basis for calculation of the strengthening effect of the strengthening effect of all the obstacle type strengthening mechanisms. In the following sections, an overview of the strengthening mechanisms with emphasis on quantitative models is presented.

2.4.1 Dislocation strengthening

Dislocations cutting other dislocations on their glide plan can result in immobilization of the gliding dislocations. To overcome the pinning effect of the dislocation-dislocation interaction, higher stresses are required for dislocation glide. The most widely accepted model for dislocation strengthening is the Kocks-Mecking-Estrin model, which attributes added strength to the increased resolved shear stress when mobile dislocations cross the immobile (forest) dislocations. According to this model, the flow stress of a dislocation is proportional to the square root of the dislocation density according to Eq. 2-5 for a single crystal and Eq. 2-6 for polycrystalline metal [70,71].

$$\tau = \alpha G b \sqrt{\rho} \quad \text{Eq. 2-5}$$

$$\sigma_{dis} = \alpha M G b \sqrt{\rho} \quad \text{Eq. 2-6}$$

In these equations, α is a parameter that depends on the type of the dislocation, M is the Taylor factor, G is the shear modulus of the crystal, b is the Burgers vector of the dislocation and ρ is the dislocation density. Eq. 2-5 can be derived from Eq. 2-4 where $L = \frac{1}{\sqrt{\rho}}$ and $\alpha = \cos\left(\frac{\phi_c}{2}\right)$. For microalloyed steels value of 0.88 is

recommended for α [7]. Dislocation strengthening in microalloyed steels is important for the ferritic microconstituents that form via a displacive mechanism. This includes bainitic ferrite, bainite and martensite. Displacive transformation of austenite to ferrite is accompanied with a large Bain strain which is usually accommodated by the creation of a significant number of dislocations [36]. On the other hand, microconstituents that form with a reconstructive mechanism, such as polygonal and quasi polygonal ferrite, do not contain dislocations in quantities that would create a considerable strengthening effect. Dislocation strengthening in microalloyed steels will play an important role for higher strength grades that are predominantly bainitic or martensitic in nature [72].

2.4.2 Solid solution strengthening

Local stress fields of dissolved impurity atoms can inhibit the dislocation movement and increase the strength. There are two types of impurity atoms, substitutional and interstitial. If an atom dissolves by replacing the original lattice atoms it is a substitutional atom and if it dissolves by occupying the spaces between the lattice atoms it is an interstitial one. What determines the type of the dissolved atom is the relative size of the impurity and host atoms. When the size of the two atoms is relatively close, the impurity atom replaces the original atoms, but when the impurity atom is considerably smaller than the host atom, it chooses to dissolve by entering an interstice rather than replacing the host atom.

The impurity atom creates a local stress field in the host crystal that can interact with a nearby dislocation's stress field. As an example, substitutional atoms can diffuse to an edge dislocation and, depending on their stress field, replace lattice atoms above or below the dislocation line to neutralize the dislocation's stress field as shown in Figure 2-15. Substitutional atoms that are larger than the host atoms create a hydrostatic compressive stress field and are attracted to the tensile stress field below the dislocation line. In contrast, substitutional impurity atoms that are smaller than the host atoms create a hydrostatic tensile stress field which attracts them to the compressive stress field above the dislocation line [34].

Interstitial atoms can create both hydrostatic and shear stress fields depending on the geometry of the interstice in which they are located. For example, carbon and nitrogen in BCC ferrite are both interstitial elements. When these atoms dissolve in the ferrite lattice, they create a tetragonal distortion by distorting the lattice more in the (c) direction of the unit cell than in the (a) direction. This allows carbon and nitrogen to interact with both edge (hydrostatic and shear stress fields) and screw dislocations (shear stress fields). As a result, interstitial elements are more effective inhibitors for dislocation motion in ferrite than substitutional elements[73,74].

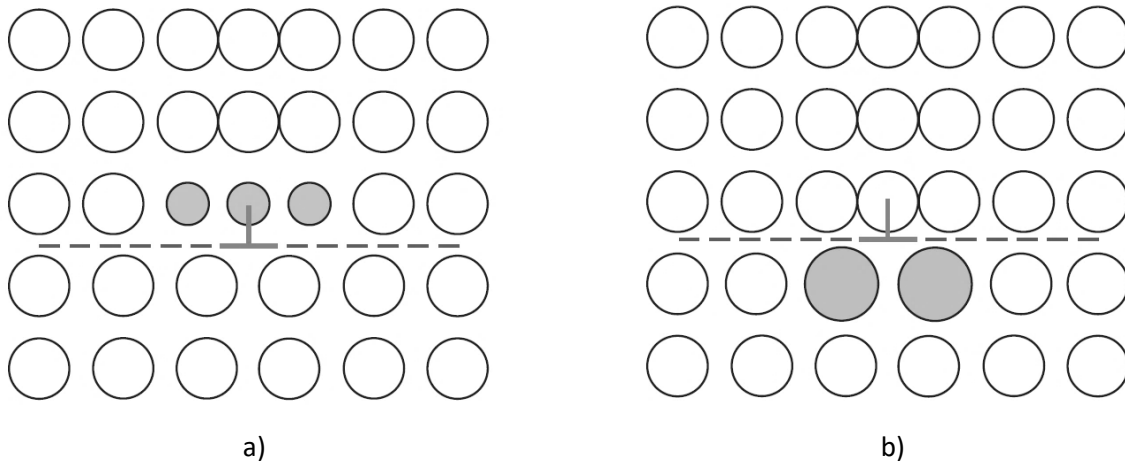


Figure 2-15. Interaction of substitutional impurity atoms with an edge dislocation. a) Impurity atom is smaller than the host atom and b) impurity atom is larger than the host atom [34].

The interaction between an impurity atom and a dislocation is better explained in terms of change in the strain energy. Assuming the distribution of solute atoms and dislocations are completely random, a solute atom can either increase the dislocation energy or decrease it. For example, a large solute atom above a positive edge dislocation increases the stored energy since two compressive stress fields would interfere with each other. The same atom below the dislocation line would reduce the strain energy. If the interaction increases the energy, the dislocation would need more force to get closer to the solute atom and pass it. If the interaction reduces the energy of the dislocation, getting close to impurity atom is not an issue since the closer the dislocation is to the impurity the lower the energy would be. However, moving away from the solute atom is more difficult and requires extra force. This concept is the basis of all the solute–dislocation interaction models. The classical model of solid solution strengthening is the one proposed by Labusch and Nabarro, which calculates the interaction energy for the impurity atom and dislocation by assuming a linear elastic stress field around the dislocation core [75,76]. In their model, the change in the strain energy depends on two factors, (δ) the strain of the Burgers vector originating from size difference of the impurity and host atoms and (η) originating from the change in the shear modulus (G) by adding the impurity atom to lattice. These two factors can be calculated using Eq. 2–7 and Eq. 2–8.

$$\delta = \frac{1}{a} \cdot \frac{\partial a}{\partial c} \quad \text{Eq. 2-7}$$

$$\eta = \frac{1}{G} \cdot \frac{\partial G}{\partial c} \quad \text{Eq. 2-8}$$

In these equations, (a) denotes the lattice parameter of the host lattice and (c) denotes the concentration of the solute. According to Labusch – Nabarro model, the strength increase by the impurity atom is a function of the concentration of the impurity atom as shown in Eq. 2–9.

$$\Delta\tau = c^{2/3}\epsilon_L^{4/3} \quad \text{Eq. 2-9}$$

where c is the concentration of the impurity element and ϵ_L is the Labusch's effective interaction parameter that is calculated from δ and η using .

$$\epsilon_L = \sqrt{\delta^2 + \alpha^2\eta^2} \quad \text{Eq. 2-10}$$

α is a factor between $\frac{1}{16}$ for an edge dislocation and $\frac{1}{3}$ for a screw dislocation [76,77]. It must be mentioned that alternative formulas for the interaction parameter (Eq. 2-10) exist. One example is the Fleischer interaction parameter which is calculated using Eq. 2-11 [78-80]

$$\epsilon_L = \sqrt{\eta'^2 + \alpha^2\delta^2}, \left\{ \begin{array}{l} \alpha = 3 - 16 \\ \eta' = \frac{\eta}{1+0.5|\eta|} \end{array} \right\} \quad \text{Eq. 2-11}$$

The importance of Eq. 2-9 is in the dependence of the strength increase on $C^{2/3}$. The importance of the exponent $\left(\frac{2}{3}\right)$ will be discussed in the overall strength section. Figure 2-16 shows the change in strength of Cu alloys as a function of different alloying element content. The linear trends in Figure 2-9a show that the power law with exponent $\left(\frac{2}{3}\right)$ applies to Cu alloys and the $\left(\frac{3}{4}\right)$ slope in Figure 2-16b confirms that the effect of alloying elements depends on the Labusch combined interaction parameter (Eq. 2-10).

Although Labusch theory for solid solution is shown to work for some alloy systems especially for the FCC ones, many factors such as thermal effects, clustering of alloying atoms and concentration of the alloying element cause deviation from predicted $\left(\frac{2}{3}\right)$ exponent. It is shown that strengthening effect of alloying elements can vary linearly with $c^{1/2}$, $c^{3/4}$ and even c^1 rather than $c^{2/3}$ [81,82]. In steels, it is shown that yield strength increases linearly by increasing concentration of alloying elements in solid solution. Figure 2-17 shows the increase in strength of steel as a function of amount of the dissolved element[21].

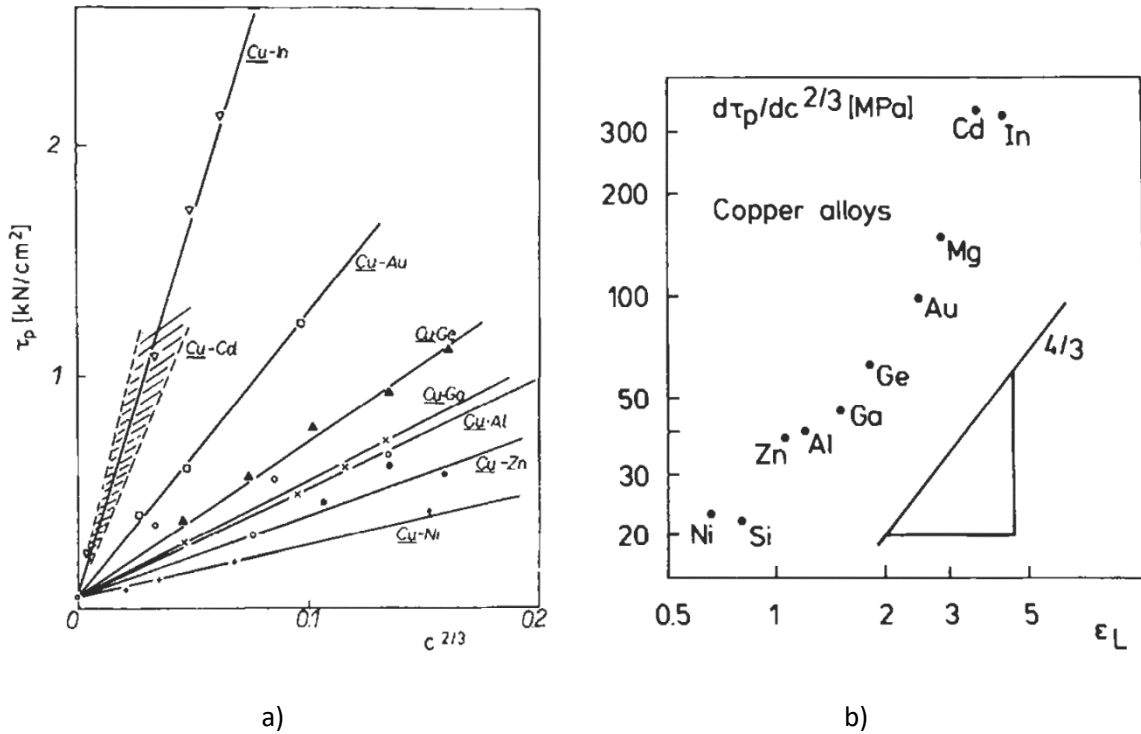
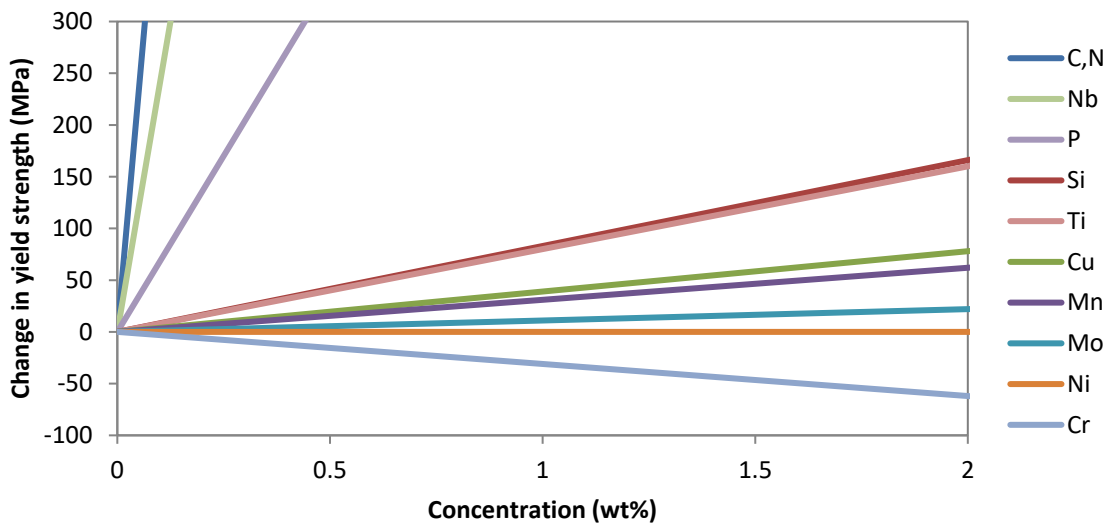
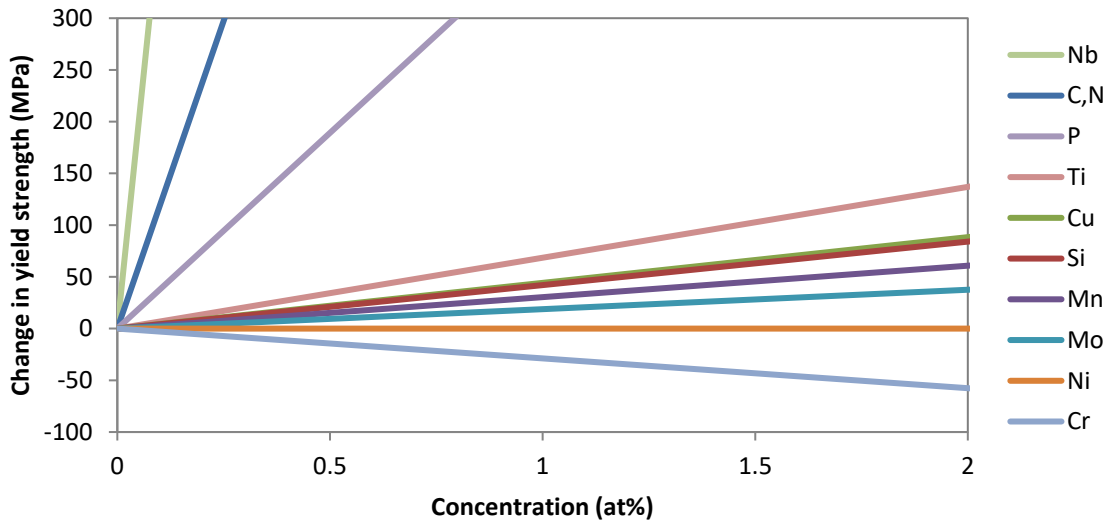


Figure 2-16. Solid solution strengthening in different Copper binary alloys. a) Linear trend for strength gain with $C^{2/3}$ (confirmation of Labusch theory for solid solution strengthening). b) Effect of the alloying element mismatch strength gain. This plot is shown on a log scale. The 4/3 slope of the trendline matches the exponent for ϵ_L suggested by Eq. 2-9 [77].



a)



b)

Figure 2-17. Change in yield strength as a function of a) weight percent of alloying elements and b) atomic percent of alloying elements. Reproduced based on the data found in the literature [2,83].

The strengthening effect of alloying elements in steel for the addition of 1 wt% can be found in Table 2-1. C and N are the most effective alloying elements for solid solution strengthening of steel. Their effectiveness is believed to be primarily due to the high lattice distortion that they can create in ferrite [84]. It must also be noted that C and N are interstitial elements which allow them to interact with both screw and edge dislocations. Although a linear relationship between strength increase and carbon concentration is widely used, analysis of the hardness of martensite (supersaturated ferrite with carbon) as a function of carbon content shows that increase in strength is a function of $c^{0.5}$ [85]. Figure 2-18a shows the hardness of martensite as a function of carbon content. Figure 2-18b shows the yield strength of martensite as a function of the square root of carbon concentration. The graph labeled “Yield strength using hardness data” is calculated using the relationship developed by Pavlina et al. [86] using the martensite hardness data extracted from Figure 2-18a and the graph labeled as “Yield strength (Eq. 2-12)” is based on Eq. 2–12 developed for the strength of martensite [87].

Table 2-1. Strength increase due to addition of 1 wt% for alloying elements for ferritic steels - all values are in MPa.

C,N [81]	Nb [2,83]	P [88]	Ti [2,83]	Si [2,83]	Cu [2,83]	Mn [2,83]	Mo [2,83]	Ni [80]	Cr [80,81]
4620 - 5544	2400	680-780	80	83	39	31	11	0 - 18	(-31) - (-7)

$$\sigma_y = 1310 \cdot (\text{wt}\% C)^{\frac{1}{2}} + 461$$

Eq. 2-12

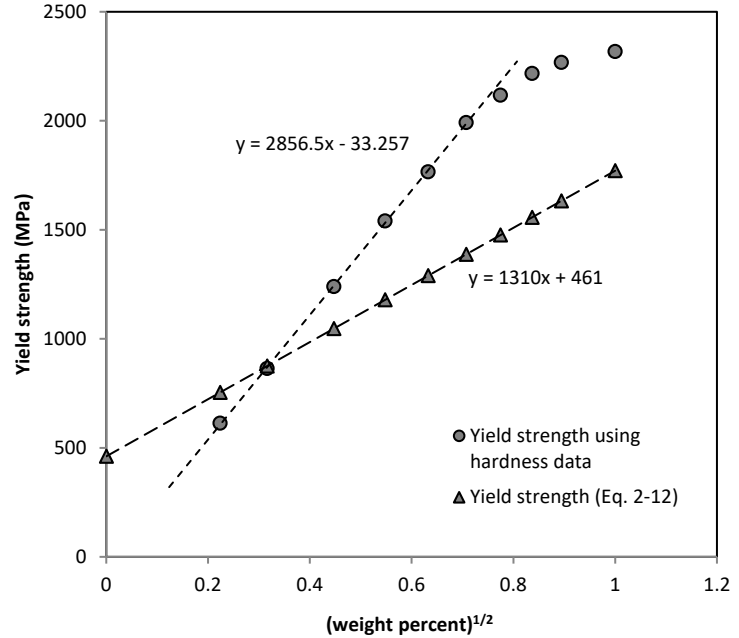
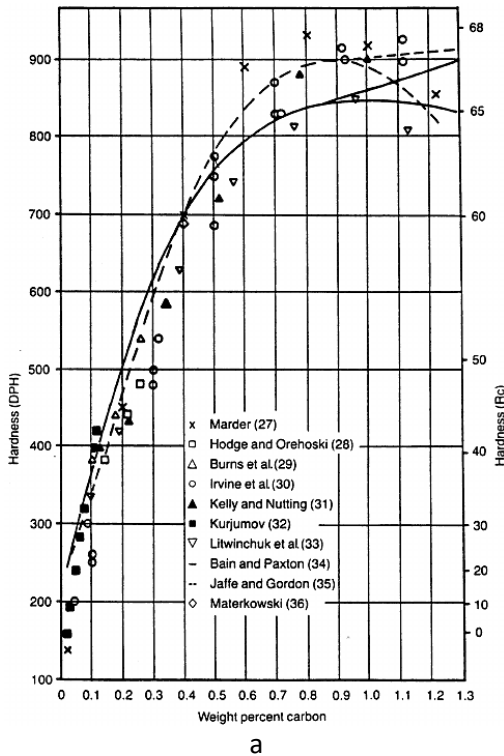


Figure 2-18. The strength of martensite (ferrite) as a function of carbon content. a) Hardness [87] and b) calculated yield strength as a function of the square root of C concentration.

The solid solution strengthening effect of most alloying elements in steels is believed to be independent of other elements. This allows for linear empirical equations such as Eq. 2-13 to calculate the overall strengthening effect of multiple alloying elements with reasonable accuracy.

$$\sigma_{SS} = \sum_{Si, Mn, \dots} (k_i \cdot C_i) \quad \text{Eq. 2-13}$$

where σ_{SS} is the solid solution strengthening due to the alloying elements, k_i is the strengthening coefficient for element i and C_i is the concentration of the element i in weight percent. This linear model has been widely used for steels and specifically for microalloyed steels [10,21] to calculate the contribution of solid solution strengthening.

2.4.3 Precipitation strengthening

Precipitates can hinder dislocation motion and increase yield strength. The mechanism by which precipitates stop dislocations depends on the interaction mechanism of the precipitate and dislocation. When a dislocation encounters a precipitates three things can happen:

1. The dislocation travels through the precipitate.
2. The dislocation bends around the precipitate and leaves a dislocation loop behind around the precipitate.
3. Dislocation climbs and avoids the precipitate by traveling above or below the precipitate.

The type of dislocation-precipitate interaction is determined based on two major factors, temperature and shear strength of the precipitate. At temperatures above 0.3 to 0.4 time the homologous temperature (T_m) [69] where self-diffusion is fast, a dislocation can avoid direct contact with a precipitate by a dislocation climb mechanism. In this mechanism, the diffusion of vacancies to the dislocation line (positive climb) or away from the dislocation line (negative climb), dislocation line travels vertically to the slip plane [71].

For steels deforming below 250°C, the self-diffusion rate is small enough to be considered negligible; therefore, the dislocation-precipitate interaction is one of the first two mechanisms. Soft precipitates allow the incoming dislocations to travel through the precipitate by a regular dislocation slip mechanism. Examples of this kind of precipitate are copper-rich precipitates in bake hardened microalloyed steels and γ' precipitates in nickel-based super alloys.

Hard precipitates usually have much higher shear strengths than the matrix. In this case, the incoming dislocation cannot shear the precipitate. Instead, the dislocation bends around the precipitate and leaves a dislocation loop when the bend angle ϕ reaches 0° . Figure 2-19 schematically shows the mechanism of Orowan looping. In this figure τ is the applied shear stress, b is the dislocation Burgers vector, T is the dislocation tension and L is the precipitate spacing. Assuming that the precipitate spacing L is much greater than the precipitate diameter, to form a complete dislocation loop the force acting on the bowed segment of dislocation (τbL) must exceed the maximum opposing force originating from dislocation tension ($2 \times T$) plus the force needed to move the dislocation in the absence of precipitates ($\tau_0 bL$). This equilibrium of forces can be expressed as Eq. 2–14.

$$\Delta\tau = \frac{2T}{bL} \quad \text{Eq. 2–14}$$

In this equation $\Delta\tau = \tau - \tau_0$ is the increase in shear yield strength due to presence of precipitates. Dislocation line tension can be calculated from Eq. 2–3. By substituting for T in Eq. 2–14 using Eq. 2–3, the

increase in shear yield strength due to precipitates can be calculated from Eq. 2–15, which is known as the Orowan equation[2,9,89].

$$\Delta\tau = \frac{Gb}{L}$$

Eq. 2–15

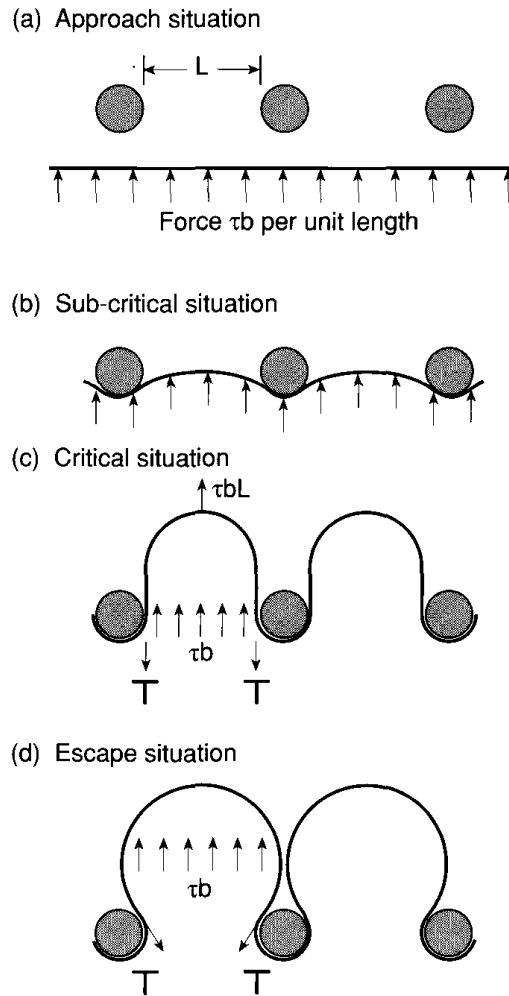


Figure 2-19. Mechanism of dislocation looping [2].

Eq. 2–15 assumes that all particles are cut along the glide plane on their largest cross section and the precipitate array is exactly perpendicular to the direction of dislocation glide. The Orowan equation later was modified by considering the randomness of particle distribution and dislocation motion resulting in Eq. 2–16 [2], which is known as the Ashby-Orowan equation.

$$\Delta\tau_y = 0.157 \left(\frac{Gb}{L}\right) \ln\left(\frac{x}{2b}\right)$$

Eq. 2–16

where x is the diameter associated with the mean area of intersection of the particles. x is related to particle diameter X according to Eq. 2–17.

$$X = \sqrt{\frac{3}{2}} \cdot x \quad \text{Eq. 2–17}$$

For steels, with $b = 2.5 \times 10^{-4} \mu\text{m}$ and $G = 80.3 \text{ GPa}$, and by modifying Eq. 2–16 to use volume fraction (f) and particle diameter (X) instead of particle spacing (L), Eq. 2–18 is achieved.

$$\Delta\sigma_y(\text{MPa}) = \left(10.8 \frac{\sqrt{f}}{X}\right) \left(\ln\left(\frac{X}{6.125 \times 10^{-4}}\right)\right) \quad \text{Eq. 2–18}$$

where f is the volume fraction and X is the diameter of precipitate in (μm).

As explained in Section 2.1, microalloyed steels benefit greatly from precipitation in austenite during hot deformation, which results in suppression of recrystallization. However, depending on the design of the microalloyed steel, a controlled precipitation regime can contribute significantly to overall strength as well. To understand the design parameters for precipitate strengthening, it is necessary to discuss the thermodynamics of precipitation in microalloyed steels. All the microalloying elements are strong carbide and nitride formers compared with the rest of the alloying elements found in these steels. Nb and Ti can readily precipitate as carbides and carbonitrides in austenite and ferrite. Ti is such a strong nitride former that TiN can even form in the melt during solidification, which is not a desirable form of TiN precipitation due to the large size and cubic morphology and tendency to cracking which reduces the toughness of steel [90,91]. V precipitates are unstable in austenite but form easily in the ferrite phase. Nb sits between the Ti and V in terms of its tendency to precipitate in α and γ . For a more quantitative analysis of precipitation, the process of precipitation could be looked at as a chemical reaction rather than a solid state phase change. From this point of view, precipitation is controlled by solubility limit of the precipitating elements for a given matrix phase; i.e., ferrite or austenite. Solubility limit is the amount of solubility product calculated using the concentrations of reactants for a precipitate at equilibrium with its soluble elements in the matrix. For a chemical reaction of type $aM + bX \xrightleftharpoons{\text{equilibrium}} M_aX_b$, the solubility product is calculated as Eq. 2-19.

$$k_s = [w\% M]^a \cdot [w\% X]^b \quad \text{Eq. 2–19}$$

k_s is experimentally measured for different precipitation systems and is usually reported as an equation in the form of $\text{Log}(k_s) = \frac{-A}{T} + B$. Values for A and B can be found in the literature [2,33,92]. Figure 2-20 shows the solubility product of different precipitates that form in microalloyed steels. For a given chemical composition of a matrix phase, if the calculated solubility product exceeds the solubility limit, precipitation can take place to

reduce the solubility product to the amount allowed by the solubility limit. The amount of precipitate that needs to form to reduce the solubility product can be calculated by solving a system of equations that has one equation for solubility limit and equation(s) driven by mass balance of precipitating elements between the matrix and precipitate.

Figure 2-20 shows that the solubility limit of all the precipitates drops with falling temperature indicating the matrix is less welcoming to the soluble impurity atoms at lower temperatures. Another fact to be seen in this figure is the considerable difference in the solubility limit between austenite and ferrite. This behavior is of importance for precipitation strengthening of microalloyed steels as it allows for a higher driving force for precipitation in ferrite than in austenite. This increased driving force, coupled with lower diffusion rates at the low temperatures at which ferrite forms, creates a favorable condition for precipitation of large quantities of fine precipitates. A high volume fraction and small diameter are the correct combination for effective precipitation strengthening, while maintaining reasonable ductility in microalloyed steels [93].

Precipitates in commercial microalloyed steels are often complex and involve more than two elements. It has been shown that precipitates that form in an alloy with more than one microalloying element tend to be smaller in size [94]. Precipitates in microalloyed steels can also contain alloying elements other than microalloying ones. Elements such as Mo and Cr co-precipitate with microalloying carbides and nitrides. This effect is an interesting phenomenon from a metallurgical standpoint as it can contribute to precipitate refinement [95] and from a financial stand point as it potentially can allow for replacement of more costly microalloying ferroalloys with cheaper ones while maintaining the precipitate volume fraction.

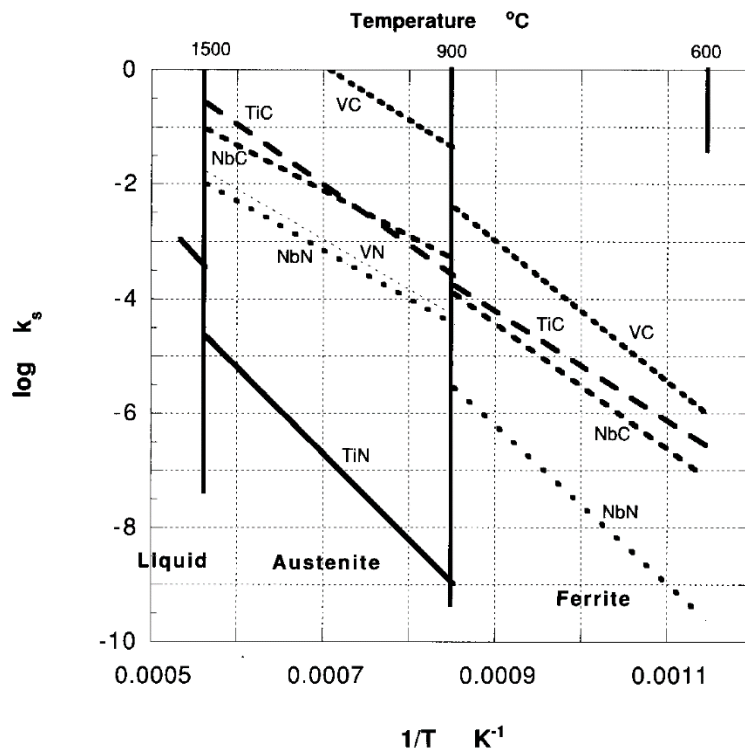


Figure 2-20. Comparison of solubility limit product for microalloying precipitates [2].

In microalloyed steels, fine precipitates found in ferrite nucleate in different ways depending on the mechanism of ferrite transformation. For bainitic and acicular ferrite, where ferrite forms by a displacive mechanism, high supersaturation of microalloying elements and possibly C or N occurs within ferrite. This high supersaturation, plus high dislocation density created by the displacive transformation, creates a favorable condition for heterogeneous nucleation of precipitates on dislocations [92,96]. Dislocations provide high energy sites for formation of the new phase which reduces the critical energy for nucleation [9]. On the other hand, dislocations enhance transport of precipitating elements to the precipitate by providing high diffusion paths. This increases the nucleation rate of precipitates. Faster diffusion on dislocations also increases the growth kinetics [22].

In contrast to bainitic and acicular ferrite, polygonal and quasi polygonal ferrite transform by a reconstructive mechanism. While heterogeneous precipitation of microalloying carbide and nitride on dislocations and preexisting precipitates are observed in polygonal ferrite [23,97] a unique precipitation behavior is also seen for polygonal ferrite. In reconstructive transformation of polygonal ferrite, the ferrite/austenite phase boundary moves much slower compared with the displacive transformation of bainite. This slower motion allows for pile-up of precipitating elements on the grain boundary. This high concentration of precipitating elements plus the

high energy nature of the grain boundary enhance precipitation on the phase boundary [98–101]. This results in periodic formation of fine microalloying precipitates. The periodic appearance of interphase precipitates is a result of the ledge or quasi-ledge mechanism for formation of ferrite [102]. The spacing is equal to the height of the ferrite ledge [2]. Figure 2-21 shows the two mentioned types of precipitates.

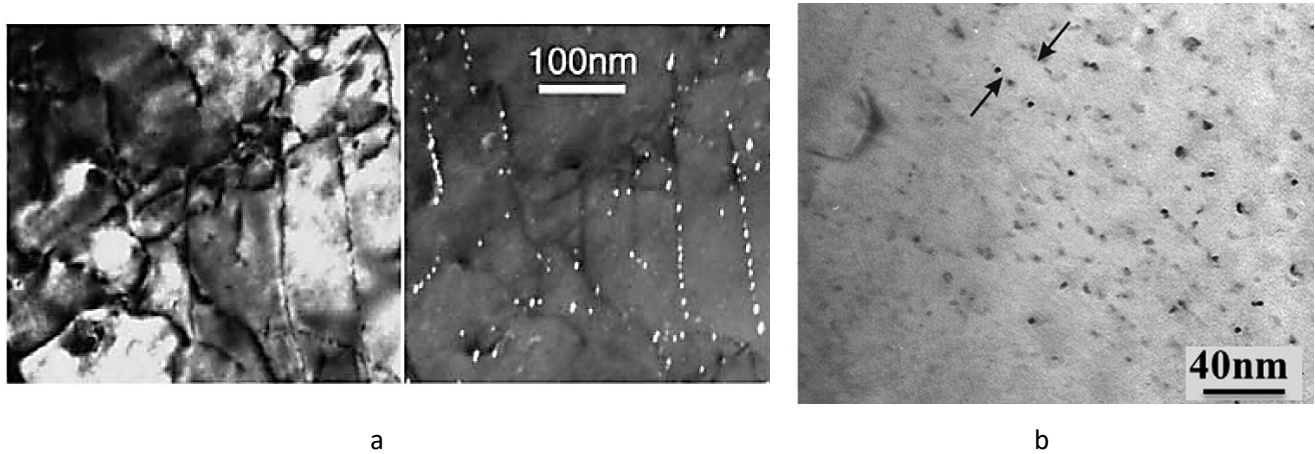


Figure 2-21. a) Precipitation on dislocations in a Nb microalloyed steel. Left, bright field and right dark field image [92]. b) Rows of precipitates formed periodically on the moving phase boundary in a Ti-Mo microalloyed steel [98].

2.4.4 Grain boundary strengthening

A grain boundary is a region between two adjacent grains that have different crystallographic orientation. It is well-known that a reduction in grain size results in an increase in the yield strength. The famous Hall-Petch equation, which was discovered empirically, relates yield strength to the diameter of the grains according to Eq. 2–20 [71].

$$\sigma_{gb} = \frac{k_y}{\sqrt{D}} \quad \text{Eq. 2–20}$$

where σ_{gb} is the contribution of grain boundaries to overall strength, k_y is the strengthening coefficient for grain boundaries and D is the average diameter of grains. Although the validity of Hall-Petch equation is not disputed, the exact mechanism by which the grain boundaries can produce strengthening - as expressed by Hall-Petch equation - is not agreed upon and multiple explanations exist [74]. One theoretical rationalization for this equation is based on assuming that yielding happens when pile-up of dislocations in one grain can activate a dislocation source in an adjacent and less favorably oriented grain. This creates dislocation glide across the boundary as shown in Figure 2-22. This pile-up intensifies the stress acting on the first dislocation and allows it to enter the adjacent grain. The amount of stress intensification is related to the length of the pile-up and longer

dislocation pile-up creates higher stress intensification. The longest pile-up distance in a grain is the one crossing the grain diagonally and this is how the diameter of grains becomes a factor in yielding process.

The Hall-Petch equation holds over a wide range of grain sizes, but as the grain size approaches submicron levels yield strength deviates from the Hall-Petch equation. This suggests that in the ultra-fine grained structures the mechanism for grain boundary strengthening may be different from the suggested pile-up mechanism [103].

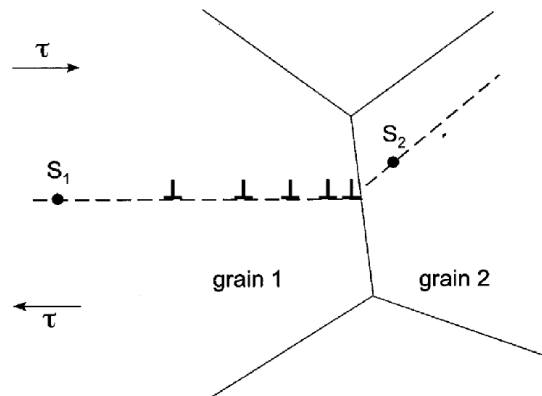


Figure 2-22. Dislocation pile-up emitted from source 1 in grain 1 creates enough local stress at the boundary to activate source 2 in grain 2.

Grain boundary strengthening has been the central part of most microalloyed steel designs for many decades. Grain refinement in microalloyed steels not only contributes to strength, but also increases the toughness of the steel. Both of these properties are vital requirements for high performance microalloyed steel grades [104]. It has been shown that the Hall-Petch equation is valid over a wide range of grain sizes and carbon contents (Figure 2-23) . Table 2-2 shows the reported values of k and σ_0 for microalloyed steels as well other low alloy steels.

Although there is general agreement on the validity of the Hall-Petch equation, the definition of a grain boundary plays a key role in the accuracy of predictions made by this equation. It is believed that low angle boundaries do not contribute to strength the way that high angle boundaries do. As a result, low angle boundaries may not be considered in measuring grain size when it comes to using the Hall-Petch equation [105]. This view on the effect of low angle grain boundaries is also in line with findings on the relationship between grain size and toughness in microalloyed steels. Reduction in grain size increases toughness as the crack front is forced to change direction more often while propagating in materials with lower grain sizes. However, low angle

boundaries are not capable of creating such large deviation and they are essentially ignored by the crack. As a result, when relating grain size to toughness, an effective grain size is suggested to be used which is defined as having a misorientation angle above 15° [106].

Table 2-2. Hall-Petch parameters found in the literature for steel.

σ_0 (MPa)	K (MPa.mm ^{1/2})	Reference
55	----	[107]
54	21.5-23.5	[2]
40-74	17	[7]
---	23.6	[108]
54	18	[109]

Contribution of low angles boundaries to strength in bainite and martensite is usually calculated using Langford-Cohen equation (Eq. 2-21).

$$\sigma_{cell} = \frac{k_y}{\sqrt{d}} \quad \text{Eq. 2-21}$$

Where d is the mean linear intercept diameter of cell in micron and k_y is a structural constant ranging from 157[110]- 450[109].

2.4.5 Overall strength

The overall strength of a metal is a function of contributions from the individual strengthening mechanisms stated above. If the contribution of each strengthening mechanism is independent of the others, the overall strength can be calculated using the linear superposition equation shown in Eq. 2-22 [2].

$$\sigma_y = \sigma_0 + \sigma_{ss} + \sigma_{gb} + \sigma_{dis} + \sigma_{ppt} \quad \text{Eq. 2-22}$$

where σ_0 is the friction stress of the lattice and the rest of strength contributions have been introduced above. The linear summation can result in overestimation of the overall strength. This shows that the strengthening

mechanisms are not independent. To overcome the limitation of linear superposition a number of non-linear superposition equations have been suggested that have the general form of Eq. 2-23 [74,111].

$$(\sigma - \sigma_0)^q = \sum_i \sigma_i^q \tag{Eq. 2-23}$$

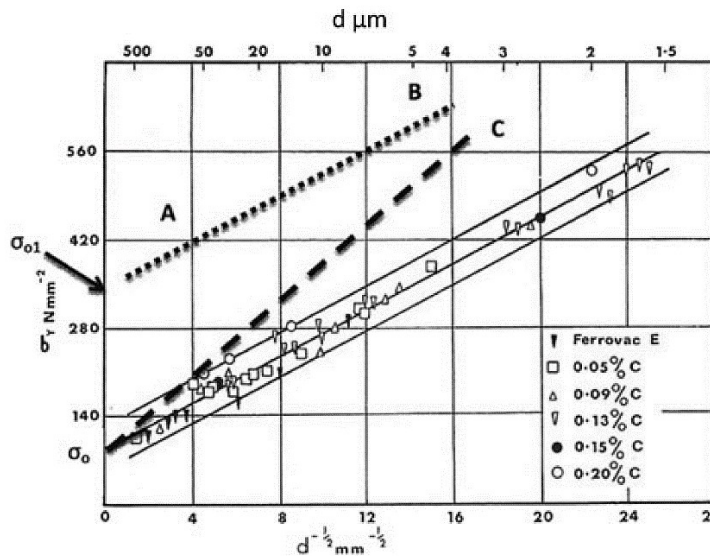


Figure 2-23. Change in strength as a function of grain size ($d^{-\frac{1}{2}}$). Line AB shows the effect of precipitation strengthening added to grain boundary strengthening. Line C shows the estimated GB strengthening effect when k in the Hall-Petch equation is increased [7].

where σ_0 is lattice friction stress of the pure metal, exponent q is between 1 and 2 and σ_i is the obstacle type strengthening mechanism, i.e., precipitate, solid solution, grain boundary or dislocation strengthening. Values suggested for q include 1 (linear superposition), 1.5 [111,112] and 2 [10,113]. There have been attempts to determine q based on the characteristics of the obstacles provided by each strengthening mechanism. Vaucorbeil et al. [114] have suggested q is determined by the relative strength of the obstacles. A strong obstacle locks dislocations more effectively; therefore, a dislocation would have to bend more to bypass it. The strength of an obstacle is usually measured by the critical bend angle (ϕ_c) of the obstacle, as shown in Figure 2-14. The value of the superposition exponent q for simultaneous strengthening of two different types of obstacles obtained by numerical simulation is shown in Figure 2-24. In this figure, ϕ_{1c} and ϕ_{2c} are critical bend angles for the two obstacle types. According to Vaucorbeil et al., q ranges from 1 for the two strengthening mechanisms providing very different obstacle strength to 2 for obstacles of equal strength.

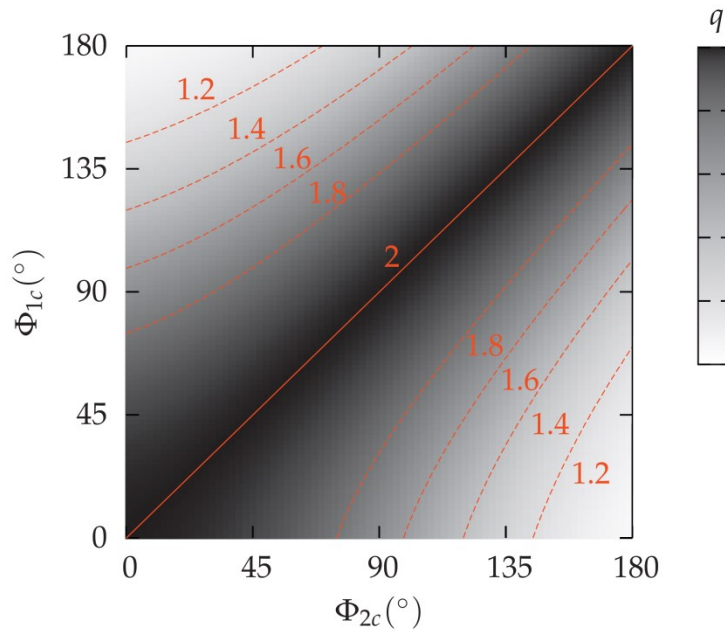


Figure 2-24. The value of superposition exponent q is a function of critical bend angle for two different types of obstacles [114].

Despite the majority of literature reporting ($1 \leq q \leq 2$), there has been at least one report of q being equal to 2.5 [115]. The wide range of formula proposed for superposition of strengthening mechanisms is a result of the disconnect between the models proposed to calculate individual strengthening mechanisms and their cooperative effect. This can be shown by simply applying the superposition formula to calculate the total strengthening effect when the quantity of the strengthening component (volume fraction of precipitates, density of dislocation or concentration of alloying elements) is doubled. In this case the strength of the doubled quantity can be calculated in two ways. One method involves directly calculating the strengthening effect using Eq. 2–5, Eq. 2–13 or Eq. 2–18 for the specific strengthening mechanism of interest. The other approach is superposition of the two contributions from the same strengthening effect but with each operating with 50% of the number of obstacles in the first method. The strength calculated by the two methods must be equal if the superposition formula is applicable. For example, in the case of precipitation strengthening, having two groups of identical precipitates with a volume fraction of $\frac{f}{2}$ is the same as having one group of the same precipitates at a volume fraction of f , so their strengthening effect must be equal. The strengthening effect of a group of precipitates with volume fraction f and precipitate diameter d using Eq. 2–18 is equal to $(k\sqrt{f})$ with k equal to $\frac{10.8}{d} \ln\left(\frac{d}{6.125 \times 10^{-4}}\right)$. The strengthening effect of the same precipitate at half the volume fraction is equal to $\frac{k}{\sqrt{2}}\sqrt{f}$. Applying the superposition equation Eq. 2–23 and solving results in Eq. 2–24.

$$(k\sqrt{f})^q = \left(\frac{k}{\sqrt{2}}\sqrt{f}\right)^q + \left(\frac{k}{\sqrt{2}}\sqrt{f}\right)^q \quad \text{Eq. 2-24}$$

Solving Eq. 2-24 results in $q = 2$ which is in line with Figure 2-24 ($\phi_{1c} = \phi_{2c}$). The same approach can be applied to dislocation strengthening which will result in $q = 2$, which is the same value as for precipitate strengthening. However, applying this method to solid solution strengthening results in $q = 1$. This shows a unified approach for superposition of strengthening mechanism may not be possible with the current fundamental theories for strengthening.

Despite the issues shown for superposition, currently nonlinear superposition is widely used to calculate the overall strength of microalloyed steels based on the contributions of the strengthening mechanisms. Lu et al. have shown superposition in the form of Eq. 2-25 performs better than a number of other summation formulas for microalloyed pipeline steels [21].

$$\sigma_T = \sigma_0 + \sigma_{ss} + \sqrt{\sigma_{gb}^2 + \sigma_{ppt}^2} \quad \text{Eq. 2-25}$$

Eq. 2-25 does not include a dislocation strengthening term, since in their work dislocation strengthening was found to be negligible for hot worked or normalized microalloyed steels.

Chapter 3 Extending an empirical and a fundamental bainite start model to a continuously cooled microalloyed steel²

3.1 Introduction

Microalloyed steel plates often undergo accelerated cooling after hot rolling. Accelerated cooling in thermo-mechanical processing of microalloyed steel is used to increase strength and toughness [116]. High cooling rates improve the mechanical properties by reducing the ferrite grain size and, more importantly, by increasing the volume fraction of the stronger microstructural constituents such as bainitic ferrite and acicular ferrite. Increasing cooling rate reduces the time that austenite spends in the temperature range that produces polygonal ferrite, which has good ductility but lower strength and toughness. As a result, more austenite is left to transform to lower temperature products that exhibit superior mechanical properties [117].

The microconstituents observed in microalloyed steels and their transformation mechanisms have been well studied by many researchers [2,118,119]. The major microconstituents in a microalloyed steel are (quasi) polygonal ferrite (QPF and PF), acicular ferrite (AF), Widmanstätten ferrite (WF), bainitic ferrite (BF), (degenerate) pearlite (DP), conventional bainite (CB), martensite/austenite (M/A) and martensite. PF and its variant, QPF, form at the highest temperature that allows for austenite decomposition. Lower temperatures favor transformation to WF, BF and AF. These ferrite variants are thought to be similar in nature. For instance, they all are confirmed to show a key attribute of a displacive transformation mechanism, which is an invariant-plane strain and surface relief phenomena. The needle-like morphology of WF has been explained by considering the cooperative growth of mutually accommodating ferrite plates formed with a displacive mechanism [120].

BF is in essence bainite without carbide [36]. Despite the similarities in transformation mechanism of WF and BF, BF has different transformation kinetics and morphology. Bhadeshia [120] has suggested that WF nucleates the same way as bainite, which involves diffusion of carbon. However, the growth of WF involves long range diffusion of carbon, which is not required for bainite growth. Hillert et al. [37] have challenged this idea and suggested that the WF and BF are essentially the same transformation type. While there is evidence that AF and BF form by the same mechanism [121], there is general agreement among the scientific community that the two form at different nucleation sites. Acicular ferrite nucleates on deformation bands or inclusions [122] within austenite grains if they are present (intragranular nucleation), while BF nucleates on the grain boundaries of prior austenite. CB [58], in contrast to BF, forms from higher carbon austenite. In microalloyed steels, high carbon

² Chapter 3 is largely based on a published paper by Khodaie et al. *Mater. Sci. Eng. A* 650, 510–522 (2016).

austenite forms as a result of carbon rejection from ferrite into austenite, which happens during the transformation of austenite to PF and QPF. M/A is the carbon enriched austenite that is too stable to fully transform to martensite at room temperature. M/A is observed as an elongated second phase between BF laths or as separate islands surrounded by PF and QPF [117,123].

Microstructures that form during continuous cooling are a mixture of a number of microconstituents. As the temperature drops, diffusion becomes more difficult and conditions become less favorable for transformations that require long range diffusion of alloying elements. In microalloyed steels, the transformation to PF and QPF shows characteristics of diffusional transformations and it is accompanied by long range diffusion of at least carbon. On the other hand, temperature reduction enhances transformations that incorporate displacive mechanisms. Displacive transformations induce large lattice strains which act as an impeding force for the transformation. At lower temperatures, this impeding force can be overcome by the higher driving force for transformation. In microalloyed steels, bainite and martensite show characteristics of displacive transformations.

The critical condition that leads to a change in the transformation type from QPF to BF and, in general, bainite depends primarily on the transformation mechanism for bainite. Although bainite has been known for a long time since its discovery in 1929, its transformation mechanism remains the most debated subject in the physical metallurgy of steel [124,125]. There are two theories regarding the transformation mechanism for bainite, diffusive and displacive. The diffusive theory is based on nucleation and growth of bainite being diffusion controlled. The displacive theory states that bainite nucleates displacively, similar to martensite, and forms a ferrite that is supersaturated with carbon [39]. Diffusion of excess carbon to austenite (upper bainite) or its precipitation within ferrite (lower bainite) takes place after displacive transformation. It is beyond the scope of this chapter to discuss the details of these theories, but one of the more recent empirical models developed is based on experimental results that relate bainite start temperature (B_s) to chemical composition for a range of low alloy steels undergoing isothermal transformation [126]. This model has been shown to be useful in practical applications and helps avoid the complexity and uncertainty of the mentioned bainite transformation theories.

Macroscale mechanical properties of a microstructure are ultimately related to the type of the microconstituents present in the microstructure, their volume fraction and to a lesser degree to their morphologies. The present study has attempted to correlate transformation kinetics, microstructure and hardness in light of multiple phase transformations. The empirical equation of Lee (Eq. 3–1) [126] and Bhadeshia and Edmunds [39] has been extended to predict the bainite start temperature for a microalloyed steel undergoing continuous cooling. This approach is termed the Bainite-Intercept-Temperature (BIT) model. This model identifies the temperature and fraction of transformation that triggers the change in transformation

mechanism from QPF to BF, i.e., the bainite start temperature (B_s) on a continuous cooling transformation diagram for a microalloyed steel.

$$B_s(°C) = 745 - 110C - 59Mn - 39Ni - 68Cr - 106Mo + 17MnNi + 6Cr^2 + 29Mo^2 \quad \text{Eq. 3-1}$$

In this equation, the elements represent their concentrations in weight percent. It is worth noting that this equation does not include the effect of some bainite promoting elements such as B and Nb. These elements in the soluble form have been shown to increase the volume fraction of bainite in steel [56,127]. These elements increase the volume fraction of bainite by retarding diffusive transformation of austenite to PF/QPF that precedes transformation of bainite. This leaves more austenite to transform to bainite. It is also worth noting that Nb and B do not appear as a parameter in any of the 19 empirical B_s formulas listed by Gorni [33]. However, based on the displacive transformation theory of bainite, it is possible for any alloying element to affect B_s by changing the free energies of ferrite and austenite. This effect while possible, for microalloyed steels is negligible given the low concentrations of Nb and B used in these steels.

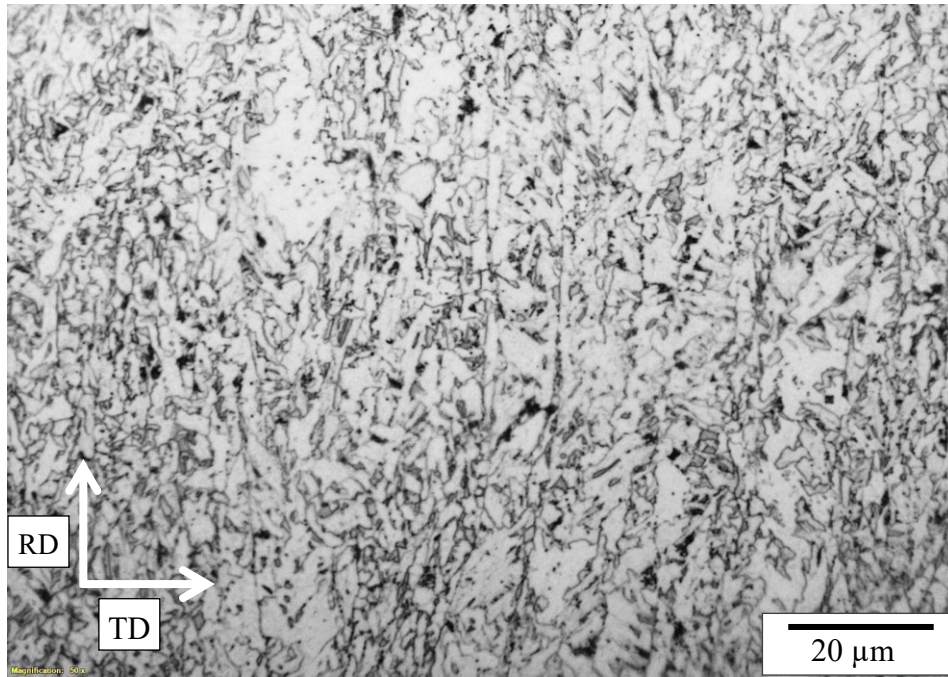
3.2 Experimental procedure

The continuous cooling transformation of an X80 steel is the focus of this chapter. The designation X refers to a pipeline steel, while 80 refers to the yield strength in ksi (550 MPa). Table 3-1 shows the chemical composition of this steel. This steel is hereafter referred to as X80-N.

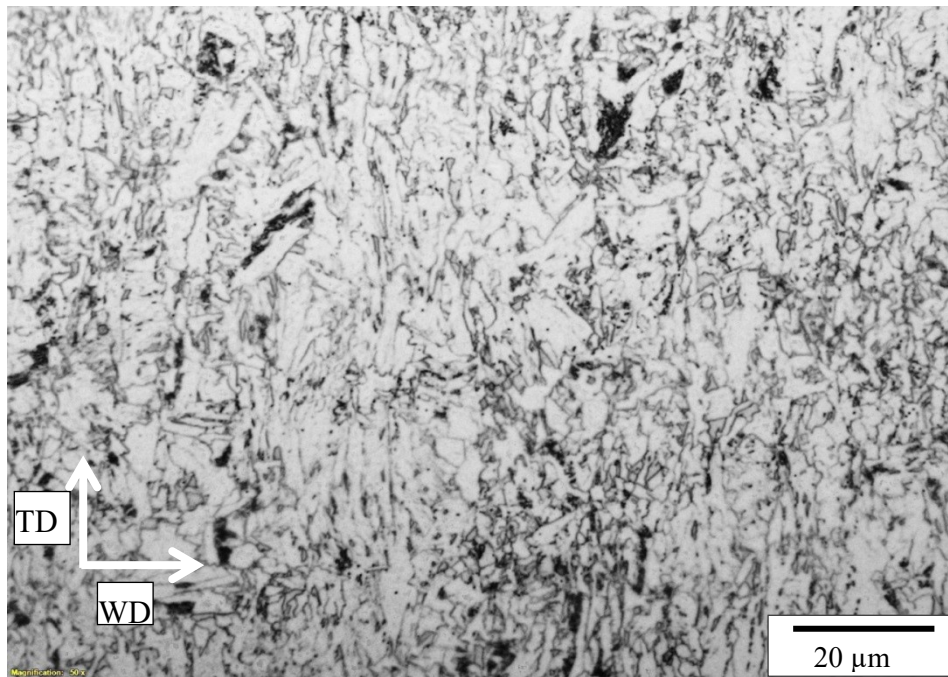
Table 3-1. Chemical composition (wt%) of the steel used in this study

	C	Mn	Si	Cr+Ni+Mo+Cu	Nb	Ti	Al	N	B
Steel X80-N	0.064	1.69	0.12	0.83	0.04	0.007	0.017	0.0064	0.0003

Figure 3-1 shows the as rolled microstructure of X80-N steel. Figure 3-1a shows the surface that is normal to the width direction (WD) of the skelp, with a grain size of $3.1 \mu\text{m} \pm 0.6 \mu\text{m}$. Figure 3-1b shows the surface that is normal to rolling direction (RD) of the skelp, with a grain size of $2.5 \mu\text{m} \pm 0.15 \mu\text{m}$. Grain size was measured using the line intercept method according to ASTM E112 [128]. In this figure (TD) stands for transverse direction. Both images were taken from the center of the skelp, from which dilatometer samples were taken.



a



b

Figure 3-1 Optical images of the microstructure for as rolled plate at the mid-thickness, from which dilatometer samples were sectioned. a) Surface normal to WD. b) Surface normal to RD.

To measure the kinetics of transformation, hollow, cylindrical samples measuring 4 mm OD, 3 mm ID and 10 mm in length were cut from the center of a 15 mm skelp with the length of the dilatometer sample in the rolling direction. Samples were then processed with a Bähr DIL 805 thermo-mechanical simulator. One experiment was done at each experimental condition. In the dilatometer, the samples were austenitized at 950°C for 15 minutes to ensure full transformation to austenite and then cooled at various rates ranging from 1°C/min to 40°C/min. The austenitizing temperature of 950°C was chosen to allow partial dissolution of NbC to create an austenite chemistry similar to the austenite after hot rolling before transforming to ferrite. Figure 3-2 shows a schematic of the thermal cycles used in the dilatometer tests.

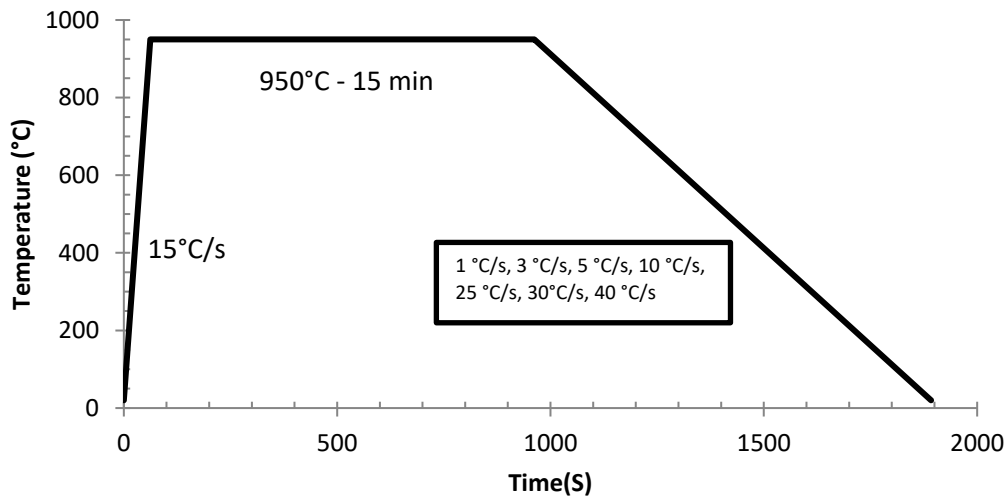


Figure 3-2. Schematic of thermal cycle used for the continuous cooling experiments.

To observe the microstructures, samples were cut in half from the mid length to expose a circular cross section. Samples were then mounted, polished and etched using 2% Nital. To observe the prior austenite grain size, modified Winstead's reagent was used. This etchant is a saturated picric acid solution in ethanol, which is activated by hydrochloric acid and enhanced by a sulfonate based compound to reduce surface tension and improve wetting. The chemical composition and preparation method of this etchant are explained in detail elsewhere [129]. Microstructural observation was done using a Hitachi S4800 field emission source scanning electron microscope (FE-SEM) operating in secondary electron (SE) mode at 5 kV and a Leica DM ILM optical microscope using incandescent light with a blue filter. Quantitative metallography was performed to measure the volume fraction of microconstituents, using a point counting technique on 5 fields of view according to ASTM E562 [130].

Hardness measurements were done using a Vickers microhardness indenter according to ASTM E384 [131]. Hardness was measured on the transverse cross sections of the sample at the mid thickness. Due to the thin wall thickness of the test samples, the indentation force was altered from 1 kg to 500 g to produce the largest possible indentation without getting too close to the edge of the sample, as specified by ASTM E384. The target indentation diameter was 50 μm to 80 μm. Full force duration was set to 10 s.

To further investigate the validity of the analysis method proposed in this chapter, results of continuous cooling transformation experiments performed on two different steels were analyzed. The chemical compositions of these two steels are shown in Table 3-2. Steel X80-K was austenitized at 945°C for 5 minutes and cooled at constant cooling rates of 5°C/s, 7°C/s, 10°C/s, 20°C/s and 50°C/s to room temperature. Steel Grade 80-L was austenitized at 1100°C for 5 minutes and cooled at constant cooling rates of 0.5°C/s, 1°C/s, 5°C/s and 10°C/s to room temperature. Additional information about these steels can be found in references [132] and [133], respectively.

Table 3-2. Chemical composition (wt%) of Grade 80-L and X80-K steels used for validation of BIT analysis

	C	Mn	Si	Cr+Ni+Mo+Cu	Nb	Ti	Al	N	B
Steel Grade 80-L	0.06	1.58	0.22	0.92	0.088	0.016	--	--	0.0004
Steel X80-K	0.058	1.65	0.25	0.73	0.091	0.016	--	--	--

3.3 Results and discussion

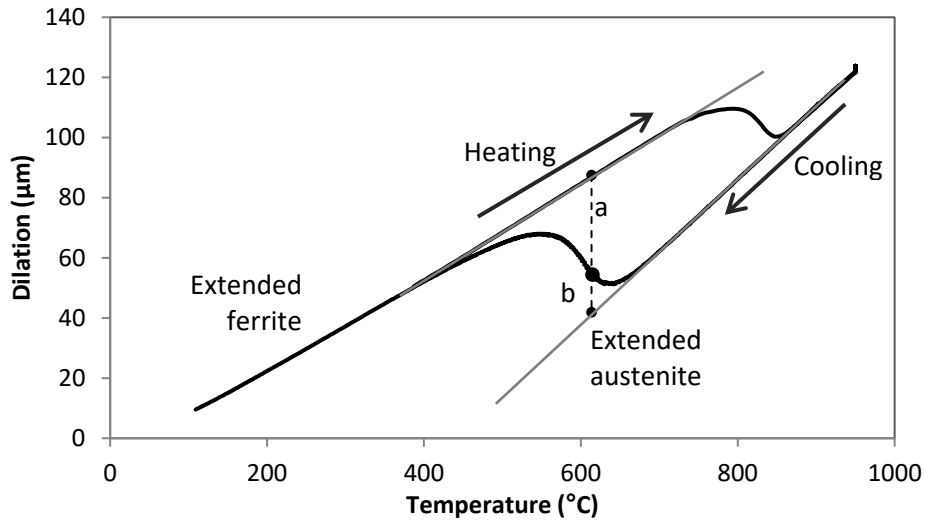
3.3.1 Dilatometry and kinetics of transformation

Dilatometry records the change in dimensions of the samples as a function of temperature and time. For continuous cooling the fraction transformed can be calculated from dilation versus temperature plots using the lever rule as shown in Figure 3-3a and Eq. 3–2.

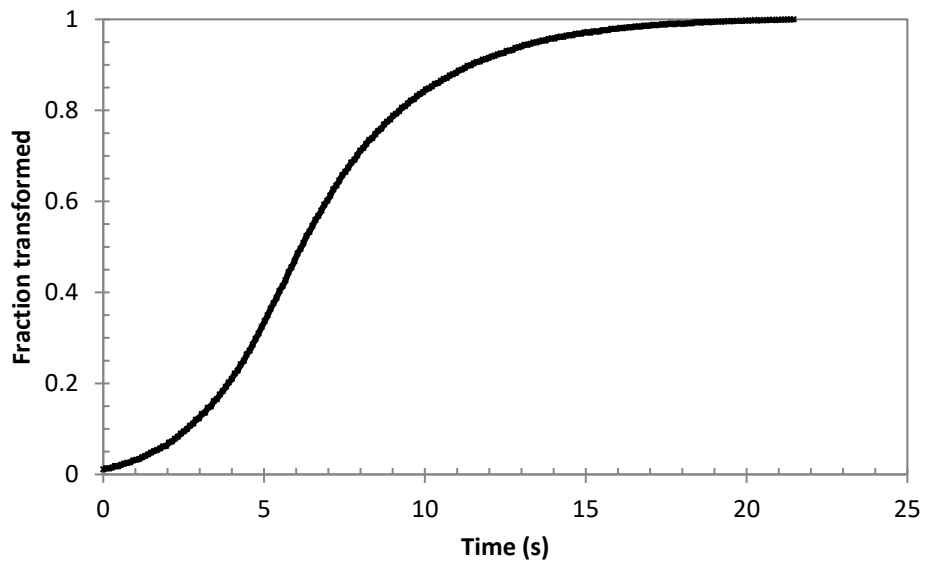
$$X = \frac{b}{a + b} \tag{Eq. 3–2}$$

In this equation, X is the fraction transformed and a and b are the distances to the extended ferrite and extended austenite lines as shown in Figure 3-3a. Figure 3-3b shows the fraction transformed calculated using

Eq. 3–2 for the dilatometry curve in Figure 3-3a. Note that it seems from the shape of the dilatometer curve shown in Figure 3-3a that there is only one product phase. Analysis of the first and second derivatives of the dilation vs temperature curve also did not produce a meaningful result about the product phase(s). Metallographic analysis of the microstructure of this sample clearly revealed that there are multiple transformation products for this sample.



a



b

Figure 3-3 Analysis of sample dilatometry data at a cooling rate of 10°C/s. a) Dilatometry curve. b) Calculated fraction transformed versus time. In this graph $t=0$ corresponds with $X=0.01$.

Using the calculated fraction transformed, the start and finish of the transformation are determined using the criteria of 1% and 99% transformation, respectively. Figure 3-4 shows the transformation start and finish lines along with the hardness of the samples after transformation. What happens between the transformation start and finish lines is the focus of the rest of this chapter. In the following sections, microstructural observations, quantitative metallography and a method called Bainite-Intercept-Temperature (BIT) are used to study multiple phase transformations. At the end of the discussion, the complete continuous cooling transformation (CCT) diagram of steel is presented.

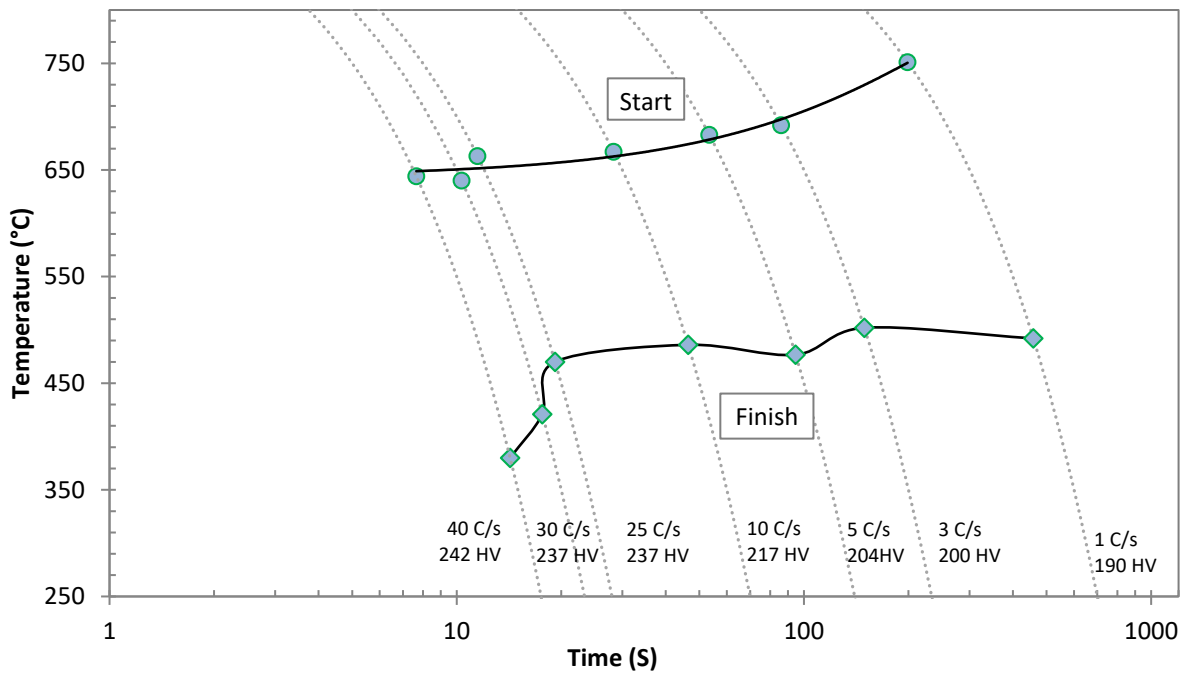


Figure 3-4. CCT diagram for the steel studied (X80-N). Start and finish lines were determined by 1% and 99% transformation criteria calculated from the dilatometry results.

3.3.2 Evolution of microstructure

The microstructure of continuously cooled samples is made up of a combination of ferrite variants (polygonal, Widmanstätten and bainitic), degenerate pearlite (DP) and bainite/martensite (B/M). Figure 3-5 shows an optical image of a water quenched sample after austenitization for 15 minutes at 950°C. The sample was etched with modified Winstead's reagent to reveal the prior austenite grain size [129]. Using the line intercept method on five fields of view, according to ASTM E 112, the average prior austenite grain size was measured as $12.7 \mu\text{m} \pm 1.2 \mu\text{m}$.

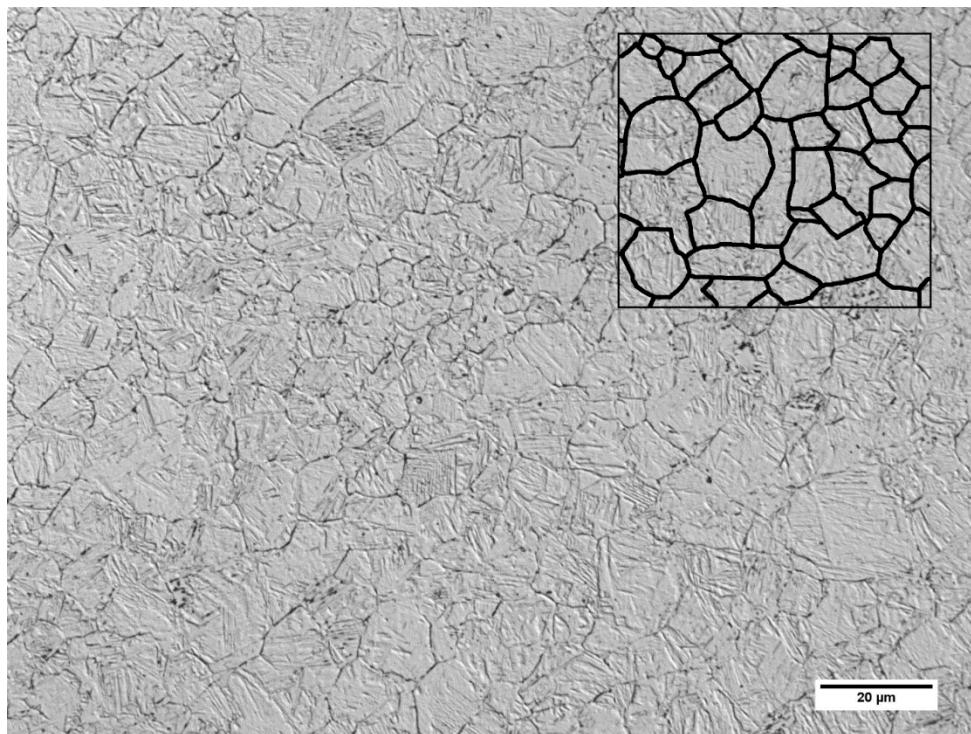
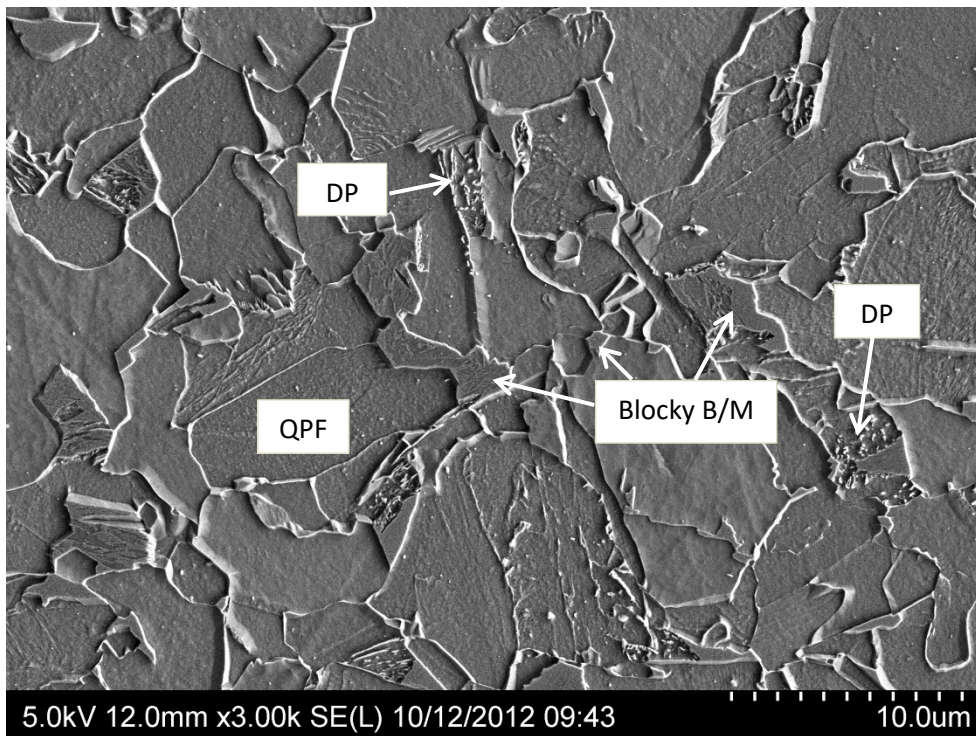
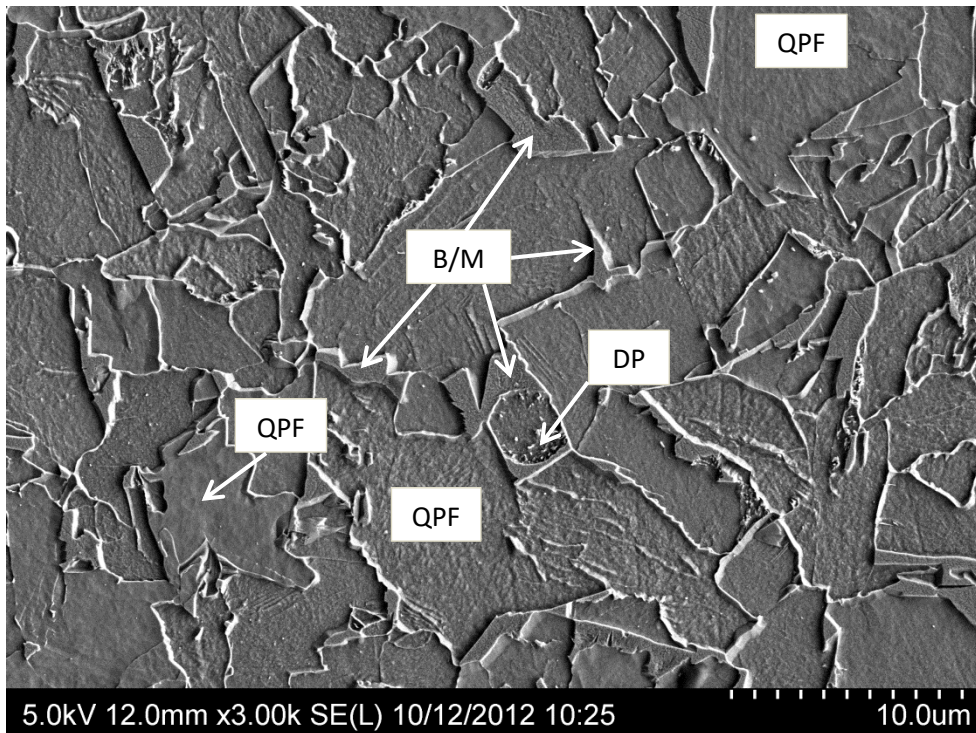


Figure 3-5. Optical image of prior austenite grains after austenitization at 950°C for 15 minutes. The average grain size is 12.7 μm .

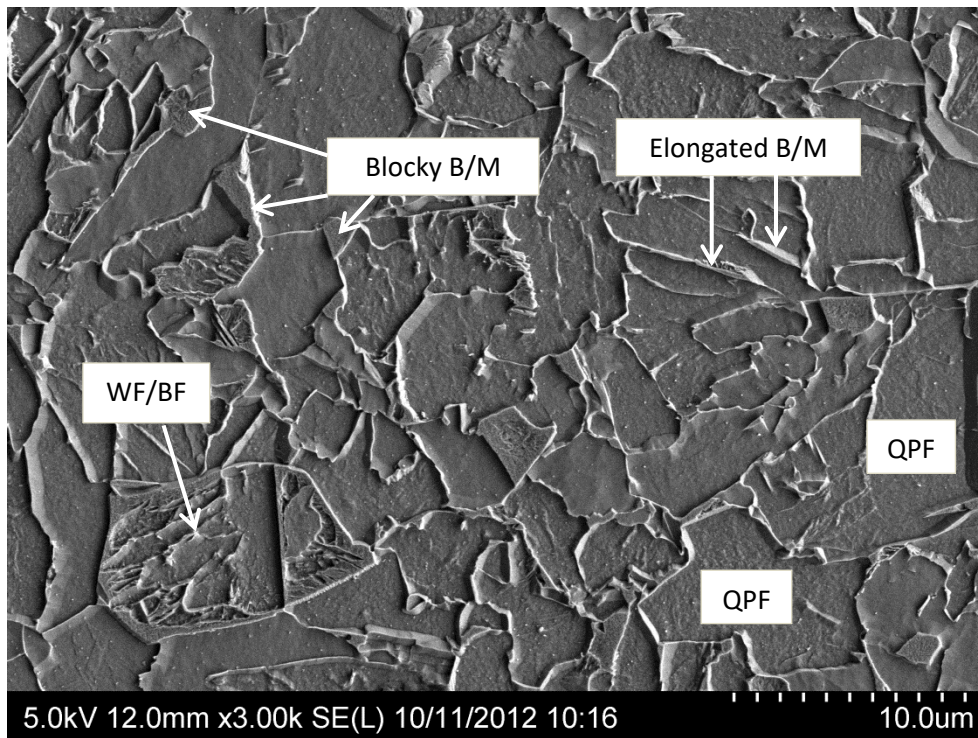
Figure 3-6.a to Figure 3-6.f show the microstructures obtained after continuous cooling at different cooling rates. The observed microconstituents, which are labeled in the micrographs, and the rationale for identification will be explained in detail in the following section. Figure 3-6.a is the microstructure of the sample cooled at 1°C/s showing relatively large PF/QPF grains with blocky B/M islands. Occasional DP colonies are also observed at this cooling rate. Figure 3-6.b shows that at 3°C/s the microstructure is similar to the 1°C/s sample, but the size of the microconstituents is smaller. By increasing the cooling rate to 10°C/s (Figure 3-6.c), DP disappears and elongated BF and interlath B/M begin forming. Figure 3-6.d to Figure 3-6.f show the microstructures of samples cooled at 25°C/s to 40°C/s. At these cooling rates the transformation of austenite is dominated by a bainitic reaction. Due to the high cooling rate, the transformation of austenite to QPF that takes place at higher temperatures is inhibited and only a few isolated QPF grains are observed. The remainder of the microstructure consists of BF and interlath B/M.



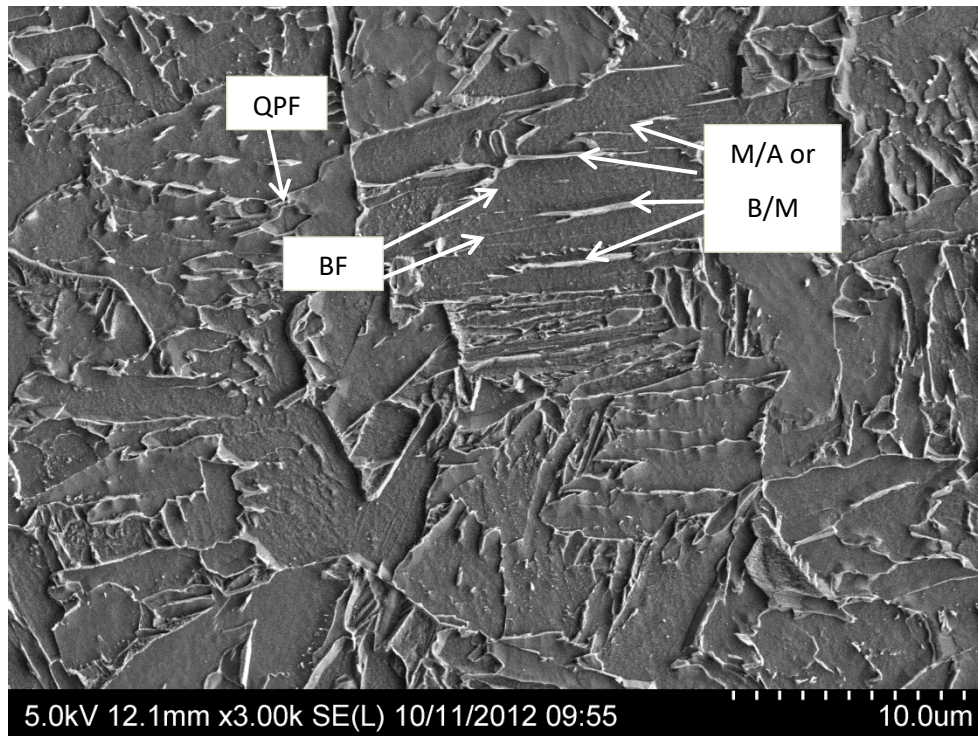
a



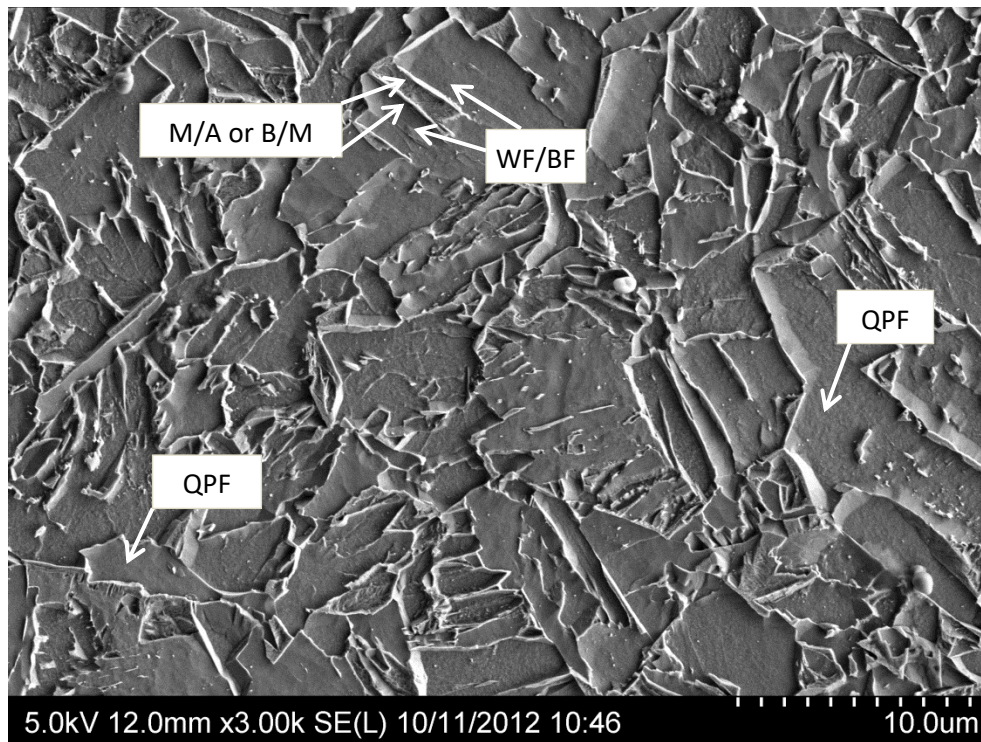
b



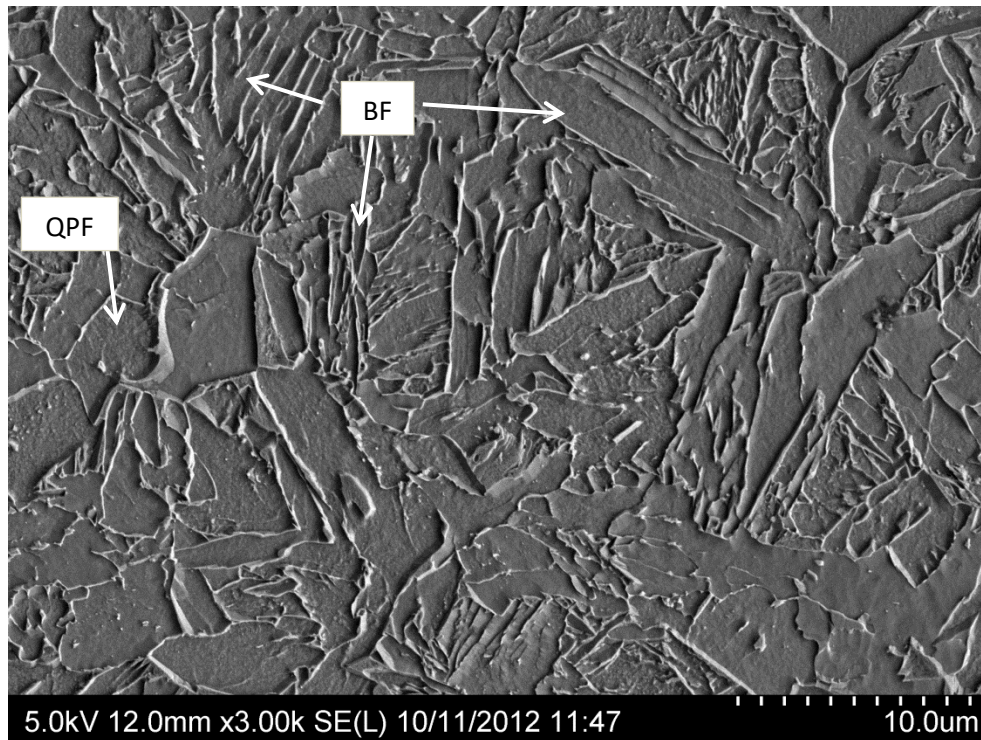
c



d



e



f

Figure 3-6. SE-SEM micrographs of the microstructures that form at different cooling rates. a) 1°C/s, b) 3°C/s, c) 10°C/s, d) 25°C/s, e) 30°C/s, f) 40°C/s.

3.3.3 Observed microconstituents

3.3.3.1 Quasi polygonal ferrite (QPF)

Quasi-polygonal ferrite appears as flat, deeply etched grains with no internal features except for occasional submicron size precipitates on the etched surfaces, which are the result of a prolonged austenitization period. QPF is the first phase to form during continuous cooling. The formation of QPF is accompanied by rejection of carbon to austenite. As the temperature drops, depending on the carbon content of austenite and the temperature, conditions can become more favorable for the formation of other microconstituents such as DP, BF and B/M. Figure 3-7 shows a higher magnification image of the microstructure that forms at 1°C/s cooling (Figure 3-6.a), depicting ferrite grains as well as other low temperature microconstituents of DP and B/M.

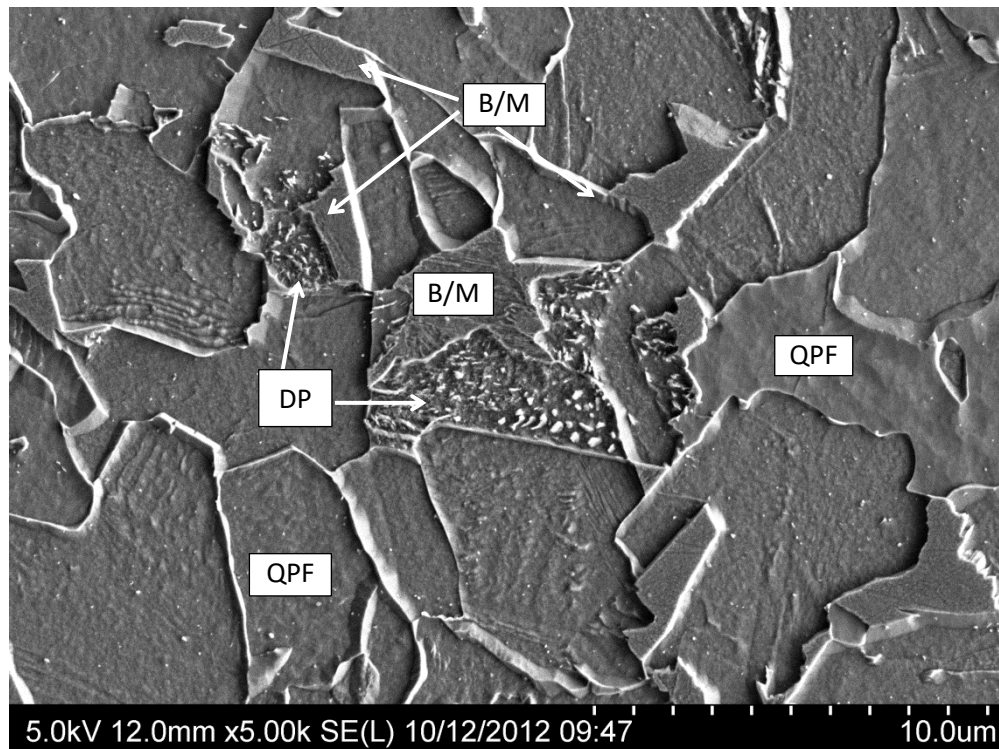


Figure 3-7. SE-SEM micrograph of sample cooled at 1°C/s. Examples of QPF are shown.

3.3.3.2 Widmanstätten /bainitic ferrite (WBF)

Although Widmanstätten ferrite (WF) and bainitic ferrite (BF) transform with slightly different mechanisms [120], Hillert [37] has suggested that similarities between WF and BF outweigh the differences. As such, both of these ferrite variants are categorized together. Both WF and BF appear as packets of elongated and parallel laths separated by low angle boundaries [134,135]. BF is proposed to nucleate on prior austenite grain boundaries

[58], while WF can nucleate both on prior austenite grain boundaries and pre-existing grain boundary allotriomorphic ferrite. The WF and BF transformation mechanism includes a displacive process; however, both are diffusion controlled.

Figure 3-8 shows a continuous and gradual change in the phase transformation mode that occurred within one austenite grain. In this figure, the dashed line shows the location of the nucleation of QPF which, judging by its straight nature, appears to be a twin boundary within the prior austenite grain. The large arrow shows the direction of propagation of the ferrite grain. It can be seen that starting from the marked prior austenite boundary, the transformation has begun by the formation of QPF which has eventually changed to WBF. This shows that the nucleation site for WBF could be the QPF/ γ phase boundary. At the far left of the image (top and bottom) blocky B/M grains are visible, which is explained in the B/M section.

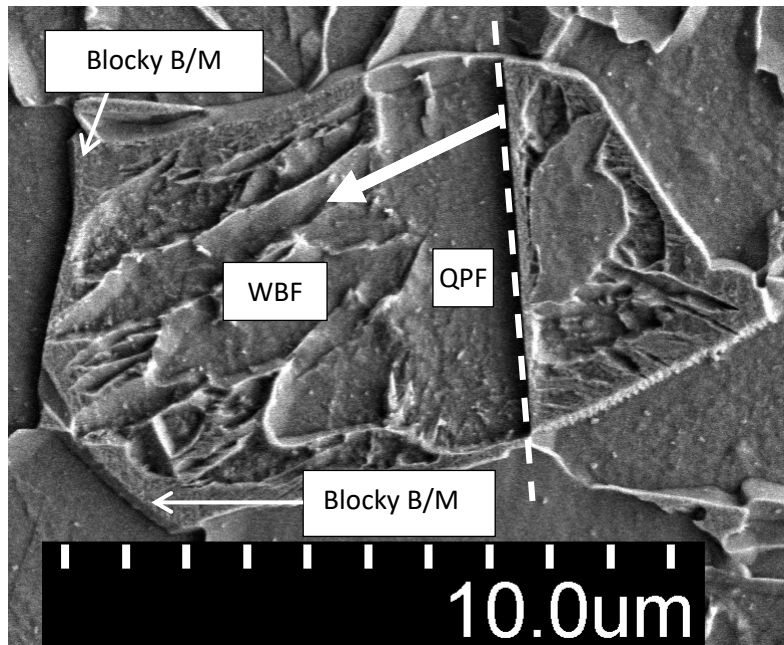


Figure 3-8. SE-SEM micrograph showing nucleation of WBF on QPF during continuous cooling at 10°C/s. The dashed line appears to be the location of an annealing twin boundary within an austenite grain and the arrow shows the direction of progress of the transformation.

Bainitic ferrite's lath shape is a result of the non-uniform growth rate of the ferrite phase. The growth rate along the axis of the lath is highest, while it is lowest in the direction perpendicular to the axis. This morphology minimizes the strain energy associated with displacive transformation of BF. This type of growth results in the rejection of carbon to the two sides of the plate. When the diffusion field of rejected carbon around the BF laths

impinges on the diffusion field of an adjacent BF lath (soft impingement) at the end of transformation, a region of high carbon austenite parallel to the axis of both plates will be left in between. This region, upon later cooling, can transform into bainite or martensite (B/M), M/A or cementite. Figure 3-9 shows bainitic ferrite with an elongated second phase between the laths. It should be noted that due to the low degree of misorientation between two adjacent BF laths, when there is no second phase present between them, the grain boundary may not be visible after etching and the two grains could appear as one. The area indicated by the dashed circle in Figure 3-9 shows the contact region of two such BF laths. However, in the bottom right hand side of Figure 3-9, lightly etched and parallel boundaries of BF can be spotted. These BF laths are about 500 nm in width. Aaronson et al. [136] and Bhadeshia [36] have defined the laths or plates that are separated by a low angle boundary as sub-units and a pack of sub-units that are separated by a carbon-rich phase as a sheaf of bainite.

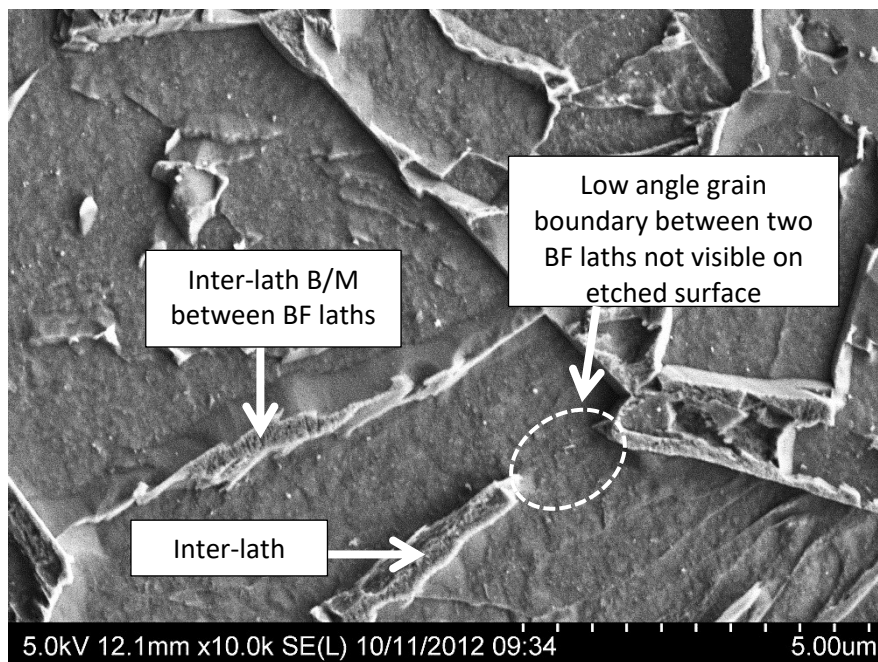


Figure 3-9. SE-SEM micrograph of sample cooled at 25°C/s. Elongated B/M with BF laths are present on both sides. Above the scale bar, lightly etched low angle boundaries of BF are visible.

3.3.3.3 Bainite/martensite (B/M)

B/M is used as a generic term for a microconstituent that can be either bainite or martensite or M/A. It is distinguished by its internal structure and by being less etched compared with surrounding ferrite grains. B/M was observed in two distinct morphologies; blocky and inter-lath type. Both morphologies of B/M have internal structure. Blocky B/M shows an equiaxed shape and is observed for cooling rates of 3°C/s to 10°C/s. It often has one or two straight boundaries forming a sharp corner. Figure 3-10 shows an example of blocky B/M. Inter-lath B/M, as implied by the name, is observed between two laths of BF and forms at cooling rates of 25°C/s and

above. The formation of inter-lath B/M is linked with the formation of BF as described in the Widmanstätten /bainitic ferrite section. Inter-lath B/M can be seen in Figure 3-9 and is marked by arrows.

The unique morphology of blocky B/M can be explained by considering the sequence of phase formation. For slow to medium cooling rates, the transformation begins by nucleation and growth of allotriomorphic ferrite on the prior austenite grain boundaries. The formation of allotriomorphic ferrite is accompanied by rejection of carbon out of ferrite. This excess carbon has to diffuse away from the ferrite front to allow the transformation to progress. Since diffusion along grain boundaries is much faster compared with diffusion in the bulk of the grain, rejected carbon atoms are removed from the ferrite front much faster along austenite grain boundaries compared with the direction normal to them. This mechanism explains the spreading of ferrite along the prior austenite grain boundaries in allotriomorphic ferrite.

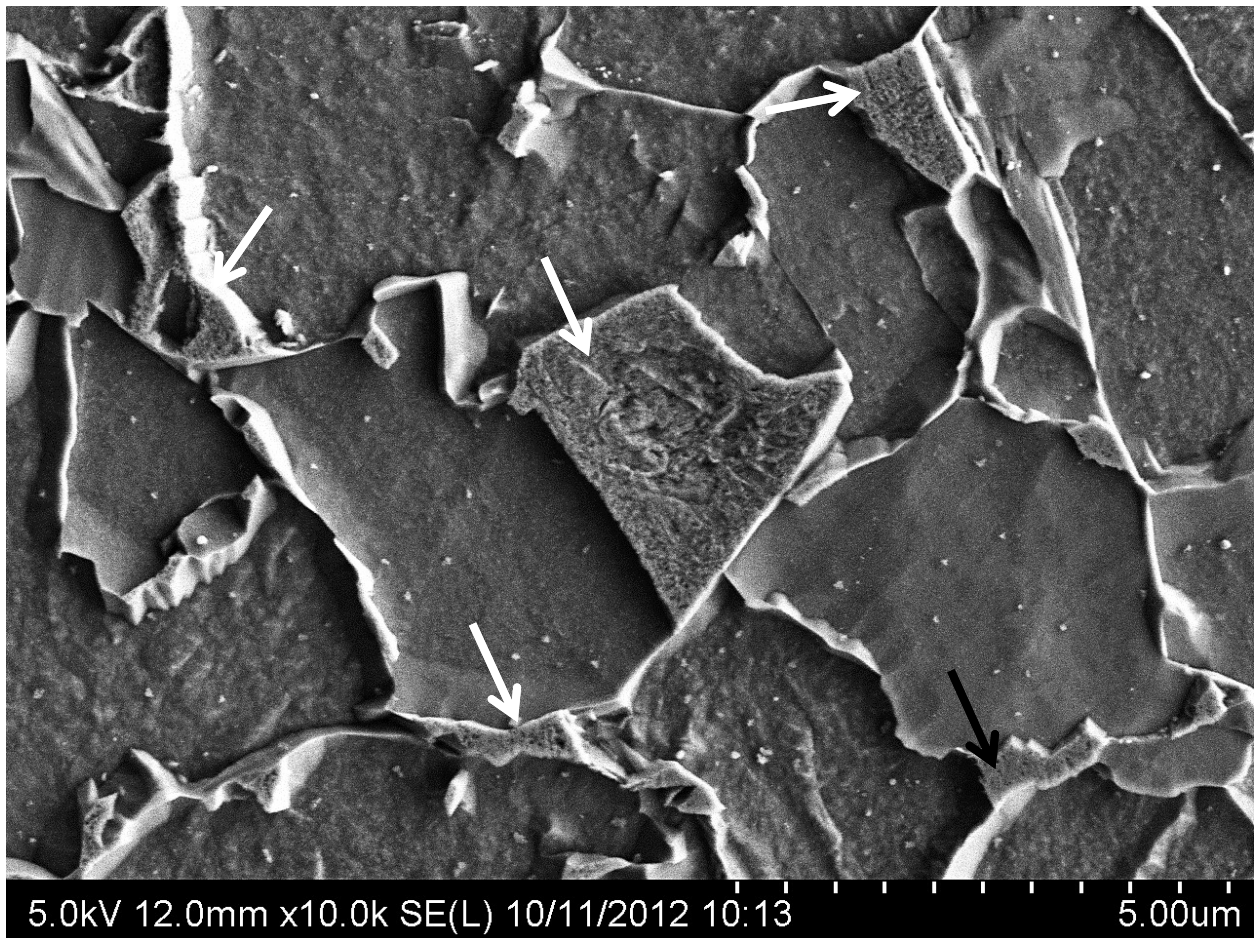


Figure 3-10. SE-SEM micrograph of sample cooled at 10°C/s. Blocky B/M regions are marked by arrows.

The excess carbon that diffuses away from ferrite increases the concentration of carbon along the austenite boundaries that have not transformed yet. It is well known that carbon reduces the Gibbs free energy of the grain boundary [137]. The high carbon levels at the grain boundaries act as a barrier for nucleation. In other words, nucleation of ferrite on a part of an austenite boundary reduces the probability of nucleation of ferrite on the rest of the boundary. As a result, on some parts of the prior austenite grain boundaries ferrite does not nucleate. This region of austenite stays untransformed until the temperature is reduced enough to permit transformation to B/M. This process is shown schematically in Figure 3-11.

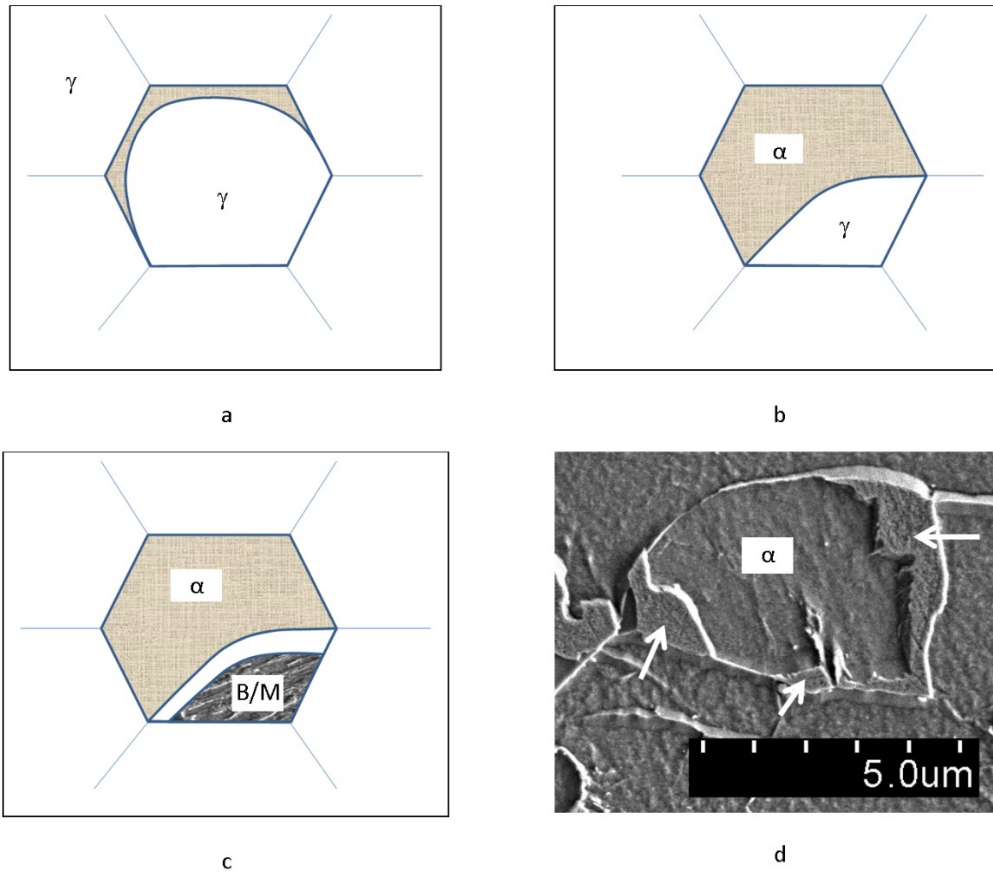


Figure 3-11. Mechanism for formation of blocky B/M. a) Formation of allotriomorphic ferrite in the form of a partial ring. b) Growth of the partial ferrite ring. c) Reduction in temperature allows nucleation of B/M. d) SE-SEM image of ferrite and blocky B/M (marked by arrows) in a sample cooled at 3°C/s.

3.3.3.4 Degenerate pearlite (DP)

Degenerate pearlite was observed at cooling rates of 1°C/s to 25°C/s with relatively low volume fractions. The maximum amount of DP was 3.9 vol%, which was observed at a cooling rate of 1°C/s. Figure 3-12 shows a packet of DP which formed at a cooling rate of 1°C/s. Since DP contains cementite particles, it can only form from a high carbon austenite which is only available after formation of QPF and rejection of excess carbon to austenite.

For this reason, DP is almost always observed in the vicinity of B/M which also forms from high carbon austenite. Considering that DP with large cementite particles needs longer diffusion distances than the fine microstructure of B/M, it can be concluded that DP forms at higher temperatures and precedes formation of B/M during continuous cooling. In Figure 3-12 it can be seen that there is a gradient in the size of cementite particles in DP from the outer boundary of the DP packet towards the B/M grain. Large particles form at higher temperature, which makes longer diffusion distances possible for carbon atoms. As the temperature drops, diffusion becomes slower and super saturation increases which results in the formation of more cementite particles that grow to a smaller size. As a result, the smallest cementite particles are always located adjacent to B/M.

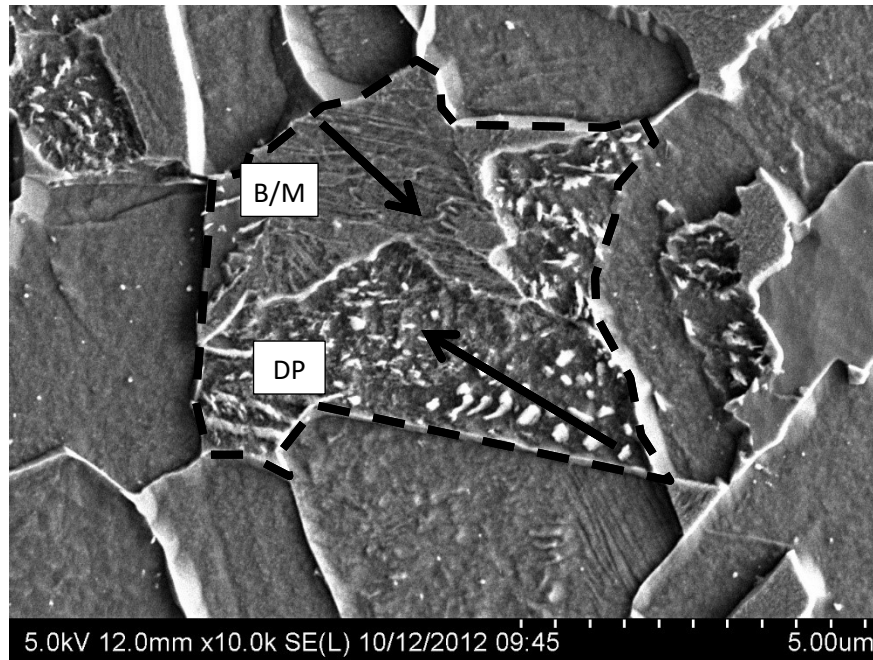


Figure 3-12. SE-SEM micrograph of sample cooled at 1°C/s. DP coexists with B/M in one prior austenite grain (outlined by dashed line). Arrows show the direction of growth of each microconstituent.

Since the largest cementite particles in DP are the ones that form first during continuous cooling, following the direction of increasing cementite particle size can lead to the nucleation site of DP. Figure 3-12 shows that cementite is larger at the prior austenite grain boundary (outlined by the dashed line) suggesting that it is the nucleation site. However, observation of DP packets similar to those in Figure 3-13 suggest otherwise. In Figure 3-13, DP is trapped between QPF and B/M. The larger cementite particles are located near the QPF. This suggests DP can nucleate at the α/γ interface. Similar to Figure 3-12, smaller cementite particles are adjacent to the B/M as expected.

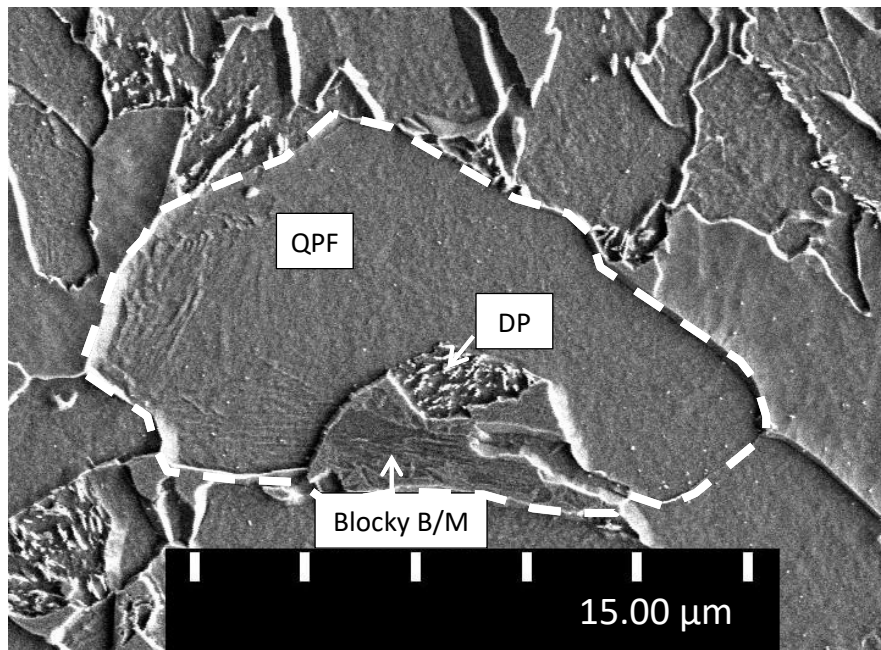


Figure 3-13. SE-SEM micrograph of the sample cooled at 1°C/s. Coexistence of QPF, DP and B/M within one prior austenite grain (outlined by dashed line) is shown. This micrograph suggests DP can nucleate at the α/γ interface.

3.3.4 Measurement of phase fractions using quantitative metallography

The point count technique was used to determine the volume fraction of distinguishable microconstituents. The three microconstituents considered in volume fraction measurements are ferrite, B/M and DP. Figure 3-14 shows the volume percent of these microconstituents. It should be mentioned that ferrite is the sum of the ferrite in BF and QPF and B/M is the sum of both blocky and inter-lath B/M. As expected from a microalloyed steel, the majority of the microstructure consists of ferrite followed by B/M and DP.

3.3.5 Continuous cooling and bainite start temperature

One of the consequences of transformation during continuous cooling is the change in the type of transformation. The obvious cause of this is the change in instantaneous temperature (caused by the cooling process) and chemical composition (caused by partitioning of alloying elements between phases). The mechanism by which temperature and chemical composition affect transformation can be explained by considering two independent yet cooperative phenomena. One of these represents the kinetics aspect of transformation and the other is the thermodynamics of transformation. The kinetic phenomenon is diffusion of atoms, which becomes slower at lower temperatures. This affects redistribution of alloying elements between ferrite and residual austenite, which ultimately affects the rate of the diffusive transformation. For the second

phenomenon, at lower temperatures the difference between the free energies of the parent and product phase increases. In steels, for instance, this increased driving force makes it possible to form metastable phases such as bainite and martensite that possess higher free energies than ferrite.

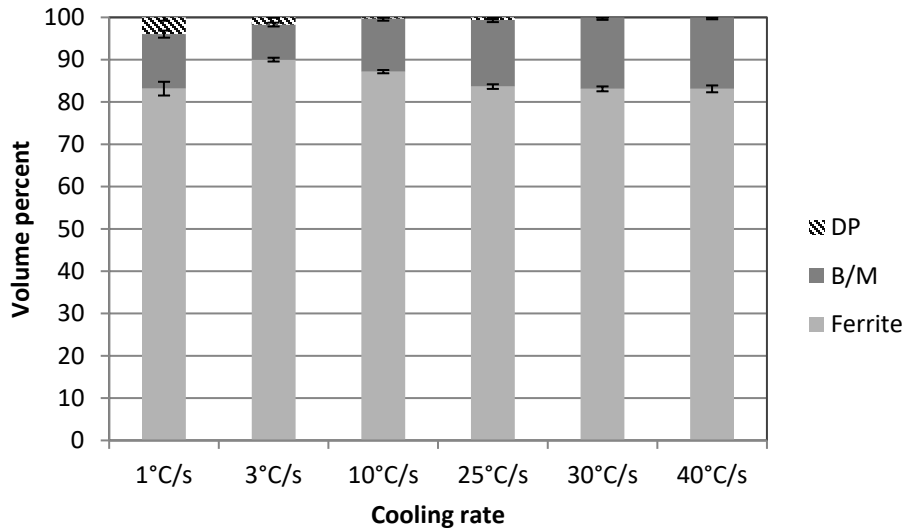


Figure 3-14. Distribution of volume fraction of microconstituents for different cooling rates.

In order to analyze multiple phase transformations, it is necessary to consider the effect of kinetics and thermodynamics at the same time. There are empirical and analytical models developed for steel that predict bainite and martensite start temperatures based on chemical composition and, in rare cases, other microstructural factors such as grain size and prior plastic deformation [36,126,138,139]. However, the application of these models for non-isothermal transformations is limited by the complications that arise from multiple phase transformations. For instance, diffusive transformation of austenite to ferrite at the very least results in the rejection of carbon to residual austenite, which continuously changes the chemical composition of the residual austenite. Therefore, it is apparent that B_s in continuous cooling is a function of the amount of austenite that is transformed prior to bainite formation.

Assuming that paraequilibrium (partitioning of interstitial but not substitutional atoms) is the mechanism responsible for partitioning of carbon during transformation to PF/QPF, it is possible to calculate the average concentration of carbon in the residual austenite using Eq. 3-3.

$$C^{\gamma} = \frac{C_0 - XC^{\alpha}}{1 - X}$$

Eq. 3-3

In this equation, C^{γ} is the amount of carbon in austenite, C^{α} is the maximum amount of carbon soluble in ferrite under paraequilibrium conditions [140], C_0 is the nominal carbon content of the steel and X is the fraction transformed. X can be measured experimentally using dilatometry data. Using Eq. 3-3 in combination with a reliable B_s model, one can determine if the instantaneous temperature during continuous cooling is low enough to permit transformation of the residual austenite to bainite. This idea is the foundation of an analysis method named Bainite-Intercept-Temperature (BIT). BIT consists of three steps. Step one is performing a carbon mass balance for PF and residual austenite using Eq. 3-3. Step two involves determining the instantaneous B_s of residual austenite and Step three compares the instantaneous temperature of austenite with its instantaneous B_s . The moment the instantaneous temperature of austenite becomes lower than the instantaneous B_s marks the beginning of the bainitic reaction.

The second step in BIT analysis is a crucial one because of the uncertainty surrounding bainite. There are a number of methods to estimate B_s . To address this issue, B_s is calculated using two methods; a fundamental method and an empirical one. The fundamental method is based on calculating the T_0 and T'_0 temperatures of austenite during transformation. T_0 is the temperature below which the formation of ferrite from austenite is possible without redistribution of any alloying elements. In other words, T_0 is the highest temperature that a diffusionless transformation is thermodynamically possible. T'_0 is a temperature lower than T_0 that allows for 400 J/mol stored energy in the ferrite phase that forms without redistribution of alloying elements. The definition of these two temperatures and their calculation method are explained in detail in Section 7.1 [39,141]. T'_0 is the best theoretical estimation of B_s known to the author at this time. Figure 3-15 shows T_0 and T'_0 of the austenite phase of steel X80-N as a function of carbon content, calculated using Thermo-Calc software and the TCFe6 database. The isothermal B_s for the X80-N steel, calculated using T'_0 , is 632°C . The isothermal B_s for this steel, with the austenitization process similar to the continuous cooling experiments as explained in the Experimental section, is measured as $612.5^{\circ}\text{C} \pm 12.5^{\circ}\text{C}$ which is about 20°C lower than the calculated T'_0 . This suggests that either the stored strain energy of ferrite is higher than 400 J/mol or other energy terms need to be considered as well.

Despite the success of the displacive theory for bainite transformation, there remain discrepancies between observations and predictions from this theory [37,142]. As an alternative method for calculating B_s , an empirical equation is also used in this chapter. There are several equations that have been developed to calculate the B_s of steels [36,138,143]. The empirical equation used in this research is the one developed by Lee (Eq. 3-1) which

is shown to perform better than predecessors at high Mn and Ni content [126]. In addition, this equation provides a better prediction of isothermal B_s for X80-N steel (613°C) compared with the experimentally measured isothermal B_s of 612.5°C ± 12.5°C.

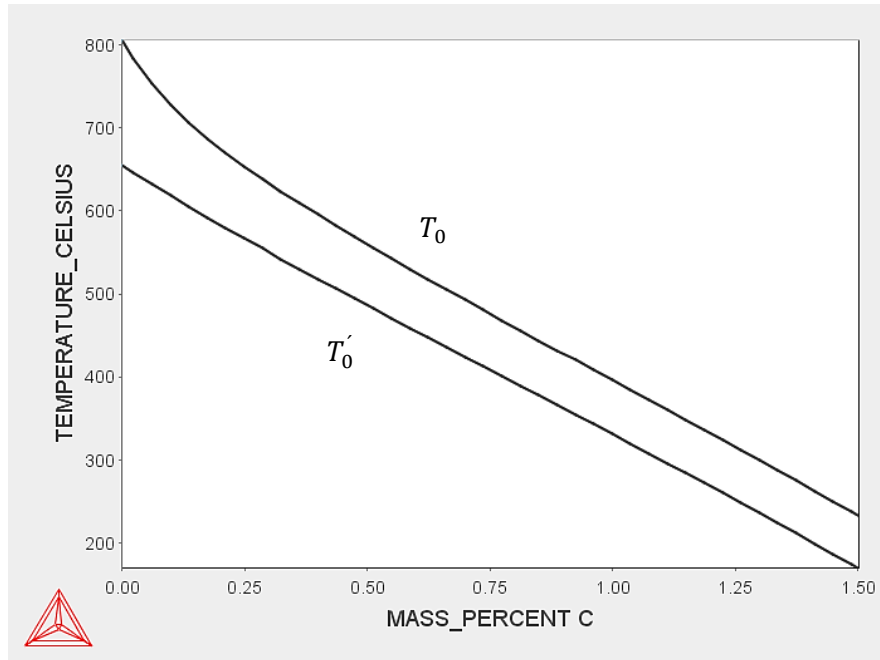


Figure 3-15. T_0 and T'_0 as a function of carbon calculated for steel X80-N.

As an example, BIT analysis is performed on dilatometry results obtained at a cooling rate of 10°C/s using the empirical equation for B_s . Figure 3-16 shows the calculated B_s using Eq. 3-1 for austenite during transformation along with the fraction of austenite transformed and the temperature plotted as a function of time. In this figure, at $t = 5.7$ s, the temperature curve intersects the B_s curve for the first time at the Bainite-Intercept-Temperature (BIT) point. The BIT point indicates the location of the change in transformation type in temperature-time space during continuous cooling. This means that during the first 5.7 s of transformation, the temperature was above the bainite start temperature for residual austenite; therefore, the conditions were favorable for diffusional transformation to PF/QPF. After this point, the temperature goes below the calculated bainite start temperature for residual austenite, allowing for the formation of bainite. After the BIT point the calculated B_s graph becomes invalid since the assumption that austenite transforms to PF/QPF is no longer valid along with the calculation of associated carbon partitioning. Using the BIT method, the amount of austenite that

transformed to PF can be easily found by looking up the fraction transformed that correlates to time of BIT (5.7s in this case). This is shown in Figure 3-17, where $t = 5.7$ s correlates to 44% transformation.

Estimation of the amount of the QPF using the BIT method provides a valuable tool to quantitatively differentiate between the two microconstituents of QPF and BF. Figure 3-18 shows a plot of polygonal ferrite volume fraction as a function of cooling rate calculated using the T'_0 line (Figure 3-15) and empirical B_s equation (Eq. 3-1). As expected, Figure 3-18 shows that increasing cooling rate reduces the volume fraction of QPF.

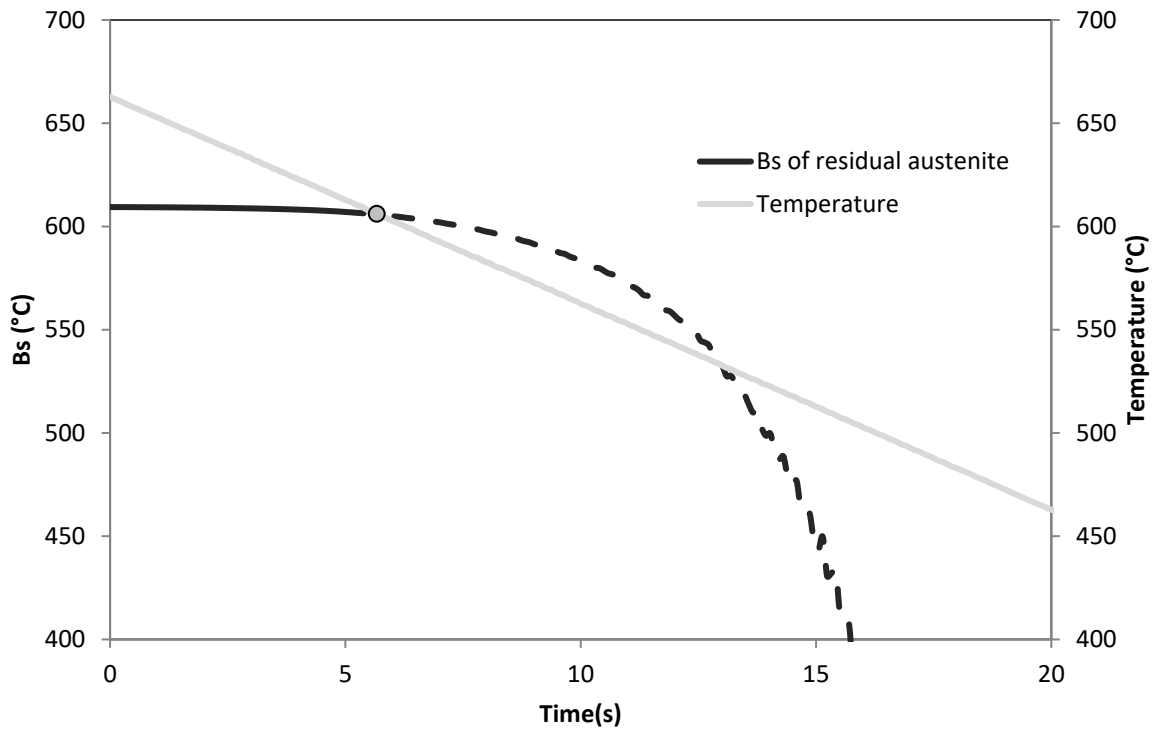


Figure 3-16. Calculated bainite start (B_s) temperature for the austenite phase versus time during transformation. Temperature and fraction transformed curves are plotted to help determine the time and phase fraction for the change in transformation from polygonal ferrite to bainite. The cooling rate is 10°C/s .

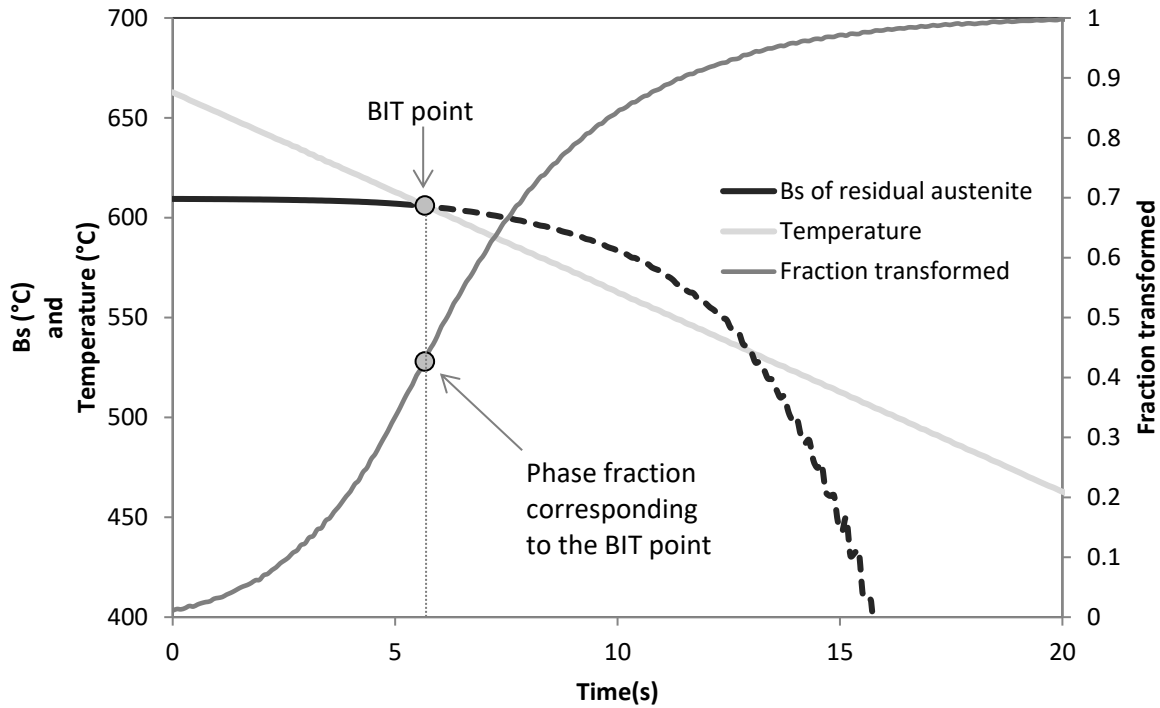


Figure 3-17. Calculation of the amount of austenite that transforms to QPF using the BIT method. B_s in this graph is calculated using Eq. 1 but could alternatively be calculated using T'_0 . The cooling rate is 10°C/s .

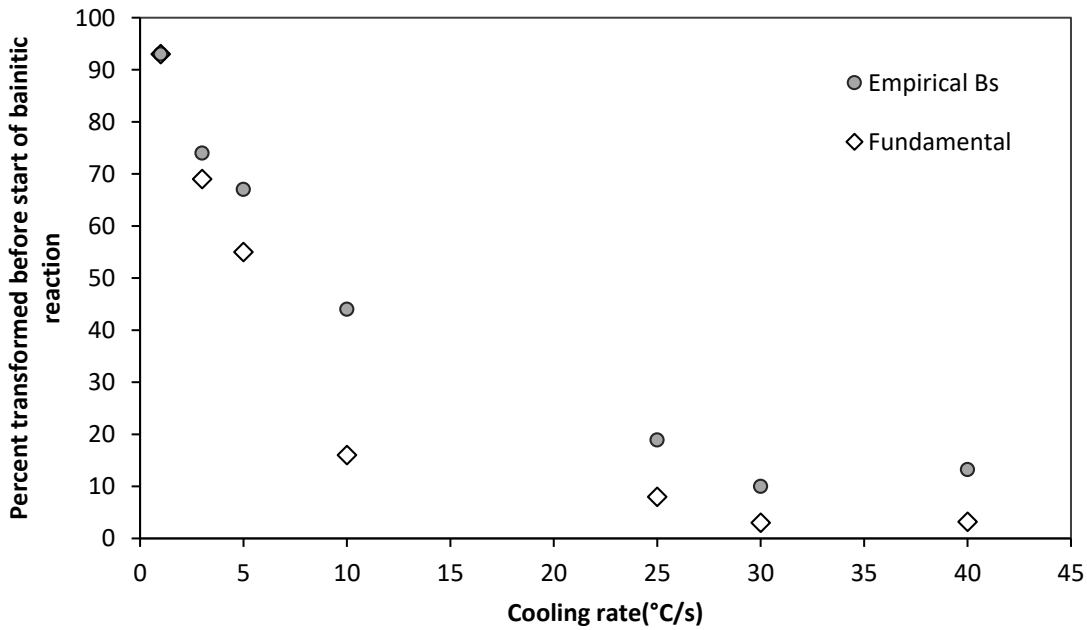


Figure 3-18. Calculated volume fraction (using the BIT method) of PF/QPF as a function of cooling rate.

Verification of the estimations based on the BIT analysis is quite challenging, as there is no reliable method to differentiate and measure volume fraction of PF/QPF and BF in a reproducible manner. Visual methods are unreliable for two reasons. The first reason is that there is no visible sharp boundary between QPF and BF, as shown in Figure 3-8. The second reason is that the plate structure of BF can look similar to flat polygonal ferrite if the viewing plane is parallel to the BF plate or at a shallow angle with it. Figure 3-19a shows an example of such misleading microstructures. The micrograph shows a large flat grain with no apparent internal structure, which appears to be polygonal ferrite; however, this micrograph is from a sample that is isothermally transformed at a temperature far below the isothermal bainite start temperature for this steel and, therefore, it is expected that the microstructure is completely bainitic. The austenitization process and chemical composition of this sample are similar to the samples used in the continuous cooling experiments as explained in the Experimental Procedure. A higher magnification image of the flat region suspected to be QPF in Figure 3-19a is shown in Figure 3-19b. In this image, it can be seen that the large grain is, in fact, comprised of two plates of BF that intersect the plane of view at a low angle. The M/A platelets that are expected to form on the boundary of the two BF plates are also visible in this figure. Diffraction based techniques are also not usable for measuring the volume fraction of QPF and BF, as both morphologies are in fact ferrite with no difference in crystal structure or chemical composition that affects the lattice parameter in a detectable way.

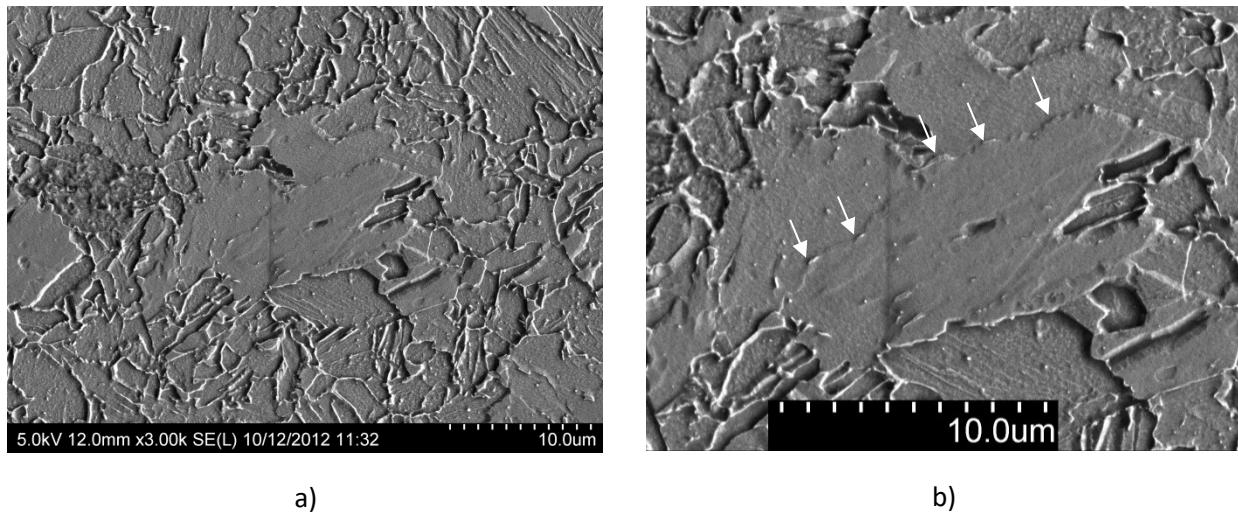


Figure 3-19. Example of inaccuracy of visual methods in distinguishing between bainite and polygonal ferrite. a) Sample isothermally transformed at 500°C. b) Higher magnification image of the flat area. Two BF plates and M/A platelets between them are visible.

Acknowledging this difficult to approach challenge, there is indirect evidence supporting BIT analysis. Assuming that the final microstructure consists of two microconstituents, i.e., QPF and mixed BF, B/M and DP, the microstructure behavior can be assumed to be similar to a two component mixture. Using the rule of

mixtures, the overall hardness is related to the hardness of individual components according to Eq. 3–4. In this equation, HV is the Vickers hardness and X is the volume fraction.

$$HV = HV^{QPF} X^{QPF} + HV^{(BF+BM+DP)} X^{(BF+BM+DP)} \quad \text{Eq. 3–4}$$

Figure 3-20 shows a plot of hardness versus the calculated volume fraction of polygonal ferrite. The data fit well to a straight line, indicating that the BIT analysis could be valid and the rule of mixtures could be applicable to the samples transformed during continuous cooling.

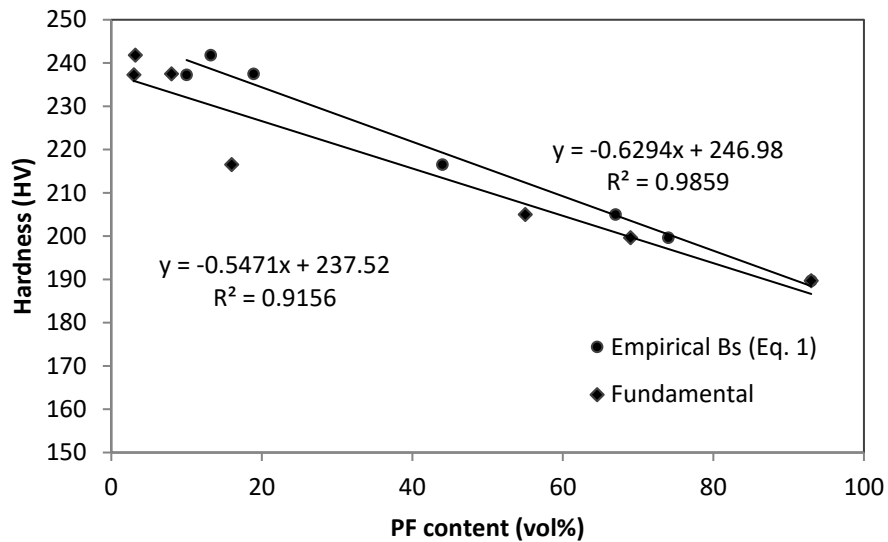


Figure 3-20. Hardness vs volume fraction of polygonal ferrite measured using the BIT method. Results for both the empirical and fundamental methods of calculating B_s are shown. The linear trend line suggests that the rule of mixtures applies and the measured volume fractions for polygonal ferrite are correct regardless of the method used for calculating B_s . This provides support for the BIT method.

Using the linear regression parameters in Figure 3-20, the hardness for QPF and mixed (BF+BM+DP) is calculated and shown in Table 3-3. This table shows that the calculated hardness values of the microconstituents are virtually the same despite the difference in the methods used to calculate B_s , which suggests both methods can be used interchangeably. Comparing the regression results with the experimentally measured hardness of these microconstituents is a way of confirming the reliability of the BIT analysis. However, measuring the hardness of QPF and mixed (BF+BM+DP) in the microstructure of continuously cooled samples is not an easy

task. The main reason is the fineness of these microstructures. For QPF, a reliable hardness measurement using an indenter should sample an area at least greater than one grain of QPF without coming close to the other microconstituents to ensure the strengthening effect of the grain boundaries is included. In the mixed microstructures that occur as a result of multiple phase transformations, this poses an unresolvable challenge to direct hardness measurement of individual phases including QPF.

Table 3-3. Hardness of microconstituents in steel X80-N calculated using linear regression of hardness vs calculated PF/QPF content using BIT method

Method used for B_s calculation	Hardness of PF/QPF	Hardness of mixed (BF,B/M and MA)
Empirical (Eq. 3-1)	184 HV	247 HV
Fundamental (T_0)	182 HV	237 HV

Despite the issue of directly measuring the hardness of QPF, hardness can be calculated theoretically by calculating the contributions of various strengthening mechanisms, i.e., solid solution, grain boundary, precipitate and dislocation strengthening. The mechanism by which each of these strengthening mechanisms contributes to overall strength is well known and theoretical models quantifying them is already explained in Chapter 2 – Literature review. Table 3-4 summarizes the equations governing each mechanism along with the value of the constants used in the calculations that follows.

To calculate the contribution of solid solution strengthening to the yield strength of QPF, it is necessary to know its chemical composition. This chemical composition can be calculated using paraequilibrium and the partitioning rule. When paraequilibrium is established between ferrite and austenite on two sides of the interphase boundary, the relative proportion of substitutional elements in ferrite and austenite stays the same as the austenite phase prior to transformation. This stems from the assumption that substitutional atoms do not move with the interphase boundary during diffusional transformation. However, interstitial atoms, e.g., C and N, are considered mobile due to their higher diffusion rates compared with the substitutional elements. These elements diffuse across the phase boundary so quickly that local equilibrium is maintained on two sides of the phase boundary exclusively for interstitial atoms. Thermodynamically this pseudo-equilibrium is expressed in terms of chemical potential being equal on two sides of the boundary ($\mu_\alpha^C = \mu_\gamma^C$ and $\mu_\alpha^N = \mu_\gamma^N$). Calculation of paraequilibrium in this study is performed using the CALPHAD method with the Thermo-Calc package that allows incorporation of the full chemical composition of the steel.

Table 3-4. Strengthening mechanisms involved in microalloyed steel

Mechanism	Equation	Parameters	Ref
Solid solution	$\sigma_{ss}(MPa) = \sum_{i=C,Mn,Si..} k_i W_i$	k_i = Constant (see table 3) W_i =W%	[83]
Precipitate	$\sigma_{ppt}(MPa) = \left(\frac{10.8 f_v^{1/2}}{d} \right) \ln \left(\frac{d}{6.125 \times 10^{-4}} \right)$	f_v = Volume fraction of ppt d = Diameter of ppt (μ m)	[2]
Grain boundary	$\sigma_{gb}(MPa) = \sigma_i + \frac{k}{\sqrt{d}}$	σ_i = 54 (MPa) Internal friction k =21.5-23.5 (MPa.mm ^{1/2}) d = Diameter of grain(mm)	[2]
Dislocation	$\sigma_{dis}(MPa) = \alpha \dot{M} b G \rho^{1/2}$	α =0.3 Dimensionless coefficient \dot{M} =3 Taylor factor ρ = Dislocation density (m ⁻²) G =80.3 (GPa) Shear modulus b =2.5×10 ⁻¹⁰ (m) Magnitude of Burger's vector	[10]

An important step before calculating the chemical composition of QPF; however, is to find the chemical composition of austenite before transformation takes place. Due to the presence of reactive elements (C, N, Ti, B, Nb, Al) in this alloy and since a relatively low austenitization temperature is used (950°C), it is inevitable to have stable precipitates form during austenitization. Also, it should be noted that the samples used in this study are taken from a commercially rolled X80 plate that at the very least forms NbC precipitates during hot rolling with the SIP mechanism [28]. Measurements using the matrix dissolution technique on a steel of similar composition and processing history showed about 75% by weight of the total Nb and Ti is in the form of carbonitride precipitates [83]. These already present precipitates increase the rate of diffusive processes of dissolution and precipitation by reducing the diffusion distance of elements involved in formation of the precipitates. Therefore, it is reasonable to assume that thermodynamic equilibrium with regard to chemical reactions of active elements can be established at the end of the austenitization time. This assumption makes it possible to calculate the equilibrium state of austenite and other precipitates at the end of austenitization. Using the Thermo-Calc package, the chemical composition of austenite after austenitization is calculated and shown in Table 3-5. Calculations also show that there are 4 types of stable precipitates present in the austenite which include AlN, BN, and two types of (Ti,Nb)(C,N), one being Ti rich and one being Nb rich. The overall volume

fraction of precipitates is calculated as 5.9×10^{-4} . The amount of Nb+Ti in the form of stable precipitates in the austenite at 950°C amounts to 85% of the total Nb+Ti in the steel chemistry.

Table 3-5. Chemical composition of austenite phase after austenitization in percent by weight

C	Mn	Si	Cu	Cr	Ni	Mo	Nb	Ti	Al	N	B
0.061	1.64	0.12	0.13	0.03	0.42	0.24	0.006	1.04E-5	0.015	0.0014	1E-5

Using the calculated chemical composition of austenite, the concentration of C and N in ferrite that formed under paraequilibrium is calculated as a function of temperature. Isothermal transformation experiments on this steel have shown that the minimum temperature that QPF can form is 625°C. Figure 3-21 shows the concentration of C and N in ferrite calculated under paraequilibrium for the temperature range of 625°C to 700°C. The sudden increase in the concentration of carbon and nitrogen in ferrite that happens at 641°C may be due to instability of austenite at this temperature compared with ferrite. In other words, a ferrite phase with the nominal composition has a lower energy than austenite without the need for redistribution of C and N. This means if there was no other source for the energy difference between austenite and ferrite other than chemical interaction of atoms, 641°C would be the temperature below which diffusionless transformation (i.e., supersaturated ferrite/martensite) would be thermodynamically possible. However, the high strain energy of forming supersaturated ferrite with interstitial atoms (C and N) postpones such a transformation to much lower temperatures (martensite start temperature). Having said that, this temperature is close to the measured and calculated isothermal bainite start temperature for steel X80-N (~613°C) as discussed in Section 3.3.5 which supports the diffusionless transformation hypothesis. Since the concentration of C and N in ferrite changes with temperature, an average concentration is used as representative for calculation of solid solution strengthening. Table 3-6 shows the constants used for calculating solid solution strengthening in QPF.

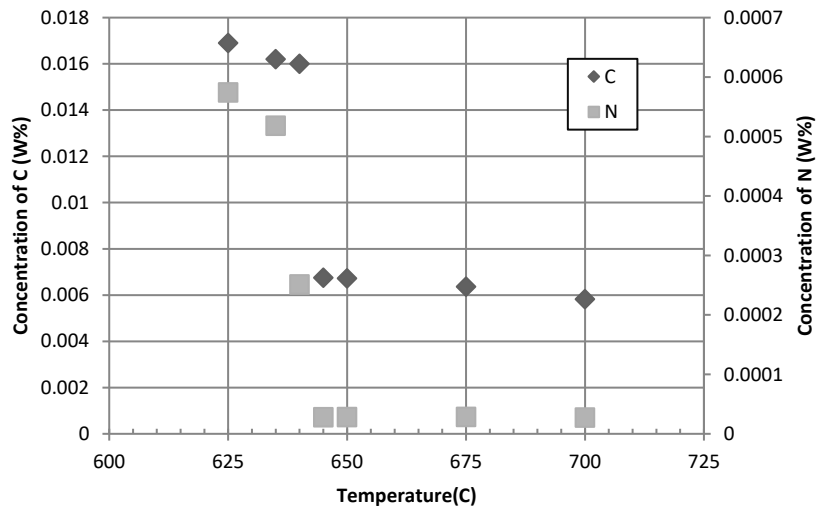


Figure 3-21. Concentration of C and N in ferrite under paraequilibrium.

Table 3-6. Solid solution strengthening coefficients of common alloying elements for steel [2,83]

	C, N	Si	Cu	Mn	Mo	Ni	Cr	Ti	Nb
$k_i(MPa)$	4620-5400	83	39	31	11	0	-31	80	2400

Knowing the volume fraction and the average size of the precipitates is necessary to calculate the contribution of precipitate strengthening to yield strength. The precipitate size was determined by analysis of carbon extraction replicas taken from the etched surface of samples cooled at 5°C/s and 10°C/s. As an example, Figure 3-22 shows a TEM bright field image of the precipitates observed in the sample with a cooling rate of 10°C/s. Analysis of the precipitates in other cooling rates showed that precipitate size and distribution were similar for all cooling rates. Two types of precipitates were observed, large Ti-rich particles and fine Nb-rich precipitates. The large Ti-rich precipitates ranged in size from 30 nm to 400 nm in diameter and can even be seen in the high resolution SEM micrographs in Figure 3-7 to Figure 3-10 as white dispersed particles. These precipitates are especially easy to find within the large evenly etched QPF/PF grains. The average size of the large precipitates is 60 nm ± 11 nm. The fine precipitates are Nb-rich with diameters ranging from 6 nm to 10 nm with an average size of 7.5 nm ± 0.4 nm. These precipitates are most likely the larger pre-existing precipitates that underwent growth/coarsening during austenitization at the expense of dissolution of finer ones.

The volume fraction of precipitates was estimated to be 85% by weight of the total microalloying content using Thermo-Calc software. This amount corresponds to the equilibrium precipitate at the austenitization temperature of 950°C. The assumption that the precipitates found in the continuously cooled sample are essentially the equilibrium precipitates at the austenitization temperature is justified based on two reasons. First, Junfang et al. [83] reported that 75% of total microalloying content of a similar steel was found in the precipitate form. This amount of precipitate is reasonably close to 85% equilibrium precipitate. During austenitization due to relatively high temperature and long time, additional precipitation pushes the precipitate content closer to equilibrium reducing the error to lower than 10%.

The second reason to assume that precipitates found in the continuously cooled samples are the same found at the end of austenitization is lack of time and driving force for more precipitation during continuous cooling to room temperature. As mentioned before observations of precipitates for different cooling rates showed no significant difference in the characteristics of the precipitates. This observation is not surprising since the amount of soluble microalloying elements that can produce further precipitation is only 15% to 25% of the nominal microalloying content. This low soluble microalloying concentration combined with relatively fast cooling rates (1°C/s to 40°C/s) does not allow for time consuming diffusive processes of nucleation, growth or coarsening to have a considerable impact on precipitate characteristics.

Table 3-7 shows the strengthening effect of the large Ti-rich and small Nb-rich precipitates. The combined strengthening effect is calculated using Eq. 2–23 with $q = 2$. This exponent was chosen based on the findings of [114] shown in Figure 2-24, which considers that the two types of precipitate are hard, undeformable particles with relatively low volume fraction and both should exhibit near 0° critical angle [2,144]. The combined strength of the two types of precipitates is calculated to be between 67.8 MPa to 72.6 MPa.

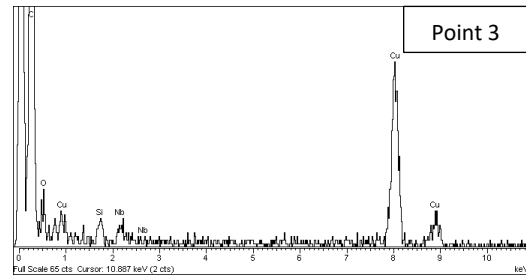
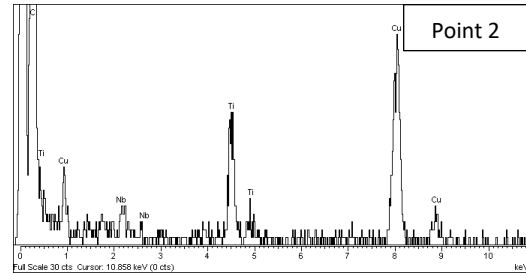
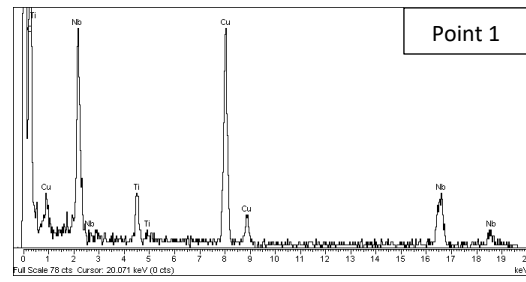
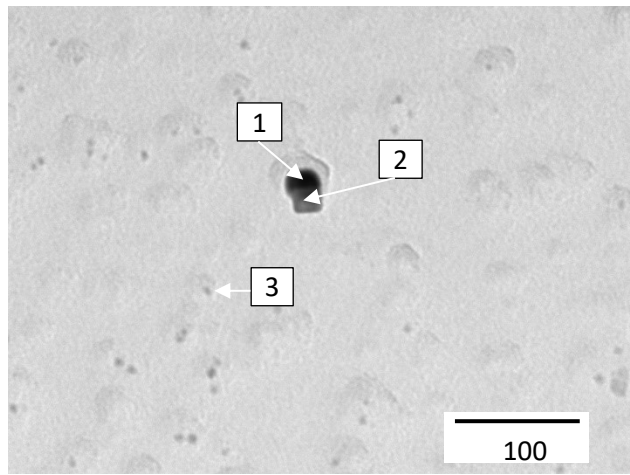
The strengthening effect of dislocations for QPF in this study is considered to be negligible. The main source of dislocations in metals is plastic deformation and displacive transformations. Since no plastic deformation has occurred in samples after formation of QPF and the transformation is not displacive, the only possible source of dislocations is accommodation of interface strain. Although the density of this kind of dislocations can be high (the bainitic transformation in microalloyed steels for instance), the amount of dislocations generated in PF and QPF from transformation induced interfacial strain is relatively low and the strain tends to be accommodated in austenite rather than ferrite [36]. Therefore, the contribution of dislocation strengthening to the overall yield strength is considered to be negligible.

Table 3-7. Strengthening effect of precipitates found in continuously cooled X80-N steel - Min and Max values are calculated based on the standard deviation of the measured precipitate diameter

PPT type	V_f	$d(\mu m)$	$\sigma_{PPT}(MPa)$
		Min - Max	Min - Max
Ti-rich	1.37×10^{-4}	0.049 – 0.071	8.5 - 11.3
Nb-rich	3.7×10^{-4}	0.0071 – 0.0079	67.2 – 71.7
		Combined effect	67.8 – 72.6

To calculate the contribution of grain boundaries to strength using Hall-Petch equation, it is necessary to know the grain diameter of QPF. It was mentioned earlier (Figure 3-19) that measuring volume fraction of QPF using visual techniques can be inaccurate. However, identifying individual grains that are most likely to be QPF is possible for cooling rates up to 10°C/s. The average grain size varied from 9 μm for a cooling rate of 40°C/s to 11 μm for 1°C/s. The maximum and minimum grain diameters are considered in calculating the upper and lower bound for the contribution of grain boundary strengthening to yield strength.

Table 3-8 summarizes contribution of each strengthening mechanism to overall strength. The various parameters used to calculate the minimum and maximum strength are listed in this table as well. The total strength is calculated by non-linear summation of the strengthening mechanisms using Eq. 2-25.



a)

b)

Figure 3-22. a) TEM carbon extraction replica of the sample cooled at 10°C/s. b) Energy dispersive x-ray (EDX) spectra from the precipitates, indicating chemical composition of different precipitates. The Cu peak is from the Cu grid used to support the replica and the Si peak is from the C film.

Table 3-8. Strengthening mechanisms involved in X80-N microalloyed steel

Mechanism	Min strength	Max strength	Changing parameter
Solid solution	123 MPa	131 MPa	$k_{C,N} = 4620 - 5540$
Precipitate	67.8 MPa	72.6 MPa	$d_{ppt} = 49nm - 71nm$
Grain boundary	226 MPa	286 MPa	$d = 9\mu m - 11\mu m$ $k = 18 MPa.mm^{-1} - 22 MPa.mm^{-1}$
Dislocation	0 MPa	0 MPa	
Total	362 MPa	481 MPa	

Considering the effect of all strengthening mechanisms for the yield strength of QPF, the hardness of QPF is estimated to be 157 HV to 198 HV. Conversion of yield strength to hardness was done using Eq. 3–5 developed by Pavlina et al. [86]. By comparing the calculated hardness range for PF (157 HV - 198 HV) with the one measured using BIT (182 HV - 184 HV), it can be seen that the calculated hardness of QPF using BIT analysis falls within the calculated hardness range of QPF by considering the strengthening mechanism.

$$Y = 2.876 HV - 90.7 \qquad \text{Eq. 3–5}$$

Y is the yield strength in MPa and HV is the Vickers hardness. Unlike QPF, directly measuring the hardness of mixed (BF+BM+DP) is possible within a known margin of error. Considering that the volume fraction of DP is very low compared with the rest of the microconstituents, the mixed (BF+BM+DP) region is essentially mixed (BF+BM) which can be reproduced using isothermal transformations to achieve 100% (BF+BM) with similar plate-like morphology. Figure 3-23 shows the hardness of isothermally transformed samples as a function of transformation temperature. The average hardness between the upper limit of BF (600°C) and the martensite start temperature ($\sim 450^\circ\text{C}$) is 253 HV. It can be seen that the average hardness of the isothermal bainitic microstructure that forms in the temperature range of 450°C to 600°C is close to the calculated hardness using BIT analysis (253 HV for the isothermal transformation versus 247 HV for continuous cooling transformation). This similarity between the hardness of the mixed microconstituent and the average hardness of isothermally transformed bainite, albeit simplistic, is a clue - if not an ultimate proof - supporting the validity of BIT analysis.

These correlations suggest that the BIT method provides a reasonable estimation of the volume fraction of the microconstituents and their contribution to overall hardness. To examine the validity of BIT analysis, dilatometry data obtained for continuous cooling of two other microalloyed steels are analyzed. The raw data for these steels were in the form of time-temperature-dilation data and they were analyzed using the BIT method. Once the bainite start temperature is calculated, the phase fraction of the austenite that transformed prior to this temperature is calculated. This phase fraction is equal to the phase fraction of QPF, as this is the phase that forms before BF. Similar to steel X80-N, B_s is calculated using both fundamental and empirical (Eq. 1) methods. Figure 3-24 shows QPF content versus hardness graphs for these steels. As was the case for steel X80-N, a linear trend exists for steels X80-K and Grade 80-L as well. This indicates BIT analysis can produce consistent results, at least for microalloyed steels.

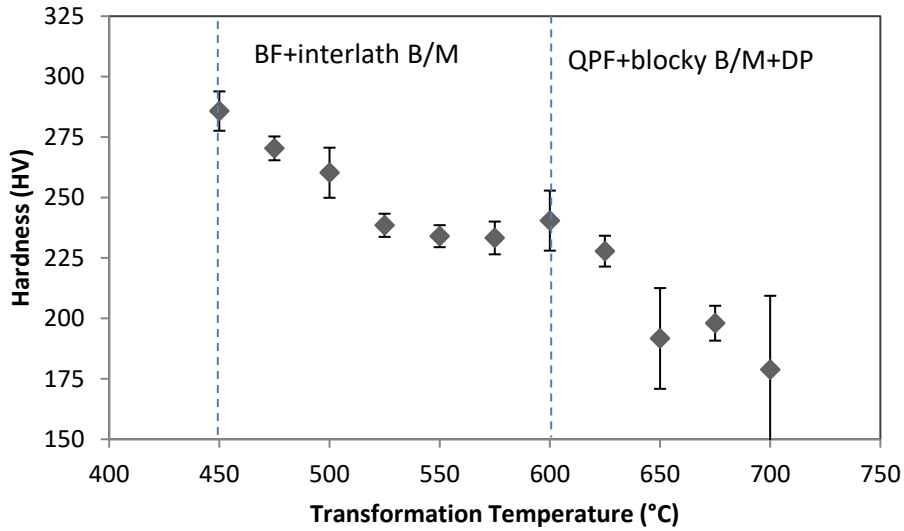


Figure 3-23. Hardness of isothermally transformed samples. The transformation below 600°C and above the martensite start temperature of this steel (452°C) is bainitic. The average hardness in this temperature range is 253 HV which is close to calculated hardness of the mixed microconstituent using BIT analysis (247 HV).

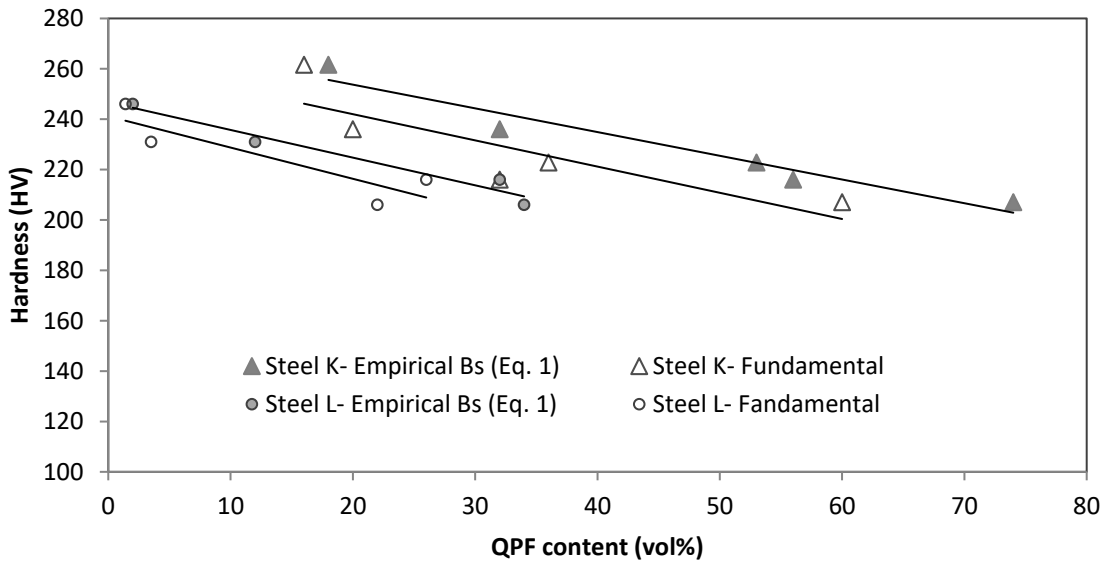


Figure 3-24. Hardness vs QPF content for steels X80-K and Grade 80-L used for validation of BIT analysis.

Combining the information about microconstituents and their relative volume fraction with BIT analysis allows for the creation of a detailed and more accurate CCT diagram for the steel, which represents multiple phase transformations more realistically. Figure 3-25 shows the final CCT diagram of steel X80-N. Figure 3-26 shows the same CCT diagram as in Figure 3-25 with added phase fraction data points along the cooling lines.

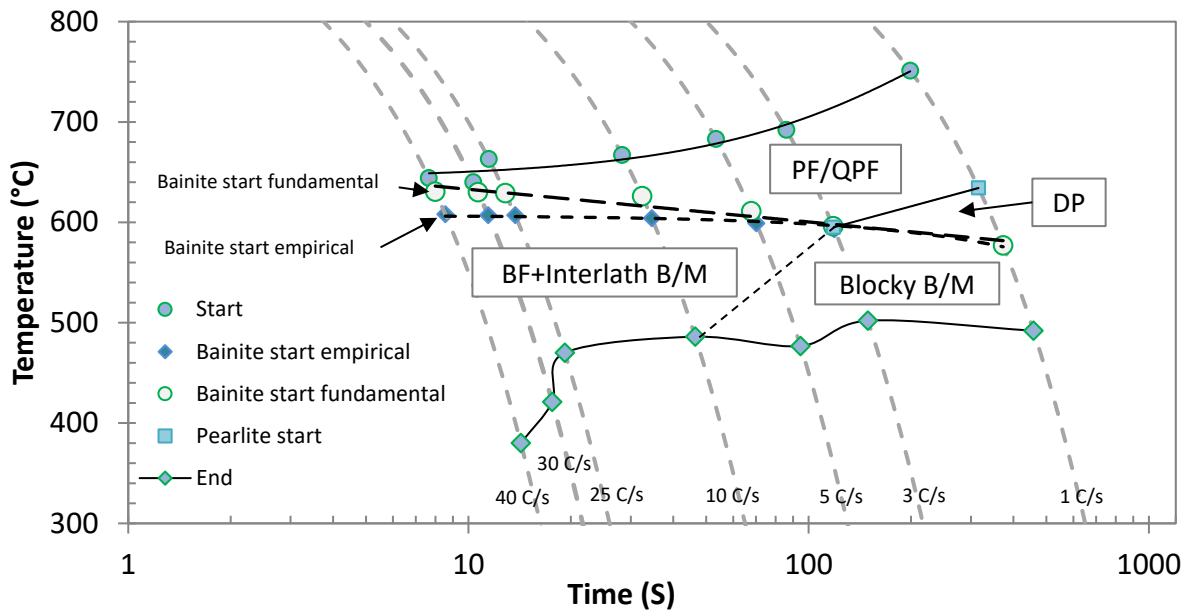


Figure 3-25. CCT diagram for the steel studied (X80-N). Start and finish lines were determined by 1% and 99% transformation criteria calculated from the dilatometry results. Bainite start (narrow dashed lines) are calculated using the BIT method.

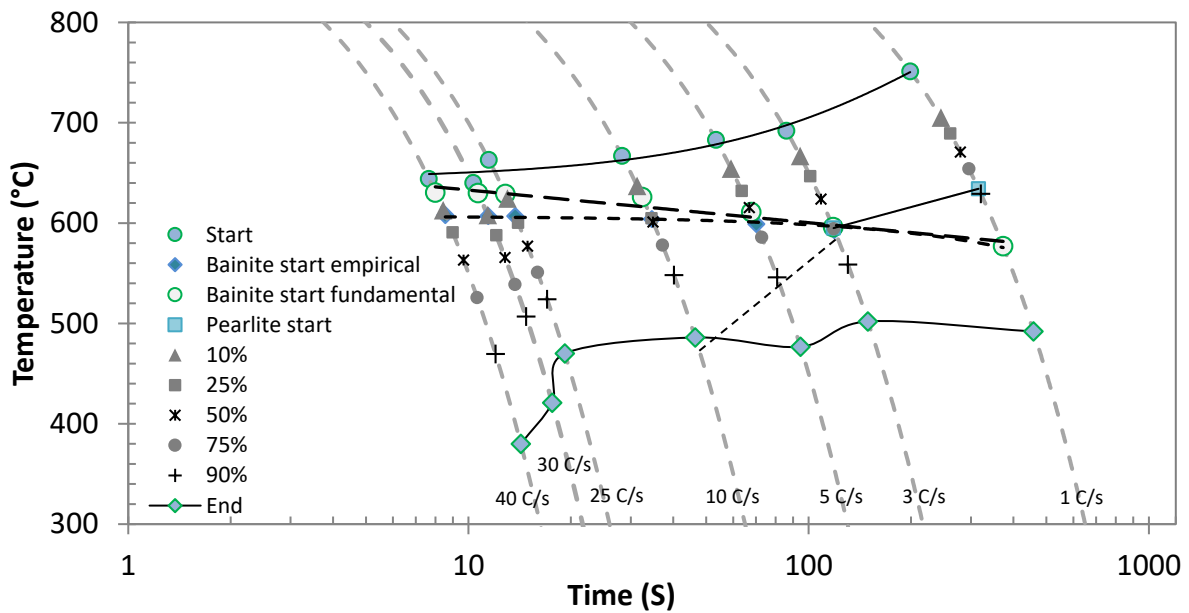


Figure 3-26. CCT diagram from Figure 3-25 with added transformed phase fraction points.

3.4 Summary

The hardness of a microalloyed steel is directly related to the volume fraction and hardness of the microconstituents present in the microstructure. It has been shown that the application of current bainite start temperature models can be extended to continuous cooling by considering paraequilibrium and the average concentration of rejected substitutional elements in austenite. This Bainite-Intercept-Temperature (BIT) analysis, coupled with transformation kinetics data obtained using dilatometry experiments, is used to quantitatively distinguish between the QPF and BF transformations without the use of metallographic techniques. It is shown that the volume fraction of microconstituents calculated based on BIT analysis indicates a correlation with the overall hardness of the microstructure, matching the rule of mixtures for a two component system. For the cooling rates used in this study, the two microconstituents are QPF and mixed (BF+BM+DP). By correlating BIT analysis with hardness data, it is possible to calculate the hardness of individual components in the microstructure.

BIT analysis is an attempt to extract quantitative phase fraction information from lever rule results. In the next chapter, it will be shown that the concept of considering carbon redistribution can be expanded to include its effect on not only phase transformation start temperatures, but also on thermo-physical properties of the phases as well. This method is named the UCD method and it is essentially a better and more complex version of the BIT method. Since UCD is capable of considering all major microconstituents in microalloyed steels, UCD results are inherently more extensive and more accurate than BIT. However, BIT is still a valid approach and an improvement over using just the lever rule to analyze dilatometry. BIT can be used when the use of UCD is not possible. This could be due to the lack of input phase property data that UCD needs or the complexity of using UCD compared with BIT. The UCD method does not invalidate the BIT method, but expands upon it.

Chapter 4 Unit cell dilation technique for analyzing dilatometry data³

4.1 Introduction

The phase transformation of austenite in steels has been the subject of an enormous amount of research in the past 100 years. Despite a wealth of knowledge generated in this area, the key role of steel in heavy industries has fueled an ever increasing demand for better and cheaper steels. Central to this research, is the austenite phase transformation as it is the main phenomenon that greatly contributes to the mechanical properties of steel in all manufacturing techniques that involve heating of steel above its A_1 temperature.

Phase transformations are usually studied by subjecting a specimen to a designed thermal cycle, ideally in a controlled environment, using a thermal or thermo-mechanical simulator machine. The most useful and accurate method to study phase transformations is dilatometric analysis. In this technique, changes in the length (dilation) and temperature of a specimen are recorded as a function of time. Subsequent analysis of the recorded data can reveal transformation start and finish temperatures without much processing, but the most valuable information that can be obtained by analyzing dilatometry data is the phase transformation kinetics. To measure the kinetics of a phase transformation, it is necessary to know the fractions of the phases during transformation. One method to calculate phase fractions from dilatometry data is the so called “lever rule”. It will be explained in detail that the lever rule is not an adequate analysis method for complex phase transformation in steels and leads to predictable errors that can be mitigated using more sophisticated analysis techniques.

One of the milestones in any research field involving measurement of a physical phenomenon is the discovery of a reliable analysis technique coupled with an available and robust analysis tool for the obtained raw data. Historically, this has happened before in the fields of crystallography with the invention of Rietveld analysis as an analysis method for XRD raw data that laid the foundation for quantitative analysis of X-ray diffraction (XRD) and neutron diffraction patterns through full pattern analysis. This, in turn, led to the creation of tools such as GSAS [145] which is freely available for analysis of XRD patterns and serves as a benchmark for other quantitative XRD analysis software.

The goals of this chapter are first to show the areas where the lever rule fails as an analysis technique and then to introduce a mathematical framework for analysis of dilatometry data, named “continuous sequential phase transformation” (CSPT). Finally, an algorithm named “unit cell dilation” (UCD) that implements the CSPT will be developed. This algorithm is used to develop computer codes “Fitter” and “Master Fitter” that carry on

³ This chapter is largely based on the published paper by Khodaie et al. Mater. Charact. 135, 84–95 (2018).

the computations and optimization of parameters, respectively. The source code for the Master Fitter program and the accompanying files are distributed under GPL-3.0 license and available for download at (<https://github.com/Nassehk/Dilatometry-analysis.git>). It is envisioned that the UCD algorithm and the computer codes implementing it will become an easily accessible and standard analysis method for dilatometry experiments. Developers and scientists in this field are encouraged to contribute to this open source project.

4.1.1 The lever rule

To begin, an understanding of the lever rule is essential and a review of how it is used will be presented. The lever rule is the easiest and most widely used method in interpreting dilatometry data. In the lever rule, it is assumed that the fraction of transformed parent phase is proportional to the distance of the dilation curve from extrapolated dilation lines of the phases before and after transformation, as shown in Eq. 3-2 and Figure 4-1 .

The lever rule has two major limitations. One is the inability of the lever rule to model sequential transformations. A sequential transformation occurs when the product of transformation is changed due to temperature or chemical changes in the parent phase. A sequential transformation commonly occurs during continuous cooling of most steels, except austenitic stainless grades. The two terms in Eq. 3-2 are defined with respect to the parent and the final product microstructure. While the parent phase is usually single phase austenite, the product phase is a mixture of phases that form during sequential phase transformation. In other words, Eq. 3-2 does not account for individual product phases but rather considers the combined effect of all phases after they have formed. Since Eq. 3-2 does not use any phase specific information when considering the products, the lever rule cannot account for sequential phase transformation and, by extension, any type of phase transformation that results in more than one phase. An experienced user, however, may be able to detect the time and temperature of changes in transformation type by looking for deviations from trends in the cooling curves. However, as will be shown later in Figure 4-9, this method can result in considerable quantitative errors.

The second limitation is the inability of the lever rule to consider the effect of chemistry dependent (non-linear) properties for parent and product phases. This type of behavior occurs in steels when the diffusion controlled formation of ferrite results in the accumulation of carbon in austenite as the transformation progresses. The additional carbon, on one hand, reduces the coefficient of thermal expansion (CTE) of austenite and, on the other hand, causes the austenite lattice to stretch and expand to accommodate the carbon atoms. When the effect of these two phenomena on austenite is considered, it is concluded that the extrapolated γ line in Figure 4-1 cannot be a linear line as assumed by the lever rule, but has to tilt upwards (as shown by the dashed line in Figure 1) to reflect the lattice expansion and CTE reduction.

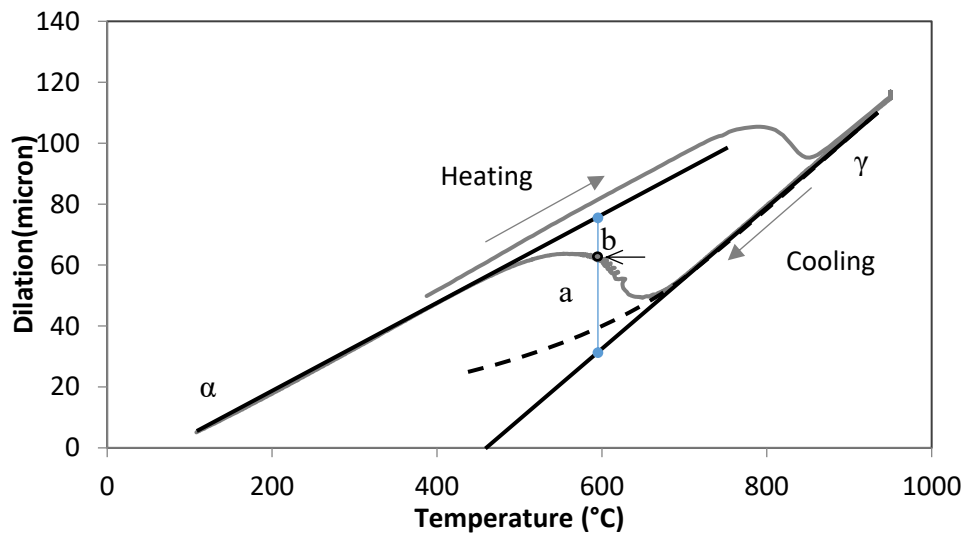


Figure 4-1. Example of dilatometry data for the austenite to ferrite transformation. The grey line is the actual dilatometer data and the black straight lines show the extrapolated austenite and ferrite dilation lines, as considered in the lever rule. The dashed line shows a schematic extrapolation of the austenite line, considering the effect of carbon accumulation in austenite.

There have been several successful attempts to address the shortcomings of the lever rule by calculating the volume change in the unit cell level [146–148]. The methods described by these papers address austenite enrichment and sequential transformation by making assumptions to simplify the mathematical solution process. As an example, Onink et al. [146] assume a uniform carbon concentration in the product, which is not generally the case, especially for bainite. This results in an inaccurate estimation of the austenite carbon content, particularly for ultra-low carbon steel such as microalloyed steel where the steel’s carbon content is of the same order as the carbon solubility limit in ferrite (0.02 w%). The uniform ferrite carbon content assumption has been utilized in the work of many researchers relying on the calculations by Onink et al. [147–150]. The current work is an attempt to expand on Onink et al.’s work and provide a reliable algorithm and computational tool to implement this approach for microalloyed and possibly hypo-eutectoid steels. A critical review of Onink’s approach and similar papers to current research work is provided in section 4.6.

4.2 Experimental procedure

The analysis of dilatometry data, obtained from an X80 steel during continuous cooling, is the subject of this chapter. X80 steel is a pipeline steel with a yield strength of 80 ksi (550 MPa) as defined by API standards. Two

steel compositions are studied in this chapter. Steel X80-N is used as the base alloy in this research while steel X80-K is used for validation of the theoretical approach. The compositions of the steels are shown in Table 4-1. The as received steel X80-N had a grain size of $3.1 \mu\text{m} \pm 0.6 \mu\text{m}$ on the surface normal to the width direction and $2.5 \mu\text{m} \pm 0.15 \mu\text{m}$ on the surface normal to rolling direction. The grain size was measured using the line intercept method according to ASTM E112 [128].

Table 4-1. Chemical composition (wt%) of steels X80-N and X80-K used in this study

	C	Mn	Si	Cr+Ni+Mo+Cu	Nb	Ti	N
X80-N	0.064	1.69	0.12	0.83	0.04	0.007	0.0064
X80-K	0.058	1.65	0.25	0.73	0.091	0.016	--

To measure the kinetics of transformation for steel X80-N, hollow, cylindrical samples measuring 4 mm OD, 3 mm ID and 10 mm in length were machined from the center of a 15 mm thick plate with the length of the dilatometer sample in the rolling direction. Samples were then processed with a Bähr DIL 805 thermo-mechanical simulator. One experiment was done for each experimental condition. In the dilatometer, the samples were austenitized at 950°C for 15 minutes to ensure full transformation to austenite and then cooled at various rates ranging from 1°C/s to 40°C/s. The austenitizing temperature of 950°C was chosen to allow for partial dissolution of NbC to create an austenite chemistry similar to the austenite present after hot rolling and before transforming to ferrite.

To observe the microstructures, following continuous cooling, samples were cut in half from the mid length to expose a circular cross section. Samples were then mounted, polished and etched using 2% Nital. Microstructural observation was done using a Hitachi S4800 field emission source scanning electron microscope (FE-SEM) operating in secondary electron (SE) mode at 5 kV and a Leica DM ILM optical microscope using incandescent light with a blue filter. Quantitative metallography was performed to measure the volume fraction of microconstituents, using a point counting technique on 5 fields of view according to ASTM E562 [130].

The experimental work and data collection for steel X80-K was done by Johnson et al. [9]. Steel X80-K was austenitized at 945°C for 5 minutes and cooled at constant cooling rates of 0.3°C/s, 0.5°C/s, 1°C/s, 5°C/s, 7°C/s, 10°C/s and 20°C/s to room temperature. The dilatometry samples were solid round bars with an OD of 6 mm and length of 10 mm. Dilatational measurements were taken from the diameter of the specimens.

Metallographic analysis was done in reference [9] using both optical and scanning electron microscopy (SEM). Additional information about steel X80-K can be found in reference [132].

4.3 Results

Dilatometry results for steel X80-N obtained at different cooling rates are shown in Figure 4-2. To allow for better comparison between different cooling rates, all dilation data is normalized such that at 800°C the dilation is 0 μm . At higher cooling rates, the transformation begins and ends at lower temperatures. Even though all the cooling curves in this figure are normalized to begin from the same starting point, the graphs end up having a different dilation when the transformation is finished. These minor differences arise from a variation in the volume fraction of microconstituents in the final microstructure. The most notable is bainite/martensite (B/M) which contains retained austenite, which is the highest density phase in steels. The UCD algorithm automatically deals with these variations.

The serrations observed on the cooling curves are caused by the rapid adjustments in cooling and heating of the sample by the dilatometry machine trying to maintain the prescribed constant cooling rate. During transformation the dilatometer needs to compensate for the released heat of transformation. This causes rapid fluctuations in the temperature which in turn results in non-uniform temperature throughout the body of the specimen. Since temperature is only recorded on a small contact area of thermocouple with the specimen, thermal contraction of the whole specimen becomes out of sync with the recorded temperature. This mismatch of the recorded dilation and temperature creates the serrations in cooling curve during transformation. These serrations are eliminated from the dilation curves by an interpolation moving average filter before applying the UCD algorithm. The result after filtering is a smooth noise free dilation curve.

Microstructural analysis of the samples processed using the dilatometer was done with a field emission scanning electron microscope (FE-SEM) operating in secondary electron mode. The micrographs for all of the cooling rates can be seen in Figure 3-6. In these figures, QPF, DP, WF and BF represent quasi polygonal ferrite, degenerate pearlite, Widmanstätten ferrite and bainitic ferrite, respectively. Detailed description of the microconstituents and microstructures observed in the continuously cooled specimens can be found in Chapter 3.

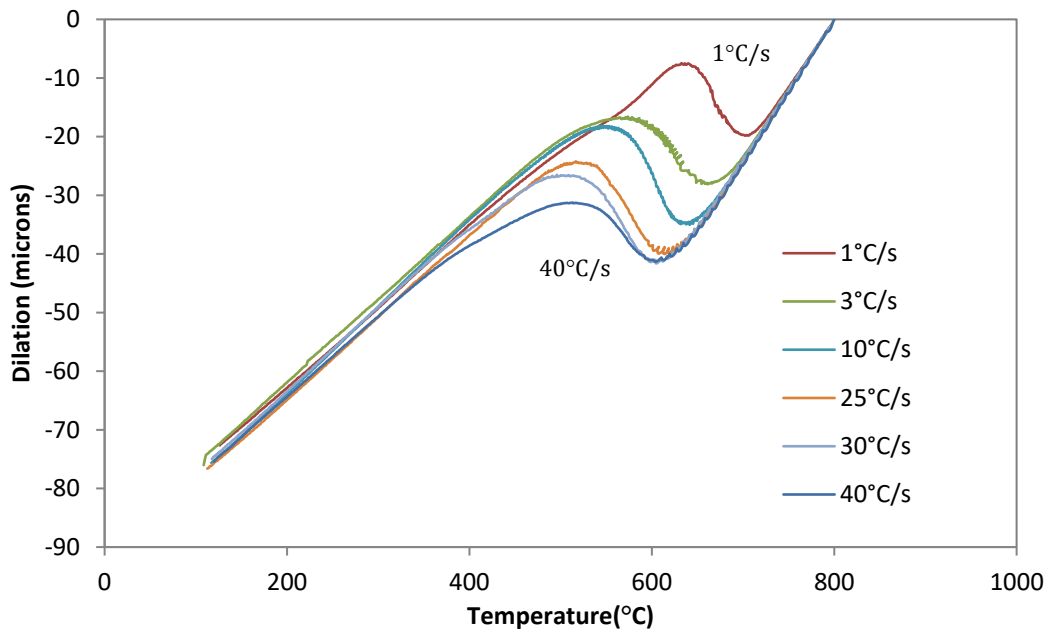


Figure 4-2. Normalized dilation graphs obtained at different cooling rates for steel X80-N.

Quantitative metallography was done on the micrographs by measuring the volume fraction of three distinguishable groups of phases, i.e., ferrite group (QPF+BF), bainite and martensite group (B/M) and degenerate pearlite (DP). The volume fraction of QPF and BF are measured in combination, primarily because it was not possible to determine a phase boundary between them. A secondary reason is that BF can be easily mistaken for QPF if the BF plates are near parallel with the surface. Both reasons are explained in detail in Chapter 3. Quantitative metallography results measured for steel X80-N at different cooling rates are shown in Figure 3-14

4.4 Discussion

4.4.1 Continuous sequential phase transformation (CSPT)

As mentioned in section 4.1.1, chemical changes can occur in the product and parent phases during transformation. As an example in steels, the carbon concentration in ferrite and austenite is dictated by the thermodynamics and kinetics of the transformation. These concentrations are often calculated using the partitioning rule. There are several partitioning rules which are used depending on the kinetics on transformation; e.g., full equilibrium at the α/γ interface is used for very slow transformations and paraequilibrium for faster transformations during which interstitial elements can be redistributed between

phases but substitutional elements cannot. As a result, in paraequilibrium molar ratio of substitutional elements to the base element of the alloy (Fe) is equal for the product and parent phase. A common feature of both full equilibrium and paraequilibrium is that the amount of carbon in ferrite is temperature dependent and determined by the solvus line in the equilibrium or paraequilibrium phase diagrams. For continuous cooling this results in chemical differences between the ferrite that forms at different temperatures. As a result, in non-isothermal phase transformation of steel instead of having just one uniform ferrite phase, a non-uniform continuum of ferrite is created. The carbon concentration gradient in ferrite can be reduced by subsequent diffusion of carbon between high carbon and lower carbon regions in ferrite. However, this is only appreciable when diffusion domains are small (early stages of transformation or small prior austenite grain size) or when the transformation rate is slow. This is not, however, applicable for all transformations, especially for microalloyed steels with rapid transformation kinetics. It can be argued that carbon concentration changes are negligible for ferrite considering the low solubility of carbon in ferrite, but later it will be shown that considering a variable carbon content for ferrite opens the door for modeling BF and martensite as variants of ferrite with the difference being supersaturation of carbon. This method in defining PF, BF and martensite allows for consideration of the transition from one phase to another as a gradual process rather than an abrupt and discontinuous shift in the nature of the transformation.

To correctly model the relationship between phase transformation and observed dilation, a new mathematical approach is required that allows for consideration of infinite sequential phase transformations. This approach must be able to (1) allow for formation of any number of phases, (2) allow for changes in the chemical composition of the product phase and take this effect into account and (3) determine the amount of the austenite consumed by the transformation at a given period by considering points (1) and (2). From an atomistic point of view, the total volume of a specimen can be calculated by summing the cell volume that each atom occupies, according to Eq. 4-1.

$$V = \sum_{i=1}^{N_{total}} v_i$$

Eq. 4-1

In this equation, v is the portion of the unit cell volume occupied by one atom (from now on referred to as volume per atom) and N_{total} is the total number of lattice atoms in the specimen. v is calculated by dividing the volume of a unit cell by the number of atoms in one unit cell. In this analysis only the number of atoms that make up the lattice structure of the phases are used in the calculations. The effect of interstitial atoms that are not

part of the lattice structure is accounted for by considering their effect on the volume per atom of the lattice atoms. Eq. 4-1 can be expanded by separating the volume of austenite from the products. Assuming the austenite phase has a uniform chemical composition, all the atoms in austenite can be assumed to be identical, so that Eq. 4-1 can be expanded as Eq. 4-2.

$$V = \sum_{i=1}^{N^p} v_i^p + N^\gamma \cdot v^\gamma \quad \text{Eq. 4-2}$$

The superscript p indicates the product phase, N^p is the number of product atoms, N^γ is the number of austenite atoms and v^γ is the volume per atom of austenite. Since the product volume is calculated by summation of very small quantities (volume per 1 atom) compared with the total product volume, the product volume term in Eq. 3 can be approximated using the integral function shown in Eq. 4-3.

$$\sum_{i=1}^{N^p} v_i^p \approx \int_0^{N^p} v^p dN^p \quad \text{Eq. 4-3}$$

Using Eq. 4-3, Eq. 4-2 can be written as Eq. 4-4.

$$V = \int_0^{N^p} v^p dN^p + N^\gamma \cdot v^\gamma \quad \text{Eq. 4-4}$$

Differentiating both sides of Eq. 4-4 turns it into an equation that can be solved using numerical methods such as finite difference; however, to correctly differentiate the equation in a way that represents the physical phenomenon of transformation, it is important to identify the independent variables and their effects on the terms in this equation. Both N^p and N^γ , the number of lattice atoms in the product phase and austenite, respectively, change during phase transformation; therefore, they are functions of time and not independent variables. The volume per atom of product and austenite are functions of three variables, i.e., phase type, temperature and chemical composition. Chemical composition itself is a function of temperature (partitioning rule) and N^p (mass balance of partitioned alloying elements). Since temperature is a time dependent variable and N^p is time dependent, all the variables in Eq. 4-4 can be expressed as time dependent functions. As a result,

Eq. 4-4 needs to be differentiated with respect to time to model the physics of the transformation correctly (Eq. 4-5).

$$\frac{dV}{dt} = \frac{d}{dt} \left(\int_0^{N^p} v^p dN^p \right) + v^\gamma \cdot \frac{dN^\gamma}{dt} + N^\gamma \cdot \frac{dv^\gamma}{dt} \quad \text{Eq. 4-5}$$

The derivative of the integral term can be expanded by using Leibniz's rule [151]. The general form of this rule for a time dependent derivative is shown in Eq. 4-6.

$$\frac{d}{dt} \left(\int_{g(t)}^{h(t)} f(x, t) dx \right) = \int_{g(t)}^{h(t)} \frac{df(x, t)}{dt} dx + f(h(t), t) \cdot \frac{dh(t)}{dt} - f(g(t), t) \cdot \frac{dg(t)}{dt} \quad \text{Eq. 4-6}$$

Using this rule, Eq. 4-5 can be written as Eq. 4-7.

$$\frac{dV}{dt} = \int_0^{N^p} \left(\frac{dv^p}{dt} \right) \cdot dN^p + v^p \cdot \frac{dN^p}{dt} + v^\gamma \cdot \frac{dN^\gamma}{dt} + N^\gamma \cdot \frac{dv^\gamma}{dt} \quad \text{Eq. 4-7}$$

Eq. 4-7 may be explained phenomenologically as follows. The left hand side is the instantaneous rate of change in volume of the specimen. This is calculated using the recorded dilatometry data. This change has four sources that create the four terms on the right hand side of the Eq. 4-7. The term $\int_0^{N^p} \left(\frac{dv^p}{dt} \right) \cdot dN^p$ calculates the instantaneous rate of change in volume that happened in the product phases that formed prior to time t. This includes mainly thermal contraction of the product phases, but can also include volume changes due to a chemical composition change of the product phase caused by a secondary process such as tempering or carbide precipitation. Hidden in the simplicity of this term is the fact that this integral assumes the product is made up of $\left(\frac{N^p}{dN^p} \right)$ product domains. These product domains can be completely different phases or the same phase with different chemical compositions. The contribution of each product domain to the overall volume change is calculated separately, which ensures that any number of phases are allowed to form. In the next section this integral will be discretized over the product domain.

The term $v^p \cdot \frac{dN^p}{dt}$ calculates the rate of the change in volume created by the formation of a new product phase at time t. The term $v^\gamma \cdot \frac{dN^\gamma}{dt}$ calculates the rate of volume change that is caused by consumption of the

austenite phase. The term $N^\gamma \cdot \frac{dv^\gamma}{dt}$ shows the rate of volume change that occurs in the austenite phase. The volume change in austenite has two equally important sources, i.e., temperature and chemical composition change caused by diffusive transformation and carbon accumulation.

Eq. 4–7 provides a robust framework for finding the number of austenite atoms that transform as a function of time. However, implementing a sound solution process depends heavily on the way v^p and v^γ are introduced to Eq. 4–7. As mentioned before, the volume per atom depends on the type of phase, the temperature and the chemical composition. Assuming that at a given time only one phase is forming (multiple phase transformations will be discussed later), the $\frac{dv}{dt}$ terms in Eq. 4–7 can be expanded as Eq. 4–8 to show the effect of these two parameters.

$$\frac{dv}{dt} = \left(\frac{\partial v}{\partial T} \Big|_{dM_i=0} \right) \cdot \frac{dT}{dt} + \sum_{i=C,Mn,Si\dots} \left(\frac{\partial v}{\partial M_i} \Big|_{dT=0} \right) \cdot \frac{dM_i}{dt} \quad \text{Eq. 4-8}$$

M_i is the concentration of element i in the phase. The concentration of elements in a phase depends on the partitioning rule that defines the proportion of concentrations in the product and austenite, but also depends on the mass balance between the two phases so that the net amount of alloying elements in the sample remains constant. Therefore, the dM_i terms are functions of dN_p , which makes Eq. 4–7 a non-linear equation. As a result, the best way to solve Eq. 4–7 without compromising the number of variables to simplify the solution, is by numerical methods. This numerical solution, which is based on the finite difference technique, has been developed in this thesis and is named Unit Cell Dilation (UCD) technique.

4.4.2 UCD algorithm

Eq. 4–7 can be solved numerically by a time stepping finite difference technique. In this method, by stepping time in small increments all the differential terms are estimated by simple algebraic expressions and solved using linear algebra methods. In general, between t_i and t_{i+1} , shown in Figure 4-3, Eq. 4–7 can be discretized according to.

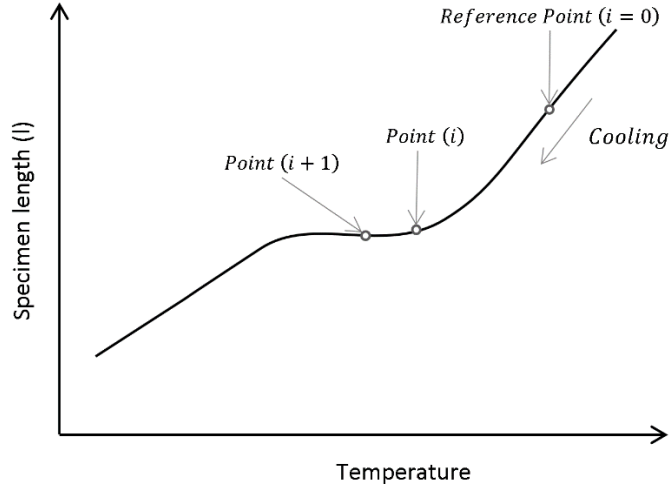


Figure 4-3. Sequential phase transformation of austenite to polygonal ferrite and bainitic ferrite.

$$\frac{(V_{i+1} - V_i)}{(t_{i+1} - t_i)} = \sum_{j=0}^{i-1} \left[\frac{(v_{i+1}^p - v_i^p)}{(t_{i+1} - t_i)} \cdot (\Delta N_j^p) \right] + v_{(i+\frac{1}{2})}^p \cdot \frac{\Delta N_i^p}{(t_{i+1} - t_i)} - v_{(i+\frac{1}{2})}^{\gamma} \cdot \frac{\Delta N_i^p}{(t_{i+1} - t_i)} \quad \text{Eq. 4-9}$$

$$+ \left(N_{total} - \sum_{j=0}^{i-1} \Delta N_j^p - \Delta N_i^p \right) \cdot \frac{(v_{i+1}^{\gamma} - v_i^{\gamma})}{(t_{i+1} - t_i)}$$

In Eq. 4-9, ΔN_k^p ($k = i$ or j), is the number of lattice atoms that have transformed to the product between steps k and $k + 1$, so that $N_{k+1}^p = N_k^p + \Delta N_k^p$. The term $v_{(i+\frac{1}{2})}^p$ indicates the volume per atom of the product at the mid-point between points i and $i + 1$. This is an estimation of the properties of the product while it is forming during one time step. Since the volume per atom is a function of chemical composition and temperature, $v_{(i+\frac{1}{2})}^p$ is calculated using the average temperature and average chemical composition between points i and $i + 1$ as shown in Eq. 4-10.

$$v_{(i+\frac{1}{2})}^p = v^p \left(M = M(T_{avr}), T_{avr} = \frac{(T_i + T_{i+1})}{2} \right) \quad \text{Eq. 4-10}$$

M shows the chemical composition, which includes the concentration of all the alloying elements in the alloy. Eq. 4-9 is an algebraic equation that can be solved numerically. However, calculation of ΔN_i^p is only possible if prior product type, chemical composition and amount at all prior steps are known. Therefore, the solution process has to begin from a reference point with a known microstructure and chemistry. The reference

point can be easily set within the single phase austenite region during cooling, as shown in Figure 4-3 which serves as the initial condition for the solution.

To solve Eq. 4–9, it is necessary to know what phase or phases form during the time step. This can be done by using a program that compares the temperature and chemistry of austenite with predetermined conditions that trigger formation of a phase. As an example, before the calculation of the current time step begins, the martensite start temperature for austenite is calculated using an empirical model [152–154]. If the average temperature of the time step is lower than the calculated martensite start temperature for austenite, the product in that time step will be considered to be martensite and appropriate functions will be used in Eq. 4–9. The condition that triggers formation of bainite was investigated in Chapter 3 and the results showed that the empirical model developed by Lee et al. [149] performed better than the T_0' method developed by Bhadeshia et al. [39]. The condition that triggers formation of cementite was considered to be equilibrium between austenite and cementite; i.e., exceeding the solubility limit of carbon in austenite would result in precipitation of cementite. Precipitation of cementite was considered to be immediate, which means the effect of kinetics on the volume fraction of precipitated cementite is not taken into account. Figure 4-4 shows the flowchart for the UCD algorithm.

4.4.3 Determination of product type(s)

One of the early steps in the UCD algorithm is determination of product types that form in a time step. There are two types of products that can form during a time step, ferrite derivative (FD) and cementite. FD can be ferrite, bainitic ferrite or martensite. A more detailed discussion on FD types is given in Section 4.4.4.2. Determination of FD type is done by calculation of B_s and M_s of the current austenite phase. If the current temperature is lower than M_s , martensite will be selected as the FD type. If the current temperature is higher than M_s but lower than B_s , bainitic ferrite will be selected as the FD type. Finally, if current temperature is above the current B_s of the austenite, ferrite is the FD type.

Cementite formation is allowed if the current carbon content of the austenite phase is above the solubility limit of the austenite with respect to $C - Fe_3C$ equilibrium. If the C content of austenite is above the solubility limit, an appropriate amount of cementite is allowed to form to bring the C concentration in austenite back to maximum allowed amount according to the solubility limit. Figure 4-5 shows the temperatures used in determining product types as a function of austenite carbon content.

4.4.4 Volume per atom

To be able to solve Eq. 4–9, it is necessary to have a reliable method to calculate the volume per atom of the phases participating in the transformation. For a crystalline phase, v can be calculated using Eq. 4–11.

$$v = \frac{\text{Volume of the unit cell}}{\text{Number of atoms in unit cell}} \quad \text{Eq. 4–11}$$

4.4.4.1 Austenite

The austenite unit cell has 4 atoms and its volume can be calculated using Eq. 4–12 to Eq. 4–14.

$$v_{unit\ cell}^{\gamma} = \left[a_{RT}^{\gamma} \left(1 + \int_{T=T_0}^T CTE^{\gamma} \cdot dT \right) \right]^3 \quad \text{Eq. 4–12}$$

$$a_{RT}^{\gamma} = a_0^{\gamma} + \sum_{j=C,Mn\dots} p_j c_j \quad \text{Eq. 4–13}$$

$$CTE^{\gamma} = CTE_0^{\gamma} + \sum_{j=C,Mn\dots} q_j c_j \quad \text{Eq. 4–14}$$

In these equations, a_0 is the lattice parameter at the reference temperature T_0 . It should be mentioned that the reference point for calculating the lattice parameter has nothing to do with the reference point selected for solving Eq. 4–9. To avoid confusion, the reference temperature for calculating the lattice parameter will be referred to as the lattice reference temperature. CTE_0 is the coefficient of thermal expansion when $c_j = 0$, j is the alloying element, c_j is the concentration of element j and p_j and q_j are the weighting factors for elements for the lattice parameter and CTE, respectively. The p_j and q_j factors can be found in the literature [149,155–157]; however, some partitioning rules such as paraequilibrium assume zero partitioning for substitutional elements, which means their concentration in the product and austenite is always the same as the nominal steel composition. This allows for simplification of Eq. 4–12 through Eq. 4–14 by just calculating the change caused by partitioning of carbon (and nitrogen if not negligible).

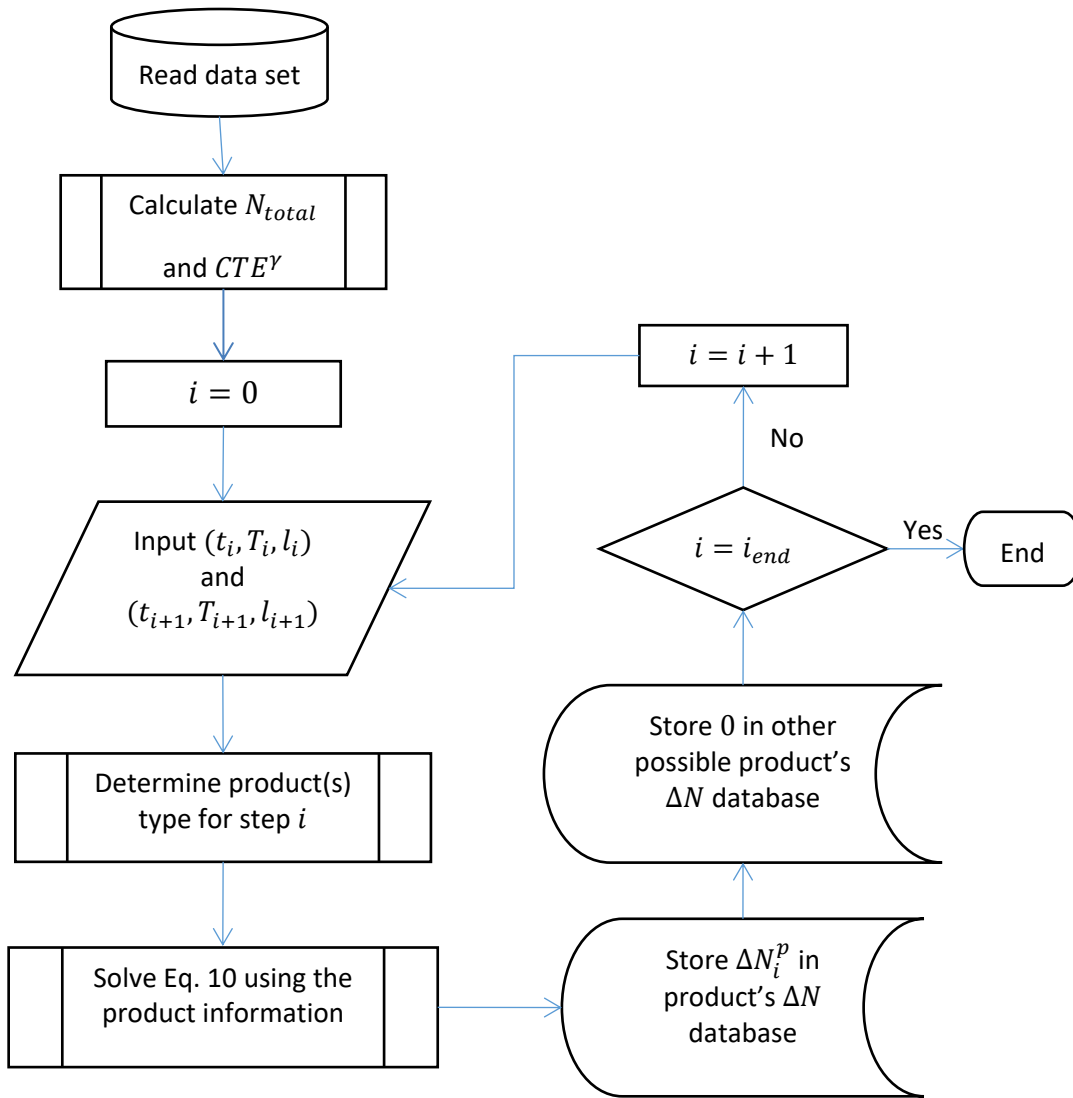


Figure 4-4. Flowchart for the UCD algorithm.

The concentration of carbon in austenite is assumed to be uniform within the austenite grain for simplicity. However, this assumption impacts the UCD calculation by introducing an error in the calculation of austenite volume. The volume of austenite is a nonlinear function of its carbon content, meaning changing just the carbon distribution within one austenite grain while keeping the average concentration constant can change the volume of the grain. The non-linearity can be shown by substituting Eq. 4-14 and Eq. 4-13 into Eq. 4-12 and differentiating it with respect to carbon content, which results in Eq. 4-15. In this equation carbon content (C) appears with exponents as high as 5 that originates from multiplication of exponents of 2 and 3, showing the non-linearity of

austenite volume with respect to carbon content. This error in calculating austenite’s volume is a cost that is justified by reduced computation time and much simpler implementation of the algorithm.

$$\frac{\partial v_{unit\ cell}^{\gamma}}{\partial C} = 3Tq_C(C \cdot p_C + a_0^{\gamma})^3 \times (T(C \cdot q_C + CTE_0^{\gamma}) + 1)^2 + 3p_C(C \cdot p_C + a_0^{\gamma})^2 (T(C \cdot q_C + CTE_0^{\gamma}) + 1)^3 \tag{Eq. 4-15}$$

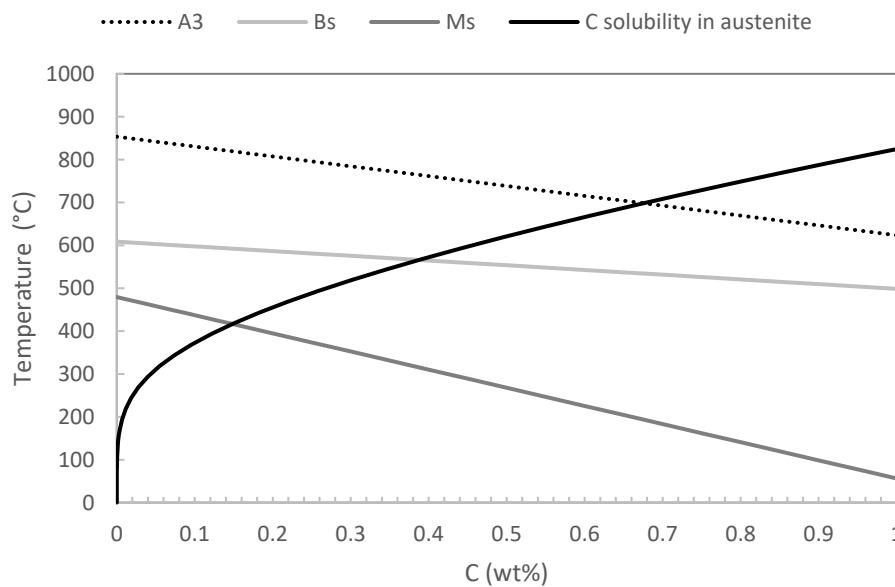


Figure 4-5. Temperatures used for determining product types that form within a time step. For steel X80-N.

4.4.4.2 Ferrite and Ferrite Derivatives (FD)

From a crystallographic point of view, the lattice for bainitic ferrite and martensite is, in fact, an extension of the ferrite lattice for pure iron with added strain due to dissolved carbon and/or nitrogen (if present). When the amount of dissolved carbon is less than 0.6 wt%, the FD unit cell is cubic or near cubic. At higher carbon contents, the body centered cubic unit cell changes to a body centered tetragonal type by stretching the unit cell in the *c* direction while slightly shrinking it in the *a* direction [84,158]. Table 4-2 shows the variation in lattice parameters of ferrite derivatives at room temperature as a function of carbon content.

Table 4-2. Change in lattice parameter of ferrite derivatives as a function of carbon content

C (wt%) < 0.6	C (wt%) > 0.6
$a_{RT}^{FD}(\dot{A}) = a_0^\alpha(\dot{A}) + W_{a.low\ C}^{FD} \cdot C$	$a_{RT}^{FD}(\dot{A}) = a_0^\alpha(\dot{A}) + W_{a.high\ C}^{FD} C$
$c_{RT}^{FD} = a_{RT}^{FD}$	$c_{RT}^{FD} = a_0^\alpha(\dot{A}) + W_{c.High\ C}^{FD} C$

$W_{a.low\ C}^{FD}$ is the carbon weighting factor for lattice parameter (a) at low carbon content, $W_{a.high\ C}^{FD}$ is the carbon weighting factor for lattice parameter (a) at high carbon content and $W_{c.High\ C}^{FD}$ is the carbon weighting factor for lattice parameter (c) at high carbon content. a_0^α can be calculated as a function of concentration of elements other than carbon in the phase, as explained by Lee et al. [155] or measured experimentally and calculated by subtracting the effect of carbon using the equations shown in Table 4-2. The unit cell volume of ferrite derivatives can be calculated using Eq. 4–16 and Eq. 4–17 [149].

$$v_{unit\ cell}^{FD} = \left[a_{RT}^{FD} \left(1 + \int_{T=T_0}^T CTE^{FD} \cdot dt \right) \right]^2 \cdot \left[c_{RT}^{FD} \left(1 + \int_{T=T_0}^T CTE^\alpha \cdot dt \right) \right] \quad \text{Eq. 4–16}$$

$$CTE^{FD} = CTE_0^{FD} + CTE_1^{FD} \cdot T + CTE_2^{FD} \cdot T^2 - CTE_3^{FD} \cdot C \quad \text{Eq. 4–17}$$

C is the carbon content in at%, T is the temperature in °C and CTE_i^{FD} are the polynomial constants. Using Eq. 4–16 and Eq. 4–17, three microconstituents, i.e., (quasi) polygonal ferrite, bainitic ferrite and martensite, can be modelled and used in Eq. 4–9. The carbon content of the FD phase has an important role in defining its true nature and properties. The lowest carbon content in a FD phase belongs to polygonal ferrite (PF). The carbon content of PF during transformation is determined by the partitioning rule. The most commonly used partitioning rule for microalloyed steels is para-equilibrium; therefore, it is the one used in this study. The carbon content assigned to FD according to paraequilibrium is the maximum thermodynamically stable amount of carbon that can dissolve in an FD phase. However, the highest amount of carbon in an FD phase occurs for martensite, which inherits all the carbon in austenite. Between the two extremes of carbon content in the FD phase, there is a situation where FD receives more carbon than the paraequilibrium content but less than the full austenite carbon content. This applies to bainitic ferrite and is explained in the following section.

4.4.4.3 Carbon content of FD

The amount of carbon dissolved in bainitic ferrite is more than the paraequilibrium content [42,159]. According to the displacive theory of bainite formation, bainitic ferrite initially receives all the carbon atoms in austenite; however, during the pause needed for recovery of austenite, some of this carbon escapes back to austenite [159,160] resulting in partial supersaturation. To model partial supersaturation of carbon in FD, it is useful to define a supersaturation fraction (SSF) as Eq. 4–18.

$$SSF = \frac{M_C^{FD} - M_{C,PE}^{FD}}{M_C^Y - M_{C,PE}^{FD}} \quad \text{Eq. 4–18}$$

M_C^{FD} is the observed concentration of carbon in the FD phase, $M_{C,PE}^{FD}$ is the concentration of carbon in FD according to paraequilibrium and M_C^Y is the concentration of the carbon in the austenite phase. SSF=1 means that all the carbon in austenite is inherited by FD, which applies to martensite. SSF=0 corresponds to $M_C^{FD} = M_{C,PE}^{FD}$, which means the amount of carbon dissolved in the FD phase is equal to the amount allowed by paraequilibrium; in other words, no supersaturation occurs. This applies to PF and QPF. Rearranging Eq. 4–18 to calculate the amount of carbon in FD results in Eq. 4–19, which is used in the UCD algorithm.

$$M_C^{FD} = SSF(M_C^Y - M_{C,PE}^{FD}) + M_{C,PE}^{FD} \quad \text{Eq. 4–19}$$

$M_{C,PE}^{FD}$ can be calculated using thermodynamic databases such as Thermo-Calc. SSF is a function of chemical composition and temperature and can be calculated by measuring the carbon content in bainitic ferrite using atom probe tomography [42,161] or XRD [42]. When SSF data is not available, SSF may be approximated as a linear function between values of zero and one at the lower bainite start temperature (LBs) and Ms temperature.

4.4.4.4 Cementite

Cementite has an orthorhombic unit cell with 12 iron atoms per unit cell. Its unit cell volume can be calculated using Eq. 4–20 [162].

$$v^{Cem.} = 153.85 + 0.00818 \times T \quad \text{Eq. 4–20}$$

In this equation T is in °C.

4.4.5 Multiple phase transformation

Multiple phase transformation refers to the simultaneous formation of two or more phases. As an example in steels, the transformation to pearlite is a multiple phase transformation of ferrite and cementite. Multiple phase transformation of cementite and FD phases are implemented in the UCD algorithm by evaluating the austenite-cementite equilibrium in the product type subroutine. If the amount of carbon in austenite exceeds the solubility limit of austenite, cementite will be allowed to form along with the FD phase. For simplicity, it is assumed that formation of cementite is faster than the formation FD phase and the maximum possible amount allowed by solubility limit, forms. This equilibrium assumption means that all the possible cementite that is thermodynamically required to form during a time step, will form regardless of kinetics of cementite precipitation. The amount of cementite that forms depends on the amount of FD phase formed at the current step, which is yet to be determined by the solver subroutine. When cementite formation is triggered, ΔN_i^p in Eq. 4–9 is replaced by $\Delta N_i^{FD} + \Delta N_i^{cem}$, which adds another unknown to Eq. 4–9. As a result, there has to be another equation relating ΔN_i^{FD} and ΔN_i^{cem} to allow for a unique solution. The second equation can be written by considering the mass balance of carbon between FD, cementite and austenite. Assuming that the carbon content of austenite after formation of cementite is equal to the solubility limit, the mass balance equation can be written as

$$\begin{aligned} & \left(N_{total} - \sum_{i=0}^{i-1} \Delta N_i^p \right) \left(\frac{C_{i-1}^Y}{1 - C_{i-1}^Y} \right) && \text{Eq. 4–21} \\ & = \Delta N_{i-1}^{FD} \cdot \left(\frac{C_i^{FD}}{1 - C_i^{FD}} \right) + \Delta N_{i-1}^{cem} \cdot \left(\frac{1}{3} \right) \\ & + \left(N_{total} - \sum_{i=0}^{i-1} \Delta N_i^p - \Delta N_{i-1}^{FD} - \Delta N_{i-1}^{cem} \right) \cdot \left(\frac{C_i^Y}{1 - C_i^Y} \right) \end{aligned}$$

C^Y is the atomic fraction of carbon in austenite and C^{FD} is the atomic fraction of carbon in FD. The left-hand side of Eq. 4–21 shows the amount of carbon in austenite before formation of the products in the current step. The right-hand side sums up the amount of carbon in FD, cementite and austenite after formation of the product. By solving Eq. 4–9 and Eq. 4–21 as a set, the amount of ΔN_{i-1}^{FD} and ΔN_{i-1}^{cem} can be calculated.

This approach to model multiple phase transformations is different than the work by Onink et al. [146] and Lee et al. [149], because independent formation of cementite is permitted here which allows for simultaneous modelling of the multiple phase transformation of pearlite (mixture of polygonal ferrite and cementite) and upper bainite (mixture of bainitic ferrite and cementite).

The equilibrium precipitation assumption, while allowing for much simpler implementation of cementite formation, introduces limitations to the UCD algorithm that need to be addressed. The formation of cementite is a diffusion controlled process. Therefore, under certain conditions, it is possible to generate less than the amount of thermodynamically predicted precipitation during a time step if the precipitation rate becomes slow compared with the rate of FD formation. Such a condition may exist at low transformation temperatures where diffusion rates decline and faster displacive transformation of austenite becomes the prevalent FD formation mechanism. In this situation, before all the excess carbon in austenite can precipitate, more FD will form in the next time step and more excess carbon will be added on top of what was left from the previous step. This accumulation of carbon will increase the carbon content of austenite over the solubility limit of carbon in austenite. Current implementation of cementite formation does not consider the effect of partial precipitation. However, devising a fix to include kinetic effects in the form of allowing for a temperature or chemistry dependent fraction of excess carbon to precipitate is possible. In an attempt to partially implement this fix, in the current implementation of UCD, it is possible to suppress precipitation below a user defined temperature. This feature may be useful for analysis of silicon containing steels as well, which cannot form cementite readily. This functionality is accessible by setting the appropriate keywords in *master_setup.txt* as explained in Section 7.2.2.

4.4.6 Implementation of UCD algorithm

The UCD algorithm is just a numerical approach, which needs proper implementation to work correctly. The implementation was done by designing two programs named “Fitter” and “Master Fitter”. The Fitter program applies UCD to one experimental data file consisting of time, temperature and dilation data. It uses the Nelder-Mead simplex minimization technique to find the molar fraction of product formed during one time step, by minimizing a cost function. The cost function in the Fitter program is the sum of the absolute value of the difference between the dilation calculated using the amount of product formed and the experimentally measured dilation at analysis points. By minimizing this difference the Fitter program ensures that the fraction transformed during each time step creates the expected dilation to match the experimental data.

The Fitter program relies on the user provided data about the material and phase properties which will be referred to as material parameters. These parameters are used to model the volume of the phases as explained in the volume per atom section. The Fitter program begins from a point with known phase content, usually austenite before the transformation begins, and then moves to the next point and calculates the phase content needed to make the modeled dilation equal to the experimentally measured value. Although possible, considering all the collected point in a data file to perform the UCD calculations, it is not practical as the speed

of calculation declines exponentially as the number of analyzed points increases. Therefore, a method must be used to pick only the important points within the raw data file. This task is assigned to a program called “Data File Conditioner”. Data File Conditioner selects a point by comparing it with the last selected point using a criterion. This criterion can be defined using time, temperature or dilation of the point or a combination of them. A time based criterion to keep constant Δt between selected points creates a different number of analysis points depending on the cooling rate, which is fine for the Fitter Program but proved to be problematic for the Master Fitter program which will be introduced later. A temperature based criterion is impractical as it would neglect all the points during isothermal periods of the thermal cycle. A dilation based selection criterion seems to be the most reliable as it is the dilation of the points that is the subject of UCD calculations. However, a functional dilation based selection criterion that works the same way regardless of the cooling rate and transformation temperature has not been found as yet. The main hurdle in implementing a dilation based criterion is the fact that dilation caused by transformation depends on the temperature of the parent and product phases, which at this point are not known. Therefore, the same amount of dilation would translate into different amounts of phase transformation for different experiments. This would cause the same problem as using constant Δt as the selection criterion, i.e., hugely different numbers of analysis points for different experiments.

To address the issues of the mentioned selection criteria, a hybrid time and temperature based selection criterion is used. In this method, a point is selected for analysis if 10s is passed ($\Delta t = 10s$) or the temperature is changed by 3°C ($\Delta T = 3^{\circ}\text{C}$) compared with the last selected point. The choice of ΔT and Δt is arbitrary and can be changed by the user. These conditions ensure that a proper number of data points are selected during both the isothermal and continuous cooling parts of a dilatometry experiment. The selected points are then stored in a new data file named “conditioned data file”. The points that do not make the selection process to be considered in the conditioned data file are used for reducing the noise in dilation and temperature of the selected point using a polynomial fit.

To allow the user to reduce the number of analysis points further, there is an option of selecting all the points in the conditioned data file or selecting 1 of every n points. The n parameter, which is referred to as the “interval”, is user defined and can be any natural number. The points that are not considered in the final calculations are used for noise reduction using a polynomial fit. The combined effect of the hybrid selection process and the interval is that at cooling rates below 0.3°C/s there is a $10n$ (s) time difference between the selected points and for cooling rates higher than 0.3°C/s there is a $3n$ ($^{\circ}\text{C}$) temperature difference between the selected points with n being the interval. A typical range for n is between 1 and 8. Higher values of n should be used for the first trials to quickly assess the ability of program to converge using the provided material properties.

The mentioned strategies allow the Master Fitter program to use variable time steps to treat the different experiments with relatively equal weight in its analysis.

As mentioned, the Fitter program uses material properties such as CTE and unit cell parameters to calculate the fraction of phases during transformation. Some of these material parameters can be measured directly from the experimental dilatometry data. As an example, CTE^{γ} can be measured experimentally since there is a temperature range, after the austenitization period and before the onset of transformation, where the microstructure is completely austenitic. During this period, the CTE of the whole specimen is equal to CTE^{γ} at the nominal steel composition. The property that is measured specifically for a phase in the material of interest provides the most reliable source of data for modeling that phase, considering the experimental error is negligible. However, not all material parameters can be measured for a specific specimen, because a single phase microstructure in the specimen is unlikely to happen. For instance, in low alloy and carbon steels, the ferrite phase is always accompanied by cementite and/or austenite. To measure CTE^{α} one would need to create a new specimen that has the identical chemical composition to the original specimen with its carbon content reduced to the solubility limit of ferrite. While it is possible to do so, for example, by decarburizing the specimen in a controlled oxidizing atmosphere, from a practical point of view this does not seem to be a solution available for every dilatometry experiment. Therefore, it is necessary to use existing developed models to calculate the material parameters under different thermal and chemical conditions. These models provide a reliable way to estimate the material parameters; however, to obtain the best results using UCD, the error arising from the use of the non-customized constants must be minimized. This was the reason for writing the second program named “Master Fitter”. This program was written to fine tune the material parameters.

The Master Fitter program finds the best combination of material parameters by analyzing a dataset rather than one data file at a time. A dataset is a collection of data files obtained for the same material. In a nutshell, Master Fitter runs the Fitter program on a dataset obtained under different conditions, such as cooling rate, using only one set of material parameters and then quantitatively evaluates the Fitter program for all the experiments. This is done by using one of the two optimization algorithms implemented in the Master Fitter program. One of the optimization algorithms uses the differential evolution technique to do a global minimization to find the best combination of parameters within a defined range for each parameter. The other one uses the Nelder-Mead simplex minimization technique starting from a user defined initial guess for the optimized parameters. Differential evolution is more reliable than Nelder-Mead in finding the best answer, but it is a much slower search algorithm compared with Nelder-Mead.

Both optimization techniques find the best parameters by minimizing a cost function. The cost function of Master Fitter is a quantitative measure of how “good” the calculated fraction of the product is at the analyzed

points. The unique feature about Master Fitter is that it determines the so-called goodness of the output of the Fitter program the same way that a human would do, by analyzing the shape of graph of the fraction transformed vs temperature for continuous cooling or the time for isothermal transformation. In human terms, a “good” result must meet the following 5 criteria.

1. At the end of the cooling cycle where the transformation is stopped, the phase fraction of products must remain constant.
2. The calculated dilation, using the material parameters, should match the experimentally measured dilations before, during and after the transformation.
3. The fraction of transformation must not exceed 1.
4. To ensure a correct fit, calculated dilations at the end of a cooling cycle must match experimental data. This is helpful since the errors for all previous analysis points accumulate and become pronounced at the point near the end of the cooling cycle.
5. The maximum amount of transformation should occur.

The first criterion is implemented by calculating a cost function as the difference between the slope of fraction transformed vs temperature $\left(\frac{df}{dT}\right)$ and the ideal end slope of 0. The cost function for the second criterion is calculated by summing the absolute value of the difference between the calculated dilation and the measured dilation for all the analysis points. Since the fraction transformed is calculated in steps, it is possible the sum of the fraction transformed exceeds one, which obviously is incorrect. To prevent this from happening, the third criterion is defined. The cost function for the third criterion is calculated by examining all the analysis points and issuing a large error for points that exceed a fraction transformed of 1. This large error ensures that the third criterion outweighs the other criteria and is always met. The fourth criterion is implemented similar to number two. The fifth criterion is implemented by calculating the cost function as the sum of the absolute value of the difference between the fraction transformed of the end points and the target fraction transformed of 1. The fifth criterion is optional and is only used when the optimization algorithm tries to meet the other four criteria by increasing the lattice parameter of ferrite, which reduces the fraction transformed to numbers close to zero. This criterion ensures that the optimization algorithm finds solutions that involve the highest amount of transformation possible. The Master Fitter program then calculates an overall cost for every experiment by linearly adding all the 5 costs using Eq. 4–22.

$$\text{cost for one experimental data} = \sum_{k=1}^5 W_k \cdot \text{cost}_k \quad \text{Eq. 4–22}$$

In this equation, W_k is the user defined weighting factor assigned to the cost function k . By changing the weighting factors, the user can alter the influence of each cost function on overall cost. This allows for better accommodation of the experimental results obtained for various types of steels and instruments. After calculating the cost for each and every experimental data file, the overall cost of the dataset is calculated by adding the cost calculated for each experiment.

4.4.7 Convergence

The UCD algorithm is essentially a 2-dimensional time-marching finite difference method in which X (molar fraction transformed) is calculated as a function of time by estimating the derivatives over discrete time steps as shown in Eq. 4-9. Similar to all finite difference techniques, estimated derivatives become more accurate as the time step becomes smaller and the numerical answer of the differential equation converges to the exact solution. However, this increased accuracy comes at a minor price of speed and computation time, but more importantly at a possible cost of instability and loss of convergence. Therefore, the UCD algorithm needs to be checked for convergence. Since the exact solution of the fraction transformed as a function of time is not known, the only way to check for convergence is to analyze the results as the time step becomes smaller. As explained in Section 4.4.6, in the current implementation of the UCD algorithm, the time step is replaced with a parameter called interval. Interval is defined as a 10 s time or 3°C temperature increase over the last analyzed point, whichever comes first. This means at cooling rates less than 0.3°C/s, 1 interval is equal to 10 s but above a cooling rate of 0.3°C/s, 1 interval is equal to 3°C. This definition for interval allows for unified treatment of continuous cooling transformation as well isothermal or very low cooling rate transformations. Figure 4-6 shows the results of the Fitter program on the experimental data obtained at 5°C/s as a function of temperature using different intervals. Since the cooling rate for this test is more than 0.3°C/s, interval is 3°C. Therefore, an interval of 7 for example, means the time step is $7 \times 3^\circ\text{C} = 21^\circ\text{C}$ or in terms of time, the time step is $21^\circ\text{C} / 5^\circ\text{C/s} = 4.2 \text{ s}$. Figure 4-6 shows the fraction transformed plots converge to the result obtained at the smallest time step, i.e., interval 1 as the time step decreases. This is especially visible in the temperature range of 550°C to 450°C.

4.5 Application of the UCD algorithm

4.5.1 Steel X80-N

To validate the UCD algorithm, dilatometry data obtained from a series of continuous cooling experiments performed on a X80 microalloyed steel were analyzed using the UCD algorithm and the results are compared with the measurements done using quantitative metallography. Figure 4-7 shows the phase content calculated by the UCD algorithm for steel X80-N. This figure shows that while the trend in change of QPF and BF is as expected, the amount of B/M stays relatively unchanged at $14.6\% \pm 1.7\%$. The underlying reason for such behavior of this steel is unclear. Figure 4-8 shows a comparison of the volume fractions of microconstituents measured metallographically with the calculated ones using the UCD algorithm and the volume fractions calculated using the lever rule. Except for the amount of pearlite, the UCD calculations are within 5% of the metallographic measurements. Although the Fitter and Master Fitter programs are capable of detecting pearlite, the code did not detect the formation of pearlite. This may be due to uncertainty in the definition of the carbon solubility limit in ferrite and austenite. Further analysis with higher carbon steels is needed to address this issue properly. The material parameters were optimized using the Master Fitter program. These parameters are shown in Table 4-3.

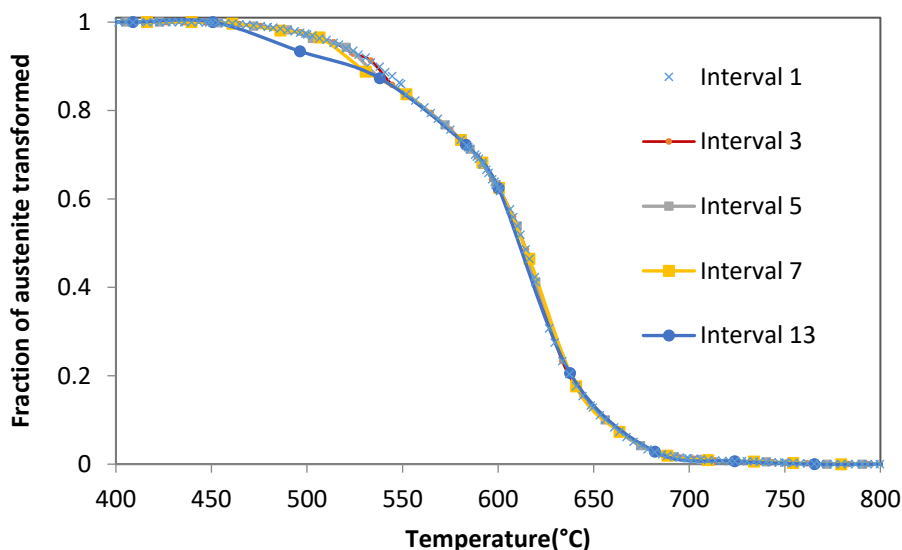


Figure 4-6. Fraction transformed as a function of temperature calculated using different intervals for steel X80-N at the cooling rate of $5^{\circ}\text{C}/\text{s}$. Smaller intervals mean smaller time steps. This figure shows that the UCD algorithm results converge as the time step become smaller.

Table 4-3. Material parameters used by the Fitter program before and after optimization by the Master Fitter*

Microconstituent	Application	Before optimization	After optimization
Austenite	Eq. 4-13	$a_0^\gamma = 0.36306 \text{ nm}$ at $T_0 = 726.85^\circ \text{ C}$ [147]	$a_0^\gamma = 0.36304 \text{ nm}$ at $T_0 = 726.85^\circ \text{ C}$
Ferrite Derivatives (FD)	Table 4-2	$a_0^\alpha = 0.28610 \text{ nm}$ at $T_0 = 0^\circ \text{ C}$ [149] $W_{a.low c}^{FD} = 0.02$ $W_{a.high c}^{FD} = 0.013 \times 10^{-10}$ $W_{c.high c}^{FD} = 0.116 \times 10^{-10}$	$a_0^\alpha = 0.286304 \text{ nm}$ at $T_0 = 20^\circ \text{ C}$ $W_{a.low c}^{FD} = 0.026$ $W_{a.high c}^{FD} = 0.013 \times 10^{-10}$ $W_{c.high c}^{FD} = 0.116 \times 10^{-10}$
	Eq. 4-17	$CTE_0^{FD} = 1.1712 \times 10^{-5} \text{ K}^{-1} +$ $CTE_1^{FD} = 1.3290 \times 10^{-8} \text{ K}^{-2} +$ $CTE_2^{FD} = -8.9475 \times 10^{-12} \text{ K}^{-3}$ [163] † $CTE_3^{FD} = 1.9 \times 10^{-4} \text{ K}^{-1}$ [149]	$CTE_0^{FD} = 1.273 \times 10^{-5} \text{ K}^{-1}$ $CTE_1^{FD} = 4.822 \times 10^{-9} \text{ K}^{-2}$ $CTE_2^{FD} = 0 \text{ K}^{-3}$ $CTE_3^{FD} = 2.52 \times 10^{-4} \text{ K}^{-1}$

* Shaded parameters were not optimized as they were not used in the calculations.

† Calculated using the CTE data for pure ferrite presented in reference [163].

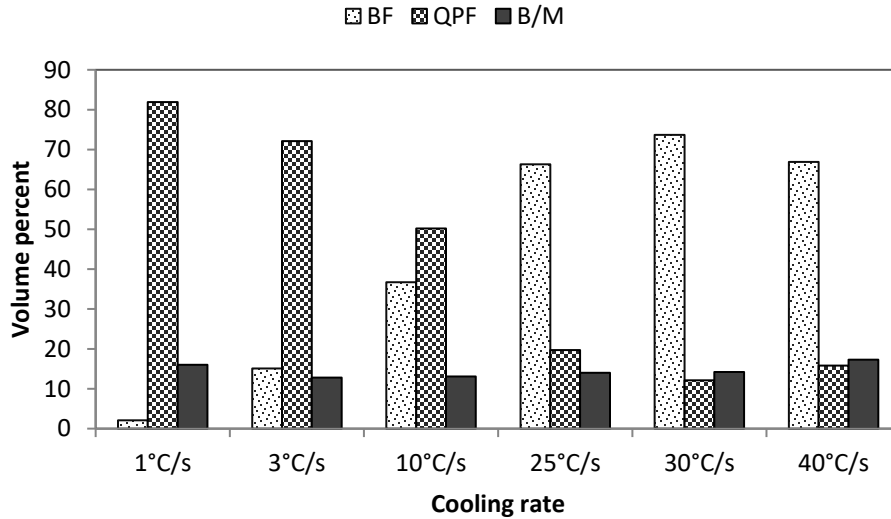


Figure 4-7. Phase content of steel X80-N calculated by the Master Fitter program.

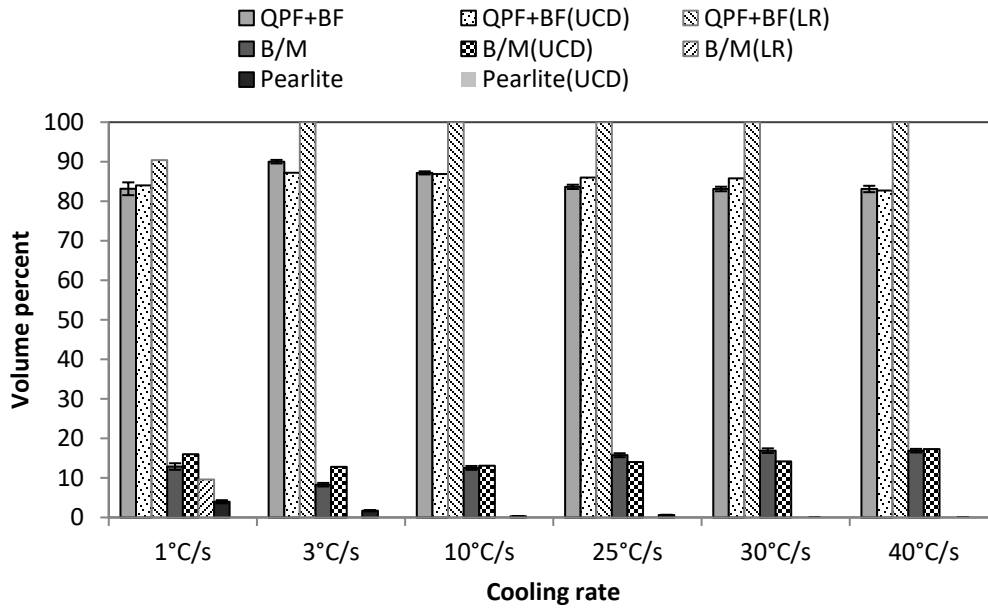


Figure 4-8. Comparison of calculations made using the UCD algorithm with quantitative metallography measurements for steel X80-N. UCD stands for unit cell dilation technique and LR stands for lever rule method.

A closer look at the phase fractions in Figure 4-8 shows that despite all the cooling rates producing a multiple phase microstructure, in all but the lowest cooling rate, the lever rule calculates the phase content only for the QPF+BF. As mentioned earlier, the lever rule does not automatically account for sequential phase transformation. However, some dilatometry plots may contain clues that indicate sequential phase transformation. One of the indicators is the formation of a linear line in the dilation vs temperature graph, between two curved regions. The entry point to the linear region is the end of the first phase transformation and the exit point from the linear region is the beginning of the second phase transformation. A linear region can only be clearly observed when there is a period between the two phase transformations where no transformation occurs, which is not a general case for all sequential phase transformations. Nevertheless, examining Figure 4-2 shows that when comparing all the cooling rates, only the dilatometry plot obtained for continuous cooling at 1°C/s shows a definitive sign of sequential phase transformation. Analyzing the first and second derivatives of the graphs in this figure did not produce meaningful and consistent evidence for detecting the onset of phase transformation that could be confirmed by the metallography results.

For clarity, the dilation curve obtained for 1°C/s is shown alone in Figure 4-9. It can be seen that during cooling two transformation ranges exist that are separated by the straight part of the cooling curve shown by the dashed line. Judging by the difference in the amount of dilation observed for these two transformations, it is expected that the product of the first transformation has a higher volume fraction compared with the

secondary phase transformation. Figure 4-10 shows the volume fraction of transformed austenite calculated using the lever rule and the UCD algorithm as a function of temperature for the cooling rate of 1°C/s. The phase fraction calculated using the lever rule shows that the linear region occurs at 90% phase transformation, while metallographic measurement showed the volume fraction of the major phase (polygonal ferrite) is 82%. In comparison, UCD calculates the volume fraction of the polygonal ferrite as 83%, which matches the quantitative metallography results. It is evident that UCD not only outperforms the lever rule in analyzing multi-phase microstructures, but makes more accurate predictions for the phase contents.

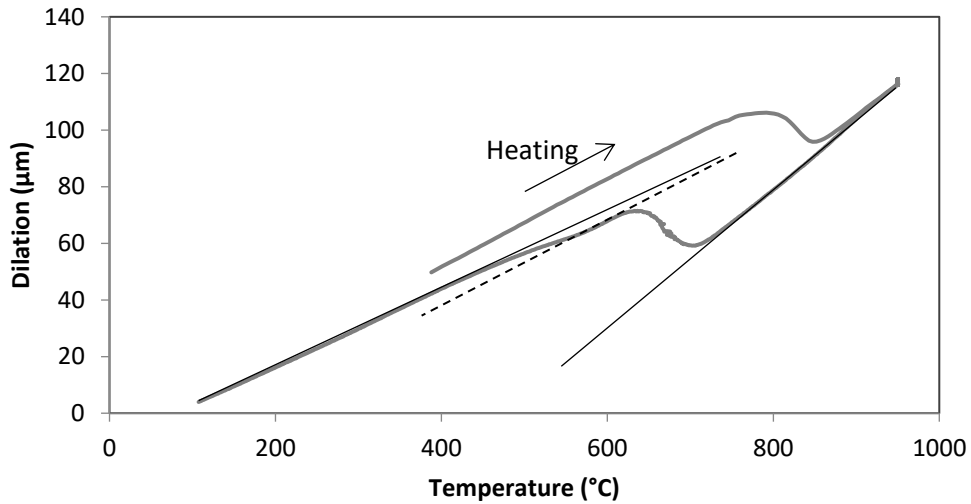


Figure 4-9. Continuous cooling at 1°C/s. Sequential phase transformation is confirmed by the formation of a linear region (dashed line) at about 600°C.

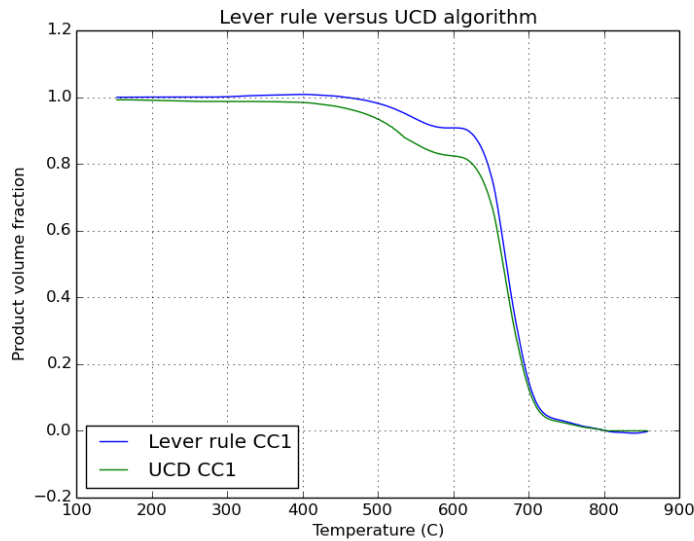


Figure 4-10. Product volume fraction vs temperature at 1°C/s calculated using UCD and the lever rule.

Figure 4-11 shows the variation in lattice parameter of austenite as a function of temperature during cooling for three cooling rates of 1°C/s, 10°C/s and 40°C/s. Before the transformation begins, the carbon content of austenite is constant; therefore, the lattice parameter is only a function of temperature with the slope of the line being proportional to CTE^{γ} . This, however, changes at lower temperatures. As the transformation begins at lower temperatures, formation of ferrite results in accumulation of carbon in austenite which, on one hand, results in swelling of the austenite unit cell causing upward deviation from the linear trend. On the other hand, carbon accumulation in austenite results in a reduction of CTE^{γ} which also causes an upward deviation from the linear trend seen before the transformation began. This upward deviation continues until the concentration of carbon in austenite reaches the solubility limit of carbon in austenite with respect to cementite. From this point, the carbon content of austenite is determined by the solubility limit function. In the absence of redistribution of substitutional atoms, the solubility limit becomes exclusively a temperature dependent function. Therefore, after the onset of cementite precipitation, the lattice parameter of austenite is the same for all cooling rates. This is the reason all three curves follow the same path after the arrows (Figure 4-11) that indicate the point where the solubility limit is reached in austenite.

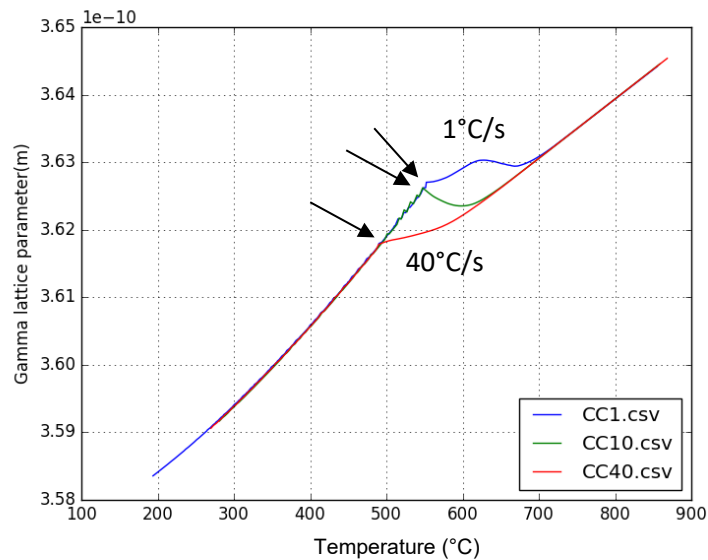


Figure 4-11. Lattice parameter of austenite as a function of temperature at different cooling rates. Arrows show the point at which the carbon content of austenite begins following the solubility limit of carbon in austenite with respect to cementite.

4.5.2 Steel X80-K

To further test the validity of the developed algorithm and codes, a dataset containing dilatometry data for continuous cooling experiments on an X80 steel was obtained from reference [132]. The raw dilatometry data is

analyzed using the Master Fitter program. Table 4-4 shows the material parameters calculated by the optimization program. Figure 4-12 shows a comparison of the phase fractions calculated using the UCD algorithm and metallographic measurements. Aside from the cooling rate 0.5°C/s, at all cooling rates good agreement is observed between the Master Fitter results and metallographic measurements of phase content. The main reason for the poor fit for a cooling rate of 0.5°C/s is the odd trend that is observed in CTE^Y during cooling. Theoretically, the CTE of a phase is only a function of its state variables, namely chemical composition, phase type, temperature and pressure. However, as shown in Figure 4-13, CTE^Y for steel X80-K appears to be a function of cooling rate. Such a trend was not observed for steel X80-N.

Table 4-4. Material parameters used by the Fitter program before and after optimization by Master Fitter*

Microconstituent	Application	Before optimization	After optimization
Austenite	Eq. 4-13	$a_0^Y = 0.36306 \text{ nm}$ at $T_0 = 726.85^\circ \text{ C}$ [147]	$a_0^Y = 0.36304 \text{ nm}$ at $T_0 = 726.85^\circ \text{ C}$
Ferrite Derivatives (FD)	Table 4-2	$a_0^\alpha = 0.28610 \text{ nm}$ at $T_0 = 0^\circ \text{ C}$ [149] $W_{a.low c}^{FD} = 0.02$ $W_{a.high c}^{FD} = 0.013 \times 10^{-10}$ $W_{c.high c}^{FD} = 0.116 \times 10^{-10}$	$a_0^\alpha = 0.286168 \text{ nm}$ at $T_0 = 20^\circ \text{ C}$ $W_{a.low c}^{FD} = 0.058$ $W_{a.high c}^{FD} = 0.013 \times 10^{-10}$ $W_{c.high c}^{FD} = 0.116 \times 10^{-10}$
	Eq. 4-17	$CTE_0^{FD} = 1.1712 \times 10^{-5} \text{ K}^{-1} \dagger$ $CTE_1^{FD} = 1.3290 \times 10^{-8} \text{ K}^{-2} \dagger$ $CTE_2^{FD} = -8.9475 \times 10^{-12} \text{ K}^{-3}$ [163] † $CTE_3^{FD} = 1.9 \times 10^{-4} \text{ K}^{-1}$ [149]	$CTE_0^{FD} = 1.274 \times 10^{-5} \text{ K}^{-1}$ $CTE_1^{FD} = 5.641 \times 10^{-9} \text{ K}^{-2}$ $CTE_2^{FD} = 0 \text{ K}^{-3}$ $CTE_3^{FD} = 3.54 \times 10^{-4} \text{ K}^{-1}$

* Shaded parameters were not optimized as they were not used in the calculations.

† Calculated using the CTE data of pure ferrite presented in reference [163].

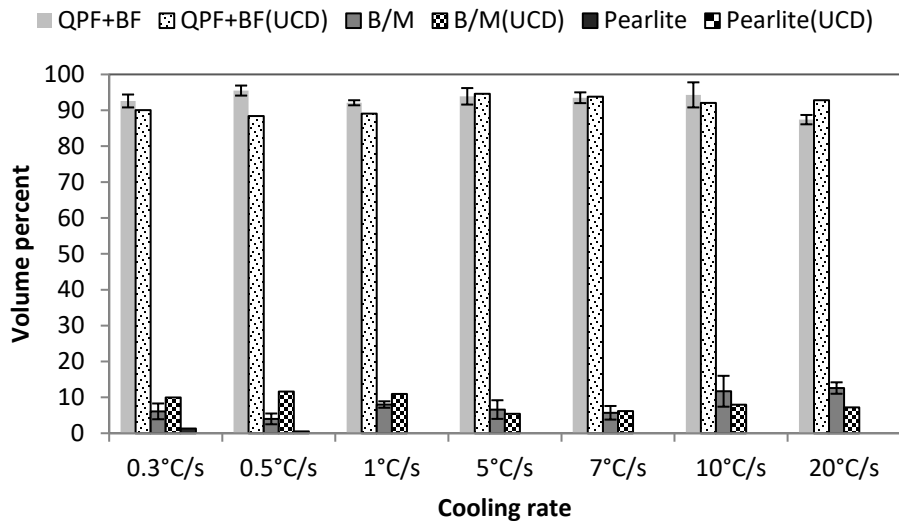


Figure 4-12. Comparison of calculations made using the UCD algorithm with quantitative metallography measurements for steel X80-K. Reproduced with permission from [132].

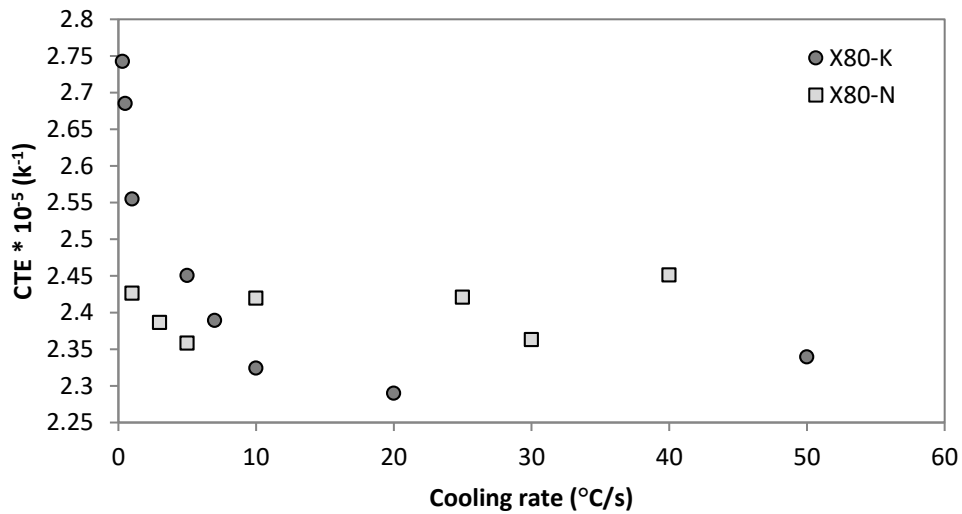


Figure 4-13. CTE of austenite during cooling after austenitization for steels X80-K and X80-N.

The dependence of CTE^Y on cooling rate may be a result of specimen creep under the force of the extensometer. This hypothesis agrees with the reduction in CTE^Y to expected values at higher cooling rates. At low cooling rates, the strain rate due to temperature reduction becomes small enough to be comparable with the small creep strain rate caused by the force applied by the extensometer. For steel X80-K, dilatometry was done using a Gleeble machine on a solid sample with dilatational measurements taken on the diameter of the specimen [132]. The extensometer force, no matter how small, can translate into a large stress when divided by

a small contact area on the surface of the specimen. For steel X80-N, dilatational measurements were taken on the length of the specimen which increases the contact area between the extensometer and the specimen.

To accommodate the observed variability of CTE^{γ} among different specimens of a dataset, the Fitter and Master Fitter programs allow for this material parameter to be different for each experiment. This is done by calculation of CTE^{γ} and N_{total} at the beginning of the calculations using the pure austenite portion of the cooling curve. Until a better method is found to account for the differences in CTE^{γ} for different cooling rates involving steel specimens with the same chemical composition, this seems to be the only way of handling this issue.

4.5.3 Sensitivity analysis of Master Fitter

Master fitter is designed to find the correct material property parameters by analyzing a pool of experimental data files. From a statistical point of view, if the error in measured data is random, increasing the number of data files in the pool would result in cancellation of the errors, ultimately improving the accuracy of the calculated parameters. Considering this, a valid question that comes to mind is how sensitive are Master Fitter results to the elimination of an individual data file in the pool. To investigate the contribution of an individual data file to the overall analysis, a sensitivity analysis is done by comparing the values of the calculated material parameters for the full dataset versus an incomplete dataset using the data obtained for steel X80-N. The incomplete dataset is created by eliminating a data file from the full dataset. For the full dataset comprising 6 data files, it is then possible to create 6 incomplete datasets. The top plot in Figure 4-14 to Figure 4-19 shows the effect of elimination of an individual data file on the fit of the calculated length of the specimen vs the experimentally measured value. The bottom plot in these figures shows the calculated mole fraction of transformation. Overall a good degree of agreement between measured and calculated length of the specimens is observed across the board. Figure 4-20a to 4-20e show the percent difference created in the material properties as a result of the elimination of a dataset from the analysis pool. Analyzing the figures shows that eliminating a data file for all cooling rates creates less than a 1% change in the calculated material parameter compared with using the full set. This indicates that for a sufficiently large pool of data files, fit parameters calculated by Master Fitter are not too reliant on a single data file.

To ensure the insensitivity of Master Fitter to an individual data file, it is suggested that for any dilatationally distinctive microconstituent in the tested steel, there should be at least 2 data files that contain a high phase fraction of that microconstituent. Having 2 data files for each microconstituent ensures that by eliminating one data file there will at least be another data file to represent that microconstituent. In a microalloyed steel, the distinct microconstituents are PF, lower BF, martensite (α') and retained austenite (γ'). This means that a pool of 8 data files, distributed in a sufficiently wide range of cooling rates to produce predominantly PF at the slowest cooling rate and martensite at the fastest cooling rate, can be a good and conservative estimate of the number of the tests needed in the dataset. It should be mentioned that 2 data files per distinctive microconstituent is a very conservative estimate.

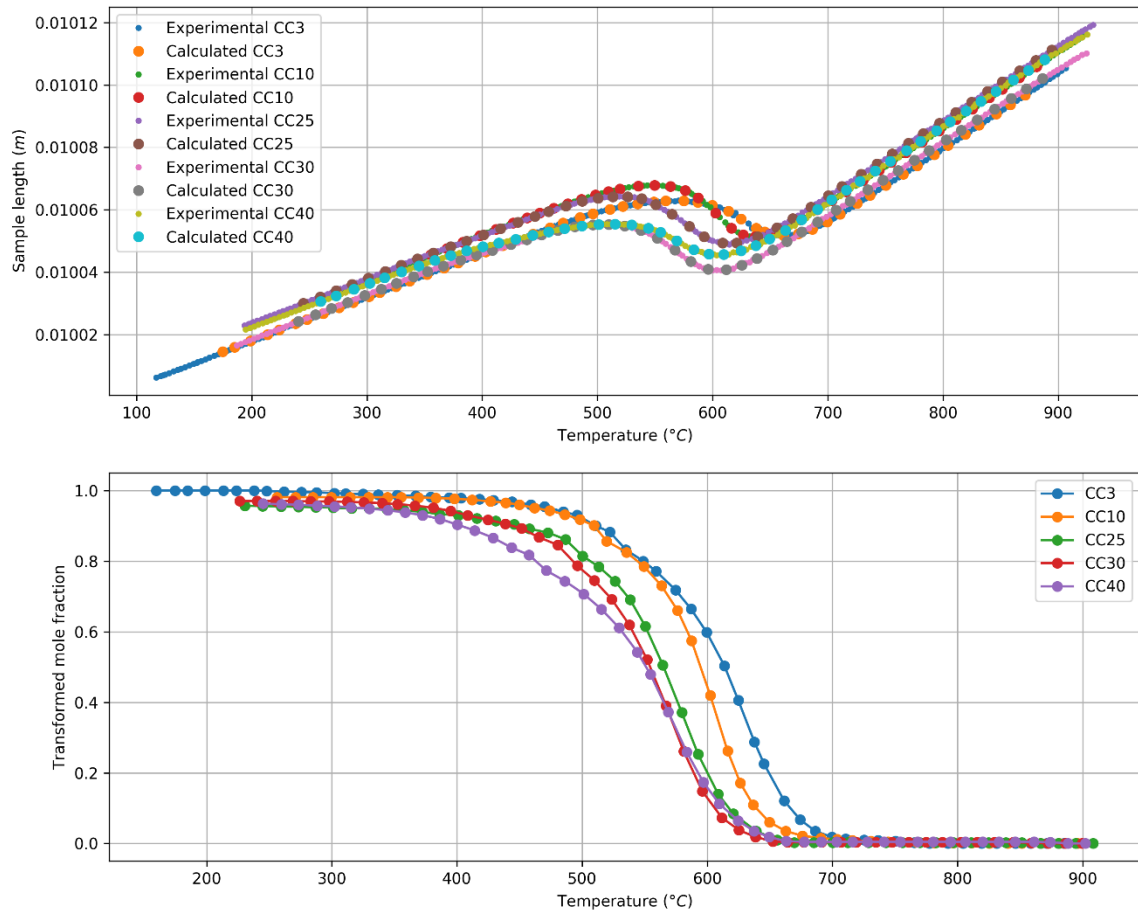


Figure 4-14. Effect of elimination of data collected at 1°C/s on dilation curve (top) and calculated fraction of transformation (bottom).

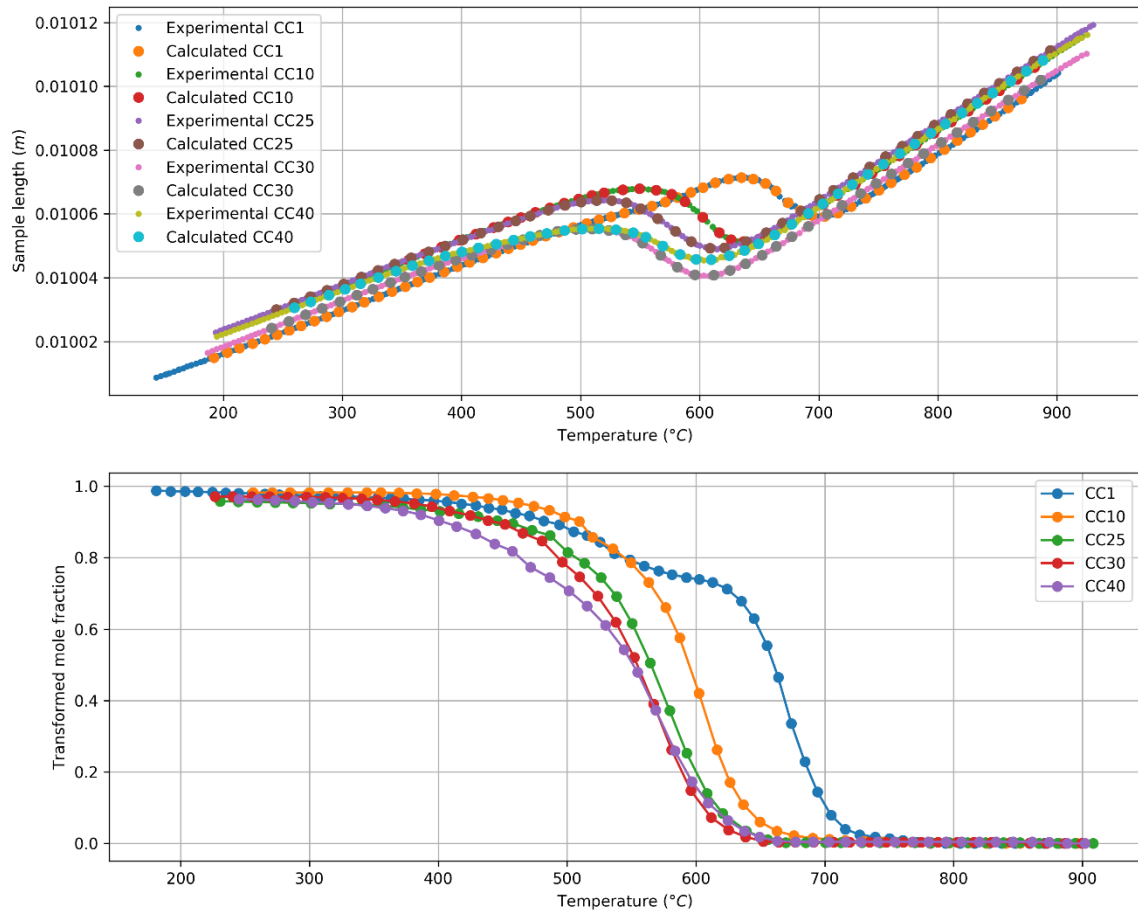


Figure 4-15. Effect of elimination of data collected at 3°C/s on dilation curve (top) and calculated fraction of transformation (bottom).

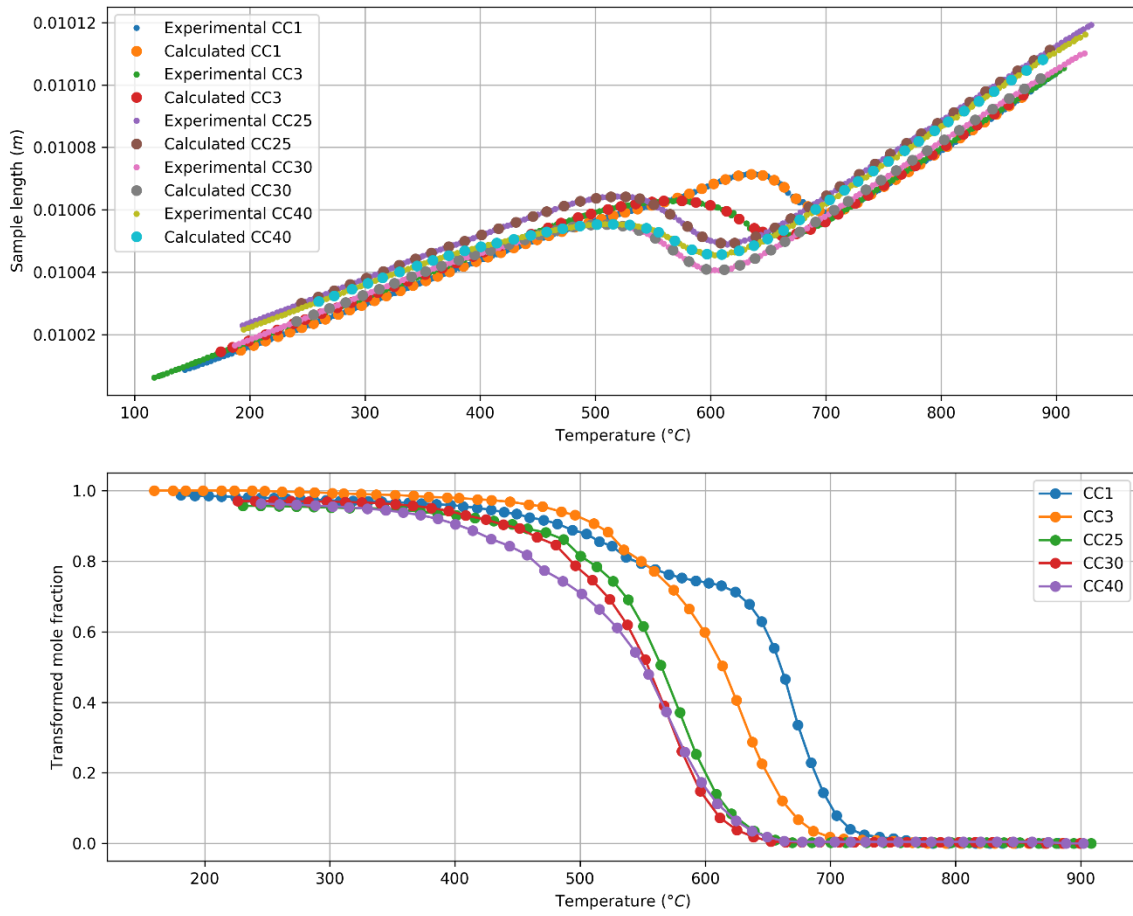


Figure 4-16. Effect of elimination of data collected at 10°C/s on dilation curve (top) and calculated fraction of transformation (bottom).

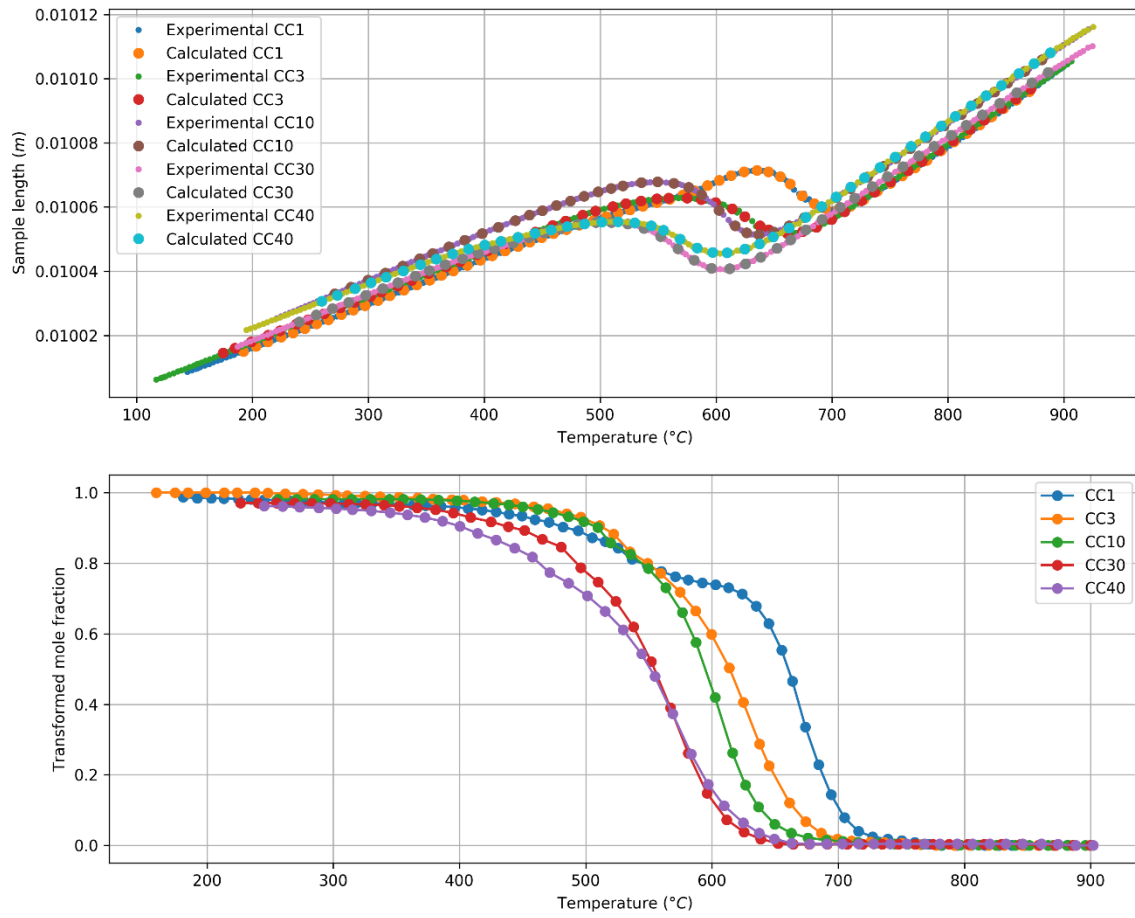


Figure 4-17. Effect of elimination of data collected at 25°C/s on dilation curve (top) and calculated fraction of transformation (bottom).

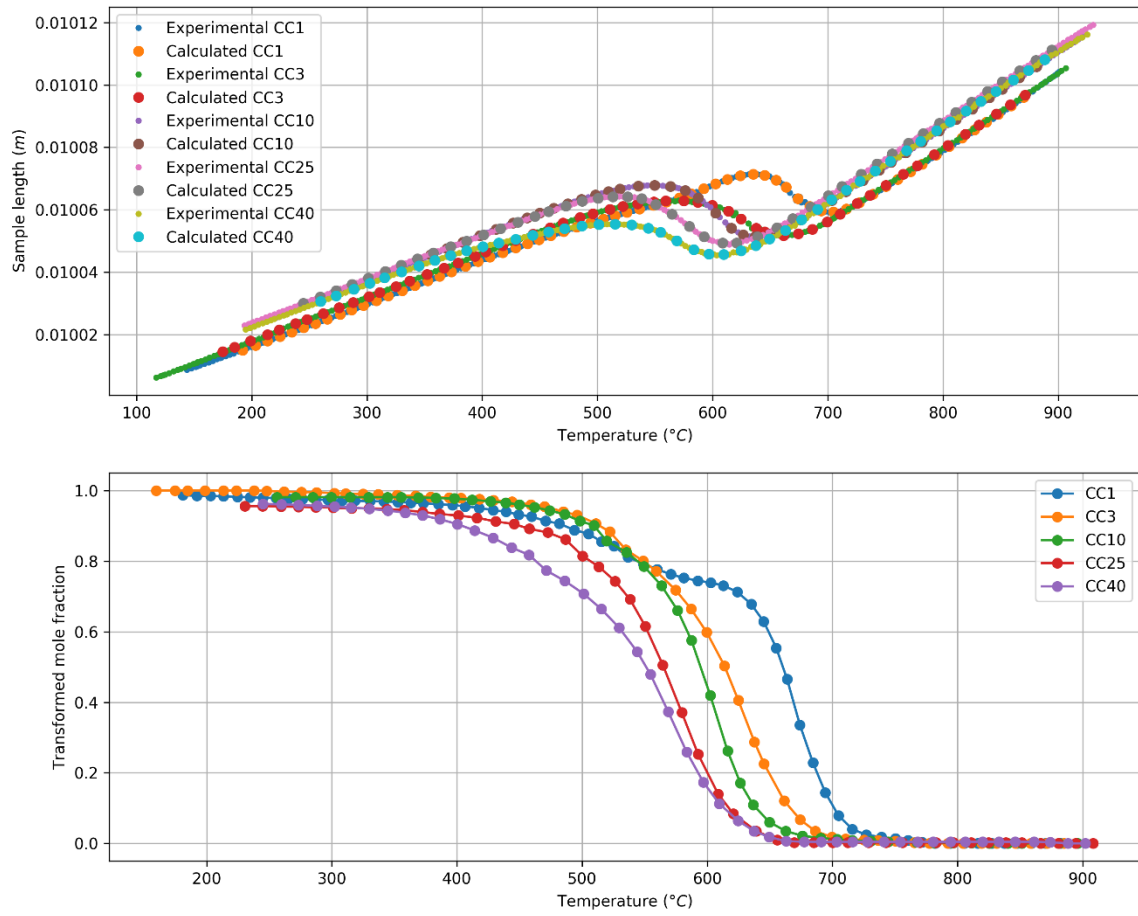


Figure 4-18. Effect of elimination of data collected at 30°C/s on dilation curve (top) and calculated fraction of transformation (bottom).

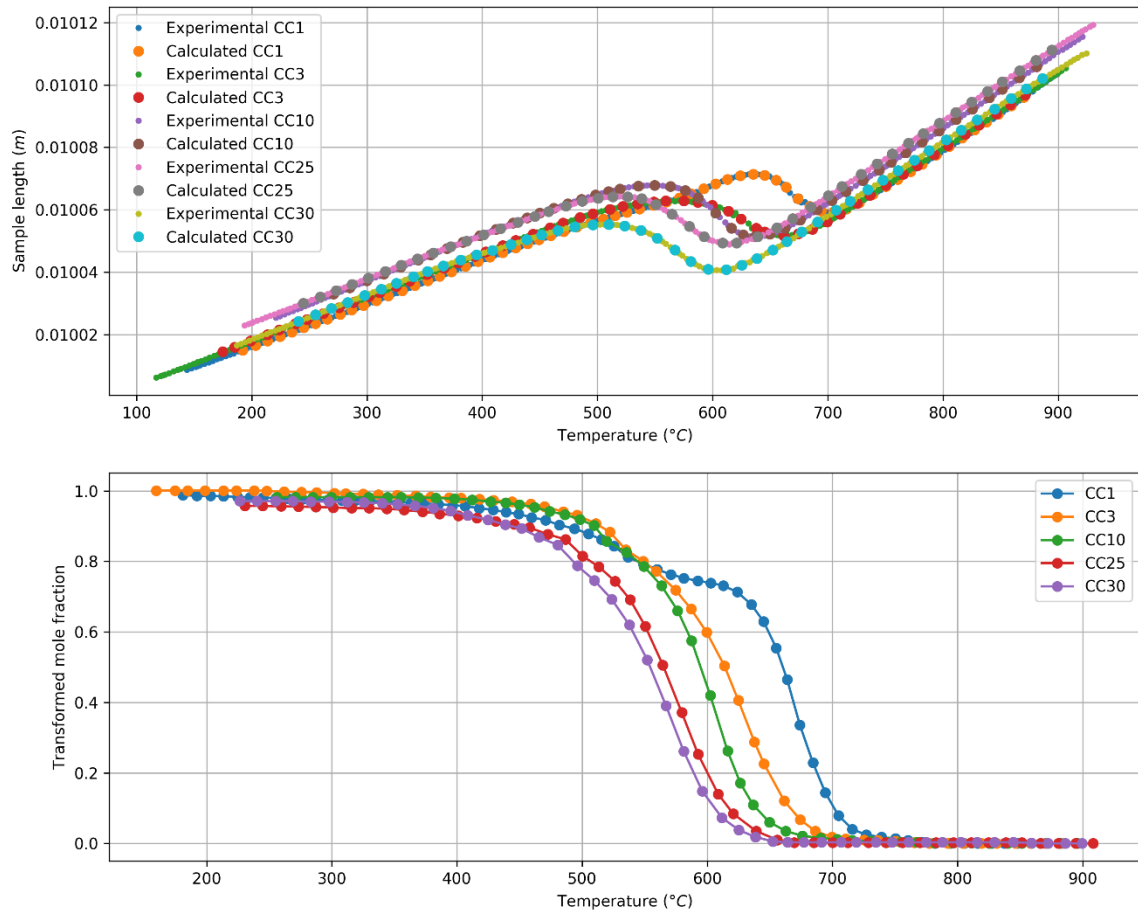
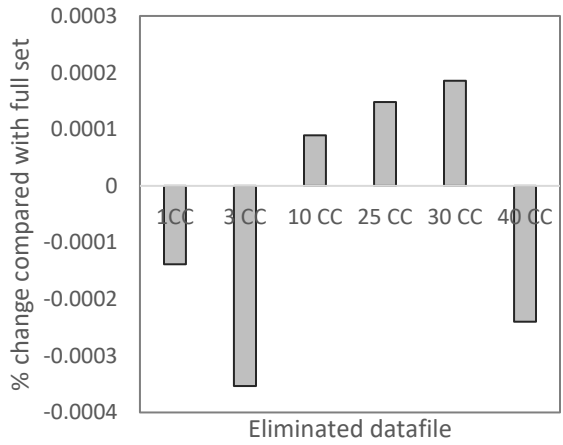
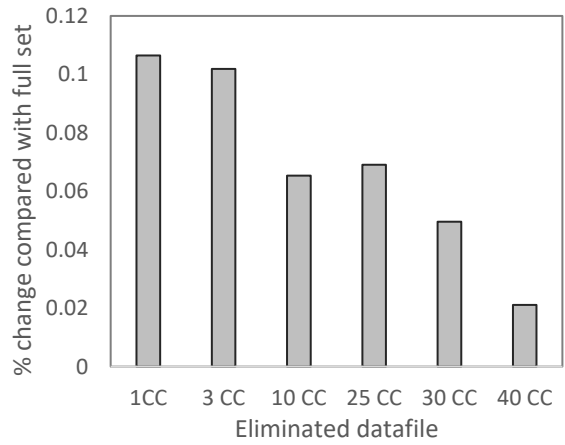


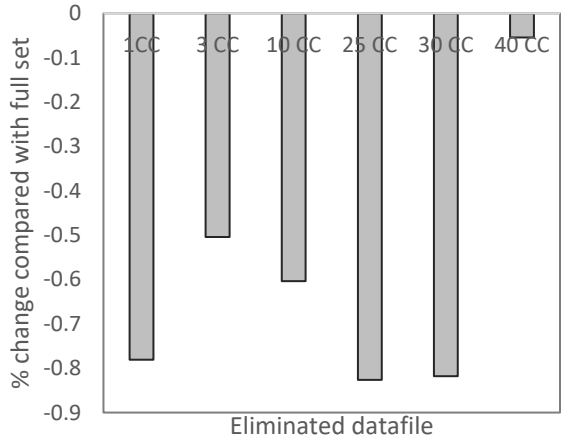
Figure 4-19. Effect of elimination of data collected at 40°C/s on dilation curve (top) and calculated fraction of transformation (bottom).



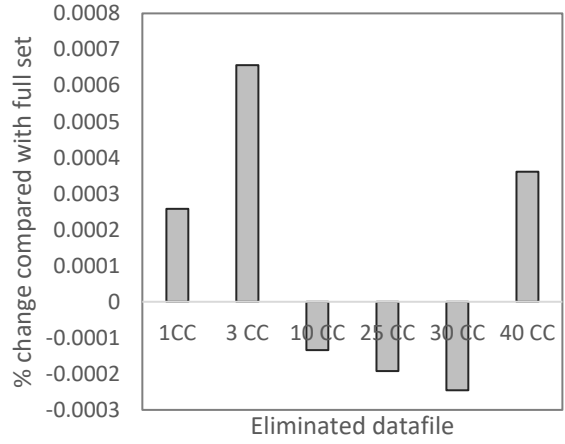
a) a_0^α



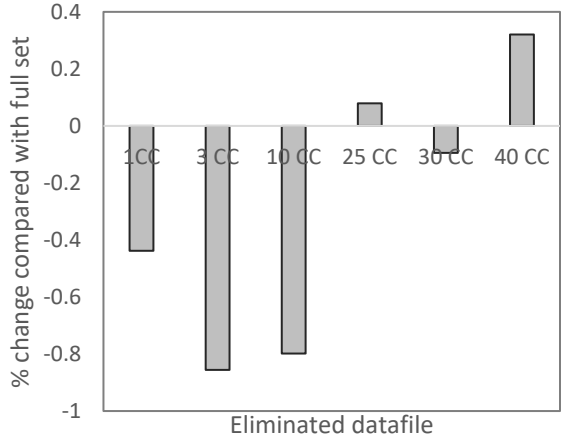
b) CTE_0^{FD}



c) CTE_1^{FD}



d) CTE_3^{FD}



e) $W_{a.low c}^{FD}$

Figure 4-20. Sensitivity analysis of Master Fitter program. The figures show the relative change in the material parameter as a function of elimination of a data file from the complete dataset.

In reality, microconstituents usually appear together in a microstructure and, in fact, this is required to allow the Master Fitter program to properly take into account the interplay between these microconstituents. Co-existence of microconstituents allows reduction of the minimum number of required experiments. Of the four mentioned microconstituents, γ' can readily be found in many steels with slow to moderate cooling rates in microalloyed steels. PF is seen in steels with slow to moderate cooling rates, while LBF and α' form at moderate to high cooling rates. Considering the possibilities of co-existence, as shown in Figure 4-21, it may be possible to have all the distinct microconstituents represented by two main microstructures of mixed PF-LBF- γ' and mixed LBF- α' - γ' , which can be achieved by carefully selecting the cooling rate. Following the logic of representing each microconstituent at least twice in the dataset, it seems possible to have a reasonable analysis done with at least 4 experiments. This number should be looked at as the absolute minimum number of experiments required; below this number, Master Fitter is not able to produce a meaningful result for microalloyed steels. This means that Master Fitter is not guaranteed to work with fewer than 4 experimental data files.

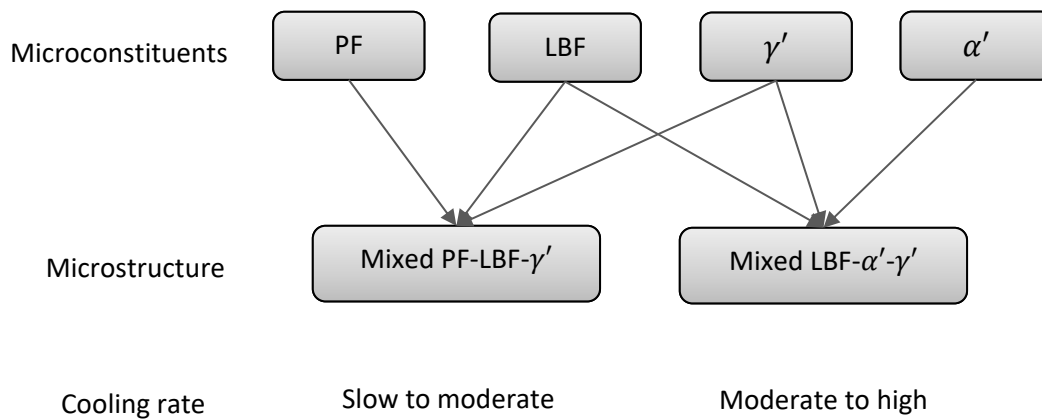


Figure 4-21. Analysis of the microstructure needed to ensure reasonable results from Master Fitter.

4.6 Advantages and disadvantages of UCD algorithm compared with alternatives

The paper by Onink et al. [146] seems to be the first published work that analyzes dilatometry based on the volume of the unit cells of the phases. Their pioneering work is hereby credited and acknowledged as the origin of unit cell based dilatometry analysis. However, some scientific criticism may be useful for further development of the method they invented. Onink's analysis is based on the unit cell definitions of dilatational changes of the phases similar to the UCD algorithm; however, the formulations of the two methods are fundamentally different. Onink's approach relies on knowledge of equilibrium phase content at a given temperature as this amount is

used in the definition of the z parameter. Equilibrium phase content is not required for the UCD method. In Onink's work, it is not explicitly mentioned how the non-linear equations are solved using experimentally measured dilation data, so it is not possible to evaluate the accuracy of the model. This is especially a sticking point for Onink's paper as they do not provide any experimental validation for his proposed analysis method. Also, although not a fundamental flaw, Onink's method does not consider the formation of lower bainite and martensite. This critique must be considered bearing in mind that Onink's paper is the first of its kind that opened a whole new avenue for dilatometry analysis.

Compared with the work of Kop et al. on a similar approach to analyze dilatometry data [147], the UCD algorithm is more flexible in terms of multiple product formation. Kop et al. do not consider the transformation of bainitic ferrite and martensite. Although the cooling rate in their experiments is not mentioned, the dilatometric curves show that transformation of all samples ends well above the approximate B_s of the steels. Therefore, the microstructures must be ferrite-pearlite type, so the exclusion of martensite and bainite does not constitute a fundamental flaw in their analysis. Their method suffers from mismatch of the utilized phase property parameter with the real values that would be needed for the different chemical compositions of steels used. Their solution to this problem is to include a scaling factor, which essentially is a "fudge" factor to make the calculation fit the observation. The source of the mismatch in their work is speculated to be experimental error or non-linearities that are not accounted for. In the current work, this problem is solved by using the Master Fitter program which optimizes the phase property values by simultaneously analyzing a pool of dilatometry data obtained at different transformation conditions. As discussed in Section 4.5.3, the more experiments provided in the analysis pool the better that accuracy of the customization. Kop et al.'s work also lacks metallographic confirmation that the volume fractions calculated by their method match the real phase content of the specimens. In their next paper on this subject [148], the team seems to address this lack of evidence by providing some metallographic measurements. This work is done under an isothermal heating condition, which is different than their previous work, but does not make any difference to the overall approach. Their analysis shows a considerable discrepancy between calculated and observed volume fractions. Their fudge factor is also increased from a single k term to two terms, k^α and k^γ .

The most complete published worked implementing the idea of Onink et al. is done by Lee et al. [149]. In their paper, the Onink way of treating dilatometry data is expanded to include bainite and martensite. A validation by comparing the calculated volume fractions with metallographic measurements is also presented only for the proeutectoid ferrite phase. One of the assumptions they have made is that all types of ferrite, as they put it "pro-eutectoid ferrite, pearlitic ferrite and bainitic ferrite", are assumed to have dissolved no carbon. This assumption does not create a major error for the ferrite phase that transforms above the lower bainite start

temperature as the solubility limit of carbon in ferrite under both equilibrium and paraequilibrium is low. However, as mentioned in Section 2.3.2, lower bainite can be partially supersaturated with carbon. This limits the applicability of Lee's method to transformations occurring above the lower bainite start temperature.

In their numerical solution, Lee et al. explain that they isolated the portion of overall strain that is caused by transformation by calculating the "the difference between the dilatational curve and the extrapolated line of thermal contraction of austenite". This treatment has two issues. The first issue, which happens to be the major flaw in their method, stems from the seemingly wrong consideration of the source of volume change during non-isothermal transformation. The observed dilatation within a time step has four sources which are: I) phase change, II) thermal contraction of austenite, III) thermal contraction of the previously formed products and IV) lattice expansion of austenite due to carbon enrichment. Lee et al. mention that only the first two sources are considered. If this oversight has really happened in their analysis, their calculations of PF volume fraction compared with metallographic measurement may be questionable.

The second and less critical issue with Lee et al.'s isolation of transformation strain is that rejection of carbon to austenite changes the coefficient of thermal expansion of austenite. As a result, austenite's thermal contraction is dependent on the amount of ferrite that formed during the time step. This makes Equation 15 in their paper a non-linear equation in which the properties of austenite would be needed to calculate the amount of product formed, but the amount of the product formed determines the properties of austenite. This issue's adverse effect can be minimized by reduction of the time step. Unfortunately Lee et al. do not provide an analysis about the effect of time step on the accuracy of their calculation. As explained in Eq. 4-11 in the UCD algorithm, austenite contraction during a time step is estimated by considering a mean carbon content which is calculated considering the carbon enrichment during the time step. The UCD algorithm and the Master Fitter program are designed to be tolerant to any kind of non-linearity.

4.7 Summary

Using the lever rule to analyze dilatometry data for diffusive phase transformations can give rise to errors that could be prevented by considering the effect of redistribution of the alloying elements on the unit cell volume of the phases. This approach, originally established by Onink et al., is further developed in this study by introducing the concept of continuous sequential transformation, which assumes that the product phase is always changing. Also, multiple phase transformations are modeled in a new way, which considers the transformation as a cooperative but independent development of two microconstituents, i.e., ferrite derivative (FD) and cementite. Each of these microconstituents form under their own thermodynamic constraints. This

allows for efficient modeling of pearlite, bainitic ferrite, upper bainite, lower bainite and martensite using just one model.

All the new adjustments were implemented in an algorithm called unit cell dilation (UCD) which is used for creating two computer codes called the Fitter and the Master Fitter. The accuracy of the two programs was verified by comparing the results of two sets of dilatometry experiments with metallographic measurements of phase content.

Chapter 5 Conclusions and recommendations for future work

5.1 Conclusions

Large thickness and high strength are attractive qualities for microalloyed steel plates used for pipe manufacturing. However, achieving both at the same time is not an easy task. Increasing thickness creates thermal gradients through the thickness of the plate during cooling on the runout table. Since the phase transformation of steel that occurs during this cooling step is affected by the cooling rate, a microstructural gradient is created through the thickness. This microstructural gradient results in non-uniform mechanical properties in the plate. At the surface layer where the cooling rate is the highest, the steel transforms to higher strength products while at the center of the plate where the cooling rate is the lowest softer phases form. To meet the requirements for pipeline steels, it is necessary to understand the products of phase transformation and their mechanical properties as the cooling cycle changes.

Microalloyed steels produce a variety of microstructures depending on their chemical composition, thermomechanical processing prior to transformation and cooling cycle after rolling. These microstructures often consist of multiple microconstituents. The microstructures that form under linear cooling were studied in this research. It was shown that the hardness of the microstructures obtained for microalloyed steel can be modeled as a two component mixture in which the components are polygonal/quasi polygonal ferrite and mixed bainitic ferrite, M/A and B/M. This finding makes it possible to estimate the hardness of a microalloyed steel by knowing only three variables – volume fraction of polygonal or quasi polygonal ferrite, its hardness and hardness of the B/M-M/A–bainitic ferrite mixture.

In this thesis, it was also shown that not considering the effect of carbon redistribution in diffusive transformations of austenite to ferrite can result in inaccurate calculations for transformation kinetics using dilatometry data. Most of the research work that involves determination of phase transformation kinetics relies on the so called lever rule to calculate the fraction of transformation. In this research, it was shown that lever rule is inadequate at best or incapable at times of determining the correct phase fraction during transformation when compared with metallographic results. Additionally, it was shown that in sequential phase transformation it is not possible to reliably determine the time and temperature at which phase transformation product changes. To solve these issues, the unit cell dilation (UCD) algorithm was proposed that can calculate phase fraction in sequential and multiple phase transformations. The UCD algorithm uses diffusive and displacive phase transformation models coupled with crystallographic and thermo-physical properties of the phases to calculate the fraction of transformation during a phase transformation with an arbitrary cooling cycle. The UCD algorithm

can account for the enrichment of austenite with carbon during diffusive formation of ferrite. The UCD algorithm can detect the formation of polygonal/quasi polygonal ferrite, bainitic ferrite, conventional bainite, martensite and pearlite in a single cooling cycle. The results of the UCD algorithm were confirmed by quantitative metallography measurements for two microalloyed steels.

The UCD algorithm relies on the accuracy of the above mentioned parameters. As these parameters are only known approximately, an optimization program called the “Master Fitter” was also created to fine tune the inaccurate parameters to find the best combination of the parameters that would result in a correct phase fraction calculation. The Master Fitter program accomplishes this by analyzing a pool of dilatometry data obtained for the same alloy at different cooling conditions. The Master Fitter program allows the UCD algorithm to not only be used to calculate phase fractions during dilatometry tests but also be used to indirectly calculate the thermo-physical properties of the phases.

5.2 Recommendations for future work

The UCD algorithm and the optimization program implementing the Master Fitter program were tested only for microalloyed steels. However, theoretically, the program is able to analyze the dilatometry results of any hypoeutectoid steel. Further experimentation with low and medium carbon steels is needed to confirm the accuracy of the results for higher carbon steels. Master Fitter uses solubility limit equations derived for solubility of carbon in ferrite and austenite. In this thesis, these solubility limits were calculated separately using the Thermo-Calc software. Integration between Master Fitter and CALPHAD software such as Thermo-Calc is recommended to improve the usability of the Master Fitter program. Integration with OpenCalphad can ensure that users can use this software free of charge as is intended.

The accuracy of calculations done by the Master Fitter program can be severely diminished when thermal gradient through the thickness of the test specimen increases. This occurs at high cooling rates or large specimen thickness. The addition of a heat transfer module can allow the Mater Fitter to correct for the effect of thermal gradients. This module is especially necessary for analysis of isothermal transformation experiments. In isothermal transformation experiments, due to the incorporation of a quenching step to reduce the temperature to the desired transformation temperature, a considerable thermal gradient immediately after quenching is inevitable.

The implementation of multiple phase transformation can be improved. In the current version of the Master Fitter, equilibrium cementite content is allowed to form in the untransformed austenite. This is similar to the

approach taken by Lee et al. [149]. This assumption is not natural to the transformation of pearlite and bainite. In the real transformation, super saturation occurs in the vicinity of the newly formed ferrite. For example, in pearlite the cementite that precipitate receives carbon only from the pearlitic ferrite and not from all of the austenite grain. This means farther away from the pearlite front can be supersaturated with carbon with respect to cementite. This is important adjustment especially in continuous cooling conditions because without this supersaturation, carbon content of remaining austenite will be limited to carbon solubility limit of austenite which quickly drops with reducing temperature. Observation of high carbon retained austenite well above solubility limit of austenite is an evidence supporting that austenite should be allowed to supersaturates beyond its solubility limit with respect to cementite. The Master Fitter program considers the austenite to product transformation to be the final metallurgical phenomenon, which is not the case for lower bainite and martensite. Tempering of these phases can occur during coiling or subsequent heating. The effect of these metallurgical phenomena can be considered in the Master Fitter program.

The knowledge generated in this research is a stepping stone towards creating a phase transformation model for microalloyed steels. This model will be able to predict the microstructure based on the cooling cycle. The results of this phase transformation model can be used as input parameters to a mechanical properties model correlating microstructure to mechanical properties. Once the two models are ready to use, it would be possible to estimate the mechanical properties of the steel through the thickness of the plate by just using the production line's thermomechanical variables as input parameters. This will allow the use of optimization routines to find the best production parameters that can produce the required steel properties regardless of how complex the cooling cycle is.

References

- [1] A.P. Institute, API 5L Specification for line pipe, 2004. doi:10.1520/G0154-12A.
- [2] T. Gladman, The Physical Metallurgy of Microalloyed Steels, The institute of materials, 2002. <http://books.google.co.in/books?id=1CpCPgAACAAJ>.
- [3] M. Witek, Possibilities of using X80, X100, X120 high-strength steels for onshore gas transmission pipelines, *J. Nat. Gas Sci. Eng.* 27 (2015) 374–384. doi:10.1016/j.jngse.2015.08.074.
- [4] J.M. Gray, Testimony of Dr . J . Malcolm Gray President , Microalloyed Steel Institute; Certain Hot-Rolled Steel Flat Products from Australia, Brazil, Japan, Korea, the Netherlands, Turkey, and the United Kingdom, Sep (2015). https://www.usitc.gov/press_room/documents/testimony/701_545_004.pdf.
- [5] A.K. Das, The Present and the Future of Line Pipe Steels for Petroleum Industry, *Mater. Manuf. Process.* 25 (2010) 14–19. doi:10.1080/10426910903202427.
- [6] J.M. Gray, An Independent view of Linepipe and Linepipe Steel for High Strength Pipelines: How To Get Pipe That's Right for the Job at the Right Price, API X80-Pipeline Cost Work. (2002) 1–19. http://www.engmarcoantonio.com.br/cariboost_files/A_C3_A7os_estruturais.pdf.
- [7] T.N. Baker, Microalloyed steels, *Ironmak. Steelmak.* 43 (2016) 264–307. doi:10.1179/1743281215Y.0000000063.
- [8] S. Hashimoto, M. Nakamura, Effects of microalloying elements on mechanical properties of reinforcing bars, *ISIJ Int.* 46 (2006) 1510–1515. doi:10.2355/isijinternational.46.1510.
- [9] R.E. Reed-Hill, L. Abbaschian, R. Abbaschian, *Physical Metallurgy Principles*, 4th ed., Thomson-Engineering, 2009.
- [10] M. Charleux, W.J. Poole, M. Militzer, A. Deschamps, Precipitation behavior and its effect on strengthening of an HSLA-Nb/Ti steel, *Metall. Mater. Trans. A Phys. Metall. Mater. Sci.* 32 (2001) 1635–1647. doi:10.1007/s11661-001-0142-6.
- [11] S.H. Park, S. Yue, J.J. Jonas, Continuous-cooling-precipitation kinetics of Nb(CN) in high-strength low-alloy steels, *Metall. Trans. A.* 23 (1992) 1641–1651. doi:10.1007/BF02804360.
- [12] T. NIU, Y. KANG, H. GU, Y. YIN, M. QIAO, Precipitation Behavior and Its Strengthening Effect of X100

Pipeline Steel, *J. Iron Steel Res. Int.* 17 (2010) 73–78. doi:10.1016/S1006-706X(10)60173-2.

- [13] J. Zhao, W. Hu, X. Wang, J. Kang, Y. Cao, G. Yuan, H. Di, R.D.K. Misra, A Novel thermo-mechanical controlled processing for large-thickness microalloyed 560MPa (X80) pipeline strip under ultra-fast cooling, *Mater. Sci. Eng. A.* 673 (2016) 373–377. doi:10.1016/j.msea.2016.07.089.
- [14] W.B. Lee, S.G. Hong, C.G. Park, K.H. Kim, S.H. Park, Influence of Mo on precipitation hardening in hot rolled HSLA steels containing Nb, *Scr. Mater.* 43 (2000) 319–324. doi:10.1016/S1359-6462(00)00411-5.
- [15] S.K. Ghosh, A. Haldar, P.P. Chattopadhyay, The influence of copper addition on microstructure and mechanical properties of thermomechanically processed microalloyed steels, *J. Mater. Sci.* 44 (2009) 580–590. doi:10.1007/s10853-008-3051-x.
- [16] S.K. Ghosh, P.S. Bandyopadhyay, S. Kundu, S. Chatterjee, Copper bearing microalloyed ultrahigh strength steel on a pilot scale: Microstructure and properties, *Mater. Sci. Eng. A.* 528 (2011) 7887–7894. doi:10.1016/j.msea.2011.06.085.
- [17] S.K. Ghosh, A. Haldar, P.P. Chattopadhyay, Effect of ageing on the mechanical properties of directly quenched copper bearing microalloyed steels, *Mater. Chem. Phys.* 119 (2010) 436–441. doi:10.1016/j.matchemphys.2009.09.020.
- [18] W.H. Zhou, V.S.A. Challa, H. Guo, C.J. Shang, R.D.K. Misra, Structure-mechanical property relationship in a low carbon Nb-Cu microalloyed steel processed through a three-step heat treatment: The effect of tempering process, *Mater. Sci. Eng. A.* 620 (2014) 454–562. doi:10.1016/j.msea.2014.09.079.
- [19] S. Cheng, X. Zhang, J. Zhang, Y. Feng, J. Ma, H. Gao, Effect of coiling temperature on microstructure and properties of X100 pipeline steel, *Mater. Sci. Eng. A.* 666 (2016) 156–164. doi:10.1016/j.msea.2016.04.066.
- [20] B.C.C. De Cooman, Structure-properties relationship in TRIP steels containing carbide-free bainite, *Curr. Opin. Solid State Mater. Sci.* 8 (2004) 285–303. doi:10.1016/j.cossms.2004.10.002.
- [21] J. Lu, O. Omotoso, J.B. Wiskel, D.G. Ivey, H. Henein, Strengthening Mechanisms and Their Relative Contributions to the Yield Strength of Microalloyed Steels, *Metall. Mater. Trans. A.* 43 (2012) 3043–3061. doi:10.1007/s11661-012-1135-3.
- [22] D.A. Porter, K.E. Easterling, M. Sherif, *Phase Transformations in Metals and Alloys*, 3rd ed., Taylor & Francis, 2009.

- [23] A. Karmakar, S. Biswas, S. Mukherjee, D. Chakrabarti, V. Kumar, Effect of composition and thermo-mechanical processing schedule on the microstructure, precipitation and strengthening of Nb-microalloyed steel, *Mater. Sci. Eng. A.* 690 (2017) 158–169. doi:10.1016/j.msea.2017.02.101.
- [24] Y. Bae, J. Lee, J. Choi, W. Choo, S. Hong, Effects of austenite conditioning on austenite/ferrite phase transformation of HSLA steel, *Mater. Trans.* 45 (2004) 137–142. doi:10.2320/matertrans.45.137.
- [25] T. Furuhashi, K. Kikumoto, H. Saito, T. Sekine, T. Ogawa, S. Morito, T. Maki, Phase Transformation from Fine-grained Austenite, *ISIJ Int.* 48 (2008) 1038–1045. doi:10.2355/isijinternational.48.1038.
- [26] V.B. Ginzburg, *Steel- Rolling Technology Theory and Practice*, Marcel Dekker Inc., 1989.
- [27] B. Dutta, C.M. Sellars, Effect of composition and process variables on Nb (C , N) precipitation in niobium microalloyed austenite, 3 (1987) 197–206.
- [28] B. Dutta, E.J. Palmiere, C.M. Sellars, Modelling the kinetics of strain induced precipitation in Nb microalloyed steels, *Acta Mater.* 49 (2001) 785–794. doi:10.1016/S1359-6454(00)00389-X.
- [29] Z. Wang, X. Sun, Z. Yang, Q. Yong, C. Zhang, Z. Li, Y. Weng, Effect of Mn concentration on the kinetics of strain induced precipitation in Ti microalloyed steels, *Mater. Sci. Eng. A.* 561 (2013) 212–219. doi:10.1016/j.msea.2012.10.085.
- [30] K.J. Lee, Recrystallization and precipitation interaction in Nb-containing steels, *Scr. Mater.* 40 (1999) 837–843. doi:10.1016/S1359-6462(99)00026-3.
- [31] Y. Cao, F. Xiao, G. Qiao, C. Huang, X. Zhang, Z. Wu, B. Liao, Strain-induced precipitation and softening behaviors of high Nb microalloyed steels, *Mater. Sci. Eng. A.* 552 (2012) 502–513. doi:10.1016/j.msea.2012.05.078.
- [32] D. Liu, F. Fazeli, M. Militzer, Modeling of Microstructure Evolution during Hot Strip Rolling of Dual Phase Steels, *ISIJ Int.* 47 (2007) 1789–1798. doi:10.2355/isijinternational.47.1789.
- [33] A.A. Gorni, *Steel Forming and Heat Treating Handbook*, 2017. www.gorni.eng.br/e/Gorni_SFHTHandbook.pdf.
- [34] C.R. Clayton, *Materials Science and Engineering: An Introduction*, 1987. doi:10.1016/0025-5416(87)90343-0.
- [35] H.K.D.H. Bhadeshia, Diffusional formation of ferrite in iron and its alloys, *Prog. Mater. Sci.* 29 (1985) 321–

386. https://ac.els-cdn.com/0079642585900040/1-s2.0-0079642585900040-main.pdf?_tid=spdf-44a63a72-5cfb-4b8d-9044-87410ec391b4&acdnat=1519824134_cf0122a4536bf536c61bcc1f877a1a06.
- [36] H.K.D.H. Bhadeshia, *Bainite in Steels Transformation, Microstructure and Properties*, 2nd ed., IOM Communications Ltd, 2001.
- [37] M. Hillert, A. Borgenstam, J. Ågren, Do bainitic and Widmanstätten ferrite grow with different mechanisms?, *Scr. Mater.* 62 (2010) 75–77. doi:10.1016/j.scriptamat.2009.09.033.
- [38] G. Kostorz, *Phase Transformations in Materials*, Wiley-VCH, 2001.
- [39] H.K.D.H. Bhadeshia, D.V. Edmonds, The mechanism of bainite formation in steels, *Acta Metall.* 28 (1980) 1265–1273. doi:10.1016/0001-6160(80)90082-6.
- [40] M. Hillert, L. Höglund, J. Ågren, Role of carbon and alloying elements in the formation of bainitic ferrite, *Metall. Mater. Trans. A Phys. Metall. Mater. Sci.* 35 A (2004) 3693–3700. doi:10.1007/s11661-004-0275-5.
- [41] H.I. Aaronson, W.T. Reynolds, G.R. Purdy, The Incomplete Transformation Phenomenon in Steel, 37 (2006) 1731–1745.
- [42] F.G. Caballero, M.K. Miller, C. Garcia-Mateo, Carbon supersaturation of ferrite in a nanocrystalline bainitic steel, *Acta Mater.* 58 (2010) 2338–2343. doi:10.1016/j.actamat.2009.12.020.
- [43] T. Furuhashi, K. Tsuzumi, G. Miyamoto, T. Amino, G. Shigesato, Characterization of Transformation Stasis in Low-Carbon Steels Microalloyed with B and Mo, *Metall. Mater. Trans. A Phys. Metall. Mater. Sci.* 45 (2014) 5990–5996. doi:10.1007/s11661-014-2584-7.
- [44] Z.-Q. Liu, G. Miyamoto, Z.-G. Yang, T. Furuhashi, Direct measurement of carbon enrichment during austenite to ferrite transformation in hypoeutectoid Fe–2Mn–C alloys, *Acta Mater.* 61 (2013) 3120–3129. doi:10.1016/j.actamat.2013.02.003.
- [45] F.G. Caballero, C. Garcia-Mateo, M.J. Santofimia, M.K. Miller, C. García de Andrés, New experimental evidence on the incomplete transformation phenomenon in steel, *Acta Mater.* 57 (2009) 8–17. doi:10.1016/j.actamat.2008.08.041.
- [46] C. Garcia-Mateo, J.A. Jimenez, H.-W. Yen, M.K. Miller, L. Morales-Rivas, M. Kuntz, S.P. Ringer, J.-R. Yang, F.G. Caballero, Low temperature bainitic ferrite: Evidence of carbon super-saturation and tetragonality, *Acta Mater.* 91 (2015) 162–173. doi:10.1016/j.actamat.2015.03.018.

- [47] M. Gouné, F. Danoix, J. Ågren, Y. Bréchet, C.R. Hutchinson, M. Militzer, G. Purdy, S. van der Zwaag, H. Zurob, Overview of the current issues in austenite to ferrite transformation and the role of migrating interfaces therein for low alloyed steels, *Mater. Sci. Eng. R Reports*. 92 (2015) 1–38. doi:10.1016/j.mser.2015.03.001.
- [48] C. Capdevila, J. Cornide, K. Tanaka, K. Nakanishi, E. Urones-Garrote, Kinetic transition during ferrite growth in Fe-C-Mn medium carbon steel, *Metall. Mater. Trans. A Phys. Metall. Mater. Sci.* 42 (2011) 3719–3728. doi:10.1007/s11661-011-0650-y.
- [49] D.R. Gaskell, *Introduction to Thermodynamics of Materials*, Fourth Ed., Taylor & Frances, 2003.
- [50] G. Krauss, S.W. Thompson, Ferritic Microstructures in Continuously Cooled Low- and Ultralow-carbon Steels., *ISIJ Int.* 35 (1995) 937–945. doi:10.2355/isijinternational.35.937.
- [51] P. Suikkanen, *Development and processing of low carbon bainitic steels*, 2009.
- [52] R. Anumolu, B.R. Kumar, R.D.K. Misra, T. Mannering, D. Panda, S.G. Jansto, On the determining role of microstructure of niobium-microalloyed steels with differences in impact toughness, *Mater. Sci. Eng. A*. 491 (2008) 55–61. doi:10.1016/j.msea.2008.01.008.
- [53] S. Zajac, V. Schwinn, K.H. Tacke, Characterisation and Quantification of Complex Bainitic Microstructures in High and Ultra-High Strength Linepipe Steels, *Mater. Sci. Forum*. 500–501 (2005) 387–394. doi:10.4028/www.scientific.net/MSF.500-501.387.
- [54] K. Radwański, Structural characterization of low-carbon multiphase steels merging advanced research methods with light optical microscopy, *Arch. Civ. Mech. Eng.* 16 (2016) 282–293. doi:10.1016/j.acme.2015.12.001.
- [55] J.Y. Koo, M.J. Luton, N. V. Bangaru, R.A. Petkovic, D.P. Fairchild, C.W. Petersen, H. Asahi, T. Hara, Y. Terada, M. Sugiyama, H. Tamehiro, Y. Komizo, S. Okaguchi, M. Hamada, A. Yamamoto, I. Takeuchi, Metallurgical design of ultra high-strength steels for gas pipelines, *Int. J. Offshore Polar Eng.* 14 (2004) 2–10.
- [56] Y.Q. Zhang, H.Q. Zhang, W.M. Liu, H. Hou, Effects of Nb on microstructure and continuous cooling transformation of coarse grain heat-affected zone in 610 MPa class high-strength low-alloy structural steels, *Mater. Sci. Eng. A*. 499 (2009) 182–186. doi:10.1016/j.msea.2007.10.118.
- [57] Z.J. Xie, Y.P. Fang, G. Han, H. Guo, R.D.K. Misra, C.J. Shang, Structure–property relationship in a 960MPa grade ultrahigh strength low carbon niobium–vanadium microalloyed steel: The significance of high

- frequency induction tempering, *Mater. Sci. Eng. A.* 618 (2014) 112–117. doi:10.1016/j.msea.2014.08.072.
- [58] I. a. Yakubtsov, P. Poruks, J.D. Boyd, Microstructure and mechanical properties of bainitic low carbon high strength plate steels, *Mater. Sci. Eng. A.* 480 (2008) 109–116. doi:10.1016/j.msea.2007.06.069.
- [59] M. Fattahi, N. Nabhani, M. Hosseini, N. Arabian, E. Rahimi, Effect of Ti-containing inclusions on the nucleation of acicular ferrite and mechanical properties of multipass weld metals, *Micron.* 45 (2013) 107–114. doi:10.1016/j.micron.2012.11.004.
- [60] J. YANG, Q. LIU, D. SUN, X. LI, Microstructure and Transformation Characteristics of Acicular Ferrite in High Niobium-Bearing Microalloyed Steel, *J. Iron Steel Res. Int.* 17 (2010) 53–59. doi:10.1016/S1006-706X(10)60114-8.
- [61] J. Speer, D.K. Matlock, B.C. De Cooman, J.G. Schroth, Carbon partitioning into austenite after martensite transformation, *Acta Mater.* 51 (2003) 2611–2622. doi:10.1016/S1359-6454(03)00059-4.
- [62] A. Kammouni, W. Saikaly, M. Dumont, C. Marteau, X. Bano, A. Charai, Effect of the bainitic transformation temperature on retained austenite fraction and stability in Ti microalloyed TRIP steels, *Mater. Sci. Eng. A.* 518 (2009) 89–96. doi:10.1016/j.msea.2009.05.015.
- [63] J.-Y. Kang, D.H. Kim, S.-I. Baik, T.-H. Ahn, Y.-W. Kim, H.N. Han, K.H. Oh, H.-C. Lee, S.H. Han, Phase Analysis of Steels by Grain-averaged EBSD Functions, *ISIJ Int.* 51 (2011) 130–136. doi:10.2355/isijinternational.51.130.
- [64] J. Wu, P.. Wray, C.. Garcia, M. Hua, A.. Deardo, Image quality analysis: A new method of characterizing microstructures, *ISIJ Int.* 45 (2005) 254–262. doi:10.2355/isijinternational.45.254.
- [65] A.J. DeArdo, C.I. Garcia, K. Cho, M. Hua, New method of characterizing and quantifying complex microstructures in steels, *Mater. Manuf. Process.* 25 (2010) 33–40. doi:10.1080/10426910903143415.
- [66] E.P. Kwon, S. Fujieda, K. Shinoda, S. Suzuki, Characterization of transformed and deformed microstructures in transformation induced plasticity steels using electron backscattering diffraction, *Mater. Sci. Eng. A.* 528 (2011) 5007–5017. doi:10.1016/j.msea.2011.03.033.
- [67] S.L. Shrestha, A.J. Breen, P. Trimby, G. Proust, S.P. Ringer, J.M. Cairney, An automated method of quantifying ferrite microstructures using electron backscatter diffraction (EBSD) data, *Ultramicroscopy.* 137 (2014) 40–47. doi:10.1016/j.ultramic.2013.11.003.
- [68] H. Zhao, B.P. Wynne, E.J. Palmiere, A phase quantification method based on EBSD data for a continuously

- cooled microalloyed steel, *Mater. Charact.* 123 (2017) 339–348. doi:10.1016/j.matchar.2016.11.024.
- [69] H.J. Frost, M.F. Ashbey, *Deformation-Mechanism Maps: The Plasticity and Creep of Metals and Ceramics*, 1st ed., Pergamon press, 1982. <http://engineering.dartmouth.edu/defmech/>.
- [70] U.F. Kocks, H. Mecking, Physics and phenomenology of strain hardening: the FCC case, *Prog. Mater. Sci.* 48 (2003) 171–273. doi:10.1016/S0079-6425(02)00003-8.
- [71] D. Hull, D.J. Bacon, *Introduction to Dislocations*, 4th ed., Butterworth-Heinemann, 2011.
- [72] A.J. DeArdo, M.J. Hua, K.G. Cho, C.I. Garcia, On strength of microalloyed steels: an interpretive review, *Mater. Sci. Technol.* 25 (2009) 1074–1082. doi:10.1179/174328409X455233.
- [73] V. Raghavan, *Physical Metallurgy - Principles and Practice*, 2nd ed., PHI Learning Pvt. Ltd., 2006.
- [74] D. Chandrasekaran, *Grain Size and Solid Solution Strengthening in Metals*, Royal Institute of Technology, 2003. doi:urn:nbn:se:kth:diva-3641.
- [75] L. Vitos, *Computational Quantum Mechanics for Materials Engineers: The EMTO Method and Application*, Springer, 2007.
- [76] D. Ma, M. Friák, J. Von Pezold, D. Raabe, J. Neugebauer, Computationally efficient and quantitatively accurate multiscale simulation of solid-solution strengthening by ab initio calculation, *Acta Mater.* 85 (2015) 53–66. doi:10.1016/j.actamat.2014.10.044.
- [77] R.W. Cahn, P. Haasen, *Physical Metallurgy Volume 3*, North-Holland, 1996.
- [78] R.L. Fleischer, Substitutional solution hardening, *Acta Metall.* 11 (1963) 203–209.
- [79] H. Sieurin, J. Zander, R. Sandström, Modelling solid solution hardening in stainless steels, *Mater. Sci. Eng. A.* 415 (2006) 66–71. doi:10.1016/j.msea.2005.09.031.
- [80] H. Zhang, B. Johansson, R. Ahuja, L. Vitos, First-principles study of solid-solution hardening in steel alloys, *Comput. Mater. Sci.* 55 (2012) 269–272. doi:10.1016/j.commatsci.2011.12.020.
- [81] Q. Lu, W. Xu, S. Van Der Zwaag, The design of a compositionally robust martensitic creep-resistant steel with an optimized combination of precipitation hardening and solid-solution strengthening for high-temperature use, *Acta Mater.* 77 (2014) 310–323. doi:10.1016/j.actamat.2014.06.007.
- [82] D. Chandrasekaran, Solid solution hardening - A comparison of two models, *Mater. Sci. Eng. A.* 309–310

(2001) 184–189. doi:10.1016/S0921-5093(00)01721-4.

- [83] J. Lu, Quantitative Microstructural Characterization of Microalloyed Steels, University of Alberta, 2009.
- [84] L. Xiao, Z. Fan, Z. Jinxiu, Z. Mingxing, Lattice-parameter variation with carbon content of martensite. I. X-ray-diffraction experimental study, *Phys. Rev. B.* 52 (1995) 9970–9978. <http://journals.aps.org/prb/abstract/10.1103/PhysRevB.52.9970> (accessed September 30, 2014).
- [85] B. Hutchinson, J. Hagström, O. Karlsson, D. Lindell, M. Tornberg, F. Lindberg, M. Thuvander, Microstructures and hardness of as-quenched martensites (0.1–0.5%C), *Acta Mater.* 59 (2011) 5845–5858. doi:10.1016/j.actamat.2011.05.061.
- [86] E.J. Pavlina, C.J. Tyne, Correlation of Yield Strength and Tensile Strength with Hardness for Steels, *J. Mater. Eng. Perform.* 17 (2008) 888–893. doi:10.1007/s11665-008-9225-5.
- [87] G. Krauss, Martensite in steel: strength and structure, *Mater. Sci. Eng. A.* 273–275 (1999) 40–57. doi:10.1016/S0921-5093(99)00288-9.
- [88] W. Guo, Z. Wang, Y. Li, N. Xu, J. Shi, Effect of Phosphorus Content on Properties of Warm-Rolled Interstitial-Free Steel Sheets, *Metallogr. Microstruct. Anal.* 2 (2013) 249–256. doi:10.1007/s13632-013-0086-4.
- [89] R.E. Smallman, R.J. Bishop, Ceramics and Glasses, in: *Mod. Phys. Metall. Mater. Eng.*, 6th ed., Elsevier, 1999: pp. 320–350. doi:10.1016/B978-075064564-5/50010-0.
- [90] P. Rocabois, J. Lehmann, H. Gaye, M. Wintz, Kinetics of precipitation of non-metallic inclusions during solidification of steel, *J. Cryst. Growth.* 198–199 (1999) 838–843. doi:10.1016/S0022-0248(98)01139-7.
- [91] W. Yan, Y.-Y. Shan, K. Yang, Y.-P. Ma, G.-Y. Su, Effect of TiN inclusions on impact toughness of low carbon microalloyed steels, *Met. Mater. Trans. A.* 37A (2006) 2147–2158.
- [92] F. Perrard, A. Deschamps, F. Bley, P. Donnadiou, P. Maugis, A small-angle neutron scattering study of fine-scale NbC precipitation kinetics in the α -Fe – Nb – C system research papers, *J. Appl. Crystallogr.* 39 (2006) 473–483. doi:10.1107/S002188980601301X.
- [93] N. Kamikawa, K. Sato, G. Miyamoto, M. Murayama, N. Sekido, K. Tsuzaki, T. Furuhashi, Stress-strain behavior of ferrite and bainite with nano-precipitation in low carbon steels, *Acta Mater.* 83 (2015) 383–396. doi:10.1016/j.actamat.2014.10.010.

- [94] C.Y. Chen, H.W. Yen, F.H. Kao, W.C. Li, C.Y. Huang, J.R. Yang, S.H. Wang, Precipitation hardening of high-strength low-alloy steels by nanometer-sized carbides, *Mater. Sci. Eng. A.* 499 (2009) 162–166. doi:10.1016/j.msea.2007.11.110.
- [95] C.Y. Chen, C.C. Chen, J.R. Yang, Microstructure characterization of nanometer carbides heterogeneous precipitation in Ti-Nb and Ti-Nb-Mo steel, *Mater. Charact.* 88 (2014) 69–79. doi:10.1016/j.matchar.2013.11.016.
- [96] F. Perrard, A. Deschamps, P. Maugis, Modelling the precipitation of NbC on dislocations in α -Fe, *Acta Mater.* 55 (2007) 1255–1266. doi:10.1016/j.actamat.2006.10.003.
- [97] Z. Peng, L. Li, S. Chen, X. Huo, J. Gao, Isothermal precipitation kinetics of carbides in undercooled austenite and ferrite of a titanium microalloyed steel, *Mater. Des.* 108 (2016) 289–297. doi:10.1016/j.matdes.2016.06.108.
- [98] S. Mukherjee, I. Timokhina, C. Zhu, S.P. Ringer, P.D. Hodgson, Clustering and precipitation processes in a ferritic titanium-molybdenum microalloyed steel, *J. Alloys Compd.* 690 (2017) 621–632. doi:10.1016/j.jallcom.2016.08.146.
- [99] I. Timokhina, M.K. Miller, J. Wang, H. Beladi, P. Cizek, P.D. Hodgson, On the Ti-Mo-Fe-C atomic clustering during interphase precipitation in the Ti-Mo steel studied by advanced microscopic techniques, *Mater. Des.* 111 (2016) 222–229. doi:https://doi.org/10.1016/j.matdes.2016.08.086.
- [100] Y.Q. Wang, S.J. Clark, V. Janik, R.K. Heenan, D.A. Venero, K. Yan, D.G. McCartney, S. Sridhar, P.D. Lee, *Acta Materialia* Investigating nano-precipitation in a V-containing HSLA steel using small angle neutron scattering, *Acta Mater.* 145 (2018) 84–96. doi:10.1016/j.actamat.2017.11.032.
- [101] Y.J. Zhang, G. Miyamoto, K. Shinbo, T. Furuhashi, Quantitative measurements of phase equilibria at migrating α/γ interface and dispersion of VC interphase precipitates: Evaluation of driving force for interphase precipitation, *Acta Mater.* 128 (2017) 166–175. doi:10.1016/j.actamat.2017.02.020.
- [102] R. Okamoto, A. Borgenstam, J. Ågren, Interphase precipitation in niobium-microalloyed steels, *Acta Mater.* 58 (2010) 4783–4790. doi:10.1016/j.actamat.2010.05.014.
- [103] E. Nes, B. Holmedal, E. Evangelista, K. Marthinsen, Modelling grain boundary strengthening in ultra-fine grained aluminum alloys, *Mater. Sci. Eng. A.* 410–411 (2005) 178–182. doi:10.1016/j.msea.2005.08.121.
- [104] Specification for Line Pipe, in: ANSI/API Specif. 5L, 44th ed., 2007.

- [105] A.J. Deardo, Metallurgical basis for thermomechanical processing of microalloyed steels, *Lronmaking Steelmak.* 28 (2001) 138–144.
- [106] S.Y. Shin, B. Hwang, S. Lee, N.J. Kim, S.S. Ahn, Correlation of microstructure and charpy impact properties in API X70 and X80 line-pipe steels, *Mater. Sci. Eng. A.* 458 (2007) 281–289. doi:10.1016/j.msea.2006.12.097.
- [107] H. Kimura, Mechanical properties of high purity iron and its dilute alloys, *Mater. Trans. JIM(Japan)*. 40 (1999) 1025–1031.
- [108] M.Y. Liu, B. Shi, C. Wang, S.K. Ji, X. Cai, H.W. Song, Normal Hall-Petch behavior of mild steel with submicron grains, *Mater. Lett.* 57 (2003) 2798–2802. doi:10.1016/S0167-577X(02)01377-0.
- [109] a. Iza-Mendia, I. Gutiérrez, Generalization of the existing relations between microstructure and yield stress from ferrite–pearlite to high strength steels, *Mater. Sci. Eng. A.* 561 (2013) 40–51. doi:10.1016/j.msea.2012.10.012.
- [110] C. Zhang, Q. Wang, J. Ren, R. Li, M. Wang, F. Zhang, Z. Yan, Effect of microstructure on the strength of 25CrMo48V martensitic steel tempered at different temperature and time, *Mater. Des.* 36 (2012) 220–226. doi:10.1016/j.matdes.2011.11.026.
- [111] D. Qiu, M.X. Zhang, Strengthening mechanisms and their superposition law in an age-hardenable Mg-10 wt pct y alloy, *Metall. Mater. Trans. A Phys. Metall. Mater. Sci.* 43 (2012) 3314–3324. doi:10.1007/s11661-012-1162-0.
- [112] R. Labusch, A Statistical Theory of Solid Solution Hardening, *Phys. Status Solidi.* 41 (1970) 659–669. doi:10.1002/pssb.19700410221.
- [113] S. Queyreau, G. Monnet, B. Devincere, Orowan strengthening and forest hardening superposition examined by dislocation dynamics simulations, *Acta Mater.* 58 (2010) 5586–5595. doi:10.1016/j.actamat.2010.06.028.
- [114] A. de Vaucorbeil, W.J. Poole, C.W. Sinclair, The superposition of strengthening contributions in engineering alloys, *Mater. Sci. Eng. A.* 582 (2013) 147–154. doi:10.1016/j.msea.2013.06.032.
- [115] V. Mohles, Superposition of dispersion strengthening and size-mismatch strengthening: Computer simulations, *Philos. Mag. Lett.* 83 (2003) 9–19. doi:10.1080/0950083021000048730.
- [116] S. Shanmugam, N.K. Ramiseti, R.D.K. Misra, T. Mannering, D. Panda, S. Jansto, Effect of cooling rate on

- the microstructure and mechanical properties of Nb-microalloyed steels, *Mater. Sci. Eng. A.* 460–461 (2007) 335–343. doi:10.1016/j.msea.2007.01.054.
- [117] M. Olasolo, P. Uranga, J.M. Rodriguez-Ibabe, B. López, Effect of austenite microstructure and cooling rate on transformation characteristics in a low carbon Nb–V microalloyed steel, *Mater. Sci. Eng. A.* 528 (2011) 2559–2569. doi:10.1016/j.msea.2010.11.078.
- [118] S. Shanmugam, N.K. Ramiseti, R.D.K. Misra, J. Hartmann, S.G. Jansto, Microstructure and high strength–toughness combination of a new 700MPa Nb-microalloyed pipeline steel, *Mater. Sci. Eng. A.* 478 (2008) 26–37. doi:10.1016/j.msea.2007.06.003.
- [119] E. Pereloma, *Phase transformations in steels*, Woodhead Publishing, 2012.
- [120] H.K.D.H. Bhadeshia, A rationalisation of shear transformations in steels, *Acta Metall.* 29 (1981) 1117–1130. doi:10.1016/0001-6160(81)90063-8.
- [121] B.L. Bramfiti, J.G. Speer, A Perspective on the Morphology of Bainite, *Metall. Trans. A.* 21A (1990) 817–829.
- [122] J. Hu, L.-X. Du, J.-J. Wang, H. Xie, C.-R. Gao, R.D.K. Misra, Structure–mechanical property relationship in low carbon microalloyed steel plate processed using controlled rolling and two-stage continuous cooling, *Mater. Sci. Eng. A.* 585 (2013) 197–204. doi:10.1016/j.msea.2013.07.071.
- [123] S. Tang, Z.Y. Liu, G.D. Wang, R.D.K. Misra, Microstructural evolution and mechanical properties of high strength microalloyed steels: Ultra Fast Cooling (UFC) versus Accelerated Cooling (ACC), *Mater. Sci. Eng. A.* 580 (2013) 257–265. doi:10.1016/j.msea.2013.05.016.
- [124] Z.-G. Yang, H.-S. Fang, An overview on bainite formation in steels, *Curr. Opin. Solid State Mater. Sci.* 9 (2005) 277–286. doi:10.1016/j.cossms.2006.06.005.
- [125] L. Fielding, The Bainite Controversy, *Mater. Sci. Technol.* 29 (2013) 383–399.
- [126] Y. Lee, Empirical formula of isothermal bainite start temperature of steels, *J. Mater. Sci. Lett.* 21 (2002) 1253–1255.
- [127] X.M. Wang, X.L. He, Effect of Boron Addition on Structure and Properties of Low Carbon Bainitic Steels, *ISIJ Int.* 42 (2002) S38–S46. doi:10.2355/isijinternational.42.Suppl_S38.
- [128] ASTM standard - E112 Standard Test Methods for Determining Average Grain Size, ASTM International,

2003.

- [129] B.L. Bramfitt, S.J. Lawrence, *Metallography and Microstructures of Carbon and Low-Alloy Steels*, *Metallography and Microstructures*, in: Vol 9, ASM Handb., ASM International, 2004: pp. 608–626.
- [130] ASTM standard E562 - Standard Test Method for Determining Volume Fraction by Systematic Manual Point Count, ASTM International, 2003.
- [131] ASTM standard E384 - Standard Test Method for Knoop and Vickers Hardness of Materials, 2003.
- [132] K. Jonsson, *Modification of the Stress-Strain Curve for High-Strength Line Pipe Steel*, University of Alberta, 2013. <https://era.library.ualberta.ca/public/view/item/uuid:7287b2cf-0b84-4168-838e-ff9edb3d5405/>.
- [133] L. Good, CCT Diagram Development, Grade 100XF, ASTM A656 Grade 80, & API 5CT Grade J55, EVRAZ Inc. NA, Intern. Rep. (2010).
- [134] S.W. Thompson, D.J. Colvin, G. Krauss, Continuous Cooling Transformations and Microstructures in a Low-Carbon, High-Strength Low-Alloy Plate Steel, *Metall. Trans. A*. 21A (1990) 1493–1507.
- [135] N. Takayama, G. Miyamoto, T. Furuhashi, Effects of transformation temperature on variant pairing of bainitic ferrite in low carbon steel, *Acta Mater.* 60 (2012) 2387–2396. doi:10.1016/j.actamat.2011.12.018.
- [136] H.I. Aaronson, C. Wells, Sympathetic Nucleation of Ferrite, *JOM*. 8 (1956) 1216–1223. doi:10.1007/BF03377853.
- [137] P. Lejček, S. Hofmann, J. Janovec, Prediction of enthalpy and entropy of solute segregation at individual grain boundaries of α -iron and ferrite steels, *Mater. Sci. Eng. A*. 462 (2007) 76–85. doi:10.1016/j.msea.2006.02.463.
- [138] W. Steven, A.G. Haynes, The temperature of formation of martensite and bainite in low-alloy steels, some effects of chemical composition, *J. Iron Steel Inst.* 183 (1956) 349–359.
- [139] T. Kunitake, Y. Okada, The Estimation of Bainite Transformation Temperatures in Steels by the Empirical Formulas, *J. Iron Steel Inst. Japan*. 84 (1998) 137.
- [140] A. Saha, G. Ghosh, G.B. Olson, An assessment of interfacial dissipation effects at reconstructive ferrite–austenite interfaces, *Acta Mater.* 53 (2005) 141–149. doi:10.1016/j.actamat.2004.09.011.
- [141] N. Saunders, A.P. Miodownik, *CALPHAD (Calculation of Phase Diagrams): A Comprehensive Guide*, Pergamon materials series, 1998.

- [142] A. Borgenstam, M. Hillert, J. Ågren, Metallographic evidence of carbon diffusion in the growth of bainite, *Acta Mater.* 57 (2009) 3242–3252. doi:10.1016/j.actamat.2009.03.026.
- [143] Z. Zhao, C. Liu, A new empirical formula for the bainite upper temperature limit of steel, *J. Mater. Sci.* 36 (2001) 5045–5056.
- [144] A.J. Kulkarni, K. Krishnamurthy, S.P. Deshmukh, R.S. Mishra, Effect of particle size distribution on strength of precipitation-hardened alloys, *J. Mater. Res.* 19 (2004) 2765–2773. doi:10.1557/JMR.2004.0364.
- [145] A.C. Larson, R.B. Von Dreele, General Structure Analysis System (GSAS), Los Alamos Natl. Lab. Rep. LAUR. 748 (2004).
- [146] M. Onink, F.D. Tichelaar, C.M. Brakman, E. Mittemeijer, S. van der Zwaag, Quantitative Analysis of the Dilatation by Decomposition of Fe-C Austenites ; Calculation of Volume Change upon Transformation, *Z. Met.* 87 (1996) 24–32.
- [147] T.A. Kop, J. Sietsma, S. Van Der Zwaag, Dilatometric analysis of phase transformations in hypo-eutectoid steels, *J. Mater. Sci.* 36 (2001) 519–526.
- [148] L. Zhao, Quantitative dilatometric analysis of intercritical annealing in a low-silicon TRIP steel, *J. Mater. Sci.* 37 (2002) 1585–1591.
- [149] S.-J. Lee, M.T. Lusk, Y.-K. Lee, Conversional model of transformation strain to phase fraction in low alloy steels, *Acta Mater.* 55 (2007) 875–882. doi:10.1016/j.actamat.2006.09.008.
- [150] M. Jung, S.-J. Lee, Y.-K. Lee, Microstructural and Dilatational Changes during Tempering and Tempering Kinetics in Martensitic Medium-Carbon Steel, *Metall. Mater. Trans. A.* 40 (2009) 551–559. doi:10.1007/s11661-008-9756-2.
- [151] W. Kaplan, *Advanced Calculus*, Redwood City, Calif. : Addison-Wesley, Advanced Book Program, 1991.
- [152] K.W. Andrews, Empirical Formulae for the Calculation of Some Transformation Temperatures, *J. Iron Steel Inst.* 203 (1965) 721–727.
- [153] C. Capdevila, F.G. Caballero, C.G. de Andrés, Determination of martensite-start temperature in steels: Bayesian neural network model, *ISIJ Int.* 42 (2002) 894–902.
- [154] W.G. Vermeulen, P.F. Morris, A.P. de Weijer, S. van der Zwaag, Prediction of martensite start temperature using artificial neural networks, *Ironmak. Steelmak.* 23 (1996) 433–437.

- [155] S.-J. Lee, Y.-K. Lee, Quantitative analyses of ferrite lattice parameter and solute Nb content in low carbon microalloyed steels, *Scr. Mater.* 52 (2005) 973–976. doi:10.1016/j.scriptamat.2005.01.028.
- [156] M. Onink, C.M. Brakman, F.D. Tichelaar, E.J. Mittemeijer, S. van der Zwaag, J.H. Root, N.B. Konyer, THE LATTICE PARAMETERS OF AUSTENITE AND FERRITE IN Fe-C ALLOYS AS FUNCTIONS OF CARBON CONCENTRATION AND TEMPERATURE, *Scr. Metall. Mater.* 29 (1993) 1011–1016.
- [157] N.N. Rammo, O.G. Abdulah, A model for the prediction of lattice parameters of iron–carbon austenite and martensite, *J. Alloys Compd.* 420 (2006) 117–120. doi:10.1016/j.jallcom.2005.10.075.
- [158] O.D. Sherby, J. Wadsworth, D.R. Lesuer, C.K. Syn, The c/a Ratio in Quenched Fe-C and Fe-N Steels - A Heuristic Story, *Mater. Sci. Forum.* 539–543 (2007) 215–222. doi:10.4028/www.scientific.net/MSF.539-543.215.
- [159] S.A. Mujahid, H.K.D.H. Bhadeshia, Coupled diffusional/displacive transformations: Effect of carbon concentration, *Acta Metall. Mater.* 41 (1993) 967–973. doi:10.1016/0956-7151(93)90031-M.
- [160] S.A. Mujahid, H.K.D.H. Bhadeshia, Partitioning of carbon from supersaturated ferrite plates, *Acta Metall. Mater.* 40 (1992) 389–396. doi:10.1016/0956-7151(92)90313-4.
- [161] F.G. Caballero, M.K. Miller, C. Garcia-Mateo, J. Cornide, M.J. Santofimia, Temperature dependence of carbon supersaturation of ferrite in bainitic steels, *Scr. Mater.* 67 (2012) 846–849. doi:10.1016/j.scriptamat.2012.08.007.
- [162] R. Reed, J. Root, Determination of the temperature dependence of the lattice parameters of cementite by neutron diffraction, *Scr. Mater.* 38 (1997) 95–99. <http://scholar.google.com/scholar?hl=en&btnG=Search&q=intitle:DETERMINATION+OF+THE+TEMPERATURE+DEPENDENCE+OF+THE+LATTICE+PARAMETERS+OF+CEMENTITE+BY+NEUTRON+DIFFRACTION#0>.
- [163] L.R. Smith, W.C. Leslie, Properties of Pure Metals, Properties and Selection: Nonferrous Alloys and Special-Purpose Materials, in: *ASM Handb. Vol. 2*, ASM International, 1990: pp. 1099–1201.

Appendix

A1- Calculation of T_0 and T'_0

In studying diffusionless transformation of steel it is beneficial to analyze the phase transformation from a thermodynamics perspective. At temperatures below A_3 on the Fe-Fe₃C phase diagram, ferrite becomes a stable phase. If undercooling is not too large, the formation of ferrite becomes linked to the redistribution of carbon between ferrite and austenite. In this case, ferrite rejects some carbon atoms to the remaining austenite enriching it with carbon compared with the original parent austenite before the transformation began. Redistribution allows the system to reach a combination of ferrite and austenite with their own carbon contents with a lower Gibbs free energy compared with just austenite in the undercooled state. However, at large enough undercooling, a situation exists where ferrite containing all the carbon of the parent austenite has a lower free energy compared with the parent austenite. This means that, from an energy standpoint, austenite can transform to ferrite without the need for carbon diffusion. All that is needed for this kind of transformation is re-arrangement of iron atoms in the FCC austenite unit cell to create the BCC ferrite unit cell. The temperature below which ferrite is more stable than an austenite of similar composition is known as T_0 . To find this temperature, Eq. A-1 is solved.

$$G^\gamma = G^\alpha \quad \text{Eq. A-1}$$

where G^i is the Gibbs free energy of phase i . Note that G is a function of temperature. For steels with a complicated chemistry, Eq. A-1 can be solved using the CALPHAD method, with the following set of equations [141]:

$$G^\gamma = G_{Ref}^\gamma + G_{mix}^{ideal,\gamma} + G_{mix}^{xs,\gamma} \quad \text{Eq. A-2}$$

$$G^\alpha = G_{Ref}^\alpha + G_{mix}^{ideal,\alpha} + G_{mix}^{xs,\alpha} \quad \text{Eq. A-3}$$

$$G_{Ref} = \sum x_i G_i^0 \quad \text{Eq. A-4}$$

$$G_{mix}^{ideal} = RT \sum_{i=1}^n x_i \ln x_i \quad \text{Eq. A-5}$$

$$G_{mix}^{xs} = \sum_{i=1}^n \sum_{j=i+1}^{n+1} x_i x_j \left[\Omega_{ij}^0 + \Omega_{ij}^1 (x_i - x_j) + \Omega_{ij}^2 (x_i - x_j)^2 \dots \right] \quad \text{Eq. A-6}$$

n is the number of elements, G_i^0 is the standard Gibbs free energy of element i , G_{Ref} is the reference energy of the solution calculated using linear regression of the standard Gibbs free energy of elements in that phase, x_i represents the mole fraction of element i in the mixture, G_{mix}^{ideal} is the ideal free energy of mixing, G_{mix}^{xs} is the

excess free energy of mixing and Ω_{ij}^k is the k th order interaction parameter of elements i and j . Equation A-6 is the generalized form of the excess energy of regular solutions.

Since T_0 is calculated for a diffusionless transformation, the chemical composition of austenite and ferrite should be considered to be the same when solving the equations. These equations can be solved numerically using commercially available software such as Thermo-Calc, MTDATA and the open source OpenCALPHAD package, which include a database of Gibbs free energies and interaction parameters.

The diffusionless transformation of austenite to bainitic ferrite, however, is a displacive transformation and creates a strain in the bainitic ferrite phase that is known as Bain strain [36]. The formation of this strain in the ferrite phase increases the energy of ferrite. At temperatures below T_0 , diffusion of carbon is not necessary, but for the bainitic reaction to happen more undercooling is needed to overcome the energy barrier of the Bain strain. The temperature at which the Bain strain can be overcome is called T'_0 . T'_0 is always lower than T_0 . To calculate T'_0 , the stored energy of bainitic ferrite should be added to the right hand side of Eq. A-3 as an extra term before solving the system of equations. This energy is calculated as 400 J/mol for steels [36,39].

A-2 Computer codes

All the following computer codes are written in Python 2.7 language. These codes are guaranteed to work on the Linux operating system; however, some codes may also work on any Mac OS and Windows. Syntax highlighting is done using an online tool at <http://markup.su/highlighter> using IDLE style.

A2-1 Master Fitter Program

The Master fitter program is the optimization code that performs the curve fitting using the Unit Cell Dilation algorithm. It can be used in two modes with optimization being on or off. In the optimization off mode, Master Fitter just performs curve fitting using the predefined materials properties. In the optimization on mode the output of the Master Fitter is the phase fraction of the phases that form during cooling. In the optimization on mode, Master Fitter searches for the best combination of materials properties that results in the best curve fitting at the same time for a number of dilatometry data files. In this mode the results of Master Fitter are optimized material properties as well as phase fractions of the phases during transformation for all data files.

Master Fitter uses several input files that need to be provided by the user. These files are:

- **Dilation data files:** These files contain dilation data in *.csv format. It is highly recommended that these files be names in the specific format that tells the program about the nature of the experiment and provides some key information. So far the only type of experiment that can be analyzed is continuous cooling. Continuous cooling data files names should begin with CC and followed by the cooling rate. For example *CC5.csv* is continuous cooling experiment at the cooling rate of 5°C/s. Cooling rates less than 1 are written without the decimal point. For example *CC02.csv* means cooling rate at 0.2°C/s and *CC0004.csv* means 0.004°C/s.
- **Chemistry:** Chemical composition of steel is written in the text file named *chemistry.txt*. In this file each line contains the concentration of one element in the format *element,wt%*. The commas are important and needed. In future versions this file format can be replaced with .csv or .xlsx for simplicity and consistency. The elements that can be defined are C, Mn, Si, Ni, Cr, Mo, Al, Nb, Ti, Al and Cu.
- **Carbon solubility in austenite:** This file contains the solubility data used for determining whether carbon concentration in austenite permits precipitation of cementite. The file name should be *C_solubility_limit_austenite.xlsx*. Data is stored in the form of a Microsoft Excel file with the first column being carbon mole fraction and the second column being the temperature in °C.
- **Master Fitter setup file:** This file contains the specific information about each data file that Master Fitter needs to understand the data. This file is named *master_setup.txt*. In this file each line contains the setting for one data file written in the following format:

File name, full austenite start row number, full austenite finish row number, full product start row number, full product finish row number, sample length in meter, cementite instructions

The file name must match an existing dilation data file stored in the same folder as the Master Fitter. Row numbers are different than the row numbers found in the original dilation data files. Row numbers should be determined in the plots that *data_plotter_Vx.py* generates. In these plots row numbers of the points are shown by each point. This is because of the conditioning that *data_set_conditioner_Vx.py* does to the original data. Sample length is the length over which dilation is measured. If dilation is measured over the diameter of the specimen, the diameter is provided and if dilation is measured over length then specimen length is provided. Cementite instruction tells the program to allow, disallow (e.g., high Si) precipitation of cementite. It is also possible to determine a temperature below which cementite is not allowed to form. The syntax for these three conditions are:

- Cementite_yes

- Cementite_no
- User_XXX (XXX is the lowest temperature for cementite precipitation in °C)

Cementite_yes should be the default setting. The other two conditions must be used only if the user is certain they apply.

A2-2 Master Fitter

""""

Master_fitter_v2.48.py

Speeeeeeed! The program uses Memoizing and hash table to speed up the calculation. About 20% increase in speed is achieved this way. Functions like Ms, Bs, L ... which are shared between V10 and V10_plot are defined outside the fitter function which reduces the risk of V10 and V10_plot being different.

Vcement is imported as a C library for speed.

Dataset conditioner is upgraded to V3 which is slightly more consistent in picking analysis points.

Master_fitter_v2.44.py

Carbon Solubility in austenite can be introduced to master fitter using an excle file.

this version can calculate correction factor due to small differences in length of the samples. This can be done in two ways.

The first method is done by adding a correction factor so that CTE of individual sample becomes equal to the average CTE.

The second method is done by adding a correction factor to length so that maximum strain during heating becomes equal to the average of maximum strain for all the samples.

Correction for L0 can be shut off through run settings.

master_fitter_v2.3.py

Speed Speed Speed

Mater fitter does parallel processing (you are welcome!) Best case, have one core per data file + 1 more to handle OS calls.

Additional core will not improve speed. Two core functions a0_alpha and a0_bainite are written in C which provides orders of magnitude speed up.

master_fitter_utils is the C shared library of these two functions which needs to be compiled for every computer system.

This version can optimize the weight factor of C on CTE of martensite and the weight factor of C on expansion of martensite along with some more which can be found in the code.

Please refer to `optimized_params` for the full list.

Selective optimization of parameters is implemented.

Results are now stored in the working directory in the .XLSX format.

A module named `Results_xlsx_saver` creates the results file

Program has gotten smarter. It can handle irregular data sampling rates during dilatometry.

`data_set_conditioner` code takes care of this.

This program runs every time before `master_fitter` runs to make sure that the changes in `master_setup` are taken into consideration.

A program called `data_plotter` is written to help with creating the `master_setup_file`.

This part is still a little tricky. Follow these steps:

1. Create `master_setup.txt` file by just writing the file names. Anything written after the file name is ignored by `data_plotter`. Suggestion edit the a working `master_setup.txt` that works

2. Run the `data_plotter.py` program.

3. In the plots created by `data_plotter`, Row numbers are annotated in the plots

4. Use the plots and row numbers to identify the correct ranges for pure austenite and product.

5. Fill in the blanks. Enter pure austenite start row then enter "," then enter pure austenite range end then enter ",". Do the same for product range.

6. The last entry in each row is what you want the program to do about cementite. Read the code for more info on this.

7. You have created your `master_setup` file!

convergence:

The smaller the interval the more accurate the results are. However, the accuracy comes at the price of speed.

Speed exponentially goes up as the interval goes down.

The smallest interval is 1. Going from high to low interval has to be done gradually.

Sudden decrease in interval can make the program unstable because the fit parameters may be too far from the answer.

Important notice:

Before you run the code for the first time you need to compile the C shared library.

These functions are all gathered in master_fitter_util.so which is created using Cython tool from the source code master_fitter_utils.pyx. compile by typing

"python master_fitter_utils.py build_ext --inplace" in a terminal that is opened in the master_fitter_utils.py directory.

Sources of error:

1. Master_setup.txt is not written according to the expected layout.
2. When you get an error that refers to Vgamma_param, most likely the initial guess of N_t is too big or small.
3. "Cannot import Valpha, Vcement..." you may have to recompile the cython tools using "python master_fitter_utils.py build_ext --inplace" in a terminal that is opened in the master_fitter_utils.py directory.

Send me your questions and inputs.

email the author at: khodaie@ualberta.ca or nassehk@gmail.com

This code is distributed under MIT license. Update, upgrade, fix and share.

```
"""
```

```
__author__ = "Nasseh Khodaie"
```

```
__version__ = 2.49
```

```
#import cProfile
```

```
#def main():
```

```
import csv
```

```
import numpy as np
```

```
import matplotlib.pyplot as plt
```

```

from numpy.polynomial import polynomial as P
import scipy as scipy
from scipy import stats #for some reason it is necessary for optimize to have
stats imported.
import os
import sys as sys
import time
import pickle
from numpy import sqrt
#from numba import jit, float64, vectorize
#if sys.platform[0:3] != 'lin':
#    import winsound
from Results_xlsx_save_v2 import saver
#import data_set_conditioner_V2
import data_set_conditioner_V3
from openpyxl import load_workbook as lw
from scipy.interpolate import interp1d
import multiprocessing as mp
start=time.time()
clear = lambda: os.system('clear'if sys.platform[:5]=='linux' else 'cls')
clear()
from master_fitter_utils import Valpha,Vbainite,VCement

# global variable are solver settings that are shared between V10 and V10_plot
functions.
global sr, reg_order, interval, Bs_model, end_fit_WF, overal_fit_WF,
err_end_slop_WF
global err_maximum_transformation_WF, Bs_master_dic, Ms_master_dic, MF_dic

#####
#solver settings
end_fit_WF=9
overal_fit_WF=6
err_end_slop_WF=0
err_maximum_transformation_WF=3.0

```

```

maximize_fraction_transformed='yes' #'yes' and 'y' will trigger maximizing
transformation cost factor. Be careful with use of this. It may create incorrect
lattice parameters.
#use maximization with caution. this is a tool to get close to the final solution.
However if your final solution relies on maximization to be on, your solution
might not be correct.
sr=7
reg_order=4
interval=8
optimize='no'# It tells the program to optimize or just plot using the
parameters provided.yes / no
correct_L0='yes'
L0_correction_method=3 # 1 for CTE matching which calculates correction to make
all CTEs equal to average CTE.
# 2 for strain matching which matches the strain at
austenitization for all of the samples to average strain.
# 3 for normalizing all data to a strain at user defined
temperature during cooling.
# Method 2 is a better method for solid samples as
temperature gradient during cooling can effect CTE differently depending on the
cooling rate
normalizing_temp=940 # Only applicable for method 3 of L0_correction.
use_avr_CTE_product=0 # 1 for yes 0 for no. Setting to zero will ignore user
provided values and will calculate

Bs_model=1 # can be 1 for imperial and 2 for t zero method (model 2 only works
for Nasseh's x80)
Ms_model=3 # can be 1 for Andrews1, 2 for Andrews 2, 3 for Capdevilla, 4 for
interaction model Jiajun Wang
SSF_method="user" # can be user or genral. general assumes linear increase of SSF
from LBs to Ms, from SSF=0 to SSF=1, User defined is polynomial.
use_XRD_for_a0_alpha='no' #yes overrides user defined value for a0_alpha and
calculates a value based of literature.

#select which parameters you want to be optimized. 0 for no and 1 for yes.
optimization_method = 1
# 1 for Nelder-Mead and 2 for differential evolution

```

```

#           NM method searches for the best answer around an
#           starting point. It is faster but prone to pointing to a
#           local minimum not global. DE is more robust.
#           It searches for the best answer in a defined domain
called bounds. It is however, slower than NM.

```

```

optimized_param={'a0_gama': 0,
                'a0_alpha': 1,
                'CTE_alpha_a': 0,
                'CTE_alpha_b': 1,
                'CTE_alpha_c': 1,
                'c_wf_for_cte':1,
                'c_wf_for_a0': 1}

```

```

#bounds are used by differential evolution only

```

```

optimized_param_bounds={'a0_gama': (3.63e-10*0.98,3.63e-10*1.02),
                        'a0_alpha': (2.86e-10*0.98,2.98e-10*1.02),
                        'CTE_alpha_a': (1.33e-5*0.9,1.33e-5*1.1),
                        'CTE_alpha_b': 0,
                        'CTE_alpha_c': 1,
                        'c_wf_for_cte':(1.96e-4,8.96e-3),
                        'c_wf_for_a0': (4.53e-11,9.53e-12)}

```

```

#

```

```

#compile_C_library=1

```

```

#####

```

```

#current_dir=os.getcwd()

```

```

#if compile_C_library==1:

```

```

#   if sys.platform[:3]=="win":

```

```

#

```

```

#       return_code = subprocess.call("python %s build_ext --inplace"

```

```

#####

```

```

#starting values of the fundamental parameters of the program.
#params are used by Nelde-Mead only
a0_gama =      3.630354505175200875243544068702e-10
a0_alpha=      0.000000000286303685572245
CTE_alpha_a=   0.000000000000000000000000000000e+00
CTE_alpha_b=   0.00000000482223600080234
CTE_alpha_c=   0.0000127339731685667
c_wf_for_cte=  0.000251734890694533
c_wf_for_a0=   0.0000000000026039264325498

#####

#####

result_master_time=[]
result_master_temp=[]
result_master_dil=[]
result_master_fraction=[]
result_master_ID=[]
result_master_FD_fraction=[]
result_master_C_in_FD_fraction=[] #fraction of ferrite derivative formed
result_master_C_in_FD_WP=[]
result_master_cem_fraction=[] #fraction of cementite formed
run_parameter={}

Bs_master_dic={}
MF_dic={}
Ms_master_dic={}
C_in_alpha_master_dic={}

Bs_temp_dic={}
MF_temp_dic={}
Ms_temp_dic={}
C_in_alpha_temp_dic={}

molar_weight={'fe':56, 'mn':54.6, 'cr':51.99, 'ni':78.7, 'mo':95.96, 'si':28.08,
              'c':12, 'nb':92.9, 'ti':47.867, 'al':26.98, 'cu':63.546}

```

```

error_in_calcs=[]
elements=[]
amount0_wp=[]

if sr<interval: sr=interval

c=open('chemistry.txt','r')
for line in c:
    temp=line.split(',')
    elements.append(str(temp[0].lower()))
    amount0_wp.append(float(temp[1]))
chemistry0=dict(zip(elements,amount0_wp))
chemistry0_temp=dict(zip(elements,amount0_wp))# this is used in some calculation
and altered during the process. Should not be used for anything. use chemistry0
instead.
#def molar_fraction(elements,amounts_wp,req

for elm in molar_weight.keys():
    if chemistry0.has_key(elm):
        pass
    else:
        chemistry0.update(dict(zip([elm],[0])))

CSLA=xlw('C_solubility_limit_austenite.xlsx')
ws=CSLA.active
T_CSLA=[]
X_CSLA=[]
for i in xrange(2,int(ws.max_row),1):
    X_CSLA.append(float(ws.cell(row=i, column=1).value))
    T_CSLA.append(float(ws.cell(row=i, column=2).value))
T_CSLA=np.array(T_CSLA)
X_CSLA=np.array(X_CSLA)
Solubility=interp1d(T_CSLA,X_CSLA,kind='linear')
CSLA_der=scipy.misc.derivative(Solubility,T_CSLA[2:-2],dx=0.1,n=2)

```

```

BB=np.unravel_index(CSLA_der.argmax(),CSLA_der.shape)[0] #BB is the index of
maximum 2nd derivative of CSLA. this point is use for deviding the solubility data
into two set to make the polynomial fit possible
BB=BB+(len(T_CSLA)-BB)//3

#def Solubility_aus_cement(T): # In mole frtaction, calculates the solubility
limit of C in austenite with respect to cementite
CSLA_high=P.polyfit(T_CSLA[:BB],X_CSLA[:BB],4)
CSLA_low=P.polyfit(T_CSLA[BB:],X_CSLA[BB:],4)

#@jit(float64(float64))
def Solubility_aus_cement(T):#This function is not vectorizable because of if
statements.
    if T<T_CSLA[BB]:
        if T<T_CSLA.min():
            CSLA=0
        else:
            CSLA=P.polyval(T,CSLA_low)
    else:
        CSLA=P.polyval(T,CSLA_high)
    if CSLA<0: CSLA=0
    return CSLA

#plt.figure(87)
#plt.plot(T_CSLA,X_CSLA,'o')
CSLA=np.zeros(len(T_CSLA))
for i in xrange(len(T_CSLA)):
    CSLA[i]=Solubility_aus_cement(T_CSLA[i])

fig, ax1 = plt.subplots()
ax1.plot(T_CSLA[2:-2],scipy.misc.derivative(Solubility,T_CSLA[2:-
2],dx=0.1,n=2),'o',label='2nd derivative')
ax1.set_xlabel('Temperature')
ax1.set_ylabel('2nd derivative')
ax1.set_title('Solubility limit of C in austenite')
ax1.legend(loc='upper right')
ax2=ax1.twinx()

```

```

ax2.plot(T_CSLA,Solubility(T_CSLA),'o',label='Raw solubility data')
ax2.set_ylabel('Solubility limit mole fraction')
ax2.plot(T_CSLA,CSLA,'--',label='Fitted function')
ax2.legend(loc='lower right')

def a0_alpha_calculated():
    a0_alpha_wf={'mn':0.00006, 'si':-0.00003, 'ni':-0.00007, 'cr':0.00005,
                'p':-0.0001, 'ti':-0.0031}
    a0_alpha_XRD=0.28664 # at room temp with no alloying element.
    for element in a0_alpha_wf.keys():
        if element in chemistry0.keys():
            a0_alpha_XRD=a0_alpha_XRD+a0_alpha_wf[element]*chemistry0[element]
    return a0_alpha_XRD

if use_XRD_for_a0_alpha.lower()=='yes':
    a0_alpha=a0_alpha_calculated()

def molar_fraction(elements,amounts_wp,required):
    # elements is a list of all alloying elements (excluding fe).
    # amounts is the corresponding weight percent of the element in the alloy.
    # required is the name of the element that its molar fraction is required.
    fe_wp=100-sum(amounts_wp)
    elements.append('fe')
    amounts_wp.extend([fe_wp])
    element_mol=np.zeros(len(elements))
    for i in range(len(elements)):
        element_mol[i]=amounts_wp[i]/molar_weight[elements[i]]

    mole_fractions=element_mol/sum(element_mol)
    matched=dict(zip(elements,mole_fractions))
    return matched[required]
C0=molar_fraction(elements,amount0_wp,'c')

def MF_to_WP_generator(local_chem):

```

```

C_wp=np.linspace(chemistry0['c'],6.0,200)
C_MF=[]
for i in xrange(len(C_wp)):
    if local_chem.has_key('fe'): local_chem.pop('fe')
    local_chem['c']=C_wp[i]
    elem,amo_wp=local_chem.keys(),local_chem.values()
    C_MF.append(molar_fraction(elem,amo_wp,'c'))
MF_to_WP=P.polyfit(C_MF,C_wp,4)
return MF_to_WP
MF_to_WP=MF_to_WP_generator(chemistry0_temp)

#@vectorize([float64(float64)],nopython=True)
#@autojit

#MF_dic=mp.Manager().dict()
#MF_dic={}

#def mf_to_wp(MF):
#    return P.polyval(MF,MF_to_WP)

def mf_to_wp(MF):
#    y=0
#    for i in xrange(len(MF_to_WP)):
#        y = y + MF ** i * MF_to_WP[i]
#    return y
#    if type(MF).__name__ != ('ndarray' or 'list'): #this try except allows
mf_to_wp function to operated on single MF and on numpy arrays at the same time.
    try:#This will allow handelling numpy arrays
#        strMF="{0:.%df}"%(precision)).format(MF)
#        strMF=np.float16(MF)
        strMF=str(MF)[:precision+3]
#        if strMF in MF_dic:
            try:#This will try finding strMF in the MF_dict.
                result=MF_dic[strMF]

```

```

#         print "not bad"
#     else:
#         except:
#             result=P.polyval(MF,MF_to_WP)
#             MF_temp_dic[strMF]=result
#             print "updated Mf_dic"
#             return result
#     else:
#         except:
#             return P.polyval(MF,MF_to_WP)

def CTE_alpha(T): # T in celsius
    return CTE_alpha_a*T*T+CTE_alpha_b*T+CTE_alpha_c

current_dir=os.getcwd()
file_list=pickle.load(open(current_dir+'/working_directory/file_list_conditioned.p
kl', 'rb'))
time_master=pickle.load(open(current_dir+'/working_directory/time_conditioned.pkl'
, 'rb'))
temp_master=pickle.load(open(current_dir+'/working_directory/temp_conditioned.pkl'
, 'rb'))
dil_master=pickle.load(open(current_dir+'/working_directory/dil_conditioned.pkl', '
rb'))
delta_L_tot=0
CTE_tot=0
strain_at_normalizing_temp_master=[]
aus_line_master=[]
CTE_product_master=[]
CTE_aus_master=[]
#Let's calculate correction factors for l0s
for i in range(len(file_list)):
    delta_L_tot=delta_L_tot+np.amax(dil_master[i])/file_list[i][5]
#     L_tot=L_tot+file_list[i][5]
    row_min_aus=int(file_list[i][1])

```

```

row_max_aus=int(file_list[i][2])
#   time_analysis_aus=time[row_min_aus:row_max_aus+1]
dil_analysis_aus=dil_master[i][row_min_aus:row_max_aus+1]
temp_analysis_aus=temp_master[i][row_min_aus:row_max_aus+1]
aus_line=P.polyfit(temp_analysis_aus,dil_analysis_aus,1)
CTE_aus_master.append(aus_line[1]/file_list[i][5])
aus_line_master.append(aus_line)

strain_at_normalizing_temp_master.append(P.polyval(normalizing_temp,aus_line)/file
_list[i][5])
CTE_gama=aus_line[1]/file_list[i][5]
CTE_tot=CTE_tot+CTE_gama

CTE_avr=CTE_tot/(i+1)
delta_L_avr=delta_L_tot/(i+1)
strain_at_normalizing_T_avr=np.sum(np.array(strain_at_normalizing_temp_master))/(i
+1)
Cooling_rate_master=[]

CR_master=[]
for row in file_list:
    CR=row[0].split('.')[0][2:]

    if CR[0]=='0':
        CR_split=CR.split('0')
        i=0
        while CR_split[i].isdigit()==False:
            i+=1
#         at this point, i shows the number of zeros the are in front of the
#         name of the file which shows the number of decimal point e.g.
CC02.csv
#         means cooling rate of 0.2 C/s
        CR=float(CR)*10**(-1*i)
    else:
        CR=float(CR)
    CR_master.append(CR)

```

```

plt.figure(23)
plt.plot(CR_master,np.array(CTE_aus_master)*10e5,'-o')
plt.title('CTE of austenite vs cooling rate')
plt.xlabel('Cooling rate(C/s)')
plt.ylabel('CTE (*10e-5)')

#for i in the range(len(file_list)):
#    cooling_rate_master.append(file_list[i][0])

def corr_fact_l0(x):
    if L0_correction_method==1:
        err=(5+abs(current_dldT/(file_list[m][5]+x)-CTE_avr))**5-5**5
    if L0_correction_method==2:
        err=(5+abs(np.amax(dil_master[m])/(file_list[m][5]+x)-delta_L_avr))**5-
5**5
    if L0_correction_method==3:
        err=(5+abs(strain_at_normalizing_temp_master[m]-
strain_at_normalizing_T_avr+x/file_list[m][5]))**5-5**5

    return err

L0_correction=[]
if correct_L0.lower()=='yes':
    for m in range(len(file_list)):
        row_min_aus=int(file_list[m][1])
        row_max_aus=int(file_list[m][2])
        #    time_analysis_aus=time[row_min_aus:row_max_aus+1]
        dil_analysis_aus=dil_master[m][row_min_aus:row_max_aus+1]
        temp_analysis_aus=temp_master[m][row_min_aus:row_max_aus+1]
        current_dldT=P.polyfit(temp_analysis_aus,dil_analysis_aus,1)[1]

        x0=0#, a0_gama,CTE_0_gama,CTE_alpha_b,CTE_alpha_a]
        for i in xrange(5):
            res = scipy.optimize.minimize(corr_fact_l0,x0, method='Nelder-Mead')
            x0= res.x
            print x0

```

```

        L0_correction.append(x0[0])
    L0_correction=np.array(L0_correction)
    print L0_correction
else:
    L0_correction=np.zeros(len(file_list))
CTE_eq_order=1 #Highest power in the CTE polinomial

for i in range(len(file_list)):
    L0=file_list[i][5]+L0_correction[i]
    row_min_fer=int(file_list[i][3])
    row_max_fer=int(file_list[i][4])

    dil_analysis_fer=dil_master[i][row_min_fer:row_max_fer+1]
    temp_analysis_fer=temp_master[i][row_min_fer:row_max_fer+1]

CTE_product_coef=P.polyder(P.polyfit(temp_analysis_fer,dil_analysis_fer,CTE_eq_order+1))/L0
    CTE_product_master.append(CTE_product_coef)

CTE_temp=[]
temperature_temp=[]

plt.figure(99)
plt.title("CTE product graphs")
for i in range(len(file_list)):
    print i , " " , i

temp=np.arange(np.round(temp_master[i][int(file_list[i][4])]),np.round(temp_master[i][int(file_list[i][3])]))
    CTE=P.polyval(temp,CTE_product_master[i])
    plt.plot(temp,CTE,'.',label=file_list[i][0])
    CTE_temp=CTE_temp+list(CTE)
    temperature_temp=temperature_temp+list(temp)

CTE_product_avr_coef=P.polyfit(temperature_temp,CTE_temp,CTE_eq_order)
plt.plot(range(100,500),P.polyval(range(100,500),CTE_product_avr_coef),"--",label='Average CTE')

```

```

plt.legend()
if use_avr_CTE_product==1:
    CTE_alpha_c=CTE_product_avr_coef[0]
    CTE_alpha_b=CTE_product_avr_coef[1]
k=0 #k is the number that shows location of the current data file in the file_list

Mn= chemistry0['mn']
Ni= chemistry0['ni']
Cr= chemistry0['cr']
Mo= chemistry0['mo']
Si= chemistry0['si']
Cu= chemistry0['cu']

precision=4 # This is a number of decimal points used in rounding carbon content
for Ms and Bs calculation.

def Bs(C):# C is in mole fraction
    strC=str(C)[:precision+3]
    try:
        Bs=Bs_master_dic[strC]
    except:
        C=mf_to_wp(C)
        if Bs_model==1: # Imperical from Yong cok Lee
            Bs=745-110*C-59*Mn-39*Ni-68*Cr-106*Mo+17*Mn*Ni+6*Cr**2+29*Mo**2
        elif Bs_model==2:
            Bs=-23.3882*C**3 + 59.7411*C**2 - 359.987*C + 653.967 #works only for
my steel
        Bs_temp_dic[strC]=Bs
    # print "Ms_model must be a number between 1-4"
    return Bs

def Ms(C):# C is in mole fraction ref http://www.lucefin.com/en/siderurgia/area-
tecnica/trattamenti-termici/
    strC=str(C)[:precision+3]
    try:
        Ms=Ms_master_dic[strC]
    except:

```

```

C=mf_to_wp(C)
if Ms_model==1:
    Ms=539-423*C-30.4*Mn-17.7*Ni-12.1*Cr-7.5*Mo#-11.3*Cu-14.5*Si Ref
Andrews equation
elif Ms_model==2:
    Ms=512-453*C-16.9*Ni-9.5*Mo+212*C**2-71.5*C*Mn+15*Cr+67.6*C*Cr
elif Ms_model==3:
    Ms=764.2-302.6*C-30.6*Mn-16.6*Ni-8.9*Cr-2.4*Mo-11.3*Cu-14.5*Si-273.15
elif Ms_model==4:
    Ms=540-584.9*C-23.1*Si-117.7*Mn-42.5*Cr+49.9*Mo-
62.5*sqrt(C*Si)+178.3*sqrt(C*Mn)\
    -10*sqrt(C*Cr)+52.5*sqrt(C*Mo)+117.2*sqrt(Si*Mn)+50.9*sqrt(Si*Cr)-
142.2*sqrt(Si*Mo)\
    -29.2*sqrt(Mn*Cr)-9.7*sqrt(Mn*Mo)+69.9*sqrt(Cr*Mo)
else:
    pass
    Ms_temp_dic[strC]=Ms
return Ms

def Bainite_ss_factor(T,C): #using relaxation observed in isothermal experiments,
C is the amount of C in Austenite.
    if SSF_method.lower()=="general":
        SSF_coef=P.polyfit([Bs(C)-100,Ms(C)], [0,1],1) #this has to fixed. lower Bs
has to be used not just Bs which is for upper bainite.
        BSSF=P.polyval(T,SSF_coef)
        if BSSF<0: BSSF=0
        elif BSSF>1: BSSF=1
    elif SSF_method.lower()=="user":
        SSF_coef=np.array([ -4.82210399e+01, 2.19859596e-01, -2.45490039e-
04])#using relaxation observed in isothermal experiments, C is the amount of C in
Austenite.
        if T>512.5: BSSF=0
        elif T<450: BSSF=1
        else:
            BSSF=P.polyval(T,SSF_coef)
            if BSSF<0: BSSF=0

```

```

        if BSSF>1: BSSF=1
    else:
        print "SSF_method must be either general or custom"
    return BSSF

def C_in_alpha(T): #Mole fraction of C in alpha using thermocalc under para
equilibrium
    strT=str(T)[:precision+1]
    # print C_in_alpha_master_dic
    if strT in C_in_alpha_master_dic:
        C=C_in_alpha_master_dic[strT]
    =
    else:
        C= 1.4734491E-20*T**6 + 3.9638142E-17*T**5 - 1.1293268E-13*T**4 +
6.8406210E-11*T**3 - 9.3489472E-09*T**2 + 6.1810195E-07*T - 6.3920771E-06
    # print "calculated oldfashion"
    if C<0:
    # print "C in alpha negative"
        C==0
        C_in_alpha_temp_dic[strT]=C
    return C

def L(C): # L is an operator that changes C=N_C/(N_C+N_Fe) to N_C/N_Fe. 0<C<1
    L=C/(1-C)
    return L

output = mp.Queue()
def Fitter(filename,output,a0_gama,CTE_alpha_a,CTE_alpha_b,CTE_alpha_c,a0_alpha,\
    c_wf_for_cte,Bs_master_dic, MF_dic, Ms_master_dic, C_in_alpha_master_dic):
    global sr, reg_order, interval, Bs_model, end_fit_WF, overal_fit_WF,
err_end_slop_WF,\
    err_maximum_transformation_WF

    N_total=0
    k=0
    for var in file_list:
        if var[0]==filename:

```

```

        break
    else:
        k+=1
#    print "k=", k
    L0=file_list[k][5]+L0_correction[k]
    time=np.array(time_master[k])
    temperature=np.array(temp_master[k])
    dilation=np.array(dil_master[k])

    # determine pure austenite range
    row_min_aus=int(file_list[k][1])
    row_max_aus=int(file_list[k][2])
#    time_analysis_aus=time[row_min_aus:row_max_aus+1]
    dil_analysis_aus=dilation[row_min_aus:row_max_aus+1]
    temp_analysis_aus=temperature[row_min_aus:row_max_aus+1]

#####
    #lets calculate the CTE_0_gama using raw data
    CTE_actual_gama=P.polyfit(temp_analysis_aus,dil_analysis_aus,1)[1]/L0
    #CTE_0_gama is the CTE of austenite at zero mole fraction carbon
    CTE_0_gama=CTE_actual_gama+0.5E-6*C0*100
#####

    row_min_fer=int(file_list[k][3])
    row_max_fer=int(file_list[k][4])

#    dil_analysis_fer=dilation[row_min_fer:row_max_fer+1]
#    temp_analysis_fer=temperature[row_min_fer:row_max_fer+1]
#
CTE_product_coef=P.polyder(P.polyfit(temp_analysis_fer,dil_analysis_fer,1))/L0
#    print CTE_product_coef
    #determin the range of interest for fraction transformed calculation.
    row_min= row_min_aus
    row_max=row_max_fer

# create experimentally measured dv/dt for every data point in analysis range

```

```

time_analysis=time[row_min:row_max+1]
dil_analysis=dilation[row_min:row_max+1]
temp_analysis=temperature[row_min:row_max+1]

# def C_in_alpha(T): #Mole fraction of C in alpha using thermocalc under para
equilibrium
# C= 1.4734491E-20*T**6 + 3.9638142E-17*T**5 - 1.1293268E-13*T**4 +
6.8406210E-11*T**3 - 9.3489472E-09*T**2 + 6.1810195E-07*T - 6.3920771E-06
# return abs(C)

def Vgama_param(a0_gama,CTE_0_gama,T):
    Vgama=((a0_gama+6.5e-4*1e-9*C0*100)*(1+(CTE_0_gama-0.5E-6*C0*100)*(T-
726.85)))**3
    return Vgama

def Vgama_new (CTE_0_gama,C,T): # check if C is mole fraction
    Vgama=((a0_gama+6.5e-4*1e-9*C*100)*(1+(CTE_0_gama-0.5E-6*C*100)*(T-
726.85)))**3
    return Vgama

# def VCement(T): #T in centigrade. This function can be optimized for faster
run
# y=(1+(5.311E-6-1.942E-9*T+9.655E-12*T*T)*(T-20))
# a=0.45234E-9*y
# b=0.50883E-9*y
# c=0.67426E-9*y
# VCementite=a*b*c
# return VCementite

# @jit(nopython=True)
def
C_in_gama(timestep,current_dn_alpha,dn_alpha,C_dn,N_total,N_product,temp_fit,ID_dn
): #amount of C in gama on the timestep point
    # print "From C_in _gama,current_dn_alpha is ", current_dn_alpha

```

```

        C_total_in_ferrite=sum(dn_alpha[:timestep-1]*L(C_dn[:timestep-
1]))+current_dn_alpha*L(C_dn[timestep-1]) #this calculates total number of C atoms
in ferrite phase
        if ID_dn[timestep-1][3:6]=="Cem":
            current_dn_cem=((N_total-N_product[timestep-
1])*L(C_in_aus_molefraction[timestep-1])-
L(Solubility_aus_cement(temp_fit[timestep]))) -current_dn_alpha*(L(C_dn[timestep-
1])-L(Solubility_aus_cement(temp_fit[timestep]))))/L(0.25)-
L(Solubility_aus_cement(temp_fit[timestep])))
        else:
            current_dn_cem=0
#    print "dn_cem =" , dn_cem
        C_total_in_cement=sum(dn_cement[:timestep-1]/3.0)+current_dn_cem/3.0
        N_gama=N_total-(N_product[timestep-1]+current_dn_alpha+current_dn_cem)
        C_in_gama_local=L(C0)*N_total-C_total_in_ferrite-C_total_in_cement #No. of
C atoms in aus.
        return C_in_gama_local/(N_gama+C_in_gama_local)

def fundamental_parameters(x):
    N_t=x

modeled_l_gama=((N_t/4)*Vgama_param(a0_gama,CTE_0_gama,temp_analysis_aus))**(1/3.0
)
    residual_gama=np.sum(np.abs(modeled_l_gama-(dil_analysis_aus+L0)))
    err=residual_gama
    return err

x0=[3e22]#initial estimate of x0 (Here it represents N_t) is very important.
Too big of number will give error.
for i in xrange(5):
    res = scipy.optimize.minimize(fundamental_parameters,x0, method='Nelder-
Mead')
    x0= res.x
    N_total=x0[0]

print 'N_total of %s=%s'%(filename,N_total)
#    print 'CTE_0_gama of %s=%s'%(filename,CTE_0_gama)

```

```

# print

# raw_input('Hit enter to begin fitting points')

time_fit=np.zeros((row_max-row_min-2*sr)//interval)
temp_fit=np.zeros((row_max-row_min-2*sr)//interval)
dil_fit=np.zeros((row_max-row_min-2*sr)//interval)
# dldt_fit=np.zeros((row_max-row_min-2*sr)//interval)
num_of_analyzed_points=len(time_fit)

n=sr
for i in xrange(num_of_analyzed_points):
    #print'i= ',i
    time_fit[i]=time_analysis[n]
    coef1= P.polyfit(time_analysis[n-sr:n+sr],temp_analysis[n-
sr:n+sr],reg_order)
    temp_fit[i]=P.polyval(time_analysis[n],coef1)
    coef1= P.polyfit(time_analysis[n-sr:n+sr],dil_analysis[n-
sr:n+sr],reg_order)
    dil_fit[i]=P.polyval(time_analysis[n],coef1)
    n=n+interval

def expm_l_individual_err(x):
    previ_alpha_v=0.0
    current_step_alpha=0.0
    previ_cem_v=0.0
    current_step_cem=0.0
    dn_cem=0.0
    for j in xrange(i-1): #This for loop calculates volume of all the previous
steps. i-1 is correct
        if ID_dn[j][0:2]=="PF":

previ_alpha_v=previ_alpha_v+dn_alpha[j]/2*Valpha(a0_alpha,C_dn[j],temp_fit[i],CTE_
alpha_a,CTE_alpha_b,CTE_alpha_c, c_wf_for_cte,c_wf_for_a0, MF_to_WP)
        if ID_dn[j][0:2]=="BF":

```

```

previ_alpha_v=previ_alpha_v+dn_alpha[j]/2*Vbainite(a0_alpha,C_dn[j],temp_fit[i],CTE_alpha_a,CTE_alpha_b,CTE_alpha_c, c_wf_for_cte, c_wf_for_a0, MF_to_WP)
    if ID_dn[j][3:6]=="Cem":
        previ_cem_v=previ_cem_v+dn_cement[j]/12*VCement(temp_fit[j])
    if ID_dn[i-1][0:2]=="PF":
        current_step_alpha=x/2*Valpha(a0_alpha,C_dn[i-1],temp_fit[i],CTE_alpha_a,CTE_alpha_b,CTE_alpha_c, c_wf_for_cte, c_wf_for_a0, MF_to_WP)
    if ID_dn[i-1][0:2]=="BF":
        current_step_alpha=x/2*Vbainite(a0_alpha,C_dn[i-1],temp_fit[i],CTE_alpha_a,CTE_alpha_b,CTE_alpha_c, c_wf_for_cte, c_wf_for_a0, MF_to_WP)
    if ID_dn[i-1][3:6]=="Cem":
        AA=L(Solubility_aus_cement(temp_fit[i]))
        dn_cem=((N_total-N_product[i-1])*(AA-L(C_in_aus_molefraction[i-1]))+x*(L(C_dn[i-1])-AA))/(-1/3.0+AA)
#         dn_cem=(1/(1/3.0-L(Solubility_aus_cement(temp_fit[i]))))*((dn_alpha[:i-1]*C_dn[:i-1])+(np.sum(dn_cem[:i-1])/3.0)+(N_total-N_product[i])*L(Solubility_aus_cement(temp_fit[i]))+x*(L(C_in_alpha((temp_fit[i]+temp_fit[i-1])/2.0)))-N_total*(L(C0))))
        current_step_cem=dn_cem/12*VCement(temp_fit[i]) #12 iron atoms in one unit cell of cementite.
        current_gama_v=(N_total-sum(dn_alpha[:i-1])-x-sum(dn_cem[:i-1])-dn_cem)/4*Vgama_new(CTE_0_gama,C_in_gama(i,x,dn_alpha,C_dn,N_total,N_product,temp_fit,ID_dn),temp_fit[i]) #Vgama should be fixed to get rid of x/N_total

modeled_V=previ_alpha_v+previ_cem_v+current_step_alpha+current_step_cem+current_gama_v
    err=abs((dil_fit[i]+L0)**3-modeled_V)*10e19
    return err

def expm_l_individual(x,i):
    previ_alpha_v=0.0
    current_step_alpha=0.0
    previ_cem_v=0.0

```

```

current_step_cem=0.0
dn_cem=0.0
for j in xrange(i-1): #This for loop calculates volume of all the previous
steps. i-1 is correct
    if ID_dn[j][0:2]=="PF":

previ_alpha_v=previ_alpha_v+dn_alpha[j]/2*Valpha(a0_alpha,C_dn[j],temp_fit[i],CTE_
alpha_a,CTE_alpha_b,CTE_alpha_c, c_wf_for_cte, c_wf_for_a0, MF_to_WP)
    if ID_dn[j][0:2]=="BF":

previ_alpha_v=previ_alpha_v+dn_alpha[j]/2*Vbainite(a0_alpha,C_dn[j],temp_fit[i],CT
E_alpha_a,CTE_alpha_b,CTE_alpha_c, c_wf_for_cte, c_wf_for_a0, MF_to_WP)
    if ID_dn[j][3:6]=="Cem":
        previ_cem_v=previ_cem_v+dn_cement[j]/12*VCement(temp_fit[j])
    if ID_dn[i-1][0:2]=="PF":
        current_step_alpha=x/2*Valpha(a0_alpha,C_dn[i-
1],temp_fit[i],CTE_alpha_a,CTE_alpha_b,CTE_alpha_c, c_wf_for_cte, c_wf_for_a0,
MF_to_WP)
    if ID_dn[i-1][0:2]=="BF":
        current_step_alpha=x/2*Vbainite(a0_alpha,C_dn[i-
1],temp_fit[i],CTE_alpha_a,CTE_alpha_b,CTE_alpha_c, c_wf_for_cte, c_wf_for_a0,
MF_to_WP)
    if ID_dn[i-1][3:6]=="Cem":
#        dn_cem=((N_total-N_product[i-1])*(L(C_in_au_molefraction[i-1])-
L(Solubility_au_cement(temp_fit[i])))-x*(L(C_dn[i-1])-
L(Solubility_au_cement(temp_fit[i])))))/(L(0.25)-
L(Solubility_au_cement(temp_fit[i])))
        AA=L(Solubility_au_cement(temp_fit[i]))
        dn_cem=((N_total-N_product[i-1])*(AA-L(C_in_au_molefraction[i-
1]))+x*(L(C_dn[i-1])-AA))/(-1/3.0+AA)
        current_step_cem=dn_cem/12*VCement(temp_fit[i]) #12 iron atoms in one
unit cell of cementite.
        current_gama_v=(N_total-sum(dn_alpha[:i-1])-x-sum(dn_cement[:i-1])-
dn_cem)/4*Vgama_new(CTE_0_gama,C_in_gama(i,x,dn_alpha,C_dn,N_total,N_product,temp_
fit,ID_dn),temp_fit[i]) #Vgama should be fixed to get rid of x/N_total

```

```

modeled_V=previ_alpha_v+previ_cem_v+current_step_alpha+current_step_cem+current_ga
ma_v
    #print (raw_input('press any key to continue in individual loop'))
    return (modeled_V)**(1/3.0)

    dn_alpha=np.ones(len(temp_fit))*10**(np.log10(N_total)-4) #this is starting
point of calculation which is close enough to zero to be considered zero fraction
transformed, yet large enough to allow for optimization.
    dn_cement=np.zeros(len(temp_fit))
    C_dn=np.zeros(len(temp_fit))
    ID_dn=[]
    #print (raw_input('press any key to continue'))
    simulated_l=np.zeros(len(dn_alpha))
    C_in_aus=np.ones(len(dn_alpha))*C0
    C_in_aus_molefraction=np.ones(len(dn_alpha))*C0
#    CTE_aus_current=np.zeros(len(dn_alpha))
    N_product=np.zeros(len(temp_fit))
#    N_prod=np.zeros(len(temp_fit))

for j in xrange(1):
    #print '*****'
    i=1 # start filling dn_alpha from the third element since the first two
should be zero. the first
    for i in xrange(1,num_of_analized_points):
        T=(temp_fit[i-1]+temp_fit[i])/2

#        print i, "out of", len(temp_fit)-1 ,"points completed"
        # at every i we calculated the dn[i-1]

        # First we should determine what is the type of the product forming
between i-1 and i.
        # We do that by assuming C_in_austenite during current step is equal
to that of the last step.
        if i>1:
            if temp_fit[i-1]<Bs(C_in_aus[i-1]):
#                print "    Bainite forming according to empirical formula"

```

```

        ID_dn.append("BF")
    else:
        ID_dn.append("PF")

    if ID_dn[i-1][0:2]=="PF":
        C_dn[i-1]=C_in_alpha(T)
        if C_dn[i-1]>C_in_gama(i-1,dn_alpha[i-1],dn_alpha,C_dn,N_total,N_product,temp_fit,ID_dn):
            C_dn[i-1]=C_in_gama(i-1,dn_alpha[i-1],dn_alpha,C_dn,N_total,N_product,temp_fit,ID_dn)
        elif ID_dn[i-1][0:2]=="BF":
#            T=(temp_fit[i-1]+temp_fit[i])/2
            C_eq=C_in_alpha(T)
            C_dn[i-1]=Bainite_ss_factor(T,C_in_gama(i-1,dn_alpha[i-1],dn_alpha,C_dn,N_total,N_product,temp_fit,ID_dn))*(C_in_gama(i-1,dn_alpha[i-1],dn_alpha,C_dn,N_total,N_product,temp_fit,ID_dn)-C_eq)+C_eq
            if C_dn[i-1]>C_in_gama(i-1,dn_alpha[i-1],dn_alpha,C_dn,N_total,N_product,temp_fit,ID_dn):
                C_dn[i-1]=C_in_gama(i-1,dn_alpha[i-1],dn_alpha,C_dn,N_total,N_product,temp_fit,ID_dn)
            if file_list[k][6].lower()[-3:]=='yes' or 'y' and C_in_gama(i-1,dn_alpha[i-1],dn_alpha,C_dn,N_total,N_product,temp_fit,ID_dn)>Solubility_au_cement(temp_fit[i-1]):
                ID_dn[i-1]=ID_dn[i-1]+"+"+"Cem"
            elif (("user" in file_list[k][6].lower()) and (C_in_gama(i-1,dn_alpha[i-1],dn_alpha,C_dn,N_total,N_product,temp_fit,ID_dn)>Solubility_au_cement(temp_fit[i-1]))):
                LCT=[float(s) for s in file_list[k][7].split() if s.isdigit()][0]#LCT stands for Lowest cementite temperature
                if T>LCT:
                    ID_dn[i-1]=ID_dn[i-1]+"+"+"Cem"

    elif i==1:
        ID_dn.append("PF")
        C_dn[i-1]=C_in_alpha((temp_fit[i-1]+temp_fit[i])/2)

```

```

else:
    print "There is a problem with ID_dn"
    quit()

res=scipy.optimize.minimize(expm_l_individual_err, dn_alpha[i-1],
method='nelder-mead', options={})
K=res.x
dn_alpha[i-1]=K[0]

if ((dn_alpha[i-1])/N_total)<1e-4:
    dn_alpha[i-1]=0

if ID_dn[i-1][3:6]=="Cem":
#
    =(1/(1/3.0-
L(Solubility_aus_cement(temp_fit[i])))*(np.sum(dn_alpha[:i-1]*C_dn[:i-
1])+(np.sum(dn_cement[:i-1])/3.0)+(N_total-
N_product[i])*L(Solubility_aus_cement(temp_fit[i]))+dn_alpha[i]*(L(C_in_alpha((tem
p_fit[i]+temp_fit[i-1])/2.0)))-N_total*(L(C0)))
    AA=L(Solubility_aus_cement(temp_fit[i]))
    dn_cement[i-1]=((N_total-N_product[i-1])*(-
L(C_in_aus_molefraction[i-1])+AA)+dn_alpha[i-1]*(L(C_dn[i-1])-AA))/(-1/3.0+AA)

#
    dn_cement[i-1]=((N_total-N_product[i-
1])*(L(C_in_aus_molefraction[i-1])-L(Solubility_aus_cement(temp_fit[i])))-
dn_alpha[i-1]*(L(C_dn[i-1])-L(Solubility_aus_cement(temp_fit[i])))))/(L(0.25)-
L(Solubility_aus_cement(temp_fit[i])))
    #lets put a constraint on dn to control noise which result in
incorrect negative dn

N_product[i]=N_product[i-1]+dn_alpha[i-1]+dn_cement[i-1]
#print (raw_input('press any key to go to next point in main loop'))
simulated_l[i]= expm_l_individual(dn_alpha[i-1],i)

C_in_aus[i]=C_in_gama(i,dn_alpha[i-
1],dn_alpha,C_dn,N_total,N_product,temp_fit,ID_dn)
C_in_aus_molefraction[i]=C_in_gama(i,dn_alpha[i-
1],dn_alpha,C_dn,N_total,N_product,temp_fit,ID_dn)

```

```

no_end_points=int((row_max_fer-row_min_fer)//interval)
coef= P.polyfit(temp_fit[len(temp_fit)-
no_end_points:],N_product[len(temp_fit)-no_end_points:],1)
err_end_slope=(5+abs(coef[1]/N_total))**err_end_slop_WF-5**err_end_slop_WF
# err_end_fit issues error when fit is not good at the ferrite end. sometimes
ferrite end has fewer point that makes them less effective in overall error.
# separating them allows for increasing there value in overall error
err_end_fit=(5+sum(abs((dil_fit[len(temp_fit)-no_end_points:]+L0)-
simulated_l[len(temp_fit)-no_end_points:]))/L0)**end_fit_WF-5**end_fit_WF
err_end_fraction=float(0.0)# this issues error if end fraction goes above 1
Numer_of_high_point=int(0)
for i in xrange(len(temp_fit)//3,len(temp_fit)):
#     print i
#     print "len(temp_fit)",len(temp_fit)
    if N_product[i]>N_total:
        Numer_of_high_point+=1
        err_end_fraction+=(5+((N_product[i]-N_total)/N_total))**20-5**20

    if (maximize_fraction_transformed.lower()=='yes' or 'y'):
        err_maximum_transformation=(5+sum(abs(N_product[:-3]/N_total-
1)))**err_maximum_transformation_WF-5**err_maximum_transformation_WF
    else: err_maximum_transformation=0

    err_overal_fit=(5+sum(abs((dil_fit[1:-1]+L0)-simulated_l[1:-
1]))/L0)**overal_fit_WF-5**overal_fit_WF
#     print 'err_pure_phase=' ,err_pure_phase
#     print "err_alpha_fit",err_alpha_fit
    total_cost= err_overal_fit+ err_end_slope + err_end_fraction + err_end_fit +
err_maximum_transformation
#     err_overal_fit=err_alpha_fit

output.put([total_cost,Bs_temp_dic,Ms_temp_dic,MF_temp_dic,C_in_alpha_temp_dic])#+
err_pure_phase)#+err_gama_fit+err_alpha_fit)

```

```

def
Fitter_plot(filename,output,a0_gama,CTE_alpha_a,CTE_alpha_b,CTE_alpha_c,a0_alpha,c
_wf_for_cte, c_wf_for_a0):
    print '-----V10_plot-----'

#    a0_alpha=0.28630e-9 # measured using from XRD at 20C. Should not be
conidered in parameter finding.
    global sr, reg_order, interval, Bs_model, end_fit_WF, overal_fit_WF
#    print Ms_model
    N_total=0
    k=0
    for var in file_list:
        if var[0]==filename:
            break
        else:
            k+=1
#    print "k=", k
    L0=file_list[k][5]+L0_correction[k]
    time=np.array(time_master[k])
    temperature=np.array(temp_master[k])
    dilation=np.array(dil_master[k])

# determine pure austenite range
    row_min_aus=int(file_list[k][1])
    row_max_aus=int(file_list[k][2])
#    time_analysis_aus=time[row_min_aus:row_max_aus+1]
    dil_analysis_aus=dilation[row_min_aus:row_max_aus+1]
    temp_analysis_aus=temperature[row_min_aus:row_max_aus+1]

#####
#lets calculate the CTE_0_gama using raw data
    CTE_gama=P.polyfit(temp_analysis_aus,dil_analysis_aus,1)[1]/L0
#CTE_0_gama is the CTE of austenite at zero mole fraction carbon
    CTE_0_gama=CTE_gama+0.5e-6*C0*100
#####

```

```

# row_min_fer=file_list[k][3]
row_min_fer=int(file_list[k][3])
row_max_fer=int(file_list[k][4])

dil_analysis_fer=dilation[row_min_fer:row_max_fer+1]
temp_analysis_fer=temperature[row_min_fer:row_max_fer+1]
CTE_product_coef=P.polyder(P.polyfit(temp_analysis_fer,dil_analysis_fer,3))/L0
print CTE_product_coef
# print "CTE_product for",file_list[k][0], '=', CTE_product
#determin the range of interest for fraction transformed calculation.
row_min= row_min_aus
row_max=row_max_fer

# create experimentally measured dv/dt for every data point in analysis range

time_analysis=time[row_min:row_max+1]
dil_analysis=dilation[row_min:row_max+1]
temp_analysis=temperature[row_min:row_max+1]

#
def C_in_alpha(T): #Mole fraction of C in alpha using thermocalc under para
equilibrium
    C= 1.4734491E-20*T**6 + 3.9638142E-17*T**5 - 1.1293268E-13*T**4 +
6.8406210E-11*T**3 - 9.3489472E-09*T**2 + 6.1810195E-07*T - 6.3920771E-06
    return abs(C)

def Vgama_param(a0_gama,CTE_0_gama,T):
    Vgama=((a0_gama+6.5e-4*1e-9*C0*100)*(1+(CTE_0_gama-0.5E-6*C0*100)*(T-
726.85)))**3
    return Vgama

def Vgama_new (CTE_0_gama,C,T): # check if C is mole fraction
    Vgama=((a0_gama+6.5e-4*1e-9*C*100)*(1+(CTE_0_gama-0.5E-6*C*100)*(T-
726.85)))**3

```

```

return Vgama

#
def
C_in_gama(timestep,current_dn_alpha,dn_alpha,C_dn,N_total,N_product,temp_fit,ID_dn
): #amount of C in gama on the timestep point in mole fraction
    # print "From C_in _gama,current_dn_alpha is ", current_dn_alpha
    C_total_in_ferrite=sum(dn_alpha[:timestep-1]*L(C_dn[:timestep-
1]))+current_dn_alpha*L(C_dn[timestep-1]) #this calculates total number of C atoms
in ferrite phase
    if ID_dn[timestep-1][3:6]=="Cem":
        current_dn_cem=((N_total-N_product[timestep-
1])*L(C_in_aus_molefraction[timestep-1])-
L(Solubility_aus_cement(temp_fit[timestep]))) -current_dn_alpha*(L(C_dn[timestep-
1])-L(Solubility_aus_cement(temp_fit[timestep])))))/(L(0.25)-
L(Solubility_aus_cement(temp_fit[timestep])))
    else:
        current_dn_cem=0
    # print "dn_cem =" , dn_cem
    C_total_in_cement=sum(dn_cement[:timestep-1]/3.0)+current_dn_cem/3.0
    N_gama=N_total-(N_product[timestep-1]+current_dn_alpha+current_dn_cem)
    C_in_gama_local=L(C0)*N_total-C_total_in_ferrite-C_total_in_cement #No. of
C atoms in aus.
    return C_in_gama_local/(N_gama+C_in_gama_local)

def fundamental_parameters(x):
    N_t=x

modeled_l_gama=((N_t/4)*Vgama_param(a0_gama,CTE_0_gama,temp_analysis_aus))**(1/3.0
)
    residual_gama=np.sum(np.abs(modeled_l_gama-(dil_analysis_aus+L0)))
    err=residual_gama
    return err

```

```

x0=[8.5e22]#,a0_gama,CTE_0_gama,CTE_alpha_b,CTE_alpha_a]
for i in xrange(5):
    res = scipy.optimize.minimize(fundamental_parameters,x0, method='Nelder-
Mead')
    x0= res.x
    N_total=x0[0]

    print 'N_total of %s=%s'%(filename,N_total)
    print 'CTE_0_gama of %s=%s'%(filename,CTE_0_gama)
    print
#    raw_input('Hit enter to begin fitting points')
    plt.figure(1)
    plt.plot(temp_analysis,dil_analysis+L0,'.', label="experimental data -" +
filename)
    plt.legend(loc=2)
    plt.title('Analyzed portion of dataset and fundamental parameter fitting
result')

    simulated_aus=np.zeros(len(temp_analysis))
    for i in xrange (0, len(temp_analysis)):
        simulated_aus[i]=
(N_total/4*Vgama_new(CTE_0_gama,C0,temp_analysis[i]))**(1/3.0)

    plt.figure(1)
    plt.title('Fit of ferrite and austenite.')
    plt.plot(temp_analysis,simulated_aus, '-',label="Fitted austenite - " +
filename)
    #plt.plot(temp_analysis_fer,dil_analysis_fer+L0,'--',label="Experimental " +
dataname)
    plt.xlabel('Temperature(C)')
    plt.ylabel('Dilation (M)')
    plt.legend(loc=2)
    plt.grid()

    time_fit=np.zeros((row_max-row_min-2*sr)//interval)
    temp_fit=np.zeros((row_max-row_min-2*sr)//interval)

```

```

dil_fit=np.zeros((row_max-row_min-2*sr)//interval)
# dldt_fit=np.zeros((row_max-row_min-2*sr)//interval)
num_of_analyzed_points=len(time_fit)

n=sr
for i in xrange(num_of_analyzed_points):
    #print'i= ',i
    time_fit[i]=time_analysis[n]
    coef1= P.polyfit(time_analysis[n-sr:n+sr],temp_analysis[n-
sr:n+sr],reg_order)
    temp_fit[i]=P.polyval(time_analysis[n],coef1)
    coef1= P.polyfit(time_analysis[n-sr:n+sr],dil_analysis[n-
sr:n+sr],reg_order)
    dil_fit[i]=P.polyval(time_analysis[n],coef1)
    n=n+interval

def expm_l_individual_err(x):
    previ_alpha_v=0.0
    current_step_alpha=0.0
    previ_cem_v=0.0
    current_step_cem=0.0
    dn_cem=0.0
    for j in xrange(i-1): #This for loop calculates volume of all the previous
steps. i-1 is correct
        if ID_dn[j][0:2]=="PF":

previ_alpha_v=previ_alpha_v+dn_alpha[j]/2*Valpha(a0_alpha,C_dn[j],temp_fit[i],CTE_
alpha_a,CTE_alpha_b,CTE_alpha_c, c_wf_for_cte,c_wf_for_a0, MF_to_WP)
        if ID_dn[j][0:2]=="BF":

previ_alpha_v=previ_alpha_v+dn_alpha[j]/2*Vbainite(a0_alpha,C_dn[j],temp_fit[i],CT
E_alpha_a,CTE_alpha_b,CTE_alpha_c, c_wf_for_cte, c_wf_for_a0, MF_to_WP)
        if ID_dn[j][3:6]=="Cem":
            previ_cem_v=previ_cem_v+dn_cement[j]/12*VCement(temp_fit[j])
    if ID_dn[i-1][0:2]=="PF":

```

```

        current_step_alpha=x/2*Valpha(a0_alpha,C_dn[i-
1],temp_fit[i],CTE_alpha_a,CTE_alpha_b,CTE_alpha_c, c_wf_for_cte, c_wf_for_a0,
MF_to_WP)
        if ID_dn[i-1][0:2]=="BF":
            current_step_alpha=x/2*Vbainite(a0_alpha,C_dn[i-
1],temp_fit[i],CTE_alpha_a,CTE_alpha_b,CTE_alpha_c, c_wf_for_cte, c_wf_for_a0,
MF_to_WP)
            if ID_dn[i-1][3:6]=="Cem":
                AA=L(Solubility_aus_cement(temp_fit[i]))
                dn_cem=((N_total-N_product[i-1])*(AA-L(C_in_au_molefraction[i-
1]))+x*(L(C_dn[i-1])-AA))/(-1/3.0+AA)
                current_step_cem=dn_cem/12*VCement(temp_fit[i]) #12 iron atoms in one
unit cell of cementite.
                current_gama_v=(N_total-sum(dn_alpha[:i-1])-x-sum(dn_cement[:i-1])-
dn_cem)/4*Vgama_new(CTE_0_gama,C_in_gama(i,x,dn_alpha,C_dn,N_total,N_product,temp_
fit,ID_dn),temp_fit[i]) #Vgama should be fixed to get rid of x/N_total

modeled_V=previ_alpha_v+previ_cem_v+current_step_alpha+current_step_cem+current_ga
ma_v
        err=abs((dil_fit[i]+L0)**3-modeled_V)*10e19
        return err

def expm_l_individual(x,i):
    previ_alpha_v=0.0
    current_step_alpha=0.0
    previ_cem_v=0.0
    current_step_cem=0.0
    dn_cem=0.0
    for j in xrange(i-1): #This for loop calculates volume of all the previous
steps. i-1 is correct
        if ID_dn[j][0:2]=="PF":

previ_alpha_v=previ_alpha_v+dn_alpha[j]/2*Valpha(a0_alpha,C_dn[j],temp_fit[i],CTE_
alpha_a,CTE_alpha_b,CTE_alpha_c, c_wf_for_cte, c_wf_for_a0, MF_to_WP)
        if ID_dn[j][0:2]=="BF":

```

```

previ_alpha_v=previ_alpha_v+dn_alpha[j]/2*Vbainite(a0_alpha,C_dn[j],temp_fit[i],CT
E_alpha_a,CTE_alpha_b,CTE_alpha_c, c_wf_for_cte, c_wf_for_a0, MF_to_WP)
    if ID_dn[j][3:6]=="Cem":
        previ_cem_v=previ_cem_v+dn_cement[j]/12*VCement(temp_fit[j])
    if ID_dn[i-1][0:2]=="PF":
        current_step_alpha=x/2*Valpha(a0_alpha,C_dn[i-
1],temp_fit[i],CTE_alpha_a,CTE_alpha_b,CTE_alpha_c, c_wf_for_cte, c_wf_for_a0,
MF_to_WP)
    if ID_dn[i-1][0:2]=="BF":
        current_step_alpha=x/2*Vbainite(a0_alpha,C_dn[i-
1],temp_fit[i],CTE_alpha_a,CTE_alpha_b,CTE_alpha_c, c_wf_for_cte, c_wf_for_a0,
MF_to_WP)
    if ID_dn[i-1][3:6]=="Cem":
        AA=L(Solubility_aus_cement(temp_fit[i]))
        dn_cem=((N_total-N_product[i-1])*(AA-L(C_in_aus_molefraction[i-
1]))+x*(L(C_dn[i-1])-AA))/(-1/3.0+AA)
        current_step_cem=dn_cem/12*VCement(temp_fit[i]) #12 iron atoms in one
unit cell of cementite.
        current_gama_v=(N_total-sum(dn_alpha[:i-1])-x-sum(dn_cement[:i-1])-
dn_cem)/4*Vgama_new(CTE_0_gama,C_in_gama(i,x,dn_alpha,C_dn,N_total,N_product,temp_
fit,ID_dn),temp_fit[i]) #Vgama should be fixed to get rid of x/N_total

modeled_V=previ_alpha_v+previ_cem_v+current_step_alpha+current_step_cem+current_ga
ma_v

    #print (raw_input('press any key to continue in individual loop'))
    return (modeled_V)**(1/3.0)

#N_alpha=np.linspace(0,N_total*0.9,len(temp_fit))
# Mn= chemistry0['mn']
# Ni= chemistry0['ni']
# Cr= chemistry0['cr']
# Mo= chemistry0['mo']
# Si= chemistry0['si']
# Cu= chemistry0['cu']

#

```

```

print
# def Bainite_ss_factor(T,C): #using relaxation observed in isothermal
# experiments, C is the amount of C in Austenite in mole fraction.
#     SSF_coef=P.polyfit([Bs(C)-100,Ms(C)],[0,1],1) #this has to fixed. lower
Bs has to be used not just Bs which is for upper bainite.
#     BSSF=P.polyval(T,SSF_coef)
#     if BSSF<0: BSSF=0
#     if BSSF>1: BSSF=1
#     return BSSF
# print (raw_input('press any key to continue'))
dn_alpha=np.ones(len(temp_fit))*10**(np.log10(N_total)-4)
dn_cement=np.zeros(len(temp_fit))
#C_dn_alpha=abs((C_in_alpha((temp_fit[:-1]+temp_fitstart=time.time())t[1:])/2)))
#This is the C mole fraction associated with each dn
C_dn=np.zeros(len(temp_fit))
ID_dn=[]
#print (raw_input('press any key to continue'))
simulated_l=np.zeros(len(dn_alpha))
C_in_aus=np.ones(len(dn_alpha))*C0
C_in_aus_molefraction=np.ones(len(dn_alpha))*C0
# CTE_aus_current=np.zeros(len(dn_alpha))
N_product=np.zeros(len(temp_fit))
# N_prod=np.zeros(len(temp_fit))

for j in xrange(1):
    #print '*****'
    i=1 # start filling dn_alpha from the third element since the first two
should be zero. the first
    for i in xrange(1,num_of_analyzed_points):
        T=(temp_fit[i-1]+temp_fit[i])/2
#         print i, "out of", len(temp_fit)-1 ,"points completed"
#         # at every i we calculated the dn[i-1]
#         print (raw_input('press any key to continue in individual loop'))
# First we should determine what is the type of the product forming between i-1 and

```

i. We do that by assuming $C_{in_austenite}$ during current step is equal to that of the last step.

```

    if i>1:
        if temp_fit[i-1]<Bs(C_in_aus[i-1]):
#             print "    Bainite forming according to empirical formula"
                ID_dn.append("BF")
        else:
            ID_dn.append("PF")

            if ID_dn[i-1][0:2]=="PF":
                C_dn[i-1]=C_in_alpha(T)
                if C_dn[i-1]>C_in_gama(i-1,dn_alpha[i-
1],dn_alpha,C_dn,N_total,N_product,temp_fit,ID_dn):
                    C_dn[i-1]=C_in_gama(i-1,dn_alpha[i-
1],dn_alpha,C_dn,N_total,N_product,temp_fit,ID_dn)
                elif ID_dn[i-1][0:2]=="BF":
#                     T=(temp_fit[i-1]+temp_fit[i])/2
                    C_eq=C_in_alpha(T)
                    C_dn[i-1]=Bainite_ss_factor(T,C_in_gama(i-1,dn_alpha[i-
1],dn_alpha,C_dn,N_total,N_product,temp_fit,ID_dn))*(C_in_gama(i-1,dn_alpha[i-
1],dn_alpha,C_dn,N_total,N_product,temp_fit,ID_dn)-C_eq)+C_eq
                    if C_dn[i-1]>C_in_gama(i-1,dn_alpha[i-
1],dn_alpha,C_dn,N_total,N_product,temp_fit,ID_dn):
                        C_dn[i-1]=C_in_gama(i-1,dn_alpha[i-
1],dn_alpha,C_dn,N_total,N_product,temp_fit,ID_dn)
                    if file_list[k][6].lower()[0:3]==('yes' or 'y') and C_in_gama(i-
1,dn_alpha[i-
1],dn_alpha,C_dn,N_total,N_product,temp_fit,ID_dn)>Solubility_aus_cement(temp_fit[
i-1]):
                        ID_dn[i-1]=ID_dn[i-1]+"+"+"Cem"
                    elif (("user" in file_list[k][6].lower()) and (C_in_gama(i-
1,dn_alpha[i-
1],dn_alpha,C_dn,N_total,N_product,temp_fit,ID_dn)>Solubility_aus_cement(temp_fit[
i-1]))):
                        LCT=[float(s) for s in file_list[k][7].split() if
s.isdigit()][0]#LCT stands for Lowest cementite temperature
                        if T>LCT:

```

```

        ID_dn[i-1]=ID_dn[i-1]+"+"+"Cem"
elif i==1:
    ID_dn.append("PF")
    C_dn[i-1]=C_in_alpha((temp_fit[i-1]+temp_fit[i])/2)
else:
    print "There is a problem with ID_dn"
    quit()
res=scipy.optimize.minimize(expm_l_individual_err, dn_alpha[i-1],
method='Nelder-Mead', options={})
K=res.x
dn_alpha[i-1]=K[0]

if ((dn_alpha[i-1])/N_total)<1e-4:
    dn_alpha[i-1]=0

    if ID_dn[i-1][3:6]=="Cem":
#
        =(1/(1/3.0-
L(Solubility_aus_cement(temp_fit[i])))*(np.sum(dn_alpha[:i-1]*C_dn[:i-
1])+(np.sum(dn_cement[:i-1])/3.0)+(N_total-
N_product[i])*L(Solubility_aus_cement(temp_fit[i]))+dn_alpha[i]*(L(C_in_alpha((tem
p_fit[i]+temp_fit[i-1])/2.0)))-N_total*(L(C0)))
        AA=L(Solubility_aus_cement(temp_fit[i]))
        dn_cement[i-1]=((N_total-N_product[i-1])*(-
L(C_in_aus_molefraction[i-1])+AA)+dn_alpha[i-1]*(L(C_dn[i-1])-AA))/(-1/3.0+AA)
#
        dn_cement[i-1]=((N_total-N_product[i-
1])*(L(C_in_aus_molefraction[i-1])-L(Solubility_aus_cement(temp_fit[i])))-
dn_alpha[i-1]*(L(C_dn[i-1])-L(Solubility_aus_cement(temp_fit[i]))))/(L(0.25)-
L(Solubility_aus_cement(temp_fit[i])))
        #lets put a constraint on dn to control noise which result in
incorrect negative dn

N_product[i]=N_product[i-1]+dn_alpha[i-1]+dn_cement[i-1]
#print (raw_input('press any key to go to next point in main loop'))
simulated_l[i]= expm_l_individual(dn_alpha[i-1],i)

```

```

        C_in_aus[i]=C_in_gama(i,dn_alpha[i-
1],dn_alpha,C_dn,N_total,N_product,temp_fit,ID_dn)
        C_in_aus_molefraction[i]=C_in_gama(i,dn_alpha[i-
1],dn_alpha,C_dn,N_total,N_product,temp_fit,ID_dn)
#         C_in_aus[i]= mf_to_wp(C)
        C_total_in_ferrite=sum(dn_alpha[:i]*L(C_dn[:i]))
        C_total_in_cementite=sum(dn_cement[:i]*(1/3.0))
        C_total_in_gama=(N_total-N_product[i])*L(C_in_aus_molefraction[i])
        Initial_C=N_total*L(C0)

C_balance=(C_total_in_ferrite+C_total_in_cementite+C_total_in_gama)/Initial_C
        print "    T is" , temp_fit[i]
        print "    Current product is ", ID_dn[i-1]
        print "    Fraction transformed is ", "%.3f" %(N_product[i]/N_total)
        print "    C balance (should be 1)= ", C_balance
#         print "    dil_fit = ", dil_fit[i]
        print "-----"

dataname=filename[:-4]
f=np.zeros(len(time_fit))
f=N_product/N_total
plt.figure(2)
plt.subplot(211)
plt.plot(temp_analysis,dil_analysis+L0,'.',label= 'Experimental '+ dataname)
plt.xlabel('Temperature (C)')
plt.ylabel('Sample length(m)')
plt.grid()

plt.figure(2)
plt.subplot(211)
plt.plot(temp_fit[1:-1],simulated_l[1:-1], 'o',label= 'Calculated ' +
dataname)
plt.legend(loc=2)
plt.subplot(212)
plt.plot(temp_fit,f,'o-', label= dataname)
plt.xlabel('Temperature (C)')
plt.ylabel('Ferrite mole fraction')

```

```

plt.legend()
plt.grid()

result_master_time.append(time_fit[1:])
result_master_temp.append(temp_fit[1:])
result_master_dil.append(simulated_l[1:])
result_master_fraction.append(f[1:])
result_master_FD_fraction.append(dn_alpha/N_total)
result_master_C_in_FD_fraction.append(C_dn[:-1])
result_master_C_in_FD_WP.append(mf_to_wp(C_dn[:-1]))
result_master_cem_fraction.append(dn_cement[1:]/N_total)
result_master_ID.append(ID_dn)

def master_fiter(x):
    print '-'*49
    i=0
    for val in x: # I am a genius!
        globals()[x0_param_names[i]]=val
        print x0_param_names[i]+'=' , "%.30e" %val
        print
        i=i+1

    processes = [mp.Process(target=Fitter,
args=((file_list[k][0],output,a0_gama,CTE_alpha_a,\
    CTE_alpha_b,CTE_alpha_c,a0_alpha,c_wf_for_cte,Bs_master_dic, MF_dic,
Ms_master_dic,C_in_alpha_master_dic ))) for k in range(len(file_list))]

#    processes = [mp.Process(target=V10,
args=((file_list[0][0],file_list[0][1],file_list[0][2],output,a0_gama,CTE_0_gama,C
TE_alpha_b,CTE_alpha_a)))]
#    processes = [mp.Process(target=V10,
args=((file_list[1][0],file_list[1][1],file_list[1][2],output,a0_gama,CTE_0_gama,C
TE_alpha_b,CTE_alpha_a)))]
#    processes = [mp.Process(target=V10,
args=((file_list[2][0],file_list[2][1],file_list[2][2],output,a0_gama,CTE_0_gama,C
TE_alpha_b,CTE_alpha_a)))]

```

```

for p in processes:
    p.start()
for p in processes:
    p.join()
results = [output.get() for p in processes]
# print results
err=0
for i in range(len(results)):
    err+=results[i][0]
    Bs_master_dic.update(results[i][1])
    Ms_master_dic.update(results[i][2])
    MF_dic.update(results[i][3])
    C_in_alpha_master_dic.update(results[i][4])
print 'err=          ', "%.30e" %err
return err

x0_param_names=[]
x0_param_vals=[]
x0_param_bounds=[]
for key in optimized_param.keys():
    if optimized_param[key]==1:
        x0_param_names.append(key)
        x0_param_vals.append(eval(key))
        x0_param_bounds.append(optimized_param_bounds[key])
x0_param_vals=np.array(x0_param_vals)

#x0=[a0_gama,CTE_alpha_c,CTE_alpha_b,CTE_alpha_a,a0_alpha,c_wf_for_cte]
##master_fiter(x0)
#res = scipy.optimize.minimize(master_fiter,x0, method='Nelder-Mead')
#B= res.x

if __name__=='__main__':
# global Bs_master_dic, MF_dic, Ms_master_dic
# Bs_master_dic=mp.Manager().dict()
# MF_dic=mp.Manager().dict()
# Ms_master_dic=mp.Manager().dict()

```



```

L0_correction_report=""
if correct_L0.lower()=='yes':
    if L0_correction_method==3:
        L0_correction_report="yes with method %d, normalizing temp=%d"
%(L0_correction_method,normalizing_temp)
    else:
        L0_correction_report="yes with method %d" %L0_correction_method
else:
    L0_correction_report=correct_L0
if use_avr_CTE_product==0:
    initial_CTE_alpha_guess="no"
else:
    initial_CTE_alpha_guess='yes'
#this function saves the raw data and results as an excel file.

run_parameters={"sr":sr,"reg_order":reg_order,"interval":interval,"end_fit_WF":end
_fit_WF,
    'Bs_model':Bs_model, "Ms_model":Ms_model, "overall_fit_WF":overall_fit_WF,
"err_end_slope_WF":err_end_slop_WF,
    "err_maximum_transformation_WF":err_maximum_transformation_WF,"XRD for
a0_alpha":use_XRD_for_a0_alpha,
    "a0_gama":a0_gama,"a0_alpha":a0_alpha, "CTE_alpha_a":CTE_alpha_a,
    "CTE_alpha_b":CTE_alpha_b,
"CTE_alpha_c":CTE_alpha_c,"c_wf_for_cte":c_wf_for_cte,
    "c_wf_for_a0":c_wf_for_a0 ,
"script_name":current_script_name,'optimized':optimize,
    "L0_Correction":L0_correction_report, "use avr CTE product for initial guess
of CTE_alpha":initial_CTE_alpha_guess}

saver(file_list,time_master, temp_master, dil_master, result_master_time,
result_master_temp, result_master_dil,
result_master_fraction,result_master_ID,
    result_master_FD_fraction, result_master_C_in_FD_fraction,
result_master_C_in_FD_WP,
    result_master_cem_fraction, run_parameters)
end=time.time()
print 'run time=',end-start

```

```

if sys.platform[:3]=="lin":
    os.system("spd-say finished")
#cProfile.run('main()')
#main()
#engine = pyttsx.init()
#engine.say('program has finished running.')
#engine.runAndWait()

```

A2-3 Result Saver

```
# -*- coding: utf-8 -*-
```

```
"""
```

```
Created on Wed Dec 30 09:07:26 2015
```

```
Cross platform (Windows and Linux compatible)
```

```
@author: nasseh
```

```
"""
```

```
global sr, reg_order, interval
```

```
#this scrip saves the results of calculation in the xlsx format
```

```
def saver(file_list,time_cond_master, temp_cond_master, dil_cond_master, \
result_master_time, result_master_temp, result_master_dil, result_master_fraction, \
result_master_ID,result_master_FD_fraction, result_master_C_in_FD_fraction, \
result_master_C_in_FD_WP, result_master_cem_fraction, run_parameters):
```

```
    global sr, reg_order, interval
```

```
    from openpyxl import Workbook
```

```
    import os
```

```
    import time;
```

```
    import sys
```

```
    current_dir=os.getcwd()
```

```
    A=os.listdir(current_dir)
```

```
    if 'Results' not in A:
```

```
        if sys.platform[:3]=='win':
```

```
            os.makedirs(current_dir+'\\Results')
```

```
        else:
```

```
            os.makedirs(current_dir+'/Results')
```

```

wb = Workbook()
wb.remove_sheet(wb.get_sheet_by_name("Sheet"))
ws = wb.create_sheet(title="Run parameters")
i=0

keys=["sr", "reg_order", "interval", "end_fit_WF", "overall_fit_WF", "err_end_slope_WF",
\
"err_maximum_transformation_WF", 'Bs_model', "a0_gama", \
"a0_alpha", "CTE_alpha_a", "CTE_alpha_b", "CTE_alpha_c", "c_wf_for_cte", "c_wf_for_a0"]
for key in keys:
    i=i+1
    ws.cell(row=i, column=1, value=key)
    ws.cell(row=i, column=2, value=run_parameters[key])

for i in xrange(len(file_list)):
    ws = wb.create_sheet(title=file_list[i][0])
    col=1
    ws.cell(row=1, column=col, value="time_conditioned(s)")
    for row in xrange(2, len(dil_cond_master[i])+2):
        ws.cell(row=row, column=col, value=time_cond_master[i][row-2])

    col=2
    ws.cell(row=1, column=col, value="Temp_conditioned(C)")
    for row in xrange(2, len(dil_cond_master[i])+2):
        ws.cell(row=row, column=col, value=temp_cond_master[i][row-2])

    col=3
    ws.cell(row=1, column=col, value="dil_conditioned(m)")
    for row in xrange(2, len(dil_cond_master[i])+2):
        ws.cell(row=row, column=col, value=dil_cond_master[i][row-2])

    col=6
    ws.cell(row=1, column=col, value="time_result(s)")
    for row in xrange(2, len(result_master_time[i])+2):
        ws.cell(row=row, column=col, value=result_master_time[i][row-2])

```

```

col=7
ws.cell(row=1,column=col,value="Temp_result(C)")
for row in xrange(2,len(result_master_temp[i])+2):
    ws.cell(row=row, column=col, value=result_master_temp[i][row-2])

col=8
ws.cell(row=1,column=col,value="dil_result(m)")
for row in xrange(2,len(result_master_dil[i])+2):
    ws.cell(row=row, column=col, value=result_master_dil[i][row-2])

col=9
ws.cell(row=1,column=col,value="fraction transformed")
for row in xrange(2,len(result_master_fraction[i])+2):
    ws.cell(row=row, column=col, value=result_master_fraction[i][row-2])

col=10
ws.cell(row=1,column=col,value="phase ID")
for row in xrange(2,len(result_master_ID[i])+2):
    ws.cell(row=row, column=col, value=result_master_ID[i][row-2])

col=11
ws.cell(row=1,column=col,value="fraction FD formed")
for row in xrange(2,len(result_master_FD_fraction[i])+2):
    ws.cell(row=row, column=col, value=result_master_FD_fraction[i][row-
2])

col=12
ws.cell(row=1,column=col,value="C in FD(mole fraction)")
for row in xrange(2,len(result_master_C_in_FD_fraction[i])+2):
    ws.cell(row=row, column=col,
value=result_master_C_in_FD_fraction[i][row-2])

col=13
ws.cell(row=1,column=col,value="C in FD(W%)")
for row in xrange(2,len(result_master_C_in_FD_WP[i])+2):
    ws.cell(row=row, column=col, value=result_master_C_in_FD_WP[i][row-2])

```

```

col=14
ws.cell(row=1,column=col,value="Fe in cementite(mole fraction)")
for row in xrange(2,len(result_master_cem_fraction[i])+2):
    ws.cell(row=row, column=col, value=result_master_cem_fraction[i][row-
2])

wintime=time.strftime("%Y.%m.%d - %H.%M")

Result_file_name=wintime+".xlsx"
if sys.platform[:3]=='win':
    wb.save(current_dir+'\\Results\\'+Result_file_name)
else:
    wb.save(current_dir+'/Results/'+Result_file_name)

```

A2-4 Data Plotter

This routine is essential for identifying the row numbers used in generating *master_setup.txt*. Although data plotter is used for creating the *master_setup.txt*, it needs *master_setup.txt* to be partially created with correct file names specified in it. The row numbers in the *master_setup* are not needed for running the *data_plotter.py*.

```

# -*- coding: utf-8 -*-
"""
Created on Thu May 14 08:52:35 2015

@author: nasseh
"""
import csv
#imlport sys
import numpy as np
import glob
import matplotlib.pyplot as plt
import os
import pickle
import data_set_conditioner_V2

```

```

current_dir=os.getcwd()
file_list=pickle.load(open(current_dir+'/working_directory/file_list_conditioned.p
kl', 'rb'))
current_dir=os.getcwd()
time_master=pickle.load(open(current_dir+'/working_directory/time_conditioned.pkl'
, 'rb'))
temp_master=pickle.load(open(current_dir+'/working_directory/temp_conditioned.pkl'
, 'rb'))
dil_master=pickle.load(open(current_dir+'/working_directory/dil_conditioned.pkl', '
rb'))

for k in range(len(file_list)):
    plt.figure()
    plt.plot(temp_master[k],dil_master[k], 'o')
    plt.title(file_list[k][0])
    plt.xlabel('Temperature (C)')
    plt.ylabel('Dilation (micron)')
    xy=zip(temp_master[k],dil_master[k])
    for i in xrange(200):

plt.annotate(i*len(xy)//200,(temp_master[k][i*len(xy)//200],dil_master[k][i*len(xy)
//200]))

```

A2-5 Data-set Conditioner

This program normalizes the user provided dilation data to a smaller size, which is less noisy and more predictable.

```

# -*- coding: utf-8 -*-
"""
Created on Wed Dec 23 03:55:32 2015

@author: nasseh
"""

```

```

# This program is called data_set_conditioner. It gets rid noise and excessive
data point.

import csv
import numpy as np
import matplotlib.pyplot as plt
from numpy.polynomial import polynomial as P
import pickle
import os

#Load setup file which contains information that master_fitter and fitter needs to
work.
#each line in the set file is like this:
#filename,Aus_min_row,Aus_max_row,fer_min_row,fer_max_row,L0,cementite conditions,
#values must be separated by comma "," and all lines must end with a comma.
file_list=[]
d=open('master_setup.txt','r')
for line in d:
    temp=line.split(',')
    temp[1:6]=map(float,temp[1:6]) # get rid of end character and turn numbers
into float
    if temp[0][0]=='#' or temp[0][0]=='%': #this if statement ignores the lines in
master_setup file that begin with '#' or '%'.
        pass
    else:
        file_list.append(temp)

current_dir=os.getcwd()
A=os.listdir(current_dir)
if 'working_directory' not in A:
    os.makedirs(current_dir+'/working_directory')

output = open(current_dir+'/working_directory/file_list_conditioned.pkl', 'wb')
pickle.dump(file_list, output)
output.close()

time_master=[]

```

```

temp_master=[]
dil_master=[]
k=0

for var in file_list:
    Data=open(var[0],'r')
    D= csv.reader(Data)
    t = []
    temp = []
    dil = []
    for row in D:
        t.append(row[0])
        temp.append(row[1])
        dil.append(row[2])
    del t[0],temp [0] ,dil [0]
    Data.close()

    t = np.array(map(float,t))
    temp = np.array(map(float,temp))
    dil =np.array(map(float,dil))*1E-6
    time_master.append(t)
    temp_master.append(temp)
    dil_master.append(dil)
    del t, temp, dil, row

reg_order=2 #The order of polynomial used in noise filtering. Higher sr better
have higher reg-order
def regresser(bottom,center,top):
    time_reg=time_fit[center]
    coef1= P.polyfit(time_fit[bottom:top],temp_fit[bottom:top],reg_order)
    temp_reg=P.polyval(time_fit[center],coef1)
    coef1= P.polyfit(time_fit[bottom:top],dil_fit[bottom:top],reg_order)
    dil_reg=P.polyval(time_fit[center],coef1)
    regressed_point=[time_reg,temp_reg,dil_reg]
    return regressed_point

#def range_finder(T,dT)

```

```

start=0
time_cond=[] #conditioned time data
temp_cond=[]
dil_cond=[]

time_cond_master=[] #master file that has all of the conditioned time data
temp_cond_master=[]
dil_cond_master=[]

regressed_point_list=[]

for i in xrange(len(time_master)):
    print i
    time_cond.append(time_master[i][0])
    temp_cond.append(temp_master[i][0])
    dil_cond.append(dil_master[i][0])
    time_fit=time_master[i]
    dil_fit=dil_master[i]
    temp_fit=temp_master[i]
    points=[]
    for j in xrange(1,len(time_master[i])):
        try:
            reged_point=regresser(j-20,j,j+20)
        except:
            # print"out"
            reged_point=[time_fit[j],temp_fit[j],dil_fit[j]]
            if abs(time_fit[j]-time_cond[-1])>=10:
                points.append(j)
                time_cond.append(time_fit[j])
            elif abs(reged_point[1]-temp_cond[-1])>=3:
                points.append(j)
                temp_cond.append(temp_fit[j])
    regressed_point_list.append(points)
time_cond=[]
temp_cond=[]
dil_cond=[]

```

```

for i in xrange(len(time_master)):
    time_cond=[]
    temp_cond=[]
    dil_cond=[]
    time_cond.append(time_master[i][0])
    temp_cond.append(temp_master[i][0])
    dil_cond.append(dil_master[i][0])
    time_fit=time_master[i]
    dil_fit=dil_master[i]
    temp_fit=temp_master[i]
    points=regressed_point_list[i]
    for j in xrange(1,len(points)-1):
        regressed=regresser(points[j-1],points[j],points[j+1])
        time_cond.append(regressed[0])
        temp_cond.append(regressed[1])
        dil_cond.append(regressed[2])
    time_cond_master.append(time_cond)
    temp_cond_master.append(temp_cond)
    dil_cond_master.append(dil_cond)

output = open(current_dir+'/working_directory/time_conditioned.pkl', 'wb')
pickle.dump(time_cond_master, output)
output.close()

output = open(current_dir+'/working_directory/temp_conditioned.pkl', 'wb')
pickle.dump(temp_cond_master, output)
output.close()

output = open(current_dir+'/working_directory/dil_conditioned.pkl', 'wb')
pickle.dump(dil_cond_master, output)
output.close()

plt.figure(11)
for i in xrange(len(file_list)):
    plt.plot(time_master[i],dil_master[i], label=file_list[i][0])

```

```

for i in xrange(len(file_list)):
    plt.plot(time_cond_master[i],dil_cond_master[i],"o", label=file_list[i][0])
plt.legend()

plt.figure(12)
for i in xrange(len(file_list)):
    plt.plot(temp_master[i],dil_master[i], label=file_list[i][0])

for i in xrange(len(file_list)):
    plt.plot(temp_cond_master[i],dil_cond_master[i],"o", label=file_list[i][0])
plt.legend()

plt.figure(13)
for i in xrange(len(file_list)):
    plt.plot(time_master[i],temp_master[i],label=file_list[i][0])

for i in xrange(len(file_list)):
    plt.plot(time_cond_master[i],temp_cond_master[i],"o", label=file_list[i][0])
plt.legend()

```

A2-6 Cython tools

Cython is a program that can convert slow python script into a fast compiled C code. To speed up the master fitter some of the most frequently called functions are converted using Cython. In Linux OS, the Cython generated binaries are stored in a file named *master_fitter_utils.so*. This file needs to be created by the user. The *master_fitter_utils.so* can compile by typing "sudo python setup_master_fitter_utils.py build_ext --inplace" in a terminal that is opened in the *master_fitter_utils.py* directory. This command will translate *master_fitter_utils.pyx* to *master_fitter_utils.so*. Once the conversion is complete the .so file should be copied to Master_fitter.py directory.

The two files needed for this process are *master_fitter_utils.pyx* and *setup_master_fitter_utils.py*.

5.2.1.1 setup_master_fitter_utils.py

```
import sys
```

```

if sys.platform[:3]=='win':
    try:
        from setuptools import setup
        from setuptools import Extension
    except ImportError:
        from distutils.core import setup
        from distutils.extension import Extension
else:
    from distutils.core import setup
from Cython.Build import cythonize
from distutils.core import setup
from Cython.Build import cythonize

import numpy
setup(
    ext_modules = cythonize("master_fitter_utils.pyx"),
    include_dirs=[numpy.get_include()]
)

```

5.2.1.2 master_fitter_utils.pyx

```

import numpy as np
cimport numpy as np
from numpy.polynomial import polynomial as P

def VCement(float T): #T in centigrade.
    return 0.45234E-9*0.50883E-9*0.67426E-9*(1+(5.311E-6-1.942E-9*T+9.655E-
12*T*T)*(T-20))**3

def Valpha(float a0_alpha, float C, float T, float CTE_alpha_a,float CTE_alpha_b,
float CTE_alpha_c, float c_wf_for_cte, float c_wf_for_a0, np.ndarray[np.float_t,
ndim=1] A): #C is in mole fraction, T is in celsius
    #C= C_in_alpha(T) #This generates C in mole fraction. The next line will
change it to weight percent
    cdef float CTE_alpha_CC, y, A_alpha, C_alpha, Valpha
    CTE_alpha_CC=CTE_alpha_c-C*c_wf_for_cte
    C=P.polyval(C,A)

```

```

y = CTE_alpha_a/3*(T*T*T-8000)+CTE_alpha_b/2*(T*T-400)+CTE_alpha_CC*(T-20) #
this is the integration of the CTE equation.
if C<0.550:
    A_alpha=(a0_alpha+c_wf_for_a0*C)*(1+y)
    C_alpha=A_alpha
else:
    A_alpha=(a0_alpha-0.013e-10*C)*(1+y)
    C_alpha=(a0_alpha+0.116e-10*C)*(1+y)
return A_alpha*A_alpha*C_alpha

def Vbainite(float a0_alpha, float C, float T, float CTE_alpha_a,float
CTE_alpha_b, float CTE_alpha_c, float c_wf_for_cte,float c_wf_for_a0,
np.ndarray[np.float_t, ndim=1] A): #C is in mole fraction, T is in celsius
    #C= C_in_alpha(T) #This generates C in fole fraction. The next line will
change it to weight percent
    cdef float CTE_alpha_CC, y, A_alpha, C_alpha, Valpha
    CTE_alpha_CC=CTE_alpha_c-C*c_wf_for_cte
#    C = 13.556037046*C*C*C + 16.897583563*C*C + 21.525922793*C -
0.0000000034672863191
    C=P.polyval(C,A)
    y = CTE_alpha_a/3*(T*T*T-8000)+CTE_alpha_b/2*(T*T-400)+CTE_alpha_CC*(T-20) #
this is the integration of the CTE equation.
if C<0.55:
    A_alpha=(a0_alpha+c_wf_for_a0*C)*(1+y)
    C_alpha=A_alpha
else:
    A_alpha=(a0_alpha-0.013e-10*C)*(1+y)
    C_alpha=(a0_alpha+0.116e-10*C)*(1+y)
return A_alpha*A_alpha*C_alpha

```